CRANFIELD UNIVERSITY

HAMAD ALHAJERI

Heat Removal in Axial Flow High Pressure Gas Turbine

PhD
Academic Year 2015 -2016

Supervisor: Dr. J. Amaral Teixeira
Dr. A. Addali

CRANFIELD UNIVERSITY

SCHOOL OF ENGINEERING
Department of Power and Propulsion

PhD Thesis

HAMAD ALHAJERI

Heat Removal in Axial Flow High Pressure Gas Turbine

Supervisor: Dr. Joao Amaral Teixeira
Dr. A. Addali

April 2016

This thesis is submitted in partial fulfilment of the requirements for the degree of Doctor of Philosophy

To my Father and Mother

Executive Summary

The demand for high power in aircraft gas turbine engines as well as industrial gas turbine prime mover promotes increasing the turbine entry temperature, the mass flow rate and the overall pressure ratio. High turbine entry temperature is however the most convenient way to increase the thrust without requiring a large change in the engine size.

This research is focused on improving the internal cooling of high pressure turbine blade by investigating a range of solutions that can contribute to the more effective removal of heat when compared with existing configuration. The role played by the shape of the internal blade passages is investigated with numerical methods. In addition, the application of mist air as a means of enhanced heat removal is studied.

The research covers three main area of investigation. The first one is concerned with the supply of mist on to the coolant flow as a mean to enhancing heat transfer. The second area of investigation is the manipulation of the secondary flow through cross-section variation as a means to augment heat transfer. Lastly a combination of a number of geometrical features in the passage is investigated.

A promising technique to significantly improve heat transfer is to inject liquid droplets into the coolant flow. The droplets which will evaporate after travelling a certain distance, act as a cooling sink which consequently promote added heat removal. Due to the promising results of mist cooling in the literature, this research investigated its effect on a roughened cooling passage with five levels of mist mass percentages.

In order to validate the numerical model, two stages were carried out. First, one single-phase flow case was validated against experimental results available in the open literature. Analysing the effect of the rotational force, on both flow physics and heat transfer, on the ribbed channel was the main concern of this investigation. Furthermore, the computational

results using mist injection were also validated against the experimental results available in the literature.

Injection of mist in the coolant flow helped achieve up to a 300% increase in the average flow temperature of the stream, therefore in extracting significantly more heat from the wall. The Nusselt number increased by 97% for the rotating leading edge at 5% mist injection.

In the case of air only, the heat transfers decrease in the second passage, while in the mist case, the heat transfer tends to increase in the second passage. Heat transfer increases quasi linearly with the increase of the mist percentage when there is no rotation. However, in the presence of rotation, the heat transfers increase with an increase in mist content up to 4%, thereafter the heat transfer whilst still rising does so more gradually.

The second part of this research studies the effect of non-uniform cross-section on the secondary flow and heat transfer in order to identify a preferential design for the blade cooling internal passage. Four different cross-sections were investigated. All cases start with square cross-section which then change all the way until it reaches the 180 degree turn before it changes back to square cross-section at the outlet. All cases were simulated at four different speeds. At low speeds the rectangle and trapezoidal cross-section achieved high heat transfer. At high speed the pentagonal and rectangular cross-sections achieved high heat transfer. Pressure loss is accounted for while making use of the thermal performance factor parameter which accounts for both heat transfer and pressure loss. The pentagonal cross-section showed high potential in terms of the thermal performance factor with a value over 0.8 and higher by 33% when compared to the rectangular case.

In the final section multiple enhancement techniques are combined in the sudden expansion case, such as, ribs, slots and ribbed slot. The maximum heat enhancement is achieved once all previous techniques are used together. Under these circumstances the Nusselt number increased by 60% in the proposed new design.

TABLE OF CONTENTS

LIST OF FIGURES

Nomenclature

LIST OF ABBREVIATIONS

AR	Aspect ratio
BL	Boundary layer
Bo	Buoyancy parameter
CFD	Computational Fluid Dynamics
DR	density ratio
DPM	Discrete phase model
LE	Leading edge
PS	Pressure surface
GT	Gas Turbine
Ro	Rotation Number
RSM	Reynolds stress model
SIMPLEC	Semi-Implicit Method for Pressure Linked Equations-Consistent
SOC	Second Order Closure
SS	Suction surface
SST	Shear Stress Transport
TE	Trailing edge
TI	Turbulence intensity
TKE	Turbulence Kinetic Energy
TPF	Thermal performance factor
WF	Wall functions

LIST OF SYMBOLS

Latin symbols Definition Units

Cp	Static pressure coefficient
Dh	Hydraulic diameter
k	Turbulent kinetic energy
p	Pressure
r	Radius of curvature
R	Radius of arc
Re	Reynolds number
P	Pitch
T	Temperature
Tu	Turbulence intensity
U+	Dimensionless velocity
V	Velocity
y+	Dimensionless wall distance
q	Heat flux
m	mass flow rate
h	enthalpy
v^2	velocity scalar
f	ellipse equation
Nu	Nusselt number

V_P	velocity vector
F	Force
h_{fg}	latent heat of particle
h	convective heat transfer coefficient
T_∞	Ambient temperature of surrounding air
k	thermal conductivity

Greek symbols Definition Units

β	Flow angle
δ	Boundary layer thickness
ε	Turbulence dissipation rate
μ	Dynamic viscosity
ρ	Density
ω	Specific dissipation rate
Ω	rate of rotation
η	efficiency
λ_ε	Blending function
ϵ_p	particle emissivity
θ_R	radiation temperature
ℓ_m	turbulent length scale in Prandtl's mixing length turbulence model.
ℓ_t	turbulent length scale

1 Introduction

This chapter provides a general background presentation to gas turbines, including a brief description of how a gas turbine functions in 1.1, gas turbines, using the fundamental thermodynamic representation of the gas turbine as a Brayton cycle (1.2 gas turbine thermodynamics and efficiency). The materials for construction are then discussed in 1.3, together with gas turbine material selection. The mechanical limitations on gas turbine components efficiency are explored in 1.4, including the effect of cooling on turbine performance, together with a review of established methods of gas turbine cooling, such as film, impingement and mist cooling were highlighted. The focus of this research is the study of convection cooling, particularly where it involves the flow of a cooling fluid through the internal labyrinth passage of turbine blades.

1.1 **Gas turbines**

A gas or combustion turbine is a type of internal combustion engine that is composed of a rotating axial compressor upstream joined to a turbine downstream, with a combustion chamber between the two. Gas turbines (GTs) play a key role in power generation and modern aeronautical propulsion, and offer many advantages: they are reliable, relatively free from vibration, and have a substantial thrust-to-weight ratio. The work from a GT engine may be produced either as torque in a shaft or as thrust in a jet Figure 1. In addition to aircraft propulsion, GTs are often utilized on ships, trains, helicopters, tanks, and to a lesser degree, on cars, buses, and motorcycles. Industrial GTs are used for both power generation and mechanical drive (for example, oil and gas platforms require these engines as drivers to pump gas into wells).

There is an ongoing demand for higher thrust and power from aircraft GT engines and industrial GT prime movers respectively. The three engine cycle parameters that have the greatest effect on the GT propulsive and thermal efficiencies are turbine entry temperature, fuel mass flow rate and overall pressure ratio. Increasing turbine entry temperature is the most convenient way to increase the thrust without requiring a significant change in engine size. Increasing the turbine inlet temperature (TIT) correspondingly increases the overall efficiency of the engine, but there are limitations to increasing TIT. The maximum allowable TIT is limited by the properties of the turbine blade alloy and the deployed cooling technology. Through the development of advanced materials and cooling methods, turbine inlet temperature exceeding 2500 K can be managed. Naturally, the airfoil of the gas turbines should be cooled sufficiently for safe operation and for long-term durability and reliability.

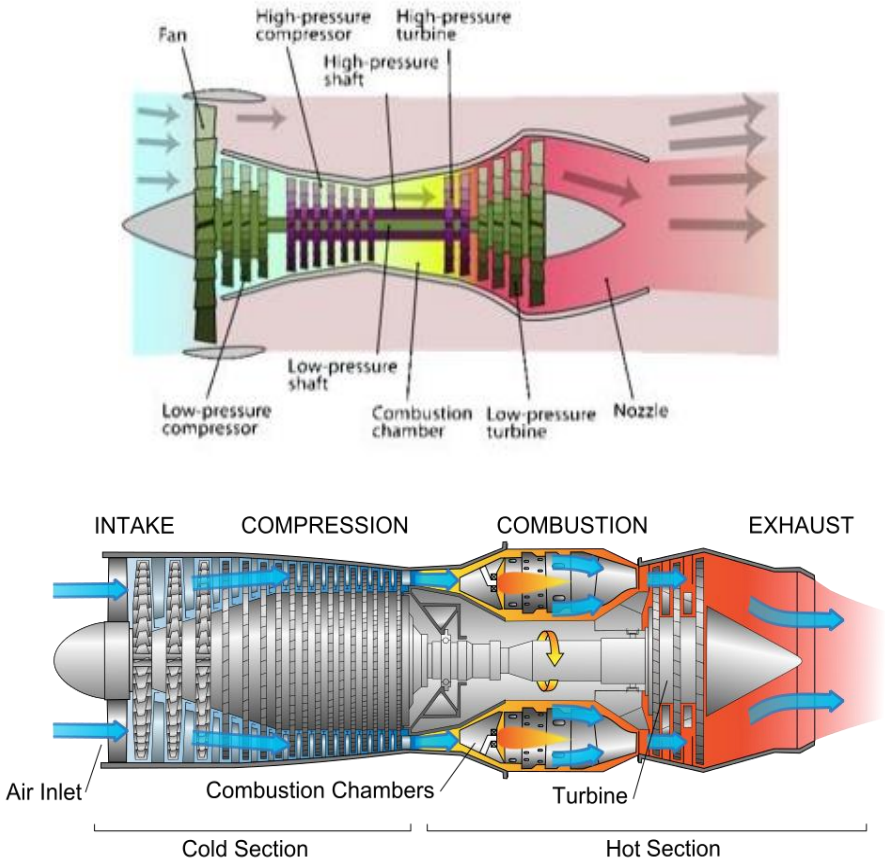

Figure 1 Schematics of turbofan and turbojet gas turbines [1]

1.2 Gas turbine thermodynamics and efficiency

The ideal cycle for a GT consists of two constant pressure processes, in essence, heating and cooling and two isentropic processes in the form of a compression and an expansion. This is called the Joule-Brayton cycle or the constant pressure cycle. The Brayton gas turbine has three main parts: a gas compressor, a burner (or a combustion chamber) and an expansion tube.

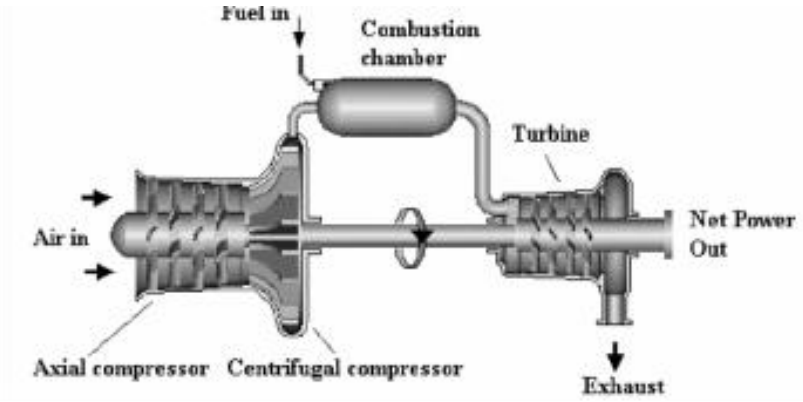

Figure 2 Schematic of a gas turbine open cycle

There are two types of GTs in use, namely the open and closed cycles. The open cycle is where atmospheric air is used in the compressor and the exhaust gases are released into the atmosphere. Open cycle GTs are used for propelling jet airplanes, and the typical layout of an open cycle GT is shown in Figure 2. It consists of a compressor, a combustion chamber, a turbine, and an exhaust nozzle.

Neither the compression nor the expansion can be completely isentropic, and losses throughout the compressor and the turbine are unavoidable working inefficiencies. The efficiency of the GT cycle is the ratio of net power output from the turbine and the heat input in the combustion chamber.

The net power output = Work done by the turbine (P_{out}) – Work required in the compressor (P_{in}) = Heat input in the combustor (φ_{in}) – Heat removed (φ_{out})

$$Thermal\ Efficiency\ (\eta) = \frac{\varphi_{in} - \varphi_{out}}{\varphi_{in}} \quad (1)$$

$$= 1 - \frac{\varphi_{out}}{\varphi_{in}} \quad (2)$$

$$= 1 - \frac{\dot{m}C_p(T_4 - T_1)}{\dot{m}C_p(T_3 - T_2)} \quad (3)$$

After some simplification, it can be shown that:

$$\eta = 1 - \frac{T_1}{T_2} = 1 - \left(\frac{P_1}{P_2}\right)^{\frac{\gamma-1}{\gamma}} \quad (4)$$

Where γ is the heat capacity ratio

The maximum temperature in the Brayton cycle occurs at the end of the combustion process and is limited by the uppermost temperature that the turbine blade material can withstand. The maximum temperature limits the operating pressure ratio (P_1/P_2) of the cycle. If the turbine inlet temperature is held constant, the total work per cycle increases as P_1/P_2 increases (which translates to a higher thermal efficiency). With less work per cycle, a greater mass flow rate (and thus a bigger system) is required to maintain the equivalent power output, which may be uneconomical. The pressure ratio of a GT ranges from about 11 to 16 in most common designs. There is an extensive body of research on various ways to increase the gas turbine output (power) using advanced gas turbine cycles. including intercooling, regenerative *reheat* and *overspray cycle*:

Over the last half century GT thermal efficiency has been steadily increased [2]. The primary reason for this improvement is due to the increase in acceptable combustor outlet temperature attributed to the astonishing progress in material science and cooling technology, which have been effectively applied to GTs. In the past, it was generally considered that optimizing the outlet temperature was the best means of increasing the efficiency of the next generation of engines; however, [3] proved that the efficiency enhancement associated with higher temperatures may be overtaken by the increased losses associated with the required additional cooling flow rates. This will be discussed further in Section 1.4.1.

1.3 **Gas turbine material selection**

The thermal efficiency and the specific energy output of a GT are both strongly influenced by pressure ratio and firing temperature. Thermal efficiency increases with firing temperature and pressure ratio. Typically, super alloys begin to melt at about 1200^{o}C (2200 F While GT material selection is important, it will be briefly discussed here only as the focus of this thesis is on cooling methods.

Components must be sufficiently cooled to maintain metal temperatures well below this melting point. For this purpose, air is channelled from the compressor to the turbine components for cooling. Manifestly, more efficient cooling systems can improve performance. The introduction of relatively cool gas from the compressor into well selected and specific places in the turbine extends engine life, and was a practise since the mid-1960s. Figure 3 illustrates various increment in turbine entry temperatures with the introduction of different cooling techniques, see Sections 1.4.2 to 1.4.7.

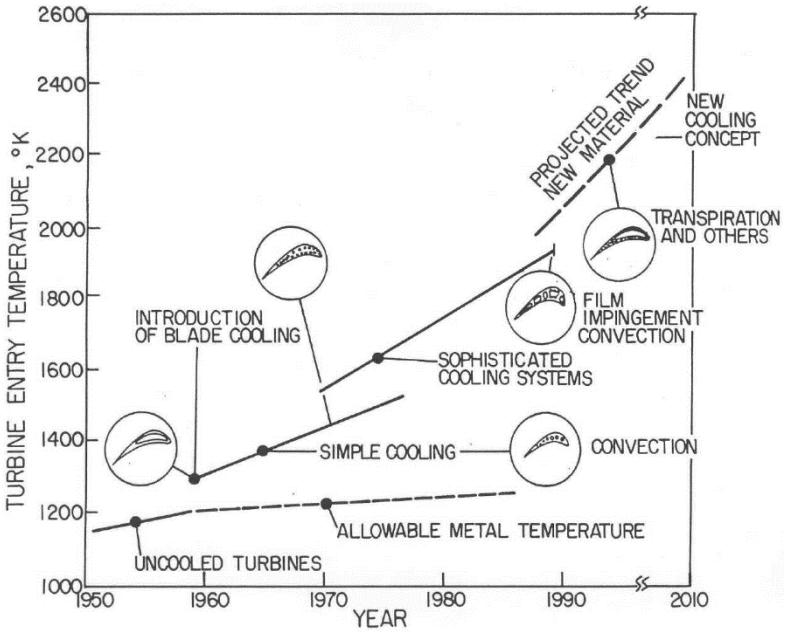

Figure 3 Turbine entry temperature over the years (Rolls Royce)

1.4 **Cooling the gas turbine**

As stated earlier, a high turbine entry temperature translates directly into high thermal efficiency, but this is constrained by the material properties of the turbine blades and nozzle guide vanes. Forced cooling of the blades and vanes allows the working temperature to exceed the melting point of the components with negligibly effect on blade and vane structural integrity. Of course, there is considerable heat conduction from the turbine blades to the turbine disc. Therefore, the discs must also be object of powerful cooling in order to prevent thermal fatigue, or uncontrolled contraction and expansion.

The cooling of turbine components is achieved by liquid or air cooling. Liquid cooling is on the whole more effective because of its inherent high specific heat capacity and the potential for evaporative cooling; however, there can be problems with, for example, leakage, corrosion, and choking. Air cooling retains therefore certain advantages because it is less susceptible to some of these problems, such as leakage.

The two major categories of cooling are, internal and external. The former includes impingement cooling and convection cooling. The latter includes cooling effusion, transpiration cooling, film cooling and mist cooling. These latter two are discussed in further detail in Sections 1.4.2 to 1.4.7.

Figure **4** shows an air cooled nozzle guide vane, turbine blade and cooling airflow. The “pre-swirl nozzles” shown in the figure are incorporated in the design in order to reduce the pressure and temperature of the cooling air flowing to the disc and blade. Engineers design the nozzles to give a significant whirl velocity to the air, which promotes efficient passage of the air into the rotating cooling sections. Cooling air for the turbine discs enters the various annular spaces between them. It then spreads outwards over the faces of the discs. Inter-stage seals control the flow rate. Once the cooling process is complete, the air is ejected into the core gas stream.

The duration of the working lives of turbine vanes and blades depends not only on their structural integrity and shape but also on the method of cooling. As such, it is important to carefully design the internal flow passages.

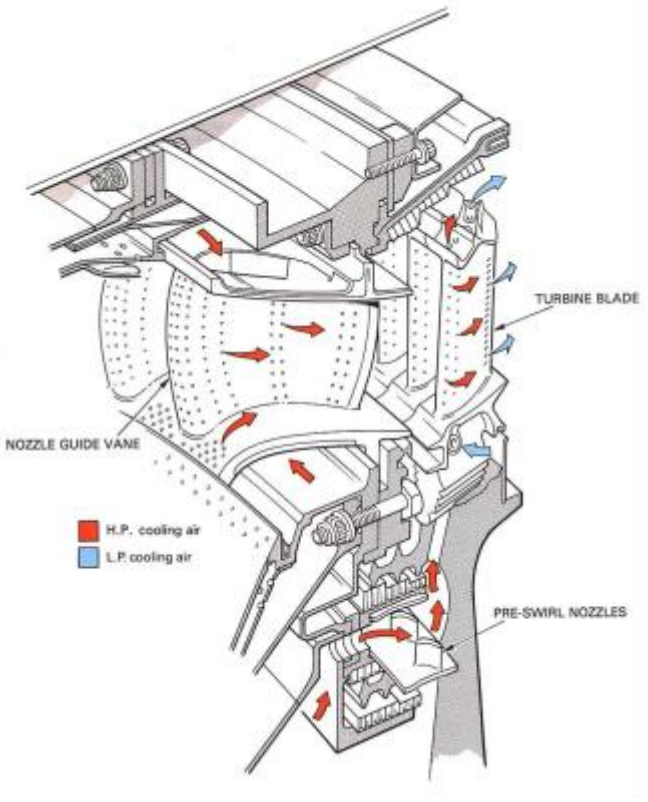

Figure 4. The nozzle guide vane, turbine blade, and nozzle setup [1]

There are numerous established turbine vane and blade design mechanisms for cooling, some of which are discussed in this report. Many cooling mechanisms have been studied, implemented and refined accordingly.

Originally, single pass internal convection cooling was used and was considered very practical and effective. Convection cooling is based on passing cooling air through channels located within the blade, which is somewhat similar to impingement cooling. Heat is carried through the blade by conduction, and into the air flowing inside the blade by convection. Of course, a larger internal surface area translates directly to enhanced heat transfer, so engineers developed various strategies to achieve this: the cooling paths tend to be winding and saturated with small ribs and the internal passages in the blade are usually circular or elliptical in cross-section. The cooling air is supplied by the compressor which

forces the air through these various passages outwards from the hub towards the blade tip. In the case of a GT, the relatively hot combusted fluid outside the blade passes through the cooling passage, joining and mixing with the main stream at the blade tip.

Turbine blade cooling is used in almost every modern engine, often with different methods of cooling such as impingement, convection, and film cooling, used in combination. Years of development have led to multi-pass internal cooling of blades, impingement cooling of vanes, film cooling of both vanes and blades, and other more complicated techniques. One example of a combined impingement and film cooling strategy is shown in Figure 7.

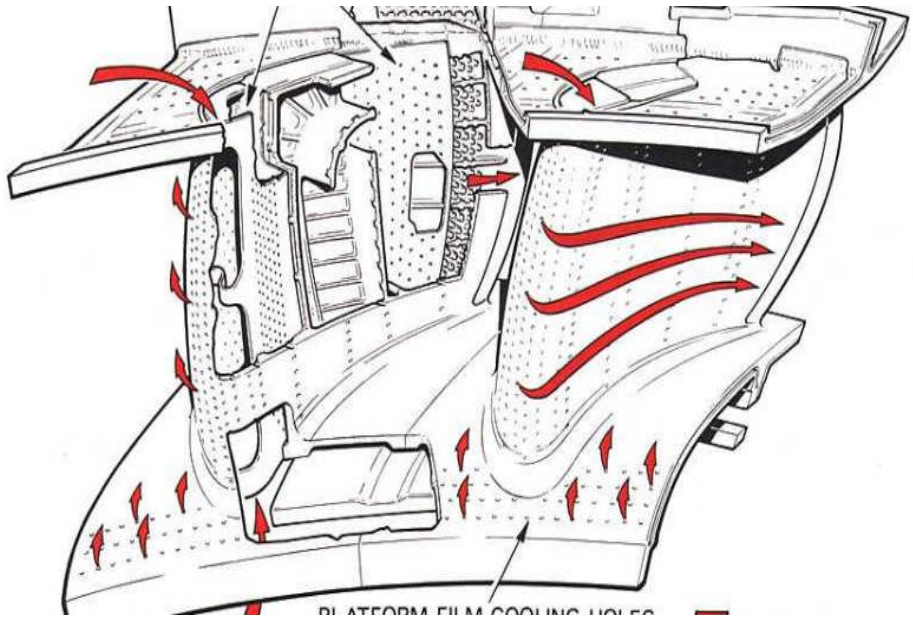

Figure 5 Construction of high pressure nozzle guide vanes and cooling air flow (Rolls Royce, 2005)

Much research has been carried out on the development of blade cooling systems, but no amount of effort would have been sufficient to satisfy the on-going demands of aero-engine designers for higher gas turbine operating temperatures. In particular, the blade leading edge

remains a very difficult area for which to optimize the most successful cooling techniques.

1.5 The effect of cooling on turbine performance

The most common definitions of the efficiency of a cooled turbine relate the real power output to an ideal (theoretical) output, which has to be calculated. Turbine engineers typically use one of two definitions. One is known as the Hartsel efficiency. In this case, the bulk/main gas flow and the various coolant flows to the rotor and stator are taken to expand isentropically and separately. In the second, unnamed definition, these flows are assumed to mix at a constant gas pressure before expanding isentropically. More recently, Horlock [4] proposed a thermodynamically more accurate definition on the basis that the coolant and gas flows mix reversibly and adiabatically before isentropic expansion.

Young and Horlock (2006) [5] presented a review paper on the theoretical development of cooled cycle efficiency of a gas turbine. The review focused on various definitions of the cooled efficiency; the traditional Hartsel efficiency, and two new definitions, mainstream pressure (MP) and weighted-pressure (WP), each of which is a fully reversible efficiency. The working fluid was assumed to be a perfect gas, flows were isentropic, and the combustor was replaced by a constant pressure heater. To complement this research, Torbidoni and Horlock [6] developed a thermodynamics-based computational method for estimating the cooling flow requirements in a high temperature gas turbine.

The new form of efficiency recommended by Young and Horlock is the so-called “fully reversible mixed” efficiency: $\eta_{fr\text{-}mix}$. The theoretical power output is based on an adiabatic, fully reversible process between a reversibly mixed entry state (of the exact stagnation enthalpy and entropy of the entering coolant and hot gas streams) and an exit state at the backpressure. The definition is given as:

$$\eta_{fr-mix} = \frac{h_{01} - h_{03}}{h_{01} - h_{03ss}} \quad (5)$$

Where h_{01} is the combined enthalpy flux of the entry coolant and gas streams, and h_{03ss} is the enthalpy flux following an isentropic expansion to the common backpressure.

Young and Horlock (2006) show unequivocally that the three efficiencies they describe for the initial cooled stage of an industrial gas turbine composed of multiple stages, increase approximately linearly with increase in the fractional coolant flow. They also developed a “fully reversible mixed” efficiency which they claimed had a sound thermodynamic foundation and demonstrated that it gave values for the efficiency that were significantly lower than other forms presently predominantly used.

They also evaluated the different irreversibilities of the flow through a cooled turbine and found that film cooling’s “thermal irreversibility” is higher than the other irreversibilities at high fractional coolant flow [3].

1.6 **Rib turbulated cooling**

A considerable amount of research has been performed on ribbed turbine cooling. Experimental and numerical efforts have been directed toward the smooth rectangular, circular, square, and triangular sections. These different shapes refer to the cross-section of the air passage, while smooth refers to the surface condition of the internal wall of the passage. Introducing repeated ribs into a duct enhances the heat transfer rate but increases friction in the duct so the enhanced heat transfer is accompanied by an unwanted increased pressure drop, which can be several times greater than that for a smooth channel. Studies have also been performed on a turbulated square passage. Turbulators are short

bumps on the surface of the passageway which break up the boundary-layer flow.

1.7 **Mist cooling**

Mist cooling is an important new cooling technique where small amounts of water are injected as mist (minute droplets) into the cooling air. The enhancement in cooling is attributed to the large amount of latent heat of evaporation absorbed by the droplets carried with the coolant air as they evaporate.

Spray cooling usually applies high concentrated steams of liquid droplets close to the surface. These droplets have high momentum with continues movement due to the high kinetic energy resulting wet surfaces. While mist cooling meant not to wet the target surface by applying it away from the surface, using low water droplets concentration that are injected in gas streams. The movement of water droplets in mist cooling is due to the gas-droplet interfacial drag.

Evaporation of mist droplets near the blade or vane surfaces reduces the gas temperature near the surface and plays a major role in protecting the surfaces. Mist droplets that impinge on the blade or vane surfaces will rapidly remove thermal energy and significantly enhance cooling effectiveness.

Each mist droplet is a minute cooling sink, and because it is carried some distance by the air flow before it has completely evaporated it provides "distributed cooling". The evaporation of such continues droplets will also develop into the blade’s downstream region where the effectiveness of single-phase air film cooling is even less.

Mist cooling is an attractive method for cooling turbine blades for the following reasons:

• High cooling effectiveness can be achieved by mist cooling due to higher effective specific heat of the mist-film mixture flow compared to single-phase airflow, which means a reduction in mist-film mean bulk temperature. Higher cooling effectiveness resulting reduction in coolant air mass flow rate so the corresponding turbine output power can be increased.

• Comparing to only airflow, water droplets take longer time to heat up resulting longer travel distance of the mist-film coolant to cover a large area of the blade it starts to blend into the main stream of the hot gas. Thus mist cooling can provide better blade coverage and may be a method for overcoming short coverage problems associated with film cooling.

• Better blade coverage obtained using mist-film cooling may enable the number of rows of coolant holes to be reduced with a consequent improvement in blade mechanical integrity. Lowering the number of coolant holes would also, potentially, reduce aerodynamic losses since less jet-main flow reaction would be expected.

• Mist-film cooling techniques would build on the accumulated experience and extensive research results obtained from the study of film cooling. It would be expected that any benefits from the introduction of mist cooling would be in addition to those obtained from existing film cooling methods.

In real GTs, where the blade temperature can be 800^{o}C - 1400^{o}C, instantaneous boiling will occur when mist droplets hit the blade surface giving rise to an “evaporation thrust force”. Due to the much greater volume of steam compared with liquid droplets, a sudden volume expansion taking place at any contact surface results in a propulsive force thrusting any surrounding water droplets away from the surface. This process greatly enhances heat transfer at the blade surface due to strong heat conduction and momentum interchange.

Barrow [7] determined the technical feasibility of spray-mist cooling by performing a theoretical study of the fundamentals of heat and mass transfer of a spherical water-droplet travelling in humid air. Their analysis began with a time-dependent form of the First Law of Thermodynamics applied to a control volume with a moving boundary/interface corresponding to the droplet surface. By excluding gravity and drag effects the surface was found to be approximately spherical. As evaporation proceeds, heat and mass transfer fluxes occur at the moving boundary, changing the thermal energy stored within the droplet.

Barrow [7] also ascertained the liquid/gas concentration at the droplet's surface using standard analytical relationships between the saturation pressure and the vapour density, as obtained from standard tables of the thermodynamic properties of water and air. Barrow argued that the heat transfer at the surface of the droplet may be due to both forced convection and radiation, and that mass transfer and enthalpy flux occur as evaporation takes place at the surface boundary. They indicated that the energy storage within the droplet is by sensible heating ($mc\Delta T$) as the result of conduction. Furthermore, they found that as the droplet's radius decreased, surface tension effects (caused by the strong hydrophobic bonds of water) increasingly impact the energy transfer process.

The approach by Barrow is sophisticated but does not apply to turbulent two-phase flow where the evaporation of droplets is influenced by many additional parameters such as continuous phase velocity, relative humidity, droplet size distribution, velocity and temperature of the droplets, and continuous phase-droplet and droplet-droplet interactions. To gain an insight into the performance of the system, a detailed knowledge of the impact of every parameter is important, but these parameters are not easily varied independently.

Computational Fluid Dynamics (CFD) is a very useful tool for performing such parametric analyses. Besides simplifying the parametric studies for complex flows like water sprays, CFD offers the advantage that

the latent heat and sensible heat fluxes during the evaporation process can be determined separately. CFD is also capable of providing whole-flow field data: in essence, information on the relevant parameters of the two phases in all points of the computational domain. In addition, it provides a high level of control over the boundary conditions [8].

1.8 **Aims and objectives**

The aim of this research is to explore the potential of controlling and improving heat transfer in turbine cooling passages through a number of means acting in isolation or in combination: manipulation of secondary flows in the cooling passages, use of ribbed turbulators configurations, and the application of mist-air for enhanced heat transfer. The objectives necessary to meet these aims are as follows:

1- Conduct an in-depth literature review on the state of the art in internal cooling for nozzle guide vanes and turbine blades.

2- Review the reported performance of modelling techniques, including turbulence modelling, and heat transfer for a nozzle guide vane and turbine blade.

3- Gain an understanding of the physics of secondary flow in cooling passages and mist-air heat transfer enhancement.

4- Perform a set of numerical investigations to validate the numerical models available for this research and identify the modelling performance of various turbulence modelling techniques (k-ε, V2F) for a nozzle guide vane and turbine blade.

5- Investigate numerically the heat transfer performance that can be obtained through the manipulation of secondary flows in cooling passages by reshaping their geometry.

6- Investigate the effect of mist-air on heat transfer in a roughened U-duct for different mist-air percentages.

2 Literature Review

This chapter provides a review of the published literature dealing with internal cooling of gas turbine blades. The review is divided into five sections:

- The cooling passage
- Rotating and non-rotating studies
- Change in cooling passage cross-section
- Cooling enhancement techniques
- Mist cooling

The introductory chapter has given an explanation of why internal cooling is required in GTs and why it is necessary to find improved ways to cool the blades and achieve better heat transfer.

2.1 **Cooling passage geometry**

Providing a passage inside the blades through which cooling air, often from an external compressor, passes, is an effective way to extract heat from the blade. This heat transfer is via convection between air and blade. To achieve maximum convective heat transfer, the internal passage should have a large surface area. To maximise the surface area and enhance heat transfer the channel is serpentine in shape combined with internal fins. Both circular and elliptical cross-sections are commonly used for the channels. The cooling air is emitted from the blade hub and flows through the blade towards the blade tip. This internal cooling air extracts heat energy from the blade surface. This method is relatively easy to implement, but it also remains robust without problems of leakage or corrosion. Today, these internal passages can be cut with a laser tool.

Because of the importance of cooling the blade surface wall, many researchers have investigated the phenomenon to gain an understanding of the physics of the flows. Meyzger and Sahm [9] conducted an experimental investigation of heat transfer distribution along a smooth pipe

with a smooth 180^{o} bend. Their data showed a steep increase of heat transfer along the pipe, reaching at its maximum at the exit location.

Today, to obtain efficient blade cooling, the rectangular cross-section cooling channel is the most used design since a square cross-section is rarely practical [10–14]. Schabacker and Bolcs [15] used PIV (Particle Image Velocimeter) to study experimentally the airflow inside a duct with a 180^{o} turn. Their data showed large scale coherence in the flow structure in the mainstream duct and also identified the flow recirculation zones inside the duct occurring after both upstream and downstream corners comprising the 180^{o} turn. It is known that coherence of flow structure is responsible for heat transfer and therefore thermal performance of the cooling airflow inside the passage.

Sewall and Tafti [16] implemented a transient CFD (Computational Fluid Dynamics) simulation with LES (Large Eddy Simulation) to model a 180^{o} bend in a stationary duct with rib turbulators. Their study showed increases in heat transfer of about 20% in the presence of the internal rib structure.

Amro et al. [17] conducted experimental measurements of heat transfer obtained with a ribbed channel with cooling air passage at different rib angles. Their data suggests the best performing rib arrangement for blade tip cooling is a rib with a 45-degree inclination to the flow.

Jia et al. [18] conducted a numerical study of the thermal performance of ducts with square cross-section with V-shaped ribs. Their model predicted enhanced heat transfer compared to a straight rib in the same ducting. Hiroshi et al. [19] studied characteristics of the cooling airflow for flows inside a duct with a 180^{o} turn. A LDV (Laser Doppler Velocimeter) was used to measure the local velocity near the duct wall both in the normal and parallel directions. The experimental results showed that the wall-normal velocity dominates heat transfer in the channel before the

180^{o} turn while the wall-parallel velocity contributes to the local heat transfer after the turn.

The frontal nose/leading edge of the turbine blade is exposed to the hottest incoming air from the combustion core region, thus it is also necessary to include cooling passages such that the cooling of the leading edge is by impingement as well as film cooling, see Figure 11. The middle portion of the blade is cooled by rib turbulated cooling. The trailing edge of blade is cooled by pin fin cooling with ejection. Figure 6 shows this multi-channel approach on a single turbine blade.

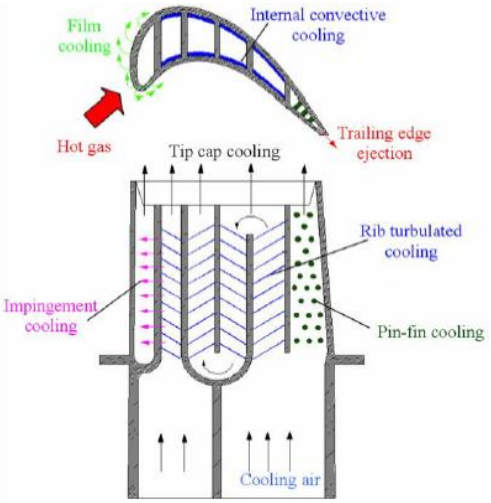

Figure 6 Multi-channel cooling passage inside a turbine blade [20]

Sushi and Sonawane [20] conducted a numerical analysis of heat transfer at the blade tip for different size (diameter and height) tip configurations for flows of Reynolds number ranging from 200,000 to 450,000. They predicted that the number of trailing edge pin fins, their locations and their arrangement play an important role in enhancing heat transfer over the turbine blade tip. The same test was also conducted experimentally by [21].

A 7-year experimental research project in Japan on a low NOx, environmentally compatible, engine for small aircraft has been carried out by Fujimoto et al. [22–25]. A new configuration called multi-slot cooling where the cooling flow was forced through a circuitous route between the

leading edge and the trailing edge with turbulence promoters at the end, replaced the conventional U-duct, see Figure 7

There were two inlets for the cooling air, one for the leading edge film cooling and the other for the multi-slot. There was a set of exits passing through the trailing edge, the flow exits as a cooling film cooling through the leading and trailing edge and through the side film holes. The test was carried out at four different Reynolds numbers for the hot gas flow: 2.2 x 10^5, 3.4 x 10^5, 4.5 x 10^5, 5.7 x 10^5.

The preliminary analysis of airfoil cooling showed that each cooling structure, multi-slot and conventional impingement cooling had its own characteristics. Thus, selection of the most appropriate cooling structure is an important element of cooling design. Bearing these points in mind, multi-slot cooling is seen as suitable for the cooling of High Pressure Turbine (HPT) airfoils [22,25]

It was confirmed that the pressure loss across the blade for the multi-slot cooling arrangement was very low for its cooling performance when compared with 180^o turns which form part of the serpentine U-duct cooling passage arrangement used by [26].

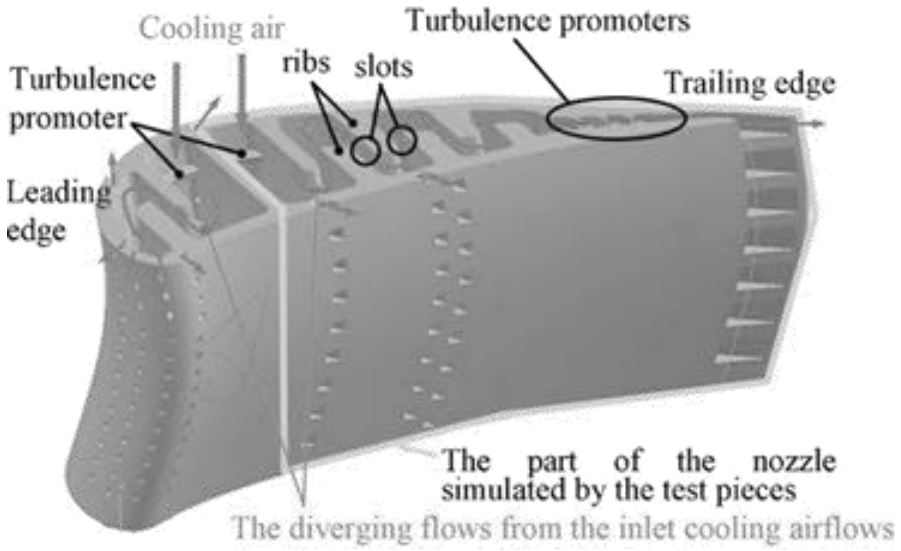

Figure 7: Multi-slot cooling [25]

2.2 **Rotating and stationary turbine blades**

In this thesis a single passage has uni-directional mean flow. A double passage has two single passages connected at one end by a 180° bend. The direction of the flow in the second passage is essentially in the opposite direction to that in the first passage.

Gallo et al. [27] have considered the case of a two-pass duct of square cross-section. They found that when such a duct is stationary, the airflow inside the duct generates small turbulence vortices internally at the four corners of the inlet duct, as shown in Figure 8(a). These are formed due to Reynolds stress anisotropy. These corner flow structures disappear when the flow approaches the turn region where the pressure at the inner wall is reduced relatively while that at the outer wall increases. This differential pressure is due to the centrifugal force experienced when the fluid flows through the 180^{o} bend. This force induces and promotes two symmetric counter-rotating vortices as shown in Figure 8(b), and this flow patterns continues into the second passage of the duct, downstream of the bend, towards the outlet. This flow structure is large scale compared to secondary near-wall vortices and is coherent. Such a flow structure is more efficient in exchanging heat energy with the wall and enhances convective heat transfer locally. As a result, heat transfer will increase and will be a maximum at the outlet.

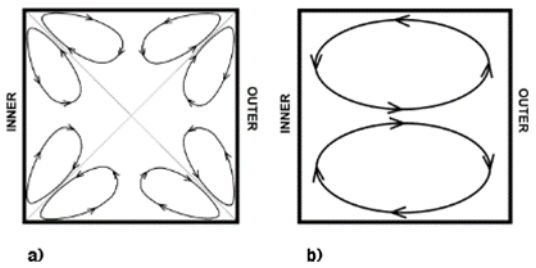

Figure 8 Secondary motions for the case of a static duct with a 180^{o} bend (a) inlet duct, and (b) turn zone and outlet duct [27]

Gallo et al. [27], also considered the condition where the duct (in the turbine blade) is rotating, and studied separately the two conditions where the inside duct wall is smooth and roughened by the addition of ribs. Gallo and his colleagues attempted to measure and map the duct wall surface temperatures experimentally, using a thermocouple array. However, despite using high resolution thermocouples this technique was not adequate to identify the flow field correlation and the convective heat transfer distribution. Gallo et al [27] used infrared thermography on the rotating channel with 180^{o} turn. When the duct was rotating, the secondary flow was found to be introduced by the sharp turn due to the action of the Coriolis forces.

The influence of axis rotation of the duct was studied by Iacovides et al. [28] based on mean and turbulence flow impact on a rotating U-duct with and without turbulators. It has been shown that the flow increases in complexity when the duct is rotating because the secondary flow is induced by both axial flow pressure gradient distribution and the Coriolis force

When the Coriolis force dominates, which occurs when a duct is rotating, it will change the temperature distribution as well as the local heat transfer coefficient (HTC). When the flow is radially outwards, the Coriolis force induces a secondary flow structure in the form of a pair of symmetric vortices perpendicular to the bulk flow in a radial motion, see Figure 13(a). In the presence of the vortex pair the heat transfer from the trailing wall is enhanced and reduced at the leading wall, when compared to the stationary condition. At the 180^{o} bend, the “turn region”, the flow is more complex with additional vortices induced in the flow, see Figure 13(b). However, after the bend the flow decreases in complexity with the presence of only a single vortex, single coherence scale, see Figure 13(c).

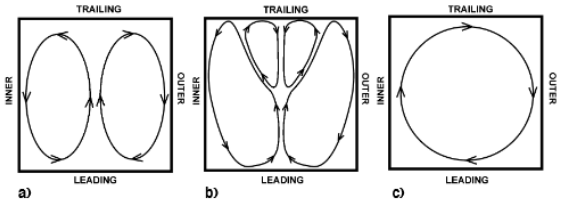

Figure 9 Secondary motions for the rotating case: (a) inlet duct (b) turn zone (c) outlet duct [27]

Chen and Liu [29] have measured the mid-span velocity profile distribution from leading to trailing wall for a rotating duct with smooth walls, see Figure 10. In the inlet duct the strength of the induced vortex pair pushes the centreline of the flow towards the trailing wall. When the speed of rotation increases, the peak velocity both increases and moves closer to the trailing wall side while the velocity near the leading wall decreases both absolutely and relatively compared to the freestream velocity.

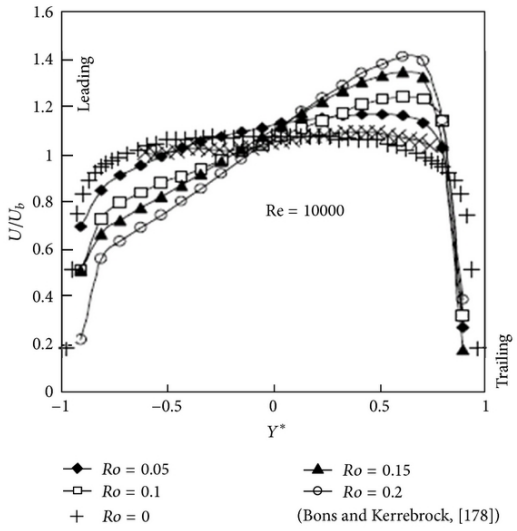

Figure 10 Mid-span velocity profile for outward radial flow in a rotating smooth-walled channel [29]

Elfert et al. [30] have confirmed that a pair of Dean vortices develops when the flow stream passes through the turning region. Figure 11 shows the visualization of such a Dean vortex pair for a rotating and non-rotating channel. In the non-rotating case, the vortex pair is symmetric. In the

rotating case, the Coriolis force acts on the flow entering the turn region and the Dean vortex pair becomes asymmetric. The flow structure in the lower pressure region is more coherent than for the higher pressure side which enhances local heat transfer.

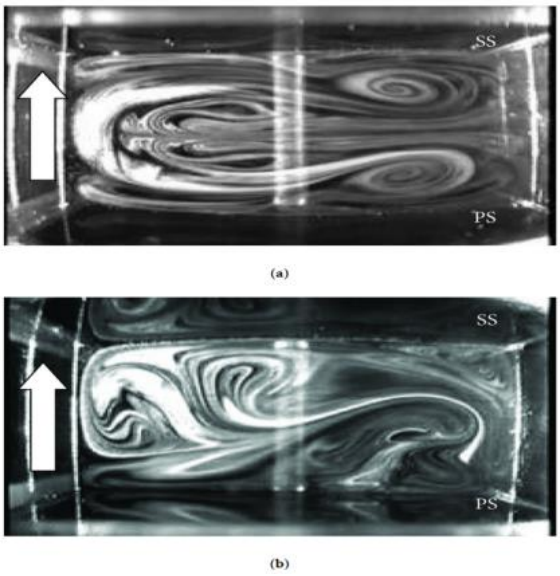

Figure 11 Dean vortex pair visualization (a) non-rotating case (b) rotating case. [30]

Due to the differences of flow structure at different sections inside the rotating and non-rotating ducts, the heat transfer performance will vary with location. In order to accurately resolve the flow field and the corresponding convective heat transfer mechanisms numerically, using the discretized Navier-Stokes equations, the details of the simulated flow structure are critical when representing the actual local flow distributions either temporally or spatially. With high order discretisation, it is expecting that more computing resources will be needed to complete the simulation. A high resolution mesh is almost always required when using a transient solver such as LES or DES (Detached Eddy Simulation). The advantage

of such a modelling approaches is better accuracy of the solutions and better representation of the behaviour such flow exhibits in the real-world.

Some of the early computational studies comparing non-rotating and rotating U-ducts included inclined ribs design [32,33]. When using different rib geometries, the mesh resolution near such features must be sufficiently fine to differentiate between the effects of the different ribs.

Ribs geometries are an integral part of the flow field and heat transfer between wall surface and cooling air. One example of numerical modelling of the effect of rotation of the turbine blade on heat transfer with rib turbulators was performed by Han and Chen [34]. Their study included various rib geometries with different aspect ratio channels. The predicted results obtained for these different shapes using the two equation turbulence model k-ε, were compared with measured values of the Nusselt number. Figure 12 is the schematic of the duct used to conduct the analysis. The boundary condition of all four walls of the U-duct was set as T=344.83K. The inlet coolant air temperature was T_i=300K. This corresponded to an inlet coolant to wall temperature ratio of 0.87 and inlet density ratio of 0.13. The Reynolds number and rotation numbers at the inlet of the duct were Re=25,000 and Ro=0.24 respectively. The inlet flow Mach number was 0.05 and the duct rotational velocity was 3132rpm.

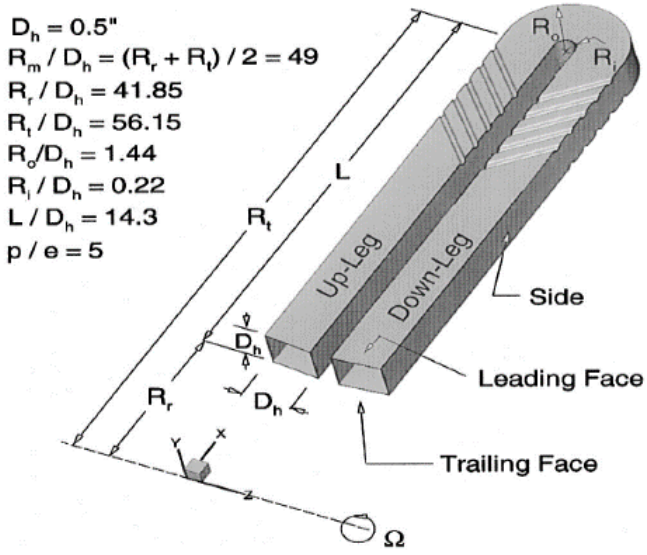

Figure 12 U-duct with 45º inclined ribs [34]

Wen-Lung [35] conducted an experimental study of the impact of buoyancy forces on heat transfer for different channel aspect ratios when the channel was rotated. This set-up included two different channels with the same two pass rectangular configuration, one with smooth walls and the other 45º ribs on the walls. The Reynolds numbers for the flow-rates are were 500, 10,000, 25,000 and 40,000. The channels aspect ratio (width to height) was varied from 4:1, 2:1, 1:1, 1:2, to 1:4. For each test, the rotational speed was maintained at 550rpm.

Their experimental data used the flow Nusselt number for performance comparison. Their results show that in the first inlet pass channel, increasing the buoyancy parameter led to a decrease in the leading edge Nusselt number but the opposite occurred at the trailing edge. Their data also showed the complexity of the Nusselt number in the second pass (the outlet channel) was due to the 180º bend. It was concluded that the channel providing maximum heat transfer had a 1:4 aspect ratio.

Lin [32] compared heat transfer performance of a U- duct of square section for both rotating and stationary conditions using a compressible Navier-Stokes equation approach. The turbulence model used the SST

(Shear Stress Transport) equation at low Mach number (M = 0.05). Their numerical framework was the FVM (Finite Volume Method) with a second-order flux-differencing splitting algorithm. The advantage of this simulation is the readiness of reporting different flow parameters which are convenient for physical interpretation. This work compared the effects of changes in Mach number, flow pressure, flow temperature, flow streamline contour and Nusselt number. It was demonstrated that there was a uni-directional flow transition to a more convoluted flow pattern when the U-duct was rotated. This change in flow pattern was deemed to be due to the combined effect of Coriolis force and the centrifugal buoyancy when ribs were present inside the 180^{o} bend.

Al-Qahtani et al. [36] have conducted a numerical study using CFD for a three-dimensional rotating two-pass smooth channel with aspect ratio of 2:1. Their findings showed that the Reynolds Stress (RT) turbulence model is sufficient to resolve flow structure and capture the effect of rotating channel impact on heat transfer distribution for a sharp 180^{o} bend. The near wall modelling was treated with a second-moment turbulence closure formulation as wall surface plays an integral part in the heat transfer mechanism. In order to ensure their simulation was effective, the Navier-Stoke equation used in the model was arranged and constructed using multi-block algorithms.

Recent experiment conducted by Li [37] have been used to develop a correlation of Nu/Nus ratio as a function of Ro ($0<Ro<1.0$) for different wall-temperature ratios and channel orientations when a square U-duct is rotated. The experiment studied three different cases based on different wall temperature ratios, and measured the heat transfer distribution for two channel angles at 0^{o} and 45^{o} respectively. The experiment also shows that the temperature ratio between the air passage to blade surface will vary exponentially from stationary to rotation state. This important finding leads to the necessity of including blade rotation effects when heat transfer performance of the blade is of interest.

In general, the impact of rotation only occurs locally. The thermal performance has been used widely to quantify the heat transfer characteristics and is described in terms that include rotation number, density ratio, buoyancy parameter and flow Reynolds number. Flow Reynolds number is defined by[38]:

$$Re = \frac{UD_h}{\upsilon} \tag{6}$$

Where, U = velocity

D_h= hydraulic diameter

Rotation number is defined by:

$$Ro = \frac{\Omega D_h}{U} \tag{7}$$

Ω = rate of rotation in RPM

Inlet density ratio is defined by:

$$DR = \frac{(\rho_w - \rho_c)}{\rho_c} \tag{8}$$

The buoyancy parameter is defined by:

$$Bo = Ro^2 \left(\frac{R}{D_h}\right) DR \tag{9}$$

Several researchers [35,39,40] have shown that the overall heat transfer performance of the cooling channel is more sensitive to flow Reynolds number than rotation number for smooth channels. This conclusion is also found to apply to channels with ribbed turbulators under rotating conditions. Since the overall thermal performance must account for both suction and pressure sides, this competing factor of both side of the walls due to rotating effect is dominant. The rotating effects are found to change with Nusselt number for both suction and pressure sides due to induced secondary flow as result of a Coriolis vortex pair. However, for channels with multiple passes and turns, the results are just the opposite. The main source of this difference between single pass and multiple

passes is that the inlet flow tends to change from a radially outward to a radially inward direction when Coriolis force influences the direction of the flow. Thus, the overall thermal performance is better on the suction side when the flow is radially inwards. In the case of multiple passages, however, this is reversed.

For flows with high Reynolds number, the effect on the heat exchange rate of changes in the Nusselt number is less pronounce for the rotating case than for the non-rotating case. This is mainly due to decrease of rotation number with increase in Reynolds number. In contrast, rotation effects are found to be more pronounced at low Reynolds number flow, especially when rib turbulators are used.

For channels in rotating blades, many investigations show a significant increase of Nusselt number when direction of flow in the passage is switched from radially outward to inward, and vice versa. This local enhancement is attributed to flow impingement on the pressure side of the wall in the turn region and the presence of a Dean pair vortex.

Generally, for rotating channels, the wall surface temperature distribution is found to increase over most of the channel but with a slight decrease in the bend region.

Different cooling mechanisms such as pin fin, impingement, dimpled surfaces, spherical protrusion arrays, trailing edge and rib turbulators have been investigated experimentally for rotating channels. There have also been experiments to measure local velocity and surface static pressure distribution for a rotating rectangular channels. All results confirm the importance of rotation effects on the thermal performance.

The study by Bo et al. [43], used three turbulence models; a k-ε viscosity model with one equation in the near wall region, a low Reynolds k-ε eddy viscosity model, and the low Reynolds algebraic stress model. The k-ε one equation EVM produced a reasonable heat transfer

prediction. However, some failings emerged at high values of Ro. The low re ASM results were similar to the measurement by [44] Figure 13.

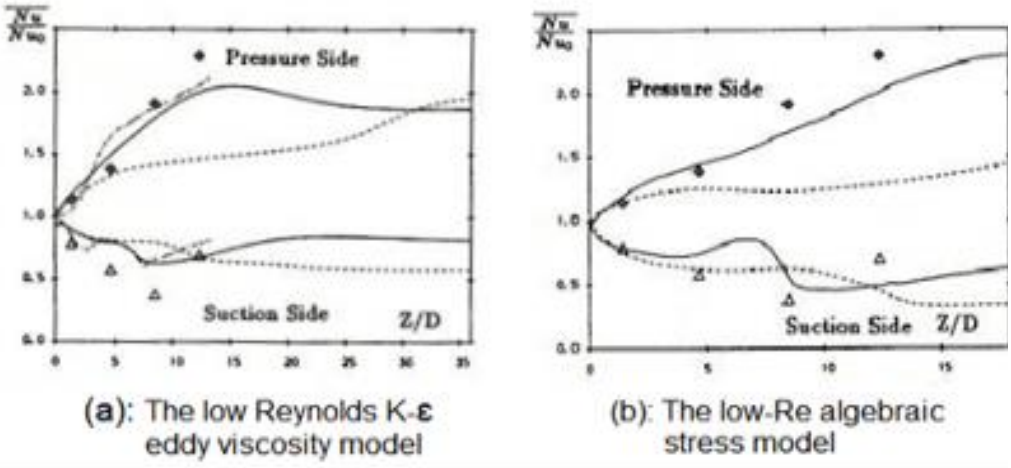

Figure 13 Comparison of the side averaged Nusselt number at Re=25000 [43]

Other interesting results have been provided by Han et al. [45], who investigated: constant wall temperature; constant heat flux; and hot leading and trailing walls with cold sidewalls, for 2,500≤Re≤25,000 and 0≤Ro≤0.352. Inconsistencies were found with previously obtained data due to, for example, varying test conditions. It was concluded that in a constant temperature experiment the Nusselt Number might be as high as 2.5-3.0 on the trailing side. On the leading side Nu might decrease to about 0.4 and then increase further downstream. It was also concluded that the heat transfer on the trailing face was 10-20% higher for the constant flux experiment than the constant wall temperature experiment. For the leading face, the heat transfer was 40-80% higher for a constant flux experiment than in a constant wall temperature experiment.

The first reported experimental investigation on flow and heat transfer in a ribbed triangular cooling passage was by Harasgama and Morris [46]. Further studies were carried out by others [17,47] on stationary and rotating triangular cooling channels with smooth and roughened walls to determine their effect on the heat transfer coefficient. A common conclusion was that the triangular channel failed to create a secondary flow in the inlet upstream channel because the triangular channel with blade cooling had less space available in which to allow the primary flow to create a secondary flow. However, in the downstream direction, secondary flow was generated after the 180^{o} bend, and the heat transfer coefficient of the triangular cross-section channel was significantly higher than that of a square duct found by Dutta et al. [48,49]. It was concluded that triangular cooling channels can be used effectively in small areas where a square duct would be unsuitable.

Morris [50] performed experiments on circular tubes with constant wall temperature. The Reynolds number varied from 15,000 to 30,000 and the rotational speed ranged from 0 and 2700 RPM. Five different power settings were used to maintain a constant wall temperature. When stationary, the leading and trailing faces showed identical heat transfer. When rotating, the Nusselt number increased with Reynolds number with the trailing face having a higher value than the leading face. The Nusselt number also increased with buoyancy force, see Figure 14.

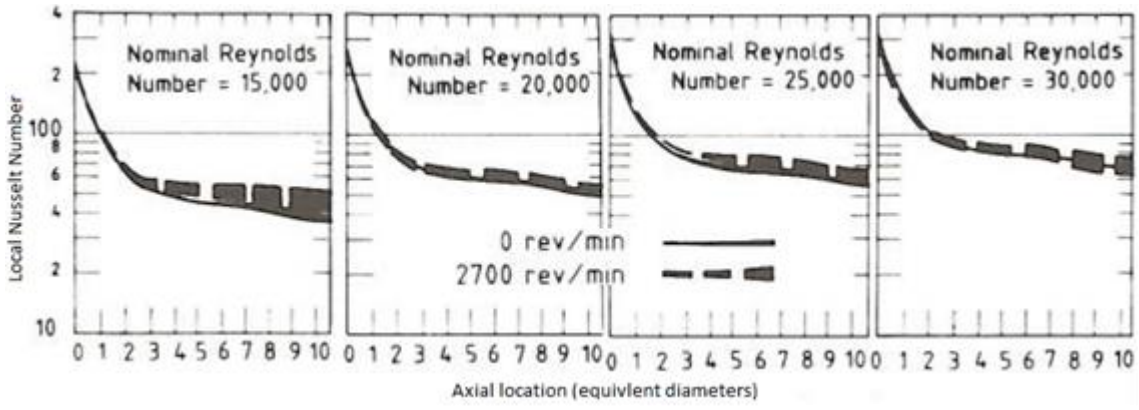

Figure 14 Comparison of effect of rotation on trailing edge heat transfer [50]

Wagner et al. [51] conducted experiments on smooth square passages having flows both radially outward and inward. They concluded that density differences and rotation effects caused large changes in heat transfer for a radially outward flow but relatively small changes for a radially inward flow. On the low pressure side, the heat transfer varied with the Buoyancy parameter, which was correlated with Density, Rotation number, and geometrical parameters, regardless of the flow direction. Increasing the Density ratio increased the heat transfer although that increase was less for a radially inward flow than for a radially outward flow, see Figure 15

Wagner et al. [51]performed a second set of experiments on square passages with turbulators and found that rotation improved heat transfer on the trailing surfaces of the 1st passage by as much as 60% at Ro=0.35 compared to the stationary condition. Rotation decreased the heat transfer on the leading side by 50%.

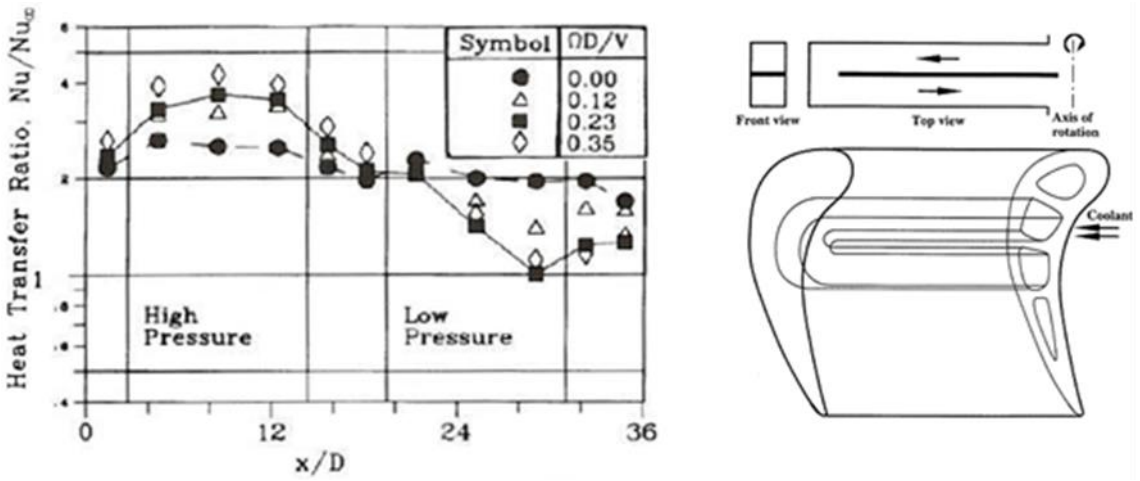

Figure 15 a) Effect of rotation number on heat transfer, and b) U-duct cooling passage, after Wagner et al., 1991[51]

In all cases involving rotation, the Nusselt number increased with rotation at low Reynolds number. The degree of the effect varies with geometry. Rotational effects are most noticeable above a rotation number of 0.10 . For this reason, it is difficult to discern the effect of rotation at Reynolds numbers above 100,000. All the high Reynolds data was obtained at a low rotation number because the high flow velocities placed limitations on the drive system.

2.3 Effect of changes in cooling passage cross-section

For the internal cooling of a GT blade, cooling airflow enters from the centre hub and leaves from the blade tip through a multi-pass passage. Generally, these multi-pass passages consist of numerous individual channels connected by 180º bends. Internal ribs and pin fins inside these channels enhance the thermal performance as the key cooling mechanism is heat convection to the airflow. Much research has been conducted based on two-pass channel geometries with various aspect ratios, different turning angles, and different shapes.

Generally, the higher the aspect ratio of the channel the greater the heat transfer but also the greater the pressure loss. Duct bends induce secondary vortices which promote heat transfer in the region downstream of the bend, especially for 180º bends. Therefore, for two-pass channels, the second pass heat transfer is higher than for the first pass. Chen and Liou [52,53] have demonstrated such heat transfer enhancement in the second pass is due to the formation of flow separation bubbles which change the local velocity distribution near the wall and increase the near wall heat transfer coefficient. As mentioned in the previous section, rotating effect also helps in increasing heat transfer due to the presence of the Coriolis force in the bend region.

An early experimental study conducted by Metzger [26] showed that adding inserts inside the turn region of a sharp 180^{o} turn channel will impact on the pressure drop of the flow. The configurations they used included 90^{o} inserts including corner fillets, radial positioned ribs and turning vanes. It was found that turning vane placed in the turning region reduced the pressure drop in the channel significantly.

Another early study with respect to the turning vane shapes was conducted numerically by Wang and Chyu [54]. Their computational study used different shapes of turning vanes such as straight corner turn, rounded corner, and a circular shaped corner. Their flow-field predicted flow recirculation when straight or rounded corner shapes are used.

Hirota et al. [55], experimentally measured the heat transfer characteristics of rectangular cross-section two-pass channels with an inclined divider mounted internally. The naphthalene sublimation method was used to measure the local heat transfer rate and their test data showed there is a trade off between heat transfer rate and the pressure loss due to the flow restriction. It was recommended that the balance between the two should to optimized using combinations of inclination angles. Rao [56] has also studied the impact of different turning vane installations on the pressure drop in a two-pass channel with cooling flow. His results demonstrated pressure drop reduction of 43-48% can be achieved with a proper turning vane installation.

Perhaps the first visualization evidence showing the size of flow separation bubbles in the presence of turning vanes was by Luo and Razinsky [57]. The reduction of pressure loss due to the presence of such flow structures is seen at the downstream corner of the divider tip. Zehnder [58] built and modelled a 45^{o} ribbed channel for testing. The results showed the pressure loss was reduced by 25% when a turning vane was installed but this was accompanied by a reduction of heat transfer in the second pass section.

It has also been found that a [6] wall has higher heat extraction efficiency than a convex wall. Saha and Acharya [59] studied numerically a two-pass cooling channel with different bend geometries, including turning vanes of different shapes; an asymmetrical bulb, a symmetrical bulb, dimples and bow shapes. The Reynolds-Averaged Navier-Stokes (RANS) model was used with the Realizable k-ε turbulence model and combined with enhanced wall treatment options for these studies. A heat transfer performance matrix was used for comparisons of the different geometries. The matrix included flow parameters based on Nusselt number, friction factor (flow restriction), and thermal performance factor. This numerical study shows that a combination of symmetrical bulb, bow feature, and dimple shapes give the best thermal performance factor at almost 40% higher than baseline.

Two years later, Saha and Acharya [60] conducted an experimental study using the bend geometries they had studied previously. Their data confirmed that the symmetry bulb shape, by removing the sharp turn, enhanced thermal performance by 29% compared to the baseline. By combining bulb and bow shapes, the thermal performance increased by 32% and the pressure loss reduced by 27%.

Namgoong [61] studied numerically a U-duct with 180^{o} bend for turbine blade cooling applications. Their study utilized the Design of Experiment (DOE) method with a surrogate design space model to perform automatic shape optimization of the U-bend to achieve minimum pressure loss. The major source of pressure loss was identified as flow separation downstream of the U-bend. Their proposed combined optimization method, would help the design of cooling passage shapes more efficiently and with less human error.

Schuler et al. [58] investigated the effect of extracting flow at different locations in the second pass of a ribbed channel on the overall heat transfer performance. Their results did not show any significant change in heat transfer with mass flow extracted.

More recently, Wang et al. [62] investigated the optimization of heat transfer with location, shape and relative size of the internal cooling passages and near-surface holes within a GT vane. The cross-sections of the passages included circles and ellipses. Full conjugate heat transfer (CHT) analyses were carried out and showed that optimization of cooling passage design would improve the thermo-mechanical performances of turbine vanes, reducing the maximum temperature of the vane by up to 50 K.

Siw et al. [63] combined experiment and CFD simulation (using commercial software code CFX) in a study of heat transfer performance for 70^o, 90^o and 110^o turning angles of the cooling passage. By suitably connecting the channels they have a zig-zag pattern which allows the flow to have longer residence time inside channel before leaving the domain. The channel size was 63.5mm by 25.4mm (aspect ratio of 2.5:1). Their numerical results suggest that the best heat transfer performance was obtained using a 110^o turn. Their experiment data suggested that the 110^o turn had the minimal pressure loss and 70^o case the worst.

2.4 **Cooling enhancement technique**

Numerous reports were found in the literature addressing cooling enhancement in two-pass channels. The shape most studied is the ribbed straight channel. Han [64], for example, studied both continuous and transverse ribs on opposite walls of a rectangular duct and measured an enhanced heat transfer 2.5 times greater than at the inlet location of the channel . When using a smooth duct, he measured an enhanced heat transfer of 1.8 times.

Peng et al. [65] investigated heat transfer in ducts with flat walls, and walls with ribs perpendicular to the flow (90^o ribs) and V-shaped ribs and their results showed secondary flow structures are induced due to the presence of such ribs. In addition, combining rib arrays with sharp bends

has shown significant increase in local heat transfer. As mentioned in the previous section, the secondary flow structure was generated in the bend region and is responsible for enhanced heat transfer near the wall.

There have been attempts to enhance heat transfer (cooling) at the blade tip as this is the region exposed to the hottest gas, particularly at the outer wall facing the heated combustion chamber. Bunker [21] experimentally tested five different pin shaped arrays mounted on the blade tip surfaces. They achieved a heat transfer enhancement factor of 2.5 with very little pressure drop penalty. Ledezma and Bunker [66] used a computational approach to study the specific locations of these pin fin arrays to achieve the maximum heat transfer and showed that optimal spacing of the pin array will be a function of flow Reynolds number. This means that each flow requires a different array to achieve optimal cooling performance.

Xie and Sunden [67] also used a computational approach with the blade surface being dimpled at the tip instead of carrying a pin array. Their results showed the heat transfer obtained with dimple shapes is twice that with a smooth tip.

Wang et al. [68] measured in detail the heat transfer and local pressure drop in the turn region of a two-pass channel. They used a smooth blade tip as baseline configuration and compared its performance with seven different rib configurations. They identified which rib configuration provided the best heat transfer augmentation and then determined the combined performance of ribs and a sharp turn on the measured heat transfer and pressure drop. They chose liquid crystal thermal imaging to measure heat transfer rate, and a manometer for pressure loss measurement over the turn region. They reported four key points when comparing smooth and ribbed turn regions:

(1) local heat transfer is dominant on the smooth outer. Both angled and V-shaped ribs showed different heat transfer distributions compared to the 90^{o} ribs.

(2) The presence of ribs increases the average heat transfer rate but also increased of the non-uniformity of the heat transfer rate.

(3) Ribs caused a greater pressure loss than a smooth wall

(4) The best thermal performer was the 45^{o} V-shaped rib configuration.

Xie et al. [69] also studied numerically the effect of guide vanes/ribs on the heat transfer performance of the blade tip surface. Their study included flow Reynolds number ranging from 100,000 to 600,000 inside a serpentine channel with and without guide vanes/ribs. The cooling effect of such flow on the blade tip was investigated.

Figure 16 show the arrangement with no vanes or ribs, and with the 3 different guide vane and rib shapes created for CFD modelling and used in their study. The channel geometry was 139.7mm wide and 69.9mm high with an aspect ratio of 1:2. The CFD predicted flow-fields for the different shapes are presented in Figure 17.

They reported three key points:

(1) the use of guide vanes/ribs increased pressure pushed the maximum flow velocity towards the tip wall shown in Figure 22 and increased the local heat transfer due to turbulent mixing.

(2) The presence of guide vanes/ribs increased thermal performance by 20% - 65% at the tip.

(3) Despite the heat transfer augmentation gained by using guide vanes/ribs, these devices do not show significant added value compared to others.

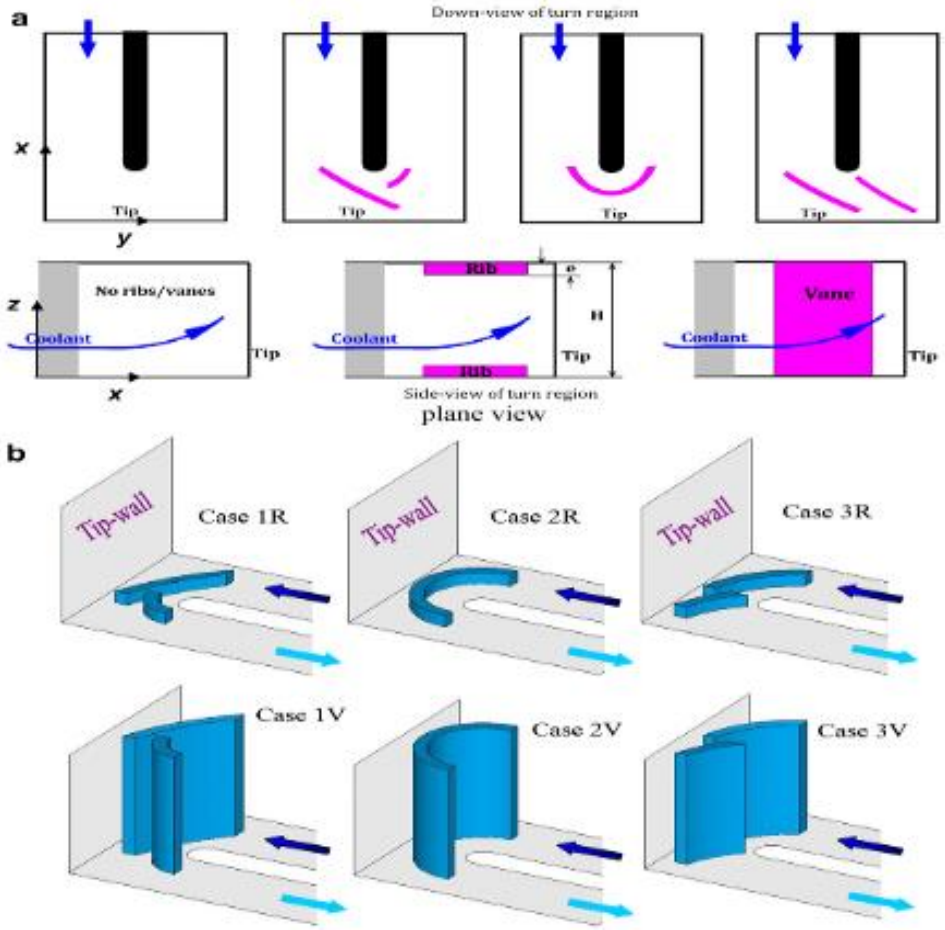

Figure 16 CFD model of guide vane geometry [69]

Generally the addition of ribs/vanes improves heat transfer performance, however, as the aspect ratio of the channel is reduced the gain become less [69] because the vortices induced by ribs diminish with increasing aspect ratio. This is due to the decrease in secondary vortex formation as the thermal boundary layer between the ribs becomes thicker. As a result, the heat transfer performance worsens. Chung et al. [70] have demonstrated, for aspect ratios of 2 to 4, that the presence of intersecting ribs reduces the thermal boundary layer between the ribs, additional vortices are generated which enhance the heat transfer locally.

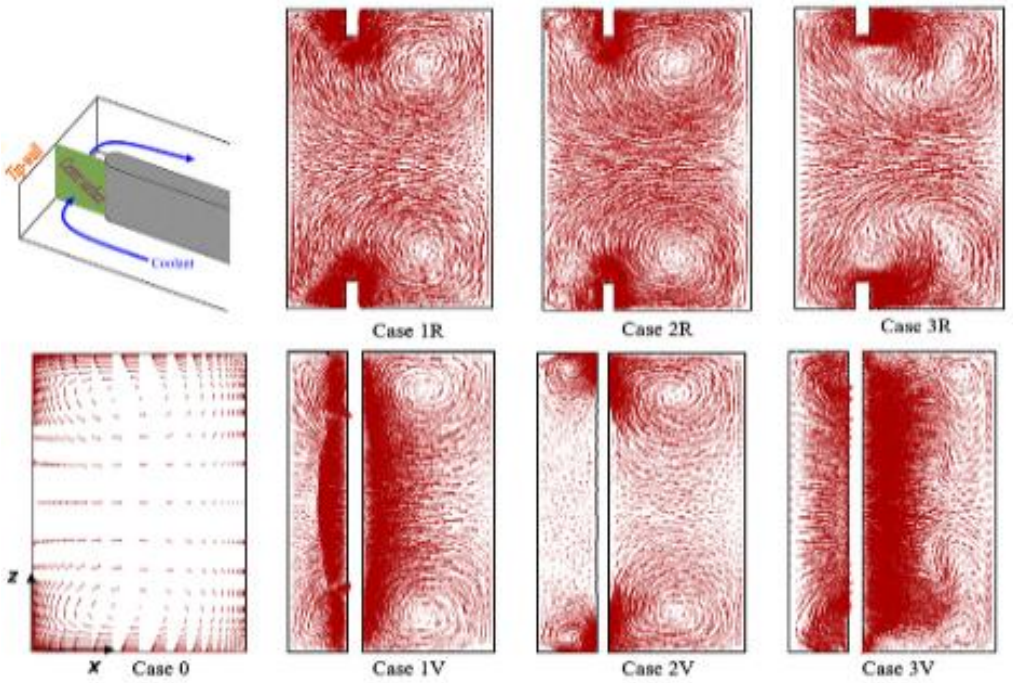

Figure 17 CFD flow-field at turn centre surface at Re=200,000 [69]

Further experimental investigation of the effects of ribbed wall design was carried out by [71] related to land-based turbines for power generation. He chose Reynolds numbers in the range from 30,000-400,000. A square channel was constructed with two opposite surfaces roughened by 45^{o} parallel ribs. The test data showed that the heat transfer performance of the ribbed channel decreases with increasing Reynolds numbers. Such performance is also correlated consistently with Nusselt number enhancement ratio.

As mentioned previously, a common technique to enhance heat transfer is to force coolant air into the channel with the wall configured with a series of rib-turbulators. Such ribs will enhance turbulence mixing, thus promoting local flow separation and reattachment and increasing the value of the local heat transfer coefficient. The drawback is an increase in pressure drop when such ribs are added. Thus the design and layout of such ribs will be an integral part in the overall performance and will vary for different applications. When the ratio of the rib spacing to rib height

(s/h) is large, both the heat transfer enhancement and friction factor penalty become small, and vice-versa, when s/h is small there will be an increase heat transfer performance. Note that inclined ribs will be more beneficial than upright angled due to secondary flow induced which is important to promote local heat transfer.

The literature review presented so far of the impact of different geometrical parameters on the heat transfer performance and friction loss factor has included; passage aspect ratio, rib inclination angle, rib spacing-to-height ratio, and rib shapes. Detailed measurement of temperature distribution in ducts with ribbed walls has been performed by Coletti et al. [72]. Blade trailing cavity was chosen for the focus of cooling path and conjugate heat transfer measurement studies. The test data showed that both the Nusselt number and non-dimensional wall surface temperature are good measures of heat transfer for use as boundary condition inputs when evaluating thermal performance of a cooling path. Using the Nusselt number for a pure convective regime instead of the overall conjugate contribution would result in a discrepancy of local heat transfer. Also, simply applying a constant heat flux to correct for heat conduction would underestimate the overall conjugate results by 26-33K. Coletti et al. concluded their report by saying that variations in the thermal conductivity of the turbine blade wall effected local surface temperatures in a negative way due to the higher temperature gradient between fluid and wall layers.

Based on previous flow visualization, the general flow structure characteristics inside a channel with ribbed wall can be represented by boundary layer separation, a curved shear layer, primary and secondary flow recirculation, boundary layer reattachment, etc. These flow structures must be modelled at least reasonable well in order to provide useful prediction in practical design applications. Some of these flow structures have already been widely studied numerically using a backward facing step such as flow separation, shear layer, and flow reattachment. The accuracy of the predictions varies depending on the turbulence models

used in the simulation. For example, the flow shear layer will impact on flow reattachment when the shear layer spreading rate is not modelled accurately.

The modelling of a rotating channel can provide details of the flow-field inside the cooling passage of a turbine blade with different ribbed wall shapes, for example. As mentioned above, rotating channels introduce the Coriolis force which plays integral part in the flow-field distribution. Wilcox and Chambers (1977) modified the k-ε equation with a new Coriolis term and their predicted results have shown an accuracy within 10% of the experimental data. The remaining discrepancy is attributed mainly to the inability of eddy-viscosity in the Reynolds Averaged Navier-Stokes (RANS) model to capture the effect of flow structure and heat transfer due to rotation and Coriolis force interaction. This first attempt has laid a solid foundation for many other researches to make improvements later.

Recently, with the rapid increase and wide availability of computing power, LES has been widely used to study heat transfer in ribbed channels. LES is capable of modelling transient flows and is extremely useful for resolving large scale flow structures allowing parallel modelling of small turbulence eddies structures at an affordable computing cost. Murata and Mochizuki [73] have used LES to study the effect of the Coriolis force for both smooth and ribbed channels. Viswanathan and Tafti [74,75] performed DES simulation on a fully developed ribbed channel in rotating mode. A hybrid of RANS and LES coupling, DES has been shown to be capable of producing good quality simulations of rotation dominated flow with reasonable computing power.

In the life cycle of a GT, an increase of material temperature of 30C, possibly due to insufficient cooling has been shown to cut the working life by half [76]. Jia and Sunden [77] have used CFD to model deformed ribs on a square duct. Their studies include three different rib configurations: square, semi-circular and modified streamlined, see Figure 18. The modified streamlined shape is aligned with the coolant flow direction to

achieve optimal performance. The report also made comparisons of three different turbulent models based on the low Reynolds number k-e model (AKN) formulation, Explicit Algebraic Stress Model (EASM), and the V2-F model. The predictions show some improvement when using the modified streamlined shape rib due to lower maximum surface temperature due to enhanced heat transfer performance.

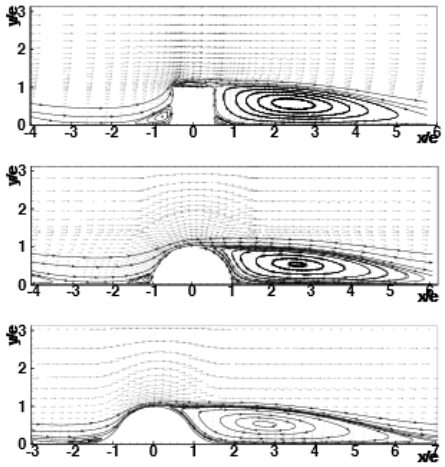

Figure 18 CFD predicted velocity vectors for three different rib configurations: square, semi-circular and modified streamlined [77]

Xie et al. [78], have conducted numerical investigations of the performance of truncated ribs, as shown in Figure 19, on airflow and heat transfer for flow Reynolds number between 8000 and 24,000. They selected the V2F model to simulate turbulence flow because V2F has been shown to predict Nusselt number reasonable well when compared to experimental data.

Xie et al. found that the truncated ribs arrangement weakened flow impingement and therefore the additional secondary vortices generated from the ribs. In this work the truncated ribs were all placed symmetically about the centre line running along the length of the duct. The flow-field produced has helped reducing pressure loss and friction factor as compared to continuous ribs. In addition, due to a small flow recirculation at the rear of the ribs formed with the truncated arrangement, the heat

transfer performance increased compared to the continuous ribs arrangement. This benefit is more obvious at higher Reynolds numbers. Among the truncated ribs configurations, the case with 12% truncated over the entire length gives the highest thermal performance.

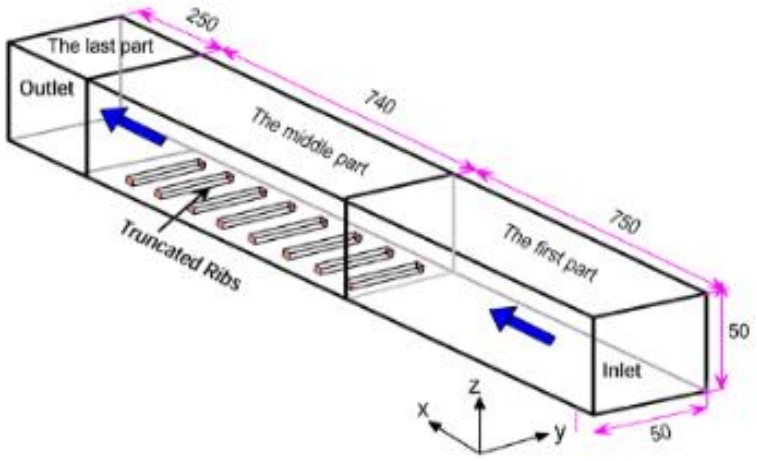

Figure 19 CFD model of truncated ribs constructed [Xie et al. [78]

Jia et al. [18] used the same V2F turbulence model to compute the effect of V-shaped ribs on the heat transfer as compared to the 90^{o} straight rib configuration. In contrast, Tafti [74] simulated a staggered ribs arrangement mounted in a duct as shown below. The set-up used a total of six ribs of square-cross-section with three mounted on each passage. The report concluded that flow recirculation was reduced after the first rib but increased after the last rib before the bend. At the locations where flow recirculation was found to be reduced it was noticed that the local Nusselt number increased. The peak heat transfer coefficient occurred ahead of the reattachment point. Using a straight-ribbed cooling channel, Arts et al. [79] identified the same behaviour of the flow-field, the pressure increases before the ribs and decreases after the ribs. In the space between the ribs, the turbulence intensity is found not to change and the heat transfer enhancement occurs near the flow reattachment points before the ribs. Experimental flow visualization of this complex airflow distribution has been found to be consistent with these numerical studies. Iacovides et al. [80], using Laser Doppler Anemometry (LDA) in a duct with aspect ratio of

0.1, a 180^{o} ribbed channel and flow Re of 100,000 captured a coherent flow structure motion and periodic behaviour, and found flow recirculation and separation bubbles after the first rib in the second pass channel.

Duct walls can be roughened by adding ribs of different geometries, distributions, and size. The ribs are placed transversely to the direction of bulk flow for heat transfer enhancement, but this requires careful consideration to avoid excessive pressure losses. This concern is addressed in a number of papers by Han et al. [81–83]. It was found that rib height affected the pressure drop that the most efficient rib height for high Reynolds number flows to avoid an excessive pressure drop was 5% to 10% of the cooling passage hydraulic height [84,85].

A systematic numerical study of wall surface roughness was carried out by Ryu et. al. [86,87], who analysed the turbulent flow in a cooling passage roughened with ribs of four different cross-sections: Square, triangular, semi-circular and sinusoidal, see Figure 20. The research used the k-ω turbulence model with near wall treatment. It was found that the greater the turbulence generated, the greater the heat transfer but the greater the flow resistance.

It was found that the square ribs produced the most resistance in a two- dimensional cooling channel, and a wavy wall the least. The triangular and semi-circular ribs were both relatively close to the square rib in terms of resistance produced whereas the wavy wall produced, relatively, very little [88].

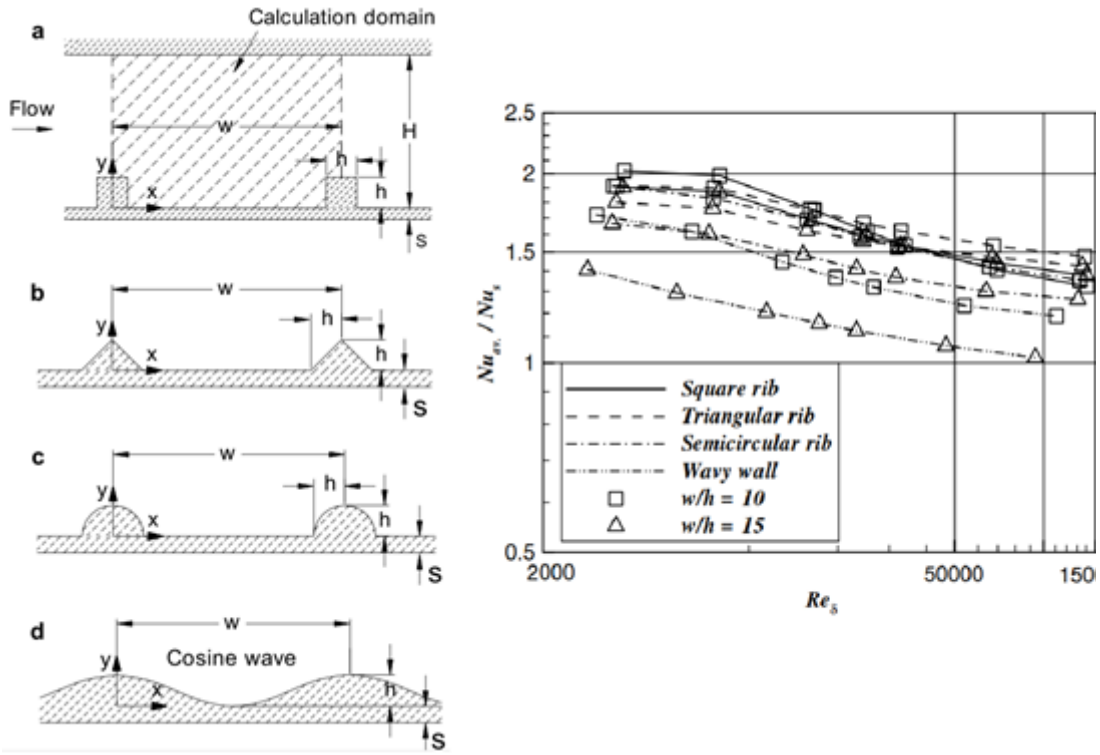

Figure 20. Shape and distribution of ribs used by Ryu et. al. [86]

2.4.1 Rib patterns

Many studies have shown that angled rib turbulators enhance heat transfer in the cooling channel by creating secondary flows [89–104].

Han and Park [64] studied the heat transfer of a rectangular cooling passage with one pair of opposite walls roughened by the addition of ribs of a square cross-section angled to the mean flow (α =30^o, 45^o, 60^o and 90^o) with a Reynolds number of 30,000. The results showed that the local Nusselt number ratio for α=30^o, 45^o and 60^o was much higher than for α=90^o, see

Rib turbulators can have many angles and shapes, see Figure 21. Chang et al. [105] have demonstrated that for a given pressure loss, V-shaped and Delta shaped ribs deliver a better heat transfer than do straight rib turbulators. Figure 29 shows that a straight rib angled to the

mean flow introduces secondary flow and creates two vortices. However, the V- shaped rib turbulators generate secondary flow with four vortices and this further enhances the heat transfer.

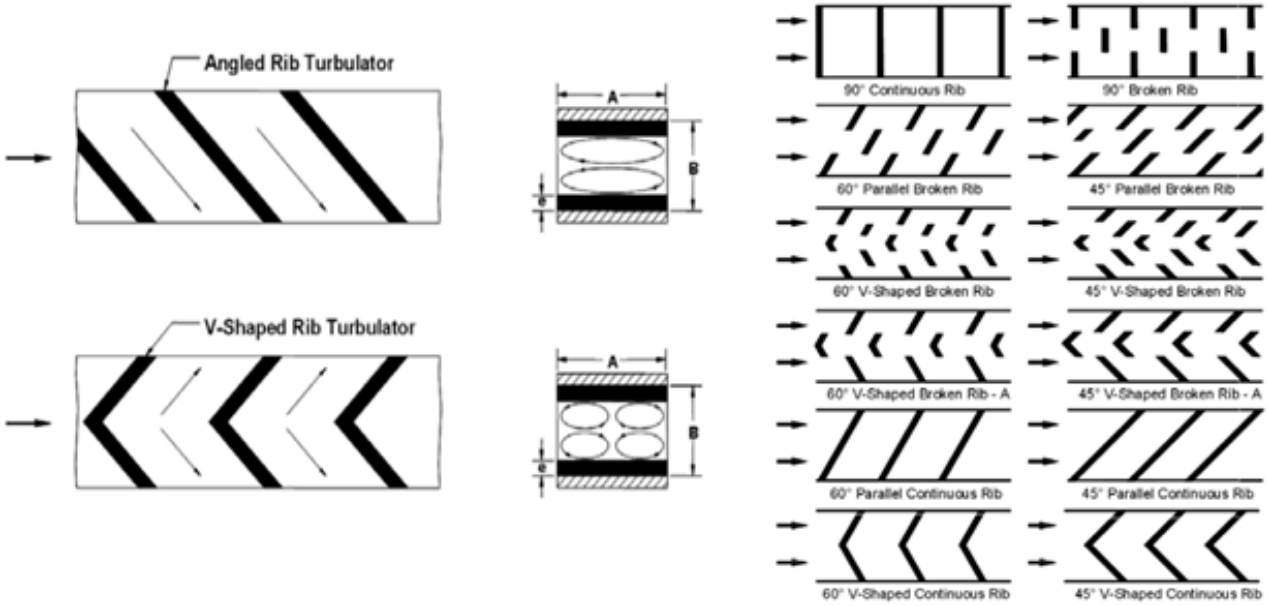

Figure 21. Secondary flow introduced by rib turbulators and different angled rib arrangements (Metzger and Haley, [106]**)**

2.5 **Mist air cooling**

Today there is ongoing pressure on design engineers to produce GT engines which operate at every ever increasing temperatures to improve efficiency. The increased gas temperature can damage the material of the turbine components such as blades and vanes which needs to be addressed. Injecting water mist into the hot gas stream is a promising technique for cooling down turbine components. The water droplets act as heat sinks which linger in the air inside the cooling passage and will eventually vaporise. It is highly desirable to understand how such a distribution can enhance local heat transfer, as a function of the design parameters of the GT components.

Fog cooling, also known as direct evaporative cooling, has recently gained popularity due to its ease of operation and low cost of installation.

There are more than 700 commercially operated GTs using fog cooling. It is, thus, important to understand the fog cooling process. Due to its ease of use, mist cooling is found in many different forms such as inlet fog cooling, overspray cooling using wet compression, and internal airfoil cooling.

Fog cooling begins with liquid water which is atomised into water droplets, also called mist, which are added to the inlet airflow. Given the inlet gas is hot, such water droplets will evaporate and extract heat energy. Compared to industrial applications, aero-engine GTs have been found to demonstrate greater performance improvement with mist cooling. Bhargava and Meher-Homji [107] reported a comprehensive parametric analysis in their study of the effect of inlet misting on wide range of operating conditions for existing GTs. Their data has shown, as might be expected, GT design parameters impact on the effectiveness of inlet misting.

The atomization process is an integral part of the misting process, and studies by Chaker et al. [108–110] have discussed how nozzle design impacts on water atomization due to its effects on droplet thermo-dynamics. Their findings were based on analysing 500 inlet fogging systems for GTs ranging in power from 5 to 250MW. They also used the experimental data gathered to investigate the complexity of the fog droplets before they entered the GT cooling path inlet.

It is rather difficult to determine droplet size quantitatively due to the lack of a consistent method for measuring atomization and droplet formation. Thus, this work was considered to be a monitoring water inlet temperature and flow rate upstream of the cooling path and how these correlated with useful thermodynamic parameters of the airflow downstream of the fogging system. Such a correlation function would be useful in improving engineering and performance interpretation for future design guidelines.

GT design, control and operation are all important for the effectiveness of mist cooling applications as any of these aspects can impact on performance and the above mentioned reports focused on these aspects. These days, the physics and transport of mist behaviour becoming better understood as more work is carried out in this area. For example, Wang et al. [111] used CFD modelling to investigate the influence of droplet dynamics on flow diffusion, turbulence and body force impacts. The simulation included evaluating the effects of droplet size, droplet distribution and air humidity on internal cooling path performance. It was concluded that evaporation occurs mostly within 2m of the mist injection with droplets of less than 10 microns diameter; and that cooling effectiveness is slightly decreased with bigger droplets of more than 50 microns diameter. It was also found that that reverse flow occurring at the diffuser outlet location can impact on the upstream evaporation because temperature near the diffuser exit location rises with lower flow rates. When the channel is a 90^{o} bend, non-uniformity of temperature distribution is found due to effect of the centrifugal force and secondary flow acting on the droplets.

Bahadur et al. [112] proposed a novel concept of a high heat flux thermal management system based on mist flow. Finely dispersed liquid droplets are introduced into a hot free stream of air and flow along the channel as shown in Figure 22. The mist generation location may be in the vicinity of the heat source. Such mist will travel with the flow and extract heat from the surrounding air, or even due to evaporation from hot surfaces. When the air-vapour mixture arrives at the downstream heat exchanger, phase change occurs and the vapour converts to liquid water. This condensate (water) and cooled air are allowed to return to the inlet channel. The process demonstrates the importance of water droplet impingement and evaporation into mist from heated surface, which is different from GT conventional spray cooling methods.

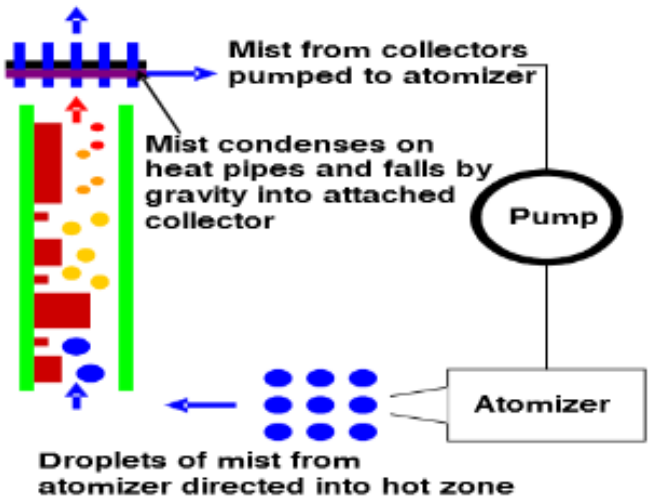

Figure 22 Schematic illustration of mist cooling Bahadur et al. [112]

Kumari et al. [113] have developed a numerical framework to model mist based cooling systems with the goal of gaining a full understanding of both flow-field and heat transfer performance of the mist cooling system. They used commercial CFD software (Fluent) to produce a model which is parameterized based on mist to air fraction and droplet size. Both parameters were found to influence the droplet evaporation process. Their work confirmed the complexity of mist dynamics and heat transfer in the flow.

They modelled the discrete phase combined with the continuous phase for a mist flow entering a copper-finned heat sink. The model allowed evaluation of the impact of inlet mist concentration on the heat dissipation capacity of the heat sink. Both thermal resistance and heat transfer coefficients of mist flow were used to describe and evaluate the thermal performance.

Li and Wang [114] reported the use of mist to enhance air film cooling. Their model is based on a 2D slot and 3D diffusive angled holes configuration as shown in Figure 23.

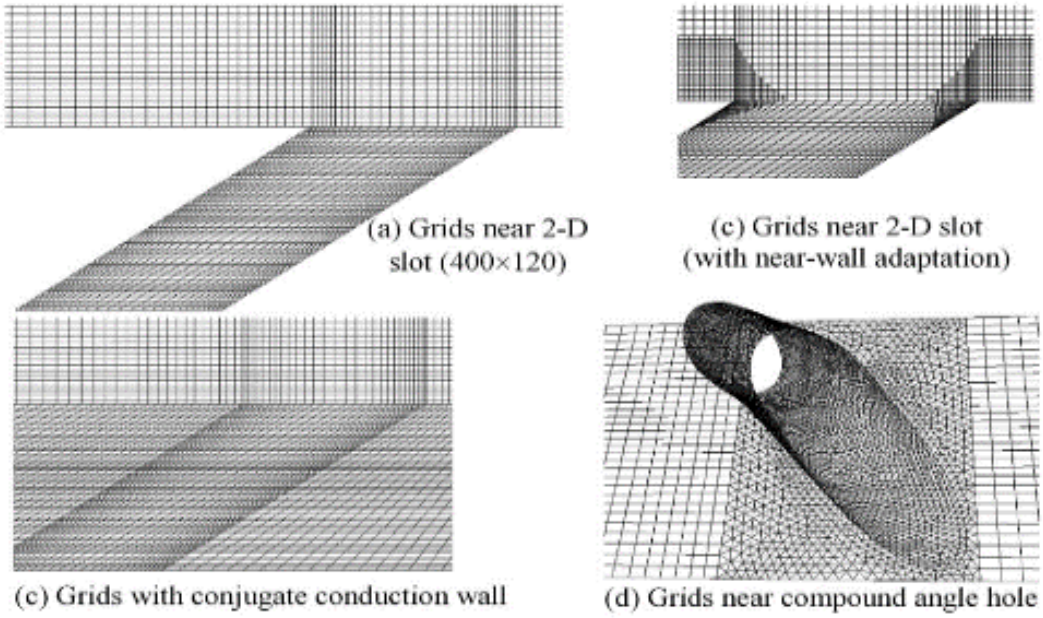

Figure 23 2D slot and 3D diffusive compound angled hole CFD models (Li et al. [114]**)**

Dhanasekaran and Wang [115] simulated results of mist injection and air film cooling for a rotating turbine blade and showed that with a small amount of mist injection, adiabatic film cooling effectiveness could be enhanced by 30% - 50%. However, mist cooling enhancement was found to be relatively more effective at lower flow conditions; lower pressure, temperature and velocity.

Jiang et al. [116] conducted a numerical study, with a CFD program, of mist cooling using realistic, C3X GT, vane geometry. They demonstrated that mist can reach the leading edge of the vane and enhance film cooling. They investigated the effects of varying mist concentration, droplet diameter size, different particle-wall interaction conditions, and effect of forces on the cooling performance. Their numerical results predict that mist injection can decrease flow boundary layer temperature while maintaining core temperature of the flow and boundary thickness.

Guo et al. [117,118] studied the cooling of a straight tube with a superheated surface by steam and mist injection. The results show that

the presence of mist significantly improved the heat transfer. With as little as 5% mist concentration ratio, an average thermal augmentation factor of 100% can be achieved. It was also found that the straight channel inner wall is hotter than outer wall but the hotter section achieves better cooling enhancement which result in much better overall cooling. Pakhomov et al. [119] used a CFD model to study the impact of low mist droplet concentration on cooling performance. His numerical predictions showed that as little as 1% of mist concentration can achieve substantial increase of heat transfer rate compared to no mist used.

Wang and Ragab [120] demonstrated a numerical approach to study the feasibility of mist transportation to the rotating blades of high pressure GTs. In this CFD model. The mist evaporation process was modelled using zero-dimensional analysis while mist transportation is modelled using Discrete Phase Modelling (DPM). This combined method allows tracking of the water droplets which is important in the evaporation process. Mist injection through cooling air passages on turbine vanes is shown in Figure 24. The detailed CFD simulation results show that water vapour is formed near the superheated surface of the vane. Such a water vapour layer is thin but has a higher specific heat capability than air. Thus, this thin layer provides thermal shielding, and water droplets tend to stay longer in a cooler air environment before evaporating. Inlet mist concentration was found useful to control the final heat transfer performance based on mist transportation.

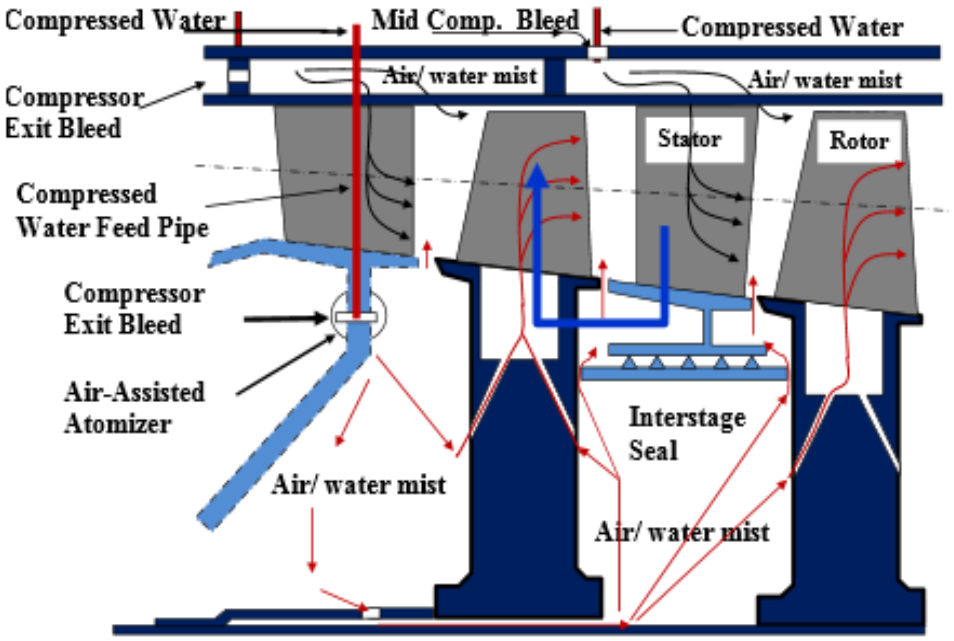

Figure 24 Mist cooling injected through cooling air passage on turbine vanes [120]

Due to the harsh environment existing within the GT, it is essential to account for the effect of heat radiation on the mist injection process, during both evaporation and condensation. Brewster [121] used a theoretical approach to model thermal radiation phenomena. He considered two cases, where the droplet particle size was 0.01-100 microns and the mist case where the nominal cloud droplet size is 20 microns in diameter. An isothermal droplet was assumed for conduction heat transfer and the resulting evaporation rate correlated well with experimental results. His results also suggest that droplet advection within the liquid phase induced by surface regression can be neglected.

The difference between cooling flows of mist/steam and mist/air is that the water droplets used in mist/air are subjected to evaporation than those in mist/steam, under same pressure and temperature.

This is due to the fact that it is the partial pressure of water vapour that determines the evaporation process of the water droplets in mist/air flow. While in mist/steam flow, the total pressure of the mixture determines the

evaporation process. For example, under conditions of saturated pressure and temperature, no evaporation occurs in a mist/steam mixture.

More intensive experimental and numerical work concerning the study of mist/steam in channels was performed by Li et al. [122]. Their numerical results have shown that at least two different flow patterns are present in the domain depending on the Reynolds number and the channel dimensions. They investigated the effect of the flow patterns on the heat transfer performance and suggested that:

(1) particle dynamics induced local turbulence mixing and therefore enhanced heat transfer,

(2) additional mass transfer is induced by evaporation of water from the liquid droplets,

(3) a thick thermal boundary creates a strong temperature gradient near the wall, and

(4) latent heat of evaporation is released when heat is transferred from wall to water droplets.

Li et al. [123] extended their previous work on mist/steam impingement on flat surfaces to surfaces with a concave shape. Such concave shaped surfaces accelerated the flow locally and thus forced the droplets to stay on the surface. When droplets are in contact with the surface, heat transfer will be enhanced due to mixing, as compared to the flat surface conditions.

Nirmalan et al. [124] used a finely dispersed water/air mixture to impinge on the heated internal channel of a turbine for cooling demonstrations. As expected, the water vaporized instantaneously if it impacted on the heated surface of the inner wall. The resulting combined mixture of water/steam/air flowed through the channel towards the exit location during which time additional water is vaporized. Three vanes were constructed for their experimental set-up which had as inlet variables; flow

Mach number, Reynolds number, temperature ratio of wall to gas, and mass flow ratio of coolant to gas. Their test data suggested that the same overall cooling effectiveness obtained with 100% air cooling can be achieved with water/air cooling using only 50% of original airflow.

Wang et al. [125] constructed an experimental turbine assembly with three rows of circular jets, cooled using a mist/steam impingement method. Their test results have shown significant cooling enhancement is achieved as compared to single row jet design. A schematic of their set-up is shown in Figure 34. The area where maximum cooling enhancement is identified spans about five jet diameters in distance. At the low heat flux condition, 3350 W/m^2, cooling is enhancement by 800% with the addition of 3.5% mist by weight. At the high heat flux condition, 13,400 W/m^2, cooling augmentation of 150% was achieved with the same mist injection. Mist injection/impingement was shown to be an effective method to lower surface temperature.

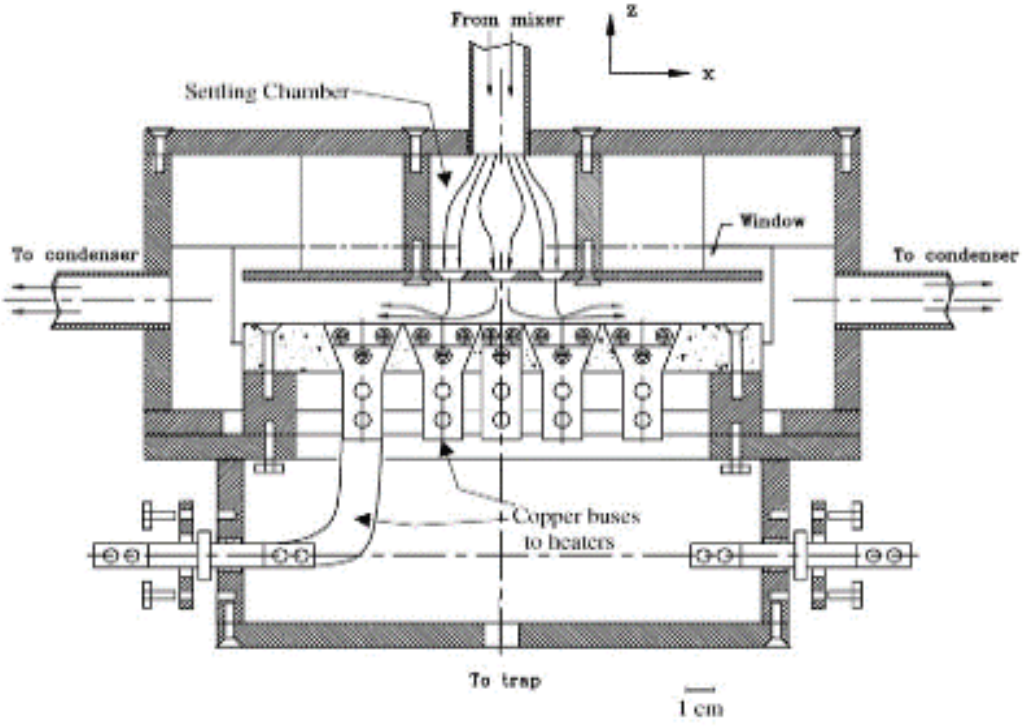

Figure 25 Schematic of three rows cooling jet using mist/steam impingement method (Wang et al. [125]**)**

Ming et al. [126] studied experimentally mist/air jet impingement cooling on a flat surface with constant heat flux, such as might be the condition for work-piece grinding. Their test data suggested that significant heat transfer augmentation is achieved when water droplets are added to the cooling airflow. Initially the heat transfer rate increases rapidly with increase in water content of the mist/air, but there comes a certain value above which the rate of increase in heat transfer slows down. Normal jet impingement (90^o) showed greater cooling enhancement for the flow stagnation region than an oblique jet. The reverse is true in those surface regions away from the stagnation point. When used with a rotating disk on a grinding platform, the direction of the mist jet is important. When the disk and cooling jet are in the same direction, more droplets are entrained onto the rotating disk and higher convective heat transfer is achieved.

Jiang et al. [116] used a numerical CFD approach to study film cooling enhancement on the leading edge of a turbine blade with mist/air injection. They studied different inputs to the model including; mist concentration, droplet diameter size, different particle wall interaction conditions and effect of forces on the cooling performance. Interestingly, their numerical results suggested that mist injection for film cooling can decrease the flow boundary layer temperature while maintaining core temperature of the flow and with no change in boundary thickness. A very high cooling rate was demonstrated as well as the feasibility of mist transportation through the flow within the blade.

2.6 **Mist in cooling passage**

Work described in the previous section has suggested an enhanced rate of cooling, by 50% - 100%, can be achieved by injecting, weight-for-weight, as little as 1% - 3% of mist into the air stream flowing in the cooling passage. The performance also depends on the surface shapes. For example, 200% - 300% cooling augmentation was achieved on tubular and flat surfaces while more than 500% cooling benefit was obtained with a 180^o bend in a channel.

Dhanasekaran and Wang [127] used CFD modelling to demonstrate mist cooling enhancement on a ribbed channel with and without rotation. Their numerical predictions showed that a mere 2% mist injection, gave almost 30% cooling enhancement at the trailing wall surface and 20% at the leading wall surface inside the first passage. The second passage achieved 20% heat transfer enhancement at both leading and trailing wall surfaces.

The numerical study also found that the Nusselt number is not affected by the droplet breakup and coalescence mechanisms. Inside the rotating 180^{o} bend channel, droplets are found to move with a spiral trajectory, suggesting that both centrifugal and Coriolis forces are acting on them.

Compared to the ribbed channel, the effect of rotation was greater on a smooth channel, where the droplets tend to be pushed towards the leading surface of the second passage. Suggesting that after passing the bend centrifugal and Coriolis forces have significant effect. Figure 26 compares the temperature for smooth and ribbed channels.

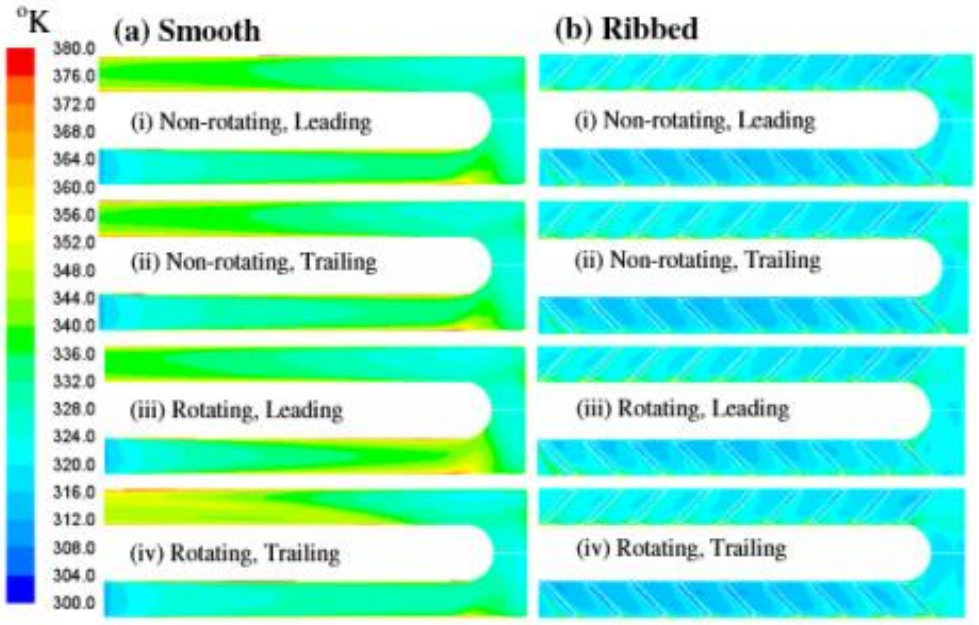

Figure 26 Temperature distributions for both leading and trailing wall surfaces of both smooth and ribbed channels at Re=25,000 (Dhanasekaran and Wang [127]**)**

Dhanasekaran and Wang [128] employed closed-loop steam cooling to demonstrate airfoil cooling. Their numerical study was performed using CFD modelling but using realistic GT operating conditions to demonstrate their cooling enhancement results obtained under different condition are valid for real-world applications. They concluded that the accuracy of their CFD model is within ±8% for prediction of conjugate heat transfer for a given wall temperature and steam-only flow conditions. The model was less accurate, ±16%, if used with mist/steam flow. They studied five different turbulence models. Prediction accuracy improved when thermal radiation was included in the model calculations. The reflect Discrete Phase Model (DPM) wall boundary condition was a better predictor than the wall-film boundary condition. For a 180º bend in a channel with rectangular cross-section, see Figure 36, maximum cooling enhancement was found at the location where mist impingement occurs most effectively. This location is at the outer wall, in the bend at the 45º point, as shown. Within the bend section, mist is pushed towards the inner wall due to the presence of secondary flow interactions and therefore enhanced local

cooling. Overall, their numerical model showed that at realistic GT operating conditions, with only 5% mist injection, 100% cooling enhancement was successfully achieved. Figure 27 is a geometric representation of 180^{o} bend and channel modelled.

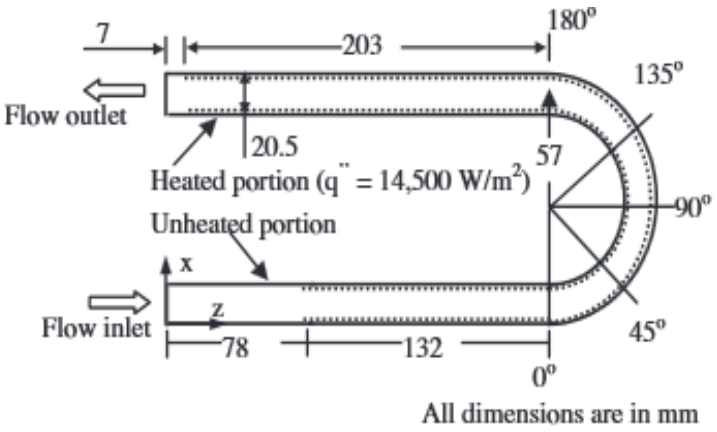

Figure 27 CFD model - 180^{o} bend in a channel with rectangular cross-section (Dhanasekaran and Wang [128]**)**

The details of their numerical model are discussed briefly. The turbulence models they used were: standard k-ω model, RNG k-ε, Realizable k-ε, and SST k-ω. Stochastic particle tracking was used together with the DPM model to trace the locations and trajectories of the water droplets. The average velocity was predicted by the RANS turbulence model. When the droplet arrived at a wall, the droplet trajectory was calculated from the discrete phase wall boundary conditions. As mentioned above, both wall film and reflecting models were used in this study. Particle breakup and coalescence were represented as stick, rebound, spread and splash types depend on the wall temperature and mass transfer.

Guo at al. [129], demonstrated the experimental application of mist/steam cooling to a circular cross-section channel with a 180^{o} bend, which was heated to 300C, see Figure 37. Flow Reynolds number ranged from 10,000 to 35,000. The mist/steam mixture is composed of a combination of finely dispersed water droplets 3-15 microns in diameter and saturated steam supplied at 1.5bar. The test result showed significant

cooling enhancement was achieved by adding the mist into the steam core flow. The maximum enhancement was again found at the 45º location in the bend section downstream from the inlet. Overall 40% - 300% cooling enhancement was achieved. Generally, the test data showed an increase of main flow increased the wall heat flux.

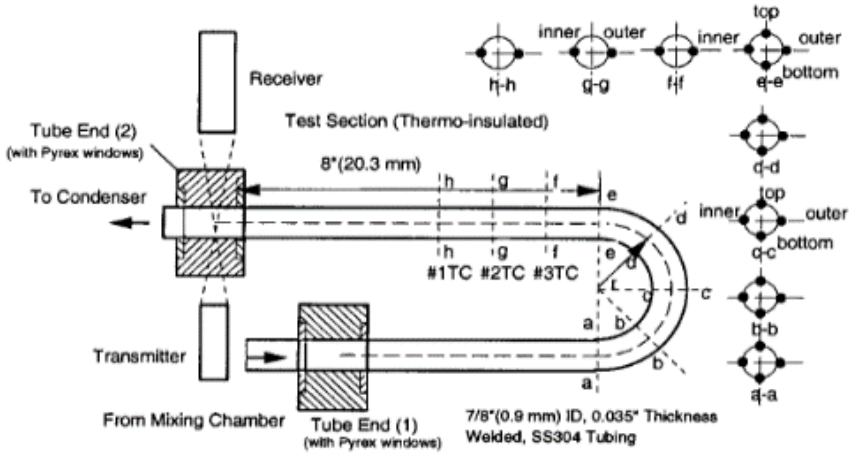

Figure 28 Circular tube test section with 180º bend (Guo at al. [129]**)**

Both two-phase flow and dispersed flow in curved pipes have been studied. It was found that the curvature of the pipe effects the onset position of the critical heat flux in post dry-out dispersed flow. It has also been observed that when such flow enters a 90º bend tube, separation of the liquid phase from the vapour phase happens as result of centrifugal effects.

Mori et al. [130] experimentally tested mist/air impingement cooling of a narrow highly heated coiled-tube. The water droplets were generated from a tube at 0.4mm diameter and forced into the main flow. The coiled-tube had a coil radius of 27mm. The test data showed the heat transfer differed between the inner and outer walls of the tube. They achieved a ten times higher heat transfer effectiveness compared to the air only case

Guo et al. [117,118] studied experimentally mist transportation, droplet dynamics and heat transfer performance of a heated horizontal tube using mist/steam cooling with an injected mist mixture ratio of between 1% and

6%. The flow Reynolds number was between 10,000 and 35,000 with a superheated wall of up to 300C. The local wall heat flux of the test section was obtained by dividing heating power by the total surface area of the section. The local wall heat flux number needs to be realistic and therefore three different source corrections were included: (1) electrical resistance variations due to temperature changes, (2) actual heat loss from the rear of the section - which was well insulated in the setup, and (3) additional heat loss via conduction from the ends of the test section to the end blocks. Measurements of droplet size and distribution were made at both inlet and outlet using a Phase Doppler Particle Analyser (PDPA).

For mist/steam flow set-up, the inlet condition was controlled by the atomization system, see Figure 38. Mist/steam mixture ratio and temperature, droplet size and distribution were controlled systematically. The atomizing system consisted of both pneumatic and pressure atomizers and a mixing chamber. In the mixing chamber, saturated vapour was blended with the mist generated from the atomizer. This mixing process occurs in the top section of the chamber before it is released into the horizontal test section.

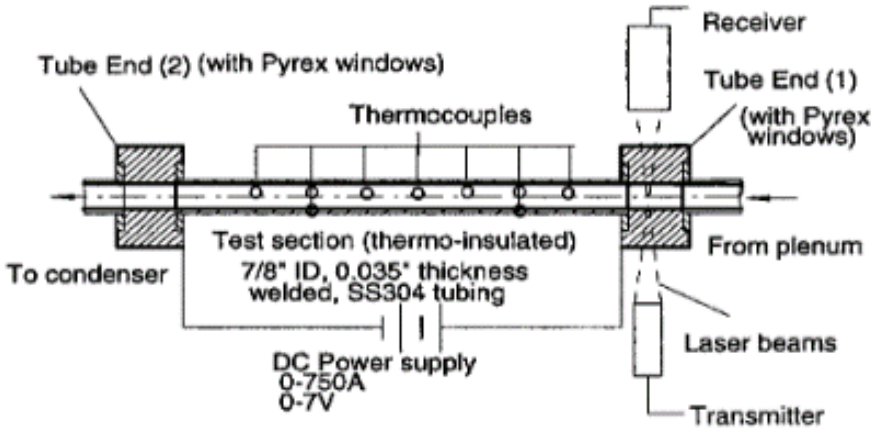

Figure 29 Heated horizontal tube for investigating mist/steam cooling (Guo et al. [117]**)**

Since water droplet size and distribution play an integral role in mist/steam cooling, measuring and quantifying them accurately is

necessary. The PDPA system combined LDV and Light-Scattering Interferometry (LCI) techniques. Before making actual droplet measurement, the system was validated and calibrated using Polymer Latex particle whose diameters were known to range from 3-22 microns.

For temperature measurements a total of seven Omega type thermocouples were placed 25.4 mm (one inch) apart along the axis inside the tube section.

Wang [131] demonstrated mist/steam cooling with a 2% - 5% mass ratio and mist diameter between 5 and 7 microns, can achieve an average enhancement in cooling performance of up to 100% for both a straight tube and a tube with 180^{o} bend. Local improvements in heat transfer can be as much as 200% - 500%, though the data suggests that the greatest benefit is obtained at low Reynolds number flows.

It was found that the modelling of the total heat transfer needed to adequately include: (1) single-phase convection model due to turbulence and mixing, (2) quenching effect in the boundary layer when mist is present, and (3) interactions with the boundary wall where droplet motion and evaporation can disturb the thermal boundary layer and increase mixing which, in turn, can improve heat transfer. Some cases were found where the quenching effect of mist droplets on the heated wall surface has added 2% of heat transfer augmentation factor.

Wang [131] used the Fluent software package for his CFD modelling and concluded that the forces acting on the droplets are primary driven by vapour drag (deceleration) and thrust (acceleration). Thermo-migration was included in the model to account for of temperature gradient as well as inter-molecular momentum transfer effects.

Prediction of the first impact of droplets onto the tube wall is expected to be accurate when the particles flux onto the surface is well estimated. But, on the other hand, downstream droplet trajectory prediction is a highly

challenging task because evaporation of droplets may occur while extracting energy from the heated wall.

For heated surfaces, at relatively low temperature conditions water droplets may coalesce and only eventually will fully evaporate. At high temperatures, a vapour film is formed on the heated surface and acts as cushion to the heated flow and so droplet contact is minimal. Wang [131] has suggested that droplets in contact with the wall can be modelled as being superheated and evaporate immediately if the local partial pressure of the vapour is lower than the saturated vapour pressure.

There are other applications which required mist cooling such as cyclone separators, dust collectors, and flame stabilization in combustion chambers. This required knowledge of single and two-phase flows and heat transfer in a pipe sudden expansion of the flow. Terekhov and Pakhomov [132] carried out a numerical study modelling the flow physics of water droplets were injected into a pipe carrying transitional air flow (Reynolds number 5,300 and 11000) upstream of a sudden expansion. Weight-for-weight the mist was 4.1%, and the mean diameter of the water droplets was 60 microns. The pipe wall is assumed to be dry and heated. Their analysis included particle dispersion distribution and heat transfer performance. Both gas and droplet phases' interactions were modelled using the Eulerian two-phase model for transport equations. The turbulence of the gas phase was modelled using a modified form of the Reynolds Stress Model. Both dispersed and main core flow simulations were conducted simultaneously using two-ways coupling. The Zaichik model was used for the turbulent heat flux equation for the dispersed flow.

When fluid flow within a pipe undergoes a sudden expansion, fine droplets will be entrained within the detached and recirculation regions and eventually distributed across the entire pipe domain. The presence of fine dispersed droplets in the pipe flow was found to weaken turbulence intensity by 25%. Terekhov and Pakhomov found that compared to single phase flow in a pipe, mist/air flow can enhance heat transfer by 100%. The

regions where heat transfer enhancement occurs were identified as correlating well with the presence of fine dispersed particles, that is in flow separation/ recirculation regions and the region of fully developed flow.

However, larger particles such as the 60 micron diameter mist did not enter the recirculation flow region but were suspended within the free shear layer region. It is in the reattachment region that the heat transfer is enhanced by the presence of the large particles.

Figure 30 shows both the two-component turbulent kinetic energy of the main core flow and dispersed particle phase. Both phases exhibit the same patterns of velocity fluctuations. The fine droplets turbulent kinetic energy (TKE) distributions are much smaller than the gas phase in the transverse direction. The location of the maximum dispersed phase velocity fluctuations is within the separated shear layer. The maximum value has also been shown to increase downstream of the core main flow. Terekhov and Pakhomov concluded that their experiment and numerical results correlated well.

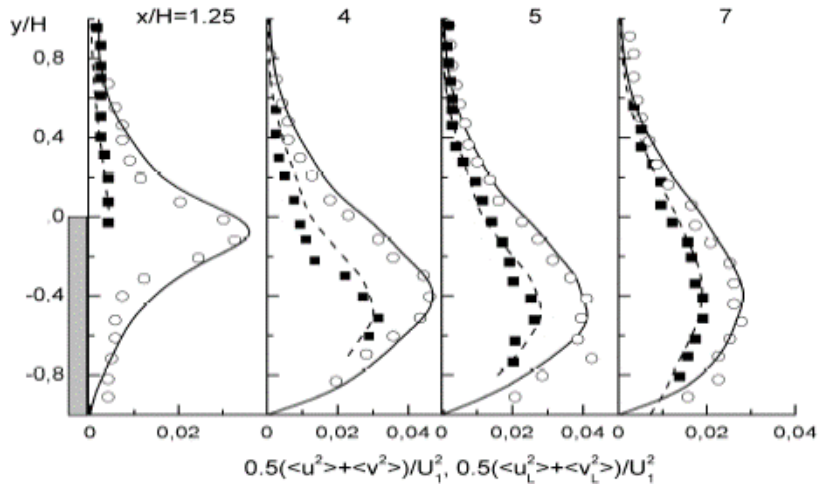

Figure 30 Computed velocity fluctuations of gas (solid lines) and of droplets (dashed lines). Points are velocity measurements of the gas (open symbols) and dispersed phase (solid symbols) (Terekhov and Pakhomov [132]**)**

From the previous literature review has been found that there is a gap on mist ratio effect on heat transfer for a rotating and non-rotating cases. For the non-uniform cross section passage one study carried for different cross section aspect ratio nonetheless no study carried on different shape of cross section were the passage start with a cross section and change near the bend

2.7 **Chapter conclusion**

The extensive review presented above describes present knowledge of the internal blade cooling techniques available in the open literature. It is believed that GT engine manufactures are in possession of additional information but this is unavailable due to commercial confidentiality. The examination of the information above highlights a number of opportunities for additional research is this area. These include investigation of the effects of varying the cooling passages shapes, with implications on the patterns of secondary flow, and hence on the heat transfer performance of these novel shapes. They also suggest that the coupling of mist cooling with "non regular" cross-section passages has not been explored and require visiting. There then are the topics explored in the investigative section of the thesis.

Research question

Does mist injection on stationary and rotating passage has same effect on heat transfer?

Is it possible to improve the heat transfer in cooling passage by manipulation the secondary flow?

Is it possible to develop a cooling passage design with multiple heat enhancement feature and still consider the pressure loss?

3 Modelling approaches

The CFD code employed in the present study is ANSYS Fluent. This code has been extensively employed in blade cooling studies, both when investigating the flow in and around the blades and in the form of conjugate heat transfer computations where in addition to the fluid flow, the heat transfer in the metal part is also computed.

Fluent is a well-established commercial CFD code as well as one of the oldest ones. The code has a large number of physical models with about a dozen turbulence models between main types and variants. There is however no comprehensive information on how to best make use of this variety of models. This is why most papers refer to a limited set of turbulence models. Below a succinct review of the most relevant ones is undertaken.

3.1 **Standard k-ε model**

This is the most used turbulence model that has been described in the literature. The reason is that it provides reasonable predictions for many flows and due to its computational economy in a wide range of cases in additional to its robustness. Establishing this model was based on the assumption that the flow is fully turbulent with no effect of molecular viscosity. Therefore, this model cannot be applied on near wall locations, as an additional model is required to consider molecular viscosity like wall functions based on semi-empirical formulas and functions. However, there were a few important cases where the Standard k-ε model performed inadequately as reported by [133,134] on flow separation and flow reattachment. Also poor prediction for flow recovery [135], secondary flow in complex geometries [136] swirling flows, rotating flows, axisymmetric jets and fully developed flows in non-circular ducts. Several improvements have been done to the standard k-ε model, the RNG model and the Realizable model are among them.

The RNG k-ε model modification included swirl effect on turbulence, better interaction between turbulence dissipation and the mean shear, Prandtl number formula and effective viscosity differential formula. These changes improved the model predictions for flow with separation and reattachment, transitional and wall heat transfer.

The turbulent viscosity or eddy viscosity, μ_t, is modelled as

$$\mu_t = \rho C_\mu \frac{k^2}{\varepsilon} \tag{10}$$

Therefore, the transport equations for turbulent kinetic energy (*k*) and turbulent dissipation rate (*ε*) need to be solved to represent the eddy viscosity. The *k* and *ε* equations are given by

$$\frac{\partial}{\partial t}(\rho k) + \frac{\partial}{\partial x_i}(\rho k \bar{u}_i) = \frac{\partial}{\partial x_j}\left[\left(\mu + \frac{\mu_t}{\sigma_k}\right)\frac{\partial k}{\partial x_j}\right] + P_k - \rho\varepsilon \tag{11}$$

$$\frac{\partial}{\partial \mathrm{t}}(\rho\varepsilon) + \frac{\partial}{\partial \mathrm{x_i}}(\rho\varepsilon\bar{\mathrm{u}}_\mathrm{i}) = \frac{\partial}{\partial \mathrm{x_j}}\left[\left(\mu + \frac{\mu_\mathrm{t}}{\sigma_\varepsilon}\right)\frac{\partial \varepsilon}{\partial \mathrm{x_j}}\right] + \mathrm{C}_{1\varepsilon}\frac{\varepsilon}{\mathrm{k}}\mathrm{P_k} - \mathrm{C}_{2\varepsilon}\rho\frac{\varepsilon^2}{\mathrm{k}} \tag{12}$$

The value of the model constants are

$$C_{1\varepsilon} = 1.44, \qquad C_{2\varepsilon} = 1.92, \qquad C_\mu = 0.09, \qquad \sigma_k = 1 \text{ and } \sigma_\varepsilon = 1.3$$

Near wall treatment for k-ε model

The standard *k-ε* model needs special treatment in the vicinity of solid walls to model the wall blocking effects due to viscosity. The turbulent viscosity must become zero at the wall to satisfy the zero Reynolds stresses at the wall. There are various techniques available in the literature for near wall treatment, namely, wall function approach and Low-Reynolds number approach and enhanced wall treatment. Wall function uses log-law near the wall to prescribe either the velocity or the wall shear stress in near wall grid point. In the low-Re models, damping functions are

used in the expression of eddy viscosity and in the transport equations to model the wall blocking effects. In enhanced wall treatment or two-layer approach, one equation model of Wolfstein is solved in the inner layer near the wall and the standard k-ε model is used in the outer layer. The inner and outer layer interface is defined on the basis of the turbulent Reynolds number (Re_y) defined as

$$Re_y = \frac{\rho y \sqrt{k}}{\mu} \tag{13}$$

The eddy viscosity is defined as

$$\mu_{t,ENH} = \Lambda_\epsilon \mu_t + (1 - \Lambda_\epsilon)\mu_{t,2Layer} \tag{14}$$

Where, μ_t is calculated from equation in the outer layer ($Re_y > 200$), whereas, $\mu_{t,2Layer}$ is calculated in the inner layer as

$$\mu_{t,2Layer} = \rho C_\mu l_\mu \sqrt{k} \tag{15}$$

The blending function, λ_ε is defined as

$$\Lambda_\epsilon = \frac{1}{2}\left[1 + tanh\left(\frac{Re_y - Re_y^*}{A}\right)\right] \tag{16}$$

The length scale in equation is defined as

$$l_\mu = y C_l^* \left(1 - e^{-Re_y / A_\mu}\right) \tag{17}$$

3.2 **The Shear Stress Transport k-ω (SST)**

This is a combined model developed by Menter [137]. It combines both a near walls k-ω turbulence model with its capability away from walls. In order to account for turbulent shear stress transport, a modified definition of turbulent viscosity was modified.

An additional turbulence model to explore is the k-ω model which has two different variations, the standard k-ω and the Shear Stress Transport model (SST). The same transport equations for k and ω are being used by

both models. However, the main differences between the two models can be summarized as follow:

A slow steady change occurs in the inner region of the boundary layer of the standard k-ω turbulence model to the outer part of the boundary layer of the k-ε turbulence model. A modified turbulent viscosity equation is being adopted by the SST model to consider the principal turbulent shear stresses transport effects. The sections below show the solving methods for all constants and turbulent viscosity as well as presenting the transport equations and explaining all the differences.

In Fluent, the standard k-ω has only one variation model which is the shear stress transport k-ω model that was developed by Menter (1994) by the use of both, the standard k-ω model and the transformed k-ε model. The Calculation of the turbulence viscosity considering the transport of the principal turbulence shear stress is the core difference. For a proper calculation of both the near wall and far-field regions, a cross-diffusion term in the B equation and a blending function were included in this model. For near wall regions, the standard k-ω model is generated by the blending function and for regions away from the surface, the k-ε-like model is adopted. Due to these differences, the SST model is the preferred model when a large variety flows occurs, rather than the standard k-ω model.

3.3 **The Reynolds Stress Model (RSM)**

This model is also called a Second Order Closure (SOC) as it can be considered a higher level turbulence model. The approach originates from Launder and Spalding [138]. A direct calculation of Reynolds stresses while the eddy viscosity approach was rejected in this model. In order to account for Reynolds stress field directional effects, the exact Reynolds stress transport equation should be applied. These closure equations can be reviewed in [14]

3.4 **V2F Model**

This model is developed by Durbin [139–141]. Durbin added two equations to the k-ε equations, the wall normal stress v^2 and a function f, so it has become a four equation eddy viscosity turbulence model. It is a simple version of the elliptic relaxation Reynolds stress model. A replacement of Reynolds stress equations system with transport equation for both velocity scalar (v^2) and ellipse equation for (f). The goal of this model is to improve the effects of wall on the turbulence. In order to avoid numerical oscillations of wall boundary, this model was rewritten as mentioned in [142]. Equations of v^2 and f can be found in [142] while both equations for turbulent kinetic energy and dissipation rate are the same as in the k-ε model.

$$\boldsymbol{u_j \frac{\partial v^2}{\partial x_j} = kf - 6v^2 \frac{\varepsilon}{k} + \frac{\partial}{\partial x_j}\left[(v + v_t)\frac{\partial v^2}{\partial x_j}\right]} \quad (18)$$

$$\boldsymbol{L^2 \frac{\partial^2 f}{\partial x_j^2} - f = \frac{1}{T}\left[(C_1 - 6)\frac{v^2}{k} - \frac{2}{3}(C_1 - 1)\right] - C_2 \frac{G}{K}} \quad (19)$$

$$\boldsymbol{T = \max\left[\frac{k}{\varepsilon}, 6\sqrt{\frac{v}{\varepsilon}}\right]} \quad (20)$$

$$\boldsymbol{L = C_L \max\left[\frac{K^{\frac{3}{2}}}{\varepsilon}, C_\eta \left(\frac{v^3}{\varepsilon}\right)^{1/4}\right]} \quad (21)$$

3.5 **Discrete phase model for water droplet injection**

The second part of this study covers heat transfer enhancement using water droplets injection in airflow. The water injection of mist was modelled using both methods namely DPM and average Cp method as discussed in

the introduction. The density is formulated as for the incompressible ideal gas law. The water vapour mass flow rate for the different analyses is considered from 2-5% of air flow. In most of work in the area of cooling enhancement, a mass flow of water droplets corresponding to 2-5 % of the bulk flow was considered.

The numerical modelling of droplet evaporation and consequent heat and mass transfer are modelled with the discrete phase model (DPM). This model is based on the Euler-Langrage approach where the Euler phase corresponds to fluid as a continuum and the Langrage approach is used for the discrete phase as particles. The fluid is modelled as continuous phase by solving the Navier-Stokes equations and the dispersed phase is calculated by tracking a number of particles as droplets in the calculated continuous flow field. The coupled Eulerian-Lagrangian modelling allows the exchange of mass, momentum and energy transfer between two phases. The particle-particle interaction can be neglected in present study as mass fraction of droplets as discrete phase is low [Fluent theory guide].

ANSYS FLUENT has modelling capabilities for the discrete phase to calculate heat, mass and momentum of particles and the exchange with continuous phase. These capabilities can be summarized as;

- Discrete phase trajectory calculation: It uses the Langrangian model that includes the discrete phase inertial force, hydrodynamic drag force, and the force of gravity.

- Turbulence calculation: The particles are dispersed due to turbulence eddies present in the continuous phase and the CFD predicts this turbulence effect.

- Heating/cooling of the discrete phase depending on the temperature difference of the discrete and continuous phases and specific heat of the liquid droplets

- Vaporization and boiling of the discrete phase: The mass fraction of liquid phase that is vaporized or evaporated is calculated depending on the temperatures of vaporization and latent heat of the discrete phase

- Particle combustion: It can model surface combustion of combusting particles, particularly for coal or char combustion.

- Two Way Coupling: It can calculate two-way effect of the continuous phase flow field prediction to the discrete phase calculations

- Particle Breakup Models: It can predict and model droplet breakup and formation of secondary droplets or coalescence of particles.

- Consideration of particle/particle collisions like coalescence and particle breakup for secondary atomization.

These modelling capabilities of DPM model provided in Ansys Fluent makes it suitable for modelling of spray dryers, liquid fuel combustion and some particle laden flows like centrifugal separators. It cannot be used for liquid-liquid mixtures, fluidized beds or any other application where particle mass fraction is significant as compared with fluid phase [Fluent user guide].

Discrete phase model predicts particle trajectories using calculated continuous phase. The net resultant force drives the particle with the magnitude and direction of velocity field using Newton’s 2nd law. There

are additional force terms which may be included in momentum equation like Saffman lift force, thermophoratic force, gravity force.

During course of motion of particle, it may encounter different situations known as fate of particle. The particle may reflect from a surface, escape from any boundary surface, evaporate or declared as incomplete. The details of these different conditions cannot be included in present report.

In most of engineering problems, like spray drying, evaporative cooling or liquid fuel evaporation, it is recommended that continuous phase should be solved first. The DPM model is set to calculate its interaction and exchange of heat, mass and momentum. The characteristics of discrete phase are defined as ‘injection’ in Fluent solver. The information of initial position, velocity, size, and temperature of injection are provided along physical properties of the discrete phase material. As discussed briefly, the trajectory of particles is based on force balance for the particle and this requires complete understanding of different options for definition of forces which are important for a particular situation. In present problem of modelling liquid water droplets in air, Saffman lift force is included whereas drag force and gravity have not been considered. The Saffman lift force is considered for submicron particles for calculation of lift force due to shear [143]

The dispersed phase can exchange mass, momentum and energy with continuous phase through diffusion, conduction, convection and radiative modes during course of its motion through continuous phase.

3.6 **DPM model setting**

The case of liquid droplets injection is modelled in ANSYS Fluent by setting initial and flow conditions of liquid spray. The inlet surface is selected for particle injection and velocity, diameter and mass flow rate of injection are provided. In present study the mass flow rate of water

droplets injection constitutes 2%, 4% and 5 % of air mass flow rate. The mass flow rate of air for Re 25000 is 0.0056 Kg/sec. The mass flow rate of particle injection is calculated for three mass fraction cases.

The surface injection type uses number of cells as particle density and these are injected normal to the boundary. The inlet surface has 2610 cells therefore same numbers of injection points are defined by solver. When particles approach a wall surface, they are assigned as ‘reflect’ boundary condition. It means that droplets will rebound off elastically when they hit or approach wall. The inlet and outlet boundary conditions are defined as 'escape' condition for droplets. The droplets approaching inlet or outlet boundary surface are escaped and are excluded from DPM calculations. The particle trajectories are updated after 10 iterations of continuous phase flow trajectory calculations. The time interval for particles is set to 0.001 sec.

The water droplets injected in present case are partly evaporated and remaining particles are escaped through outlet. As flow is analysed at ambient temperature, therefore all of droplets are not evaporated. However, the evaporated particle extracts heat of vaporization (latent heat) from air and results in higher heat transfer rates. Moreover, higher Cp of liquid water and water vapours are responsible for higher values of Nusselt number achieved.

CFD analysis of liquid water droplets injected in the flowing air involves number of physical phenomena and requires modelling a lot of process. This study has been conducted for square cross-section with ribs installed on leading and trailing surfaces.

The Nusselt number can be calculated using average wall temperature and bulk temperature of air with as calculated in the previous section:

$$Nu = \frac{hD}{k} \tag{22}$$

Here *h* is the heat transfer coefficient for a heated wall section, *D* is hydraulic diameter of rectangular channel, and k is the thermal conductivity of the coolant.

The spray of water droplets in air and their evaporation can be modelled as two-phase flow; one as continuous phase and other as discrete phase. The CFD model can compute the motion of liquid droplets and their evaporation in a continuous phase, such as air. The water evaporated will become part of a continuous phase formed by air and water vapour.

The amount of mist (liquid droplets) in air is usually very small (less than 0.1 % volume fraction), therefore the Discrete Phase Modelling (DPM) methodology can be applied. This approach involves the numerical computation of a continuous phase by Eulerian modelling, and then trajectory calculations of droplets particles (discrete phase) are performed by Langragian modelling. The impact of the dispersed phase on the continuous phase is reflected as source terms for mass, momentum, energy and species concentrations.

Continuous Phase

The time-averaged equations for conservation of mass, momentum, energy and species are given as follows for computation of the continuous phase:

$$\frac{\partial}{\partial x_i}(\rho u_i) = S_m \qquad (23)$$

$$\frac{\partial}{\partial x_i}\left(\rho u_i u_j\right) = -\frac{\partial P}{\partial x_i} + \rho \bar{g}\, j + \frac{\partial}{\partial x_i}\left(\tau_{ij} - \rho\overline{u_i' u_j'}\right) + F_j \qquad (24)$$

$$\frac{\partial}{\partial x_i}\left(\rho C_p u_i T\right) = \frac{\partial}{\partial x_i}\left(\lambda \frac{\partial T}{\partial x_i} - \rho C_p \overline{u_i T}\right) + \mu\phi + S_h \qquad (25)$$

$$\frac{\partial}{\partial x_i}\left(\rho u_i C_j\right) = \frac{\partial}{\partial x_i}\left(\rho D_j \frac{\partial C_j}{\partial x_i} - \rho\overline{u_i C_j}\right) + S_j \qquad (26)$$

The source terms for mass, momentum and energy (S_m, F_j and S_h) are used to include contributions from the discrete phase; τ_{ij} is symmetric stress tensor; $\mu\phi$ is viscous dissipation; and λ is the thermal conductivity;

C_j represents concentration of species "j". The liquid first evaporates around the droplets and is then transported away to diffuse into air. Hence, three species are included in the numerical model. The diffusion term D_j is used for bi-diffusion between vapour and air mass. The terms $\rho\overline{u_i'u_j'}$, $\rho C_p\overline{u_i T}$ and $\rho\overline{u_i C_j}$ which represent Reynolds stresses, turbulent heat fluxes and turbulent concentration for species are modelled as turbulent quantities.

For turbulence modelling, the k-ε model is used. This two-equation model formulates equations for kinetic energy (k) and its dissipation rate (ε) as follows:

$$\frac{\partial}{\partial x_i}(\rho u_i k) = \frac{\partial}{\partial x_i}\left[\left(\mu + \frac{\mu_t}{\sigma_k}\right)\frac{\partial k}{\partial x_i}\right] + G_k - \rho\epsilon \quad (27)$$

$$\frac{\partial}{\partial x_i}(\rho u_i \epsilon) = \frac{\partial}{\partial x_i}\left[\left(\mu + \frac{\mu_t}{\sigma_k}\right)\frac{\partial k}{\partial x_i}\right] + C_{1\varepsilon}G_k\frac{\epsilon}{k} - C_{2\varepsilon}\rho\frac{\epsilon^2}{k} \quad (28)$$

The turbulent viscosity can be modelled using equation:

$$\mu_t = \rho C_\mu G_k \frac{k^2}{\epsilon} \quad (29)$$

The values of constants used in the k-e model are extracted from (1) and are given here:

$$C_{1\varepsilon} = 1.44, C_{2\varepsilon} = 1.92, C_\mu = 0.09, \sigma_k = 1.0, \sigma_k = 1.3$$

The values for turbulence Prandtl number (Pr) and turbulence Schmidt number (Sc) is set to 0.85 and 0.7 respectively.

The effective thermal conductivity and effective diffusion coefficient can be calculated using equations 30 and 31.

$$\lambda_{eff} = \lambda + {}^{C_p\mu_t}/_{Pr_t} \quad (30)$$

$$D_{eff} = D + {}^{\mu_t}/_{Sc_t} \quad (31)$$

For solution of flow field in the near wall region, enhanced wall treatment can be used. The turbulence model, k-ϵ, is therefore used with the enhanced wall treatment. Formulation the computational domain is divided

into two regions: viscosity-effected region, and fully turbulent region for the application of the two-layer approach. The turbulent number is Re_y = $yk^{1/2}/\nu$, where k is turbulent kinetic energy and y is the wall distance.

This number determines that whether the flow is in a fully turbulent or viscosity-effected region. For Re_y > 2000, the flow is assumed to be fully turbulent and the k-ϵ model is applied. For Re_y< 2000, the flow is considered to be in the viscosity-effected region and one equation model is used. Instead the turbulent viscosities calculated from the two regions are smoothed with a blending function, given as equation (32), to make a seamless transition from wall to fully turbulent core flow.

$$\mu_{t,\text{enhanced}} = \theta\mu_t + (1-\theta)\mu_{t,l} \qquad (32)$$

Here, μ_t = Viscosity calculated from the k-ϵ model of high Reynolds number

$\mu_{t,l}$ = Viscosity from the near wall one-equation model

Discrete phase

The discrete phase is solved for droplet motion, evaporation, heat transfer and droplet breakup modelling.

The motion of particle can be modelled by:

$$m_p\left({}^{dV_p}/_{dt}\right) = \sum F \qquad (33)$$

Where V_P is velocity vector

The force F represents the combined force acting on the droplet. This may include hydrodynamic drag, gravity, thermophoretic force, and Saffman lift force. This study includes Saffman's force.

For computation of heat transfer due to radiation, the P1 model was used. The details of the P1 model are given here for particle heat transfer due to radiation [6]. The radiation flux (q_r) is calculated using equation (34):

$$q_r = -\frac{1}{3(a+\sigma_s)-C\sigma_s}\nabla G \tag{34}$$

Here, a is absorption coefficient; σ_s is scattering coefficient; *G* is incident radiation intensity; and *C* is the linear anisotropic phase function coefficient.

The parameter Γ is defined for factors included in equation (35) as represented by equation (13)

$$\Gamma = \frac{1}{(3(a+\sigma_s)-C\sigma_s)} \tag{35}$$

Equation 12 simplifies to:

$$q_r = -\Gamma\nabla G \tag{36}$$

The transport equation for radiation intensity is given as:

$$\nabla.(\Gamma\nabla G) - \mathrm{aG} + 4\mathrm{an}^2\sigma\mathrm{T}^4 = \mathrm{S_G} \tag{37}$$

Here, n is refractive index of the medium; σ is Stefan-Boltzmann constant; and $\mathrm{S_G}$ represents radiation heat source (or sink) defined by user.

Combining equation 14 and equation 15, gives:

$$-\nabla.q_r = \mathrm{aG} - 4\mathrm{an}^2\sigma\mathrm{T}^4 \tag{38}$$

The heat transfer for the droplet is given by the following equation:

$$m_p C_p \frac{dT}{dt} = A_p h(T_\infty - T) + \frac{dm_p}{dt}h_{fg} + A_p\epsilon_p\sigma(\theta_R^4 - T^4) \tag{39}$$

The equation accounts for heat transfer through convection, radiation, and required for evaporation. The terms given in above equation are:

m_p, C_p, T, A_p= mass, specific heat capacity, temperature and area of particle respectively.

h_{fg} = latent heat of particle material

h = convective heat transfer coefficient

T_∞ = Ambient temperature of surrounding air

ϵ_p = particle emissivity

θ_R= radiation temperature

The convective heat transfer coefficient can be obtained with an empirical expression given in equation (40):

$$Nu_d = \frac{hd}{\lambda} = 2.0 + 0.6Re_d^{0.5}Pr^{0.33} \quad (40)$$

The Nu_d, Re and Pr are the Nusselt, Reynolds and Prandtl numbers of the droplet respectively.

The vaporization rate of droplet given in equation (39) is driven by the concentration difference between the concentration at the droplet surface and that in the air stream.

$$-\frac{dm_p}{dt} = \pi d^2 k_c (C_s - C_\infty) \quad (41)$$

The concentration values C_s and C_∞ denote the values at the droplet surface and in the air stream respectively. The mass transfer coefficient k_c is determined by a correlation given in equation (42):

$$Sh_p = \frac{k_c d}{D} = 2.0 + 0.6Re_p^{0.5}Sc^{0.33} \quad (42)$$

Where Sh is the Sherwood number, Sc is the Schmidt number, and D is the diffusion coefficient

The evaporation rate of a liquid droplet can be calculated using equation (43) when droplet reaches its boiling point:

$$-\frac{dm_p}{dt} = \pi d^2 \left(\frac{\lambda}{d}\right)\left(2.0 + 0.46Re_p^{0.5}\right)\frac{\ln\left(1+C_p(T_\infty - T)/h_{fg}\right)}{C_p} \quad (43)$$

Where C_p is the specific heat of bulk flow

The droplet trajectories are calculated with the instantanous flow velocities $(\bar{u} + u')$. The time averaged velocity $\bar{u}$ does not represent particle droplet

velocity; it is affected by fluctuations in velocity. The velocity fluctuations are defined by a normally distributed random number ς, as defined by equation (44):

$$u' = \varsigma\left(\overline{u'^2}\right)^{0.5} = \varsigma(2k/3)^{0.5} \qquad (44)$$

This velocity fluctuation will be assigned to droplet particle for a period of eddy life time. The eddy life timescale is calculated using turbulent kinetic energy its dissipation rate.

The interaction of droplets with ribblets and with themselves results in droplet breakup and coalescence. The breakup mechanisms of droplets and subsequesnt creation of smaller droplets (child droplets) is modeled by Taylor Breakup (TAB) model. The coalescence of liquid droplets is modelled by the O'Rourke model [144]. The TAB model is best for low-Weber-number sprays. Extremely high-Weber-number sprays result in shattering of droplets, which is not described well by the spring-mass analogy.

O'Rourke's model is used for modeling coalescence when droplets collide. The coalescence model algorithm assumes that droplets can only collide if they are in same cell. This assumption may cause some error for colliding particles which are placed in adjacent cells. Similarly, some of the droplets are farther but may collide if they are placed in same cell. The overall accuracy is second order.

The outcome of a collision will result in either "coalescence" if it is a head-on collision, or "bouncing" if the collision is oblique. Both these models show improved results at local acceleration or deceleration points, e.g. rotation or bends in flow channel.

Model	Advantage	Disadvantages
Mixing length	• Easy to implement. requiring less computing resources • Well-established • Suitable for thin shear layers (e.g. jets. wakes)	Incapable for flows with separation/recirculation
Spalart-allmaras	• Algebraic calculation of length scale provides economic computation • Good results in flows with adverse pressure gradient • Suitable for external aerodynamics	• Definition of length scale difficult given complex geometries
Standard k-e	• Need only supply initial and/or boundary conditions • perform well for many industrially relevant flows • Most validated model	Extremely poor performance in flows with adverse pressure gradient leading separation/recirculation
RNG k-e	Good for moderately complex behavior like jet impingement, separating flows, swinging flows and secondary flow.	Subjected ID limitations due to Isotropic eddy viscosity assumption. Same problem with round Jets as standard k-e
Realizable k-e	offers largely the same benefits as RNG tut also resolves the Round-Jet anomaly.	Subjected to limitations due to isotropic eddy viscosity assumption.
Wilcox k-w	• Integration of flow solution to the wall does not require extra damping func1ions for low-Re regimes • Turbulent boundary conditions prescribed at the wall	Prediction of separation is early and excessive
SST k-w	• Blending functions allows use of k· w model near-wall and k-e in fully turbulent region far from wall • Excellent agreement for flows with or without adverse pressure gradients	Exira functions increase complexity and computational resources required

4 Model validation

In this chapter a set of numerical investigations performed by the author is described. The cases studied are available in the literature and correspond to heat transfer situations that are useful for CFD users to validate their models. Their inclusion in the present research constitute the first modelling block of the research objectives, to perform a set of numerical investigations to validate the numerical models available for this research and identify modelling performance of various turbulence modelling techniques (k-ε, k-ω and V2F) for a nozzle guide vane and a turbine blade

4.1 Introduction

It is well known that an enhancement of heat transfer can be achieved by placing turbulators such as ribs in a flow passage at periodic intervals. The flow thus induced has numerous separation zones where the ribs generate secondary motion across the passage which causes a significant increase of the turbulence and heat transfer levels. The aim of the work performed here is to obtain a level of validation of the numerical method employed in this research as well as to be used as an opportunity for the author to develop his computational skills. The experimental data is available from the European Research Community on Flow, Turbulence and Combustion, ERCOFTAC consortium and was gathered by the University of Manchester's ERCOFTAC chapter.

4.2 Backward facing step with heating

A 2D model of fluid flow and heat transfer coefficient over a backward-facing step is first demonstrated. A separation of the boundary layer followed by reattachment occurs while applying a uniform heat-flux along the sudden expansion which causes numerical difficulties for the resolution of the local heat transfer. A set of experimental data of the measured local Nusselt number distribution over the wall is used to

validate the current CFD results [145]. A non-uniform Cartesian mesh of 121x61 nodes was employed in this simulation. A fully developed, steady flow was used as inlet boundary conditions. The thickness of the incoming boundary layer is 1.1H using as reference the backward step H, as shown in Figure 40

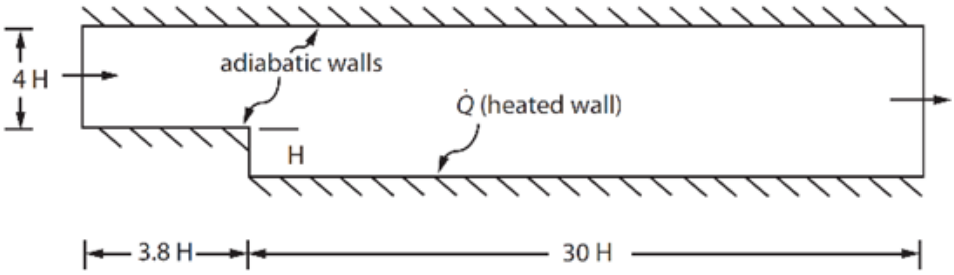

Figure 31 Backward facing step geometry

Three meshes were used in this part of the investigation denoted as coarse medium and fine as shown in Figure 32a, b and c, respectively.

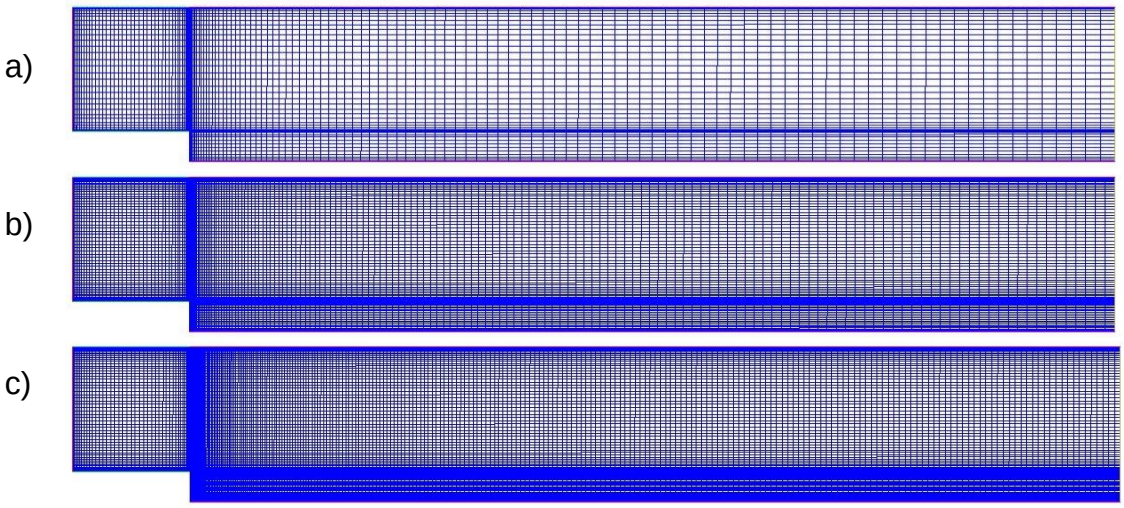

Figure 32 Backward facing step mesh

Solver and Boundary conditions

For this study, the ANSYS FLUENT solver of the 14.5 version was used. A pressure-based, steady, 2D planar setup was chosen due to the nature of the problem investigated. More details of the solver features can be found in [143].

The boundary conditions used are reported in Table 1. The ambient conditions are assumed to be at sea level and temperature 300 K,

Table 1 boundary condition and physical properties for the backward facing step

parameter	Value
Density	1.225 kg/m3
Viscosity	0.0001 kg/m-s
Conductivity	1.408 W/m-K
Specific Heat	10,000 J/kg-K
Reynolds number	28000
Heat flux	1,000 W/m2

Solution setup and convergence

For the purpose of this simple test case single precision was used for the calculations. The SIMPLEC algorithm (Semi-Implicit Method for Pressure Linked Equations-Consistent) is employed. The under relaxation factors were kept constant and equal to the default values at the start of the computation and only at the end, when the residual seem to stabilize, slightly lower under relaxation factors were used to eliminate any oscillations in the residuals. Solution initialization was performed with the inlet boundary conditions imposed.

The main parameter used to gauge iterative convergence are the residuals. These were however complemented by other measures, the mass flow rate balance at inlet and outlet were monitored. In this study the convergence criterion for all residuals was set to 10E-6, at least six orders of magnitude reduction in the residuals. A representative convergence history is shown in Figure 33

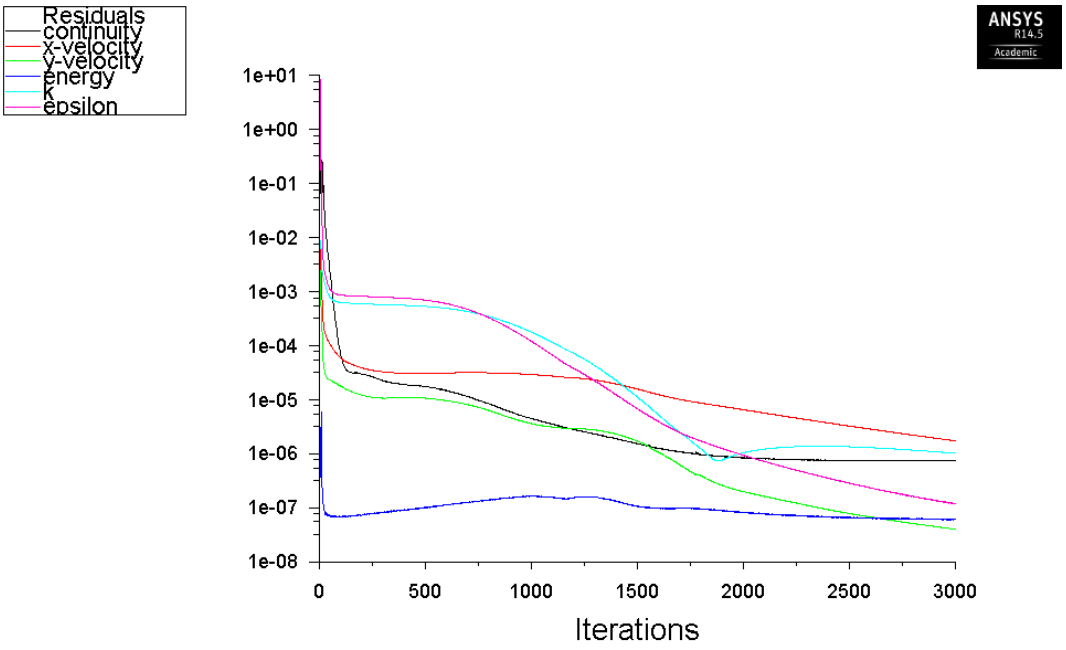

Figure 33 Solution convergence for the backward facing step

Simulation results:

A grid dependency and turbulence model study was then carried out to validate the code application in a case similar to the situations which constitute the focus of the thesis. The results obtained with the coarse mesh show a slight difference from those obtained with the other meshes, Figure 34a.

In Figure 34b a distribution of the axial distribution of the Nusselt number is plotted for four turbulence models using the medium sized

mesh. For such application the k-ε RNG proved to be the turbulence model with great accuracy based on the agreement with experimental data and compared to the three other models. The k-ω STT and v^2-f models predictions show poor agreements between the predicted and experimental values of the Nusselt number due to the separation zone on the leeward side of the step.

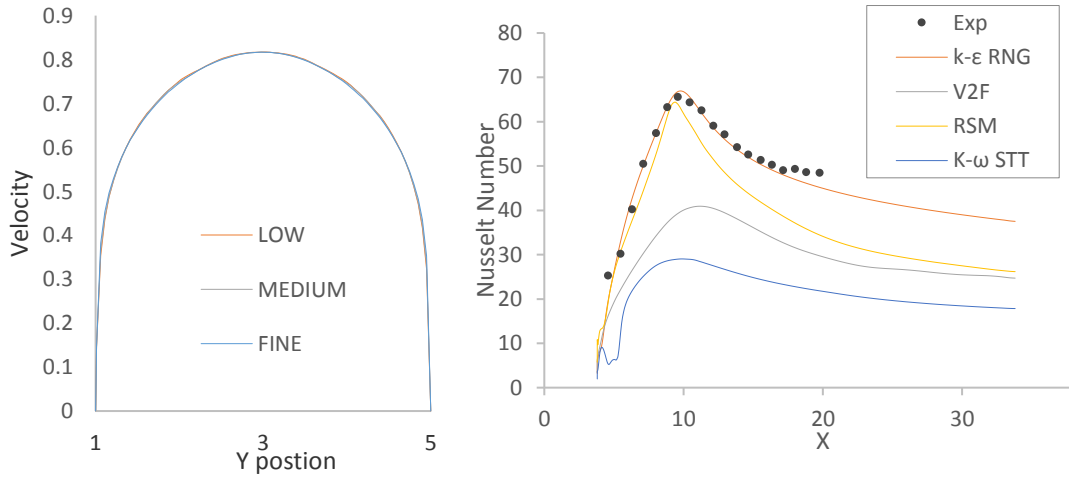

Figure 34: a) Backward facing step mesh dependency study b) Backward step turbulence model validation

4.3 Periodic Ribs

In this section a periodic geometry was investigated to find a cost-effective way, in computational terms, to simulate cooling passages and to validate the code for future work. The flow that exits the domain from the outlet re-enters at the inlet until it reaches a steady balance. Periodic boundary conditions are used for the flow and the heat transfer as would be, approximately, the case in a fully developed flow. Three grids are generated (Table 1 with the use of the ANSYS ICEM 14.5 code. Grid 1 consist of about 163,000 cells. Grid 2 was generated by doubling the node count of Grid 1. The Same procedure was applied for generating Grid 3. Figure 35 shows both grids topology and number of nodes of grid 1 to 3.

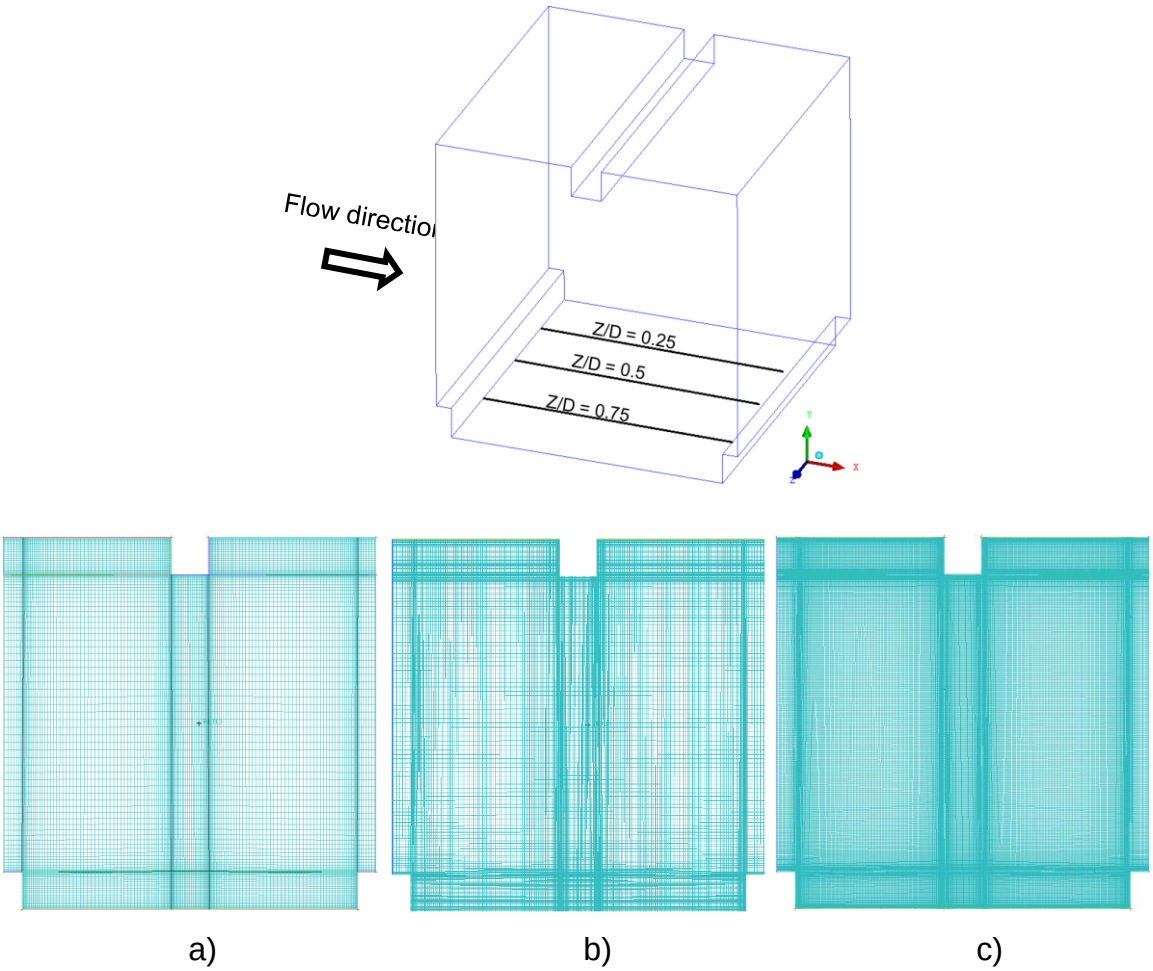

Figure 35 roughened channel with periodic function mesh. a) course b) medium c) fine

The relevant modelling and solution parameters are presented below.

Table 2

Parameter	Value
Density	1.25 kg/m3
Viscosity	0.0000179 kg/m-s
Conductivity	0.0242 W/m-K
Duct height	5 cm
Duct width	5 cm
Pitch to height ratio	10
Rib height	0.1
Reynolds number	100,000 of duct height
Bulk temperature	300 K
Wall heat transfer	800 W/m2

boundary condition and physical properties for the periodic rib

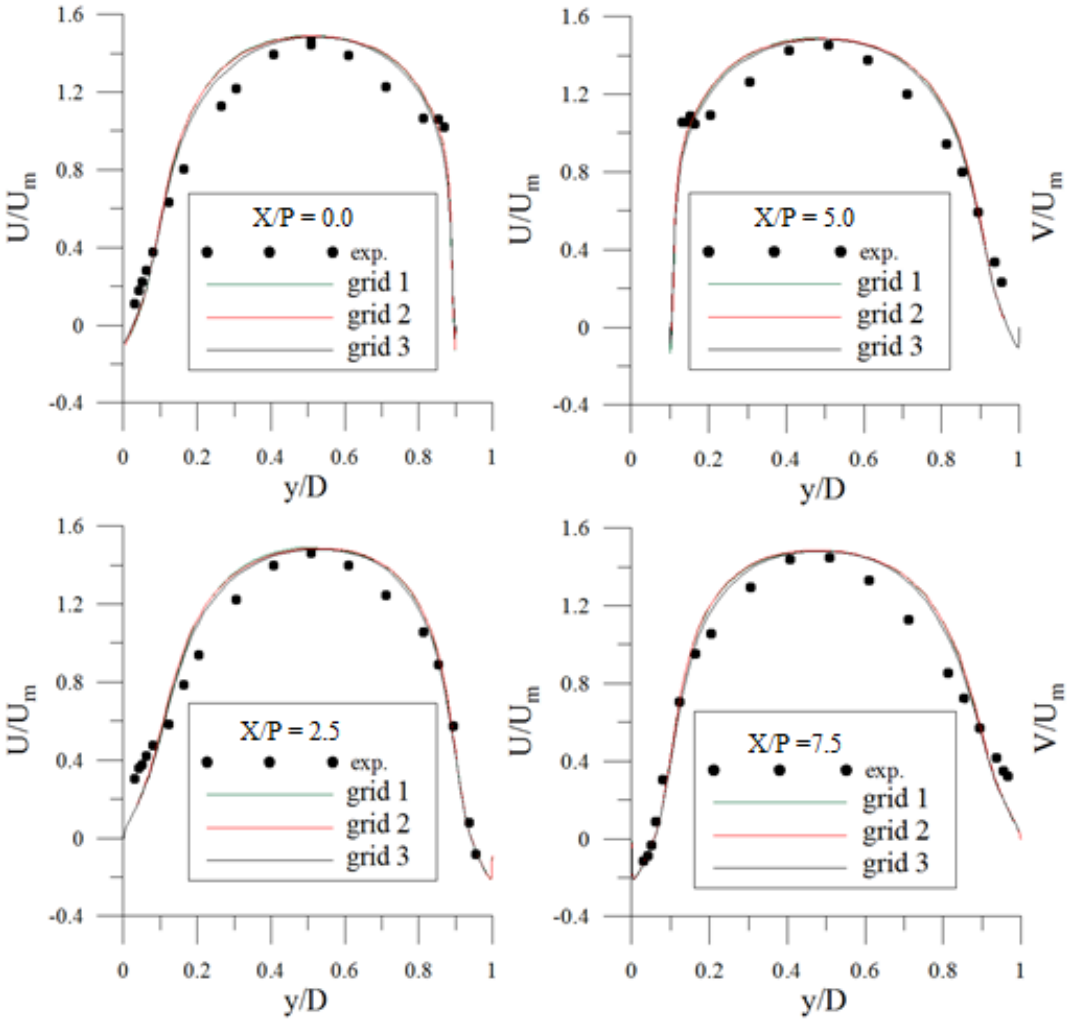

Figure 36 grid dependency study

The results for the stream wise velocity and cross-stream velocity are presented as the outcome of a grid dependency study, Figure 36. Grid 2 and 3 showed good agreement with the experimental data; both reached maximum velocity magnitude value at y/D = 0.5. The simulations for all grids predicted accurate velocity profiles at all locations. The reason for the differences which are visible at locations Y/d 0.3 and 0.7 is due to the periodic boundary conditions applied. The periodic approach is an approximation but the results confirm it is an appropriate one for his case.

.

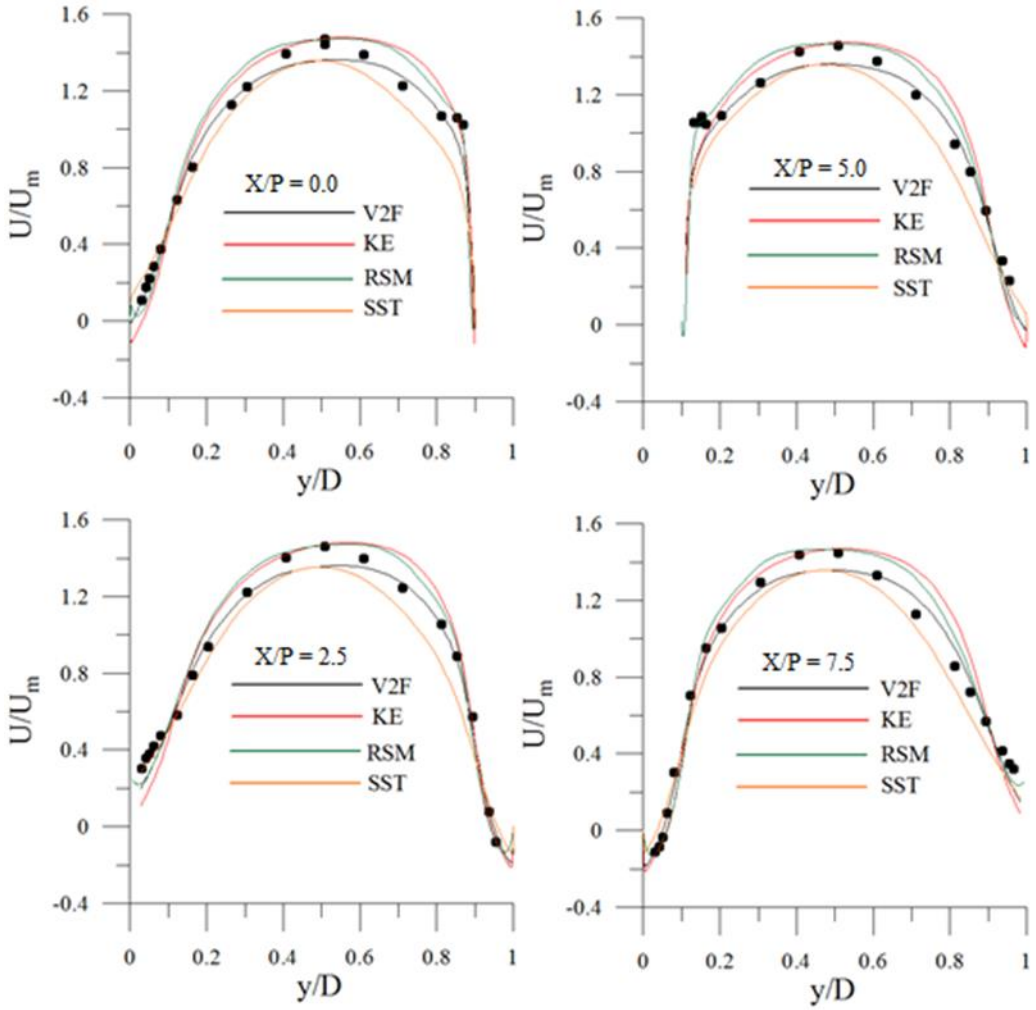

Figure 37 Turbulence model studies at different locations

Figure 37 present the results from varying the turbulence model at selected locations. Figure 37 shows the velocity at four different locations in the symmetry plane indicated in the figure. The k-ε and RSM models show a good agreement of the maximum speed in the channel centreline against the experimental result. The maximum speed velocity was underestimated by both SST and V2F model. All models poorly predict the intensity of secondary flows however. This observation can be explained by the existence of high turbulent viscosity generated by all RANS models.

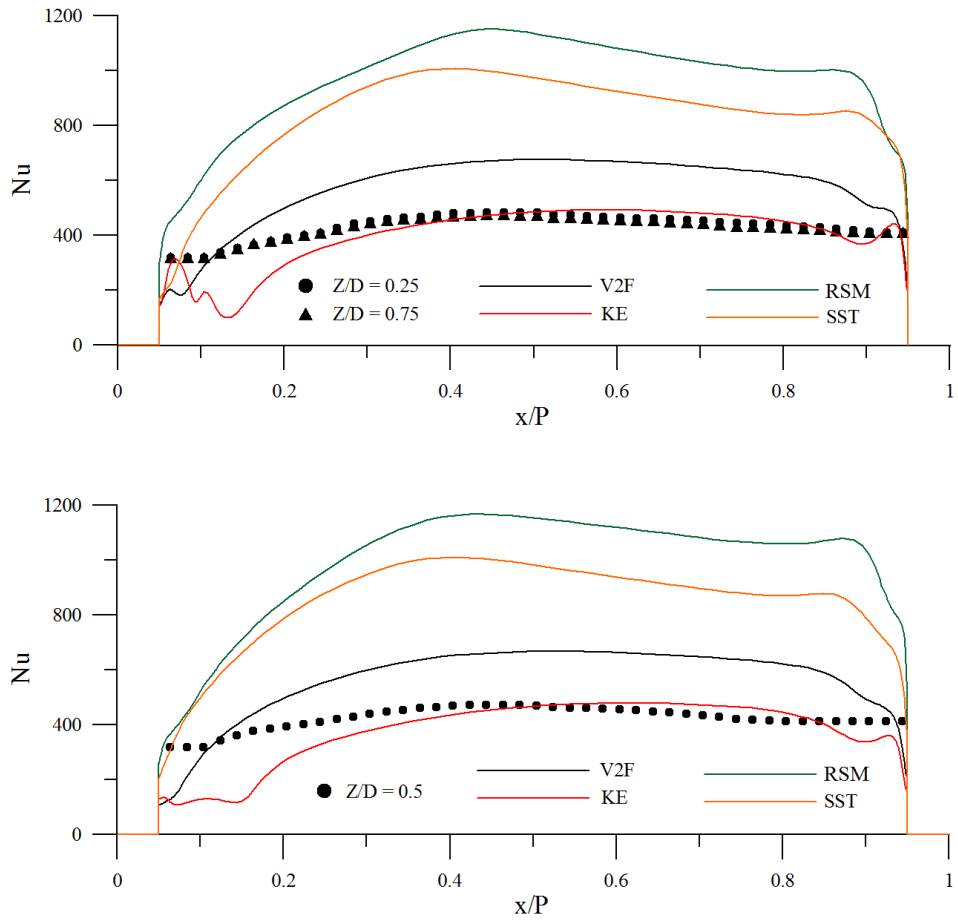

Figure 38 Nusselt number from turbulence model studies

Figure 38 shows a comparison at two Z/D locations, 0.25 and 0.75 (top) and taken at the centreline of the duct where Z/D=0.5 (bottom). Generally, the three models RSM, k- ω and V2F all show a worse disagreement with the experimental Nusselt number data (marked as dots in the graphs) when comparing to results obtained with the k-ε model. The agreement for the k-ε model is especially good between x/P 0.5 to 0.8.

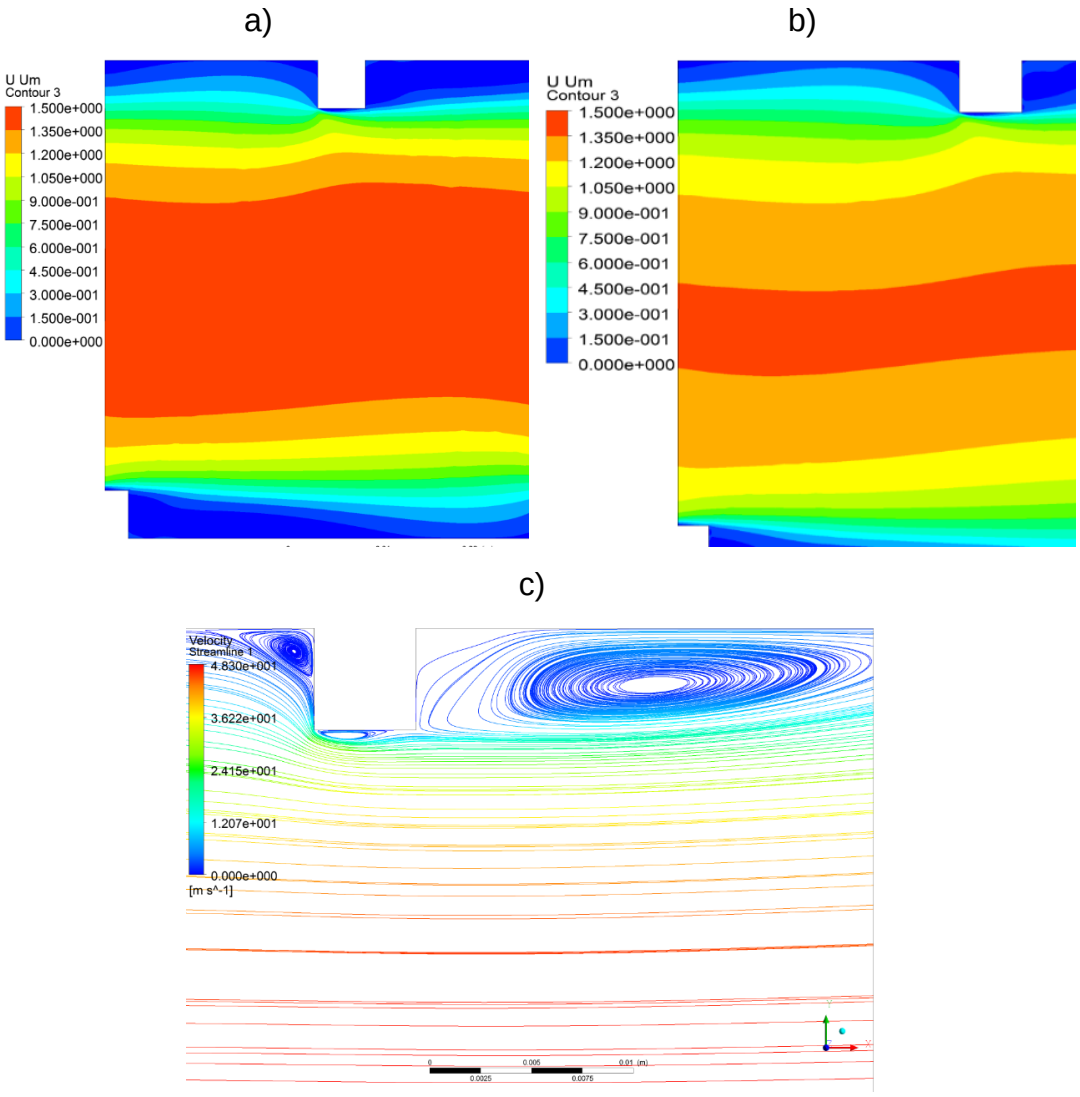

Figure 39 a) Velocity contour taken at 0.5 of the height of the passage; b) velocity contour taken at 0.25 of the height c) separation and re-circulation zone created by the rib

Figure 39 a &b below show the distribution of the dimensionless velocity for two channel heights. There are slight changes in the form of separated zones and flow. These changes have a minor effect on heat transfer rate. This can be seen inFigure 38, which shows the distribution of the Nusselt number along the wall for this location. Figure 39a. Ribs accelerate the flow in the center of the channel. Maximum flow velocity is equal to one and a half meters per second. Each rib forms three separated zones around it as shown in Figure 39c. The first separated zone was formed on

the leeward side and has a height equal to the height of the rib and the length of the first separation zone is approximately equal to half the channel width. The second separated zone was formed on the windward side and has a height of half the rib height. The second separation zone length is approximately equal to the height of the rib. The third separated zone is formed at the top of the rib and has a small height. The Length of the third separation zone is approximately equal to three-quarters of the height of the ribs.

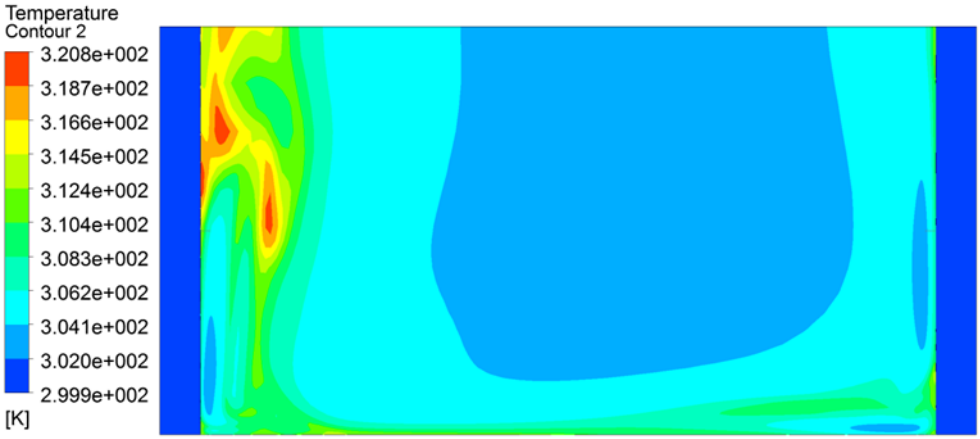

Figure 40 wall Temperature contour

Figure 40 shows temperature distribution along the channel wall. The Maximum temperature was located on the leeward side of the rib. This zone corresponds to the separation zone. The lowest Nusselt number value was noticed in this region (Figure 39c). The experimental data did not represent the low values of Nusselt numbers.

Results obtained for structured and unstructured meshes in term of mean stream-wise velocity and cross-stream velocity comparison for k-ε shown in Figure 41. Result for k-ε velocity on all locations were close to the experimental result. While, the unstructured k-ε result was slightly far-off. maximum velocity reached at x/P =0.5 for structure mesh and experimental. However, the maximum velocity for the k-ε unstructured mesh reached at x/P = 0.3. Cross-stream velocity at x/P= 0 showed a

good agreement with experimental data. However, there was a disagreement on all other locations

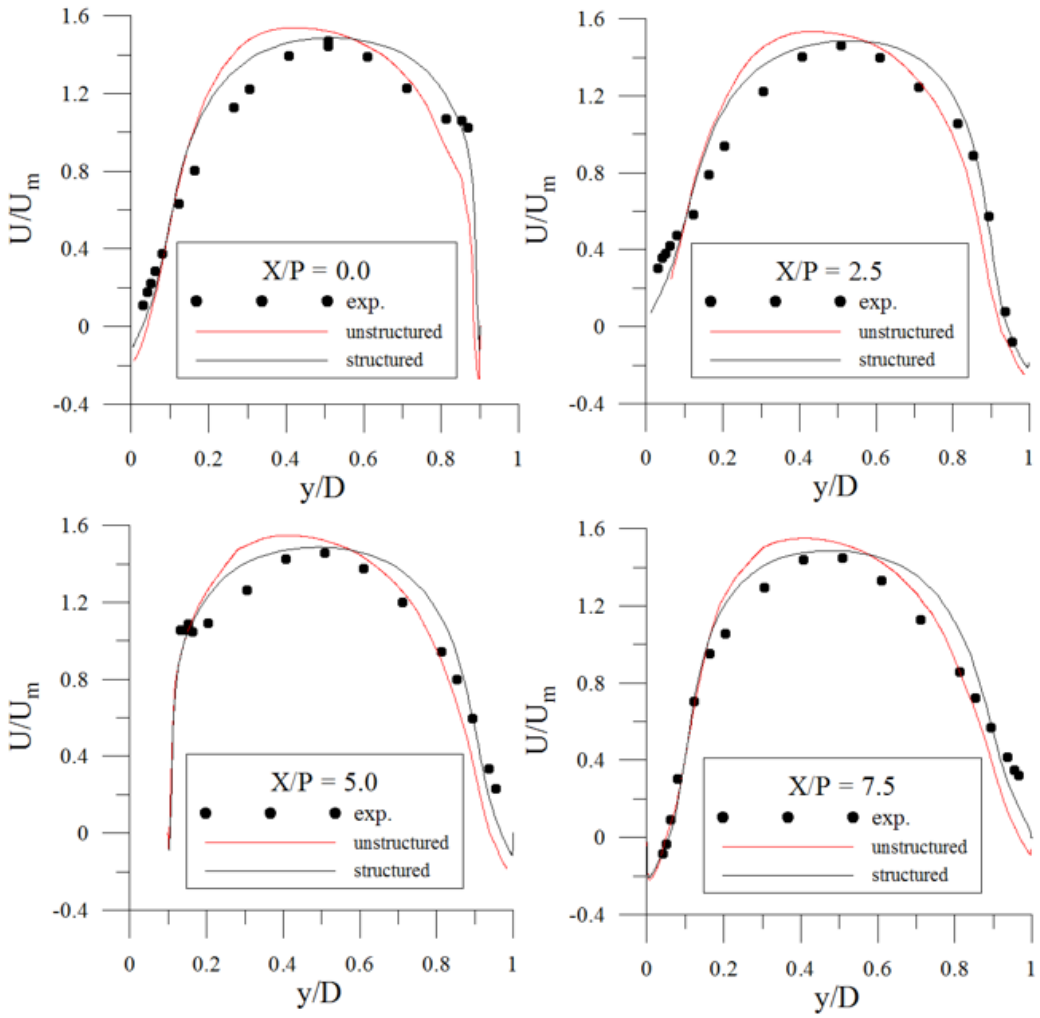

Figure 41 K-ε Streamwise velocity for structure and unstructured

Figure 42 illustrates the stream-wise and cross-wise velocity comparison for the V2-F turbulence model between structured and unstructured meshes. The result showed a very good agreement between the velocity obtained with structured mesh and the velocity obtained with unstructured mesh for both stream-wise and cross-wise. V2-F turbulence model presented great accuracy with experimental result

V2-F Turbulence model successfully captured the isothermal airflow phenomena in flow over obstacles. For the Nusselt number profile shape

where successfully demonstrated by V2-F model. However, the Nusselt number value for V2-F was 50% more than the experimental value.

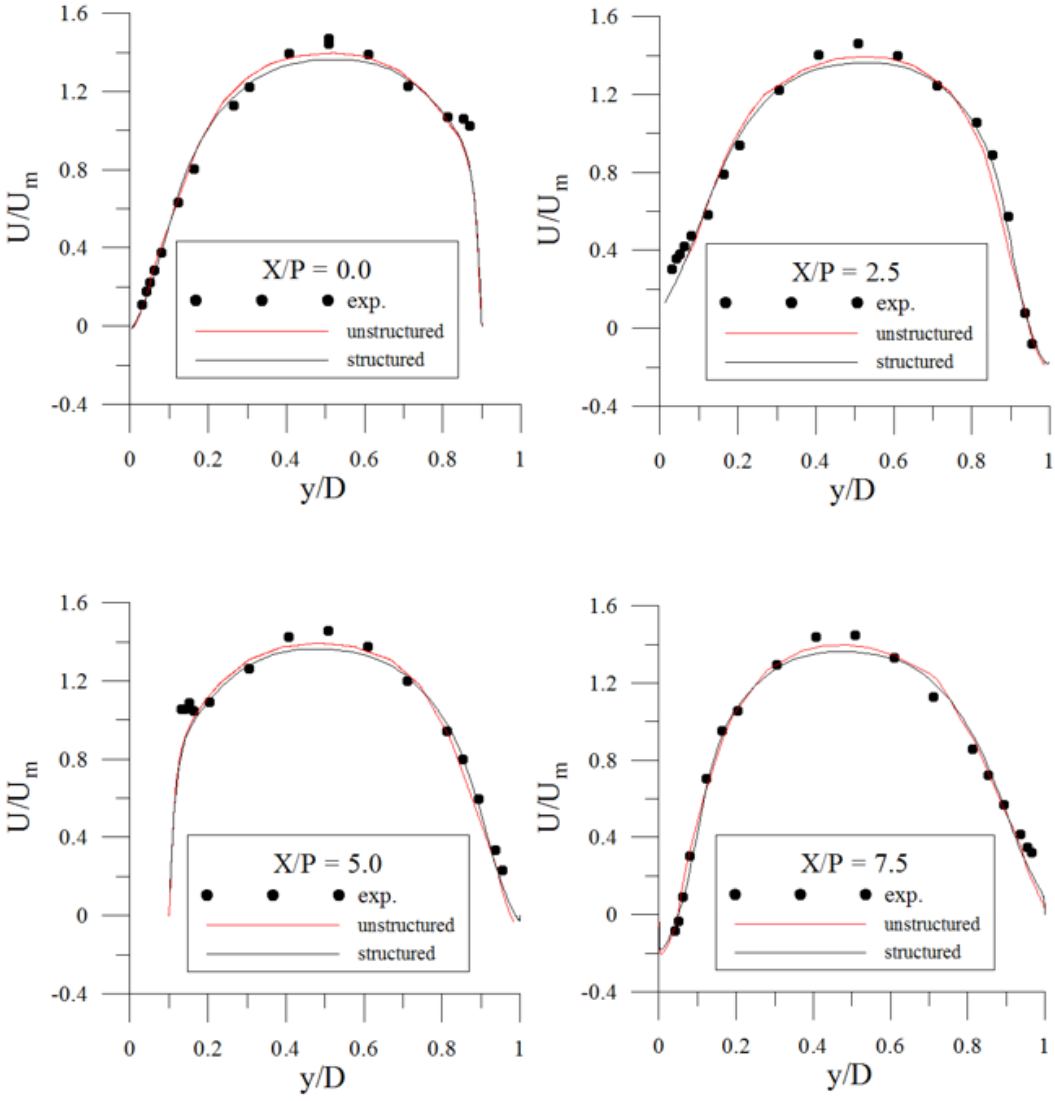

Figure 42 V2F Streamwise velocity for structure and unstructured

Overall, the k-ε model has proven to be the suitable model for such application as it gives the lowest error comparing to the other three turbulence models as was shown in these investigations. However, the instability of this turbulence model near the rib be investigated more. The result obtained with the k-ε model show a higher level of disagreement by comparison with the experimental data as distance from the wall is increased.

4.4 **U-duct**

In this part of studies air made to flows through a square cross-section of 12.7 mm × 12.7 mm area with 180-degree bend. The details of the rectangular cross-section for CFD analysis are shown in Figure 43. The square channel had unheated sections of 558 mm length at the start and end of the channels these section where used to provide the model with a greater stability and displace the boundary condition away from the immediate location of flow perturbation. The heated section has ribs at an angle of 45 degrees to the flow. There are a number of ribs installed on the two internal surfaces on the top and bottom sides of the channel. These two sides are also heated at a constant rate of 4,800 W/m^2. The remaining two sides are adiabatic walls and do not contribute in heat transfer. The heated walls contain ribs surfaces as acting as turbulators for enhancing turbulence and heat transfer. The square channel cross-section as stated above is a constant aspect ratio except in the bend region. The square ribs are 1.59×1.59 mm placed at 45-degree angle. The pitch to height ratio for ribs is 10.

Due to a constant heat flux, the walls are at elevated temperatures and need cooling using air at 300 K. The air is heated through these walls therefore exiting at a higher temperature.

The present study requires CFD analysis of the heat transfer process and air flow through a rectangular channel for validation purposes. The experimental data of Nusselt number for the air only case is available in published literature and is used as a validation for the CFD model.

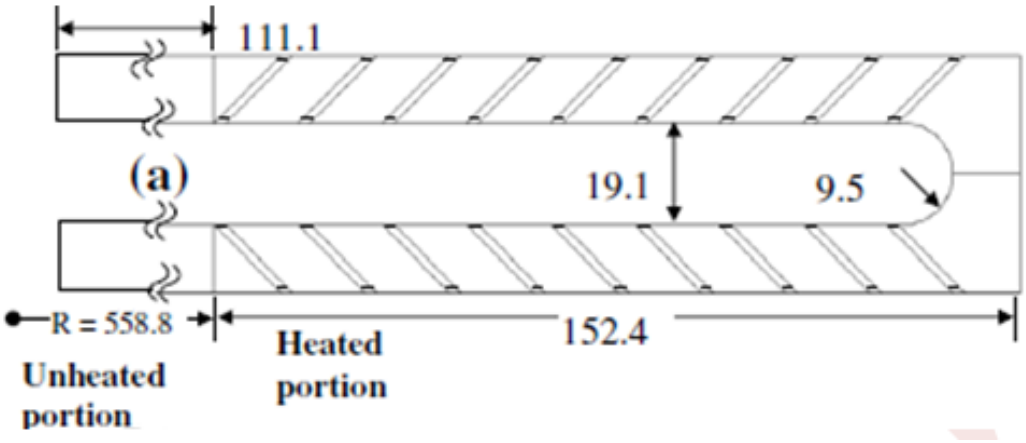

Figure 43: Computational domain

The boundary conditions for inlet and outlet are applied as velocity inlet and pressure outlet. The operating pressure and temperature are 1 atm and 300 K respectively. the turbulence modelling boundary condition are applied in the form of turbulence intensity and hydraulic diameter.

For comparison purposes The experimental results from the work of Fu et al. 2006 are available for smooth and ribbed channel configuration shown in Figure 43. For validation of CFD model applied, the problem is analysed for flow of air through smooth and ribbed channel configuration at a set four Reynolds number, 5000, 10000, 25000 and 40000.

The structured hexa mesh was created for both smooth and ribbed channels using the ICEM module of ANSYS 14. The refinements in the regions of the ribs and bend region lead to a refined mesh of about 2.5 million cells. The wall region is refined to keep the y+ less than 1. Figure 44 shows structured grid for ribbed channel. The grid generated for smooth channel computation has moderate clustering requirements in term of refinements due to absence of geometric feature such as the ribs therefore resulted in relatively smaller mesh size requirement of about 1 million cells. The Grid independence analysis made in Dhanasekaran and

Wang (2013) supports the fact that these grid sizes are sufficient for this particular application.

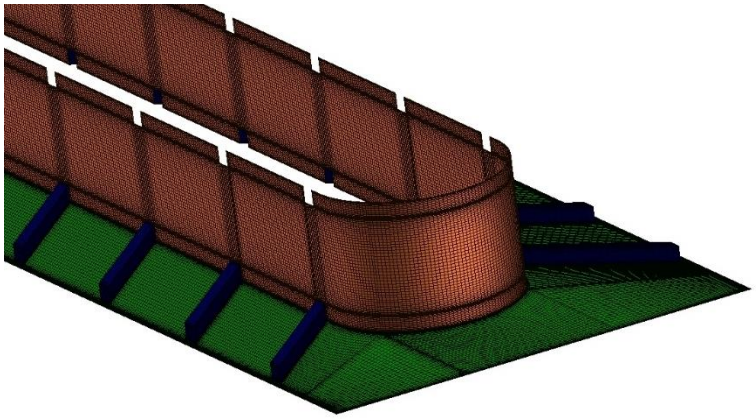

Figure 44: Hexa structured mesh for ribbed channel.

The validation phase of present study required comparison of heat transfer rate and Nusselt number for smooth and ribbed channel without rotation and mist. The material air is modelled with the ideal gas density formulation. The pressure-qbased segregated solver with SIMPLE pressure velocity coupling algorithm is used. The k-ε turbulence model with enhanced wall treatment is used for turbulence modelling. The velocity values are imposed at inlet corresponding to specific Reynolds number values. The pressure at outlet is set to 1 atm.

The heat transfer coefficient and Nusselt number can be calculated using equations,

$$h = \frac{q}{(T_w - T_b)}$$

$$Nu = \frac{hD}{k}$$

Here *h* is heat transfer coefficient and q is heat flux, 4800 W/m^2. T_w is average wall temperature of the heated walls, T_b is average bulk temperature of air. *D* is the hydraulic diameter of the square channel and

is equivalent to width or height of the inlet surface. The Thermal conductivity of coolant is denoted by *k.*

4.4.1 Non-Rotating case

Table 3 shows values of the Nusselt number obtained from computational simulation and compared these with data from experimental measurement. The comparison of the measured and the computed results shows that the CFD results are in good agreement and difference between these is minor and the CFD model can be used to predict the heat transfer and fluid flow with good acceptable degree of accuracy. This exercise formed the basis for further analysis cases using rotating domain for simulation of turbine rotor blades both with dry air and with water injection.

Table 3: Validation of CFD results for air-only flow

Case	Re	V	T_{wall}	T_{in}	T_{out}	T_b	h	Nu (CFD)	Nu (Exp)	Diff. (%)
		m/s	K	K	K	K	W/m^2-sec			
Smooth	5000	6	394.5	300	341.0	315.2	61	31	28	10
	10000	12	358.4	300	319.6	309.8	99	51	46	10
	25000	30	330.3	300	307.6	303.8	181	94	89	5
	40000	46	321.4	300	304.9	302.5	253	131	129	2
Ribbed	5000	6	355.9	300	328.0	314.0	115	59	64	7
	10000	12	336.0	300	315.9	307.9	171	89	98	9
	25000	30	319.5	300	308.2	304.1	312	162	178	9
	40000	46	314.0	300	305.8	302.9	432	224	240	6

Figure 45 shown a comparison of the computed and measured values of the Nusselt number for non-rotating, air-only cases at different Reynolds number values. The comparison shows that CFD predicts heat transfer with a good degree of accuracy. The difference of results is very small for smooth channel. The ribbed channel shows slightly under predicted values particularly at higher Re values. The flow becomes complex once the

ribblets are introduced therefore accuracy of the CFD simulations reduces significantly. In conclusion, the difference between experimental data ans simulations lies in a narrow acceptable range particularly for smooth channel and low Re values. However the ribbed channel has an enhanced cooling effectiveness due to both the greater surface area and the improved mixing brought about by the effect of the turbulators.

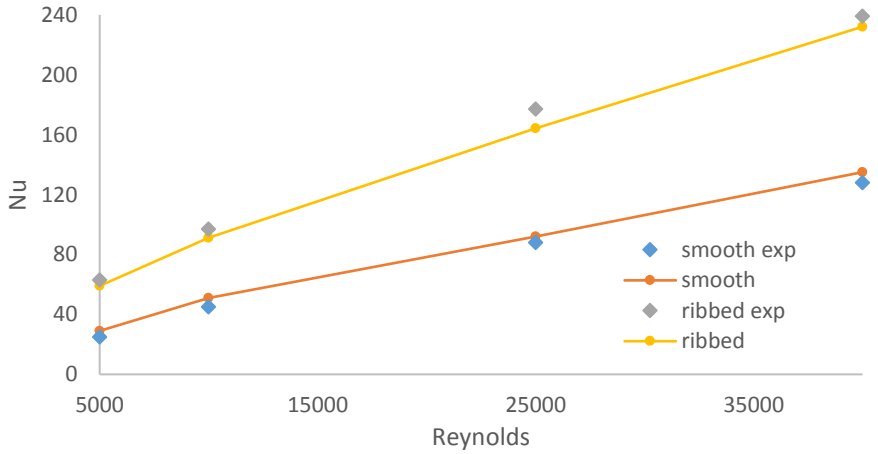

Figure 45: Comparison of CFD results with measured Nu values k-ε

4.4.2 Rotating domain investigations

The computational domain is then set with a rotating action using the frame motion option available in Fluent. Four rotational speeds are used to simulate rotating effects within the blade of the turbine. The effect of rotation is observed on the overall heat transfer and the Nusselt number results. The smooth channel is rotated at three different RPM with Re = 25000. There is an increase of 3 % to 5% on the Nusselt number for increasing RPM by a factor of 2. The linear enhancement of the heat transfer characteristic with RPM is also shown in Figure 46

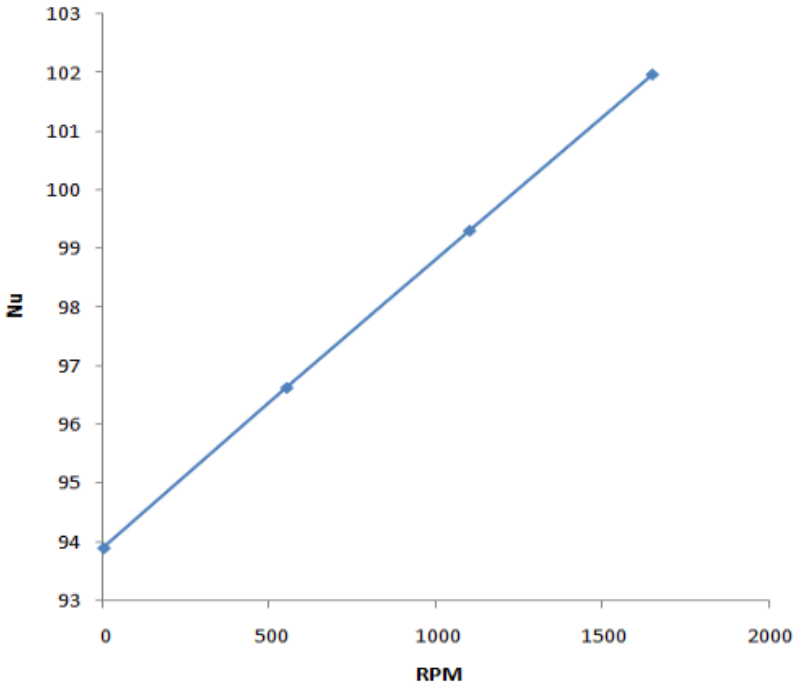

Figure 46: Effect of RPM on Nusselt number (Nu)

The rotating domain condition results in a velocity direction upward from the trailing to the leading surface. This results in flow impingement on walls due to additional centrifugal force and consequently to increased cooling rates.

To investigate the accuracy of the computational model, apart from the standard k-e turbulence model, the other four turbulence models including RNG k-ε, Realizable k-ε and the standard k-ε are employed for comparison, and the results are shown in Figure 47. The results from all the models are almost the same for the lower Re numbers and vary within ± 10% at the higher Re numbers. Comparatively, the RNG k-e model provides the closest match with the experimental results; therefore, the RNG k-e model with enhanced-wall function is employed for the other cases in this study.

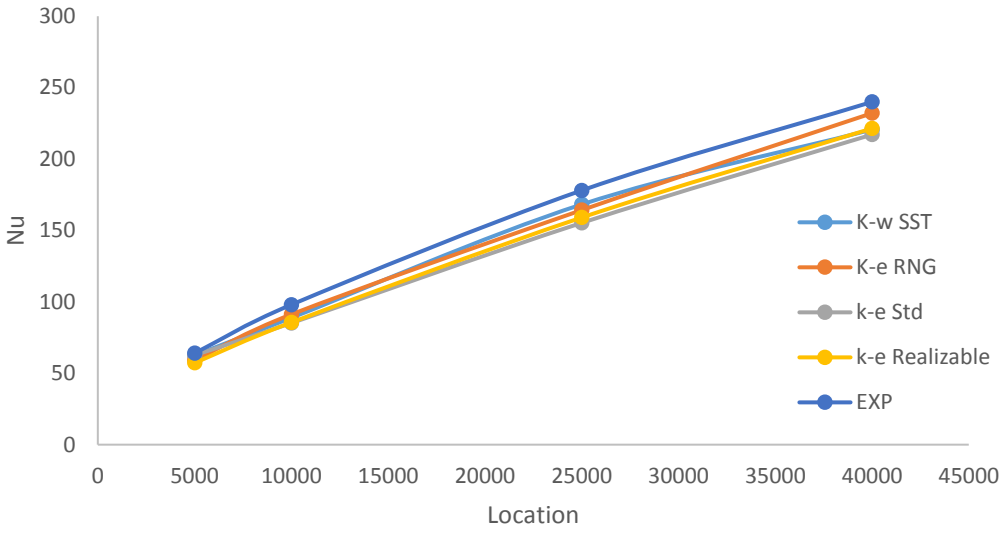

Figure 47: Turbulence model studies

In Figure 47 the Nusselt number for a long smooth U duct for non-rotating and rotating cases is shown. The Nu values are plotted against station number, from inlet to outlet, for the non-rotating case are virtually indistinguishable. Stations 1-6 represent the inlet duct section upstream of the bend. Station 7-12 correspond to the reciprocate arm of the duct past the 180-degree bend. Three distinct sections are apparent in this graph. From the inlet to Station 6 the Nusselt number drops slightly or is broadly unchanged. Between Station 6 and Station 7, the initiation and termination of the 180-degree bend, there is a rather noticeable increase in the Nusselt number brought about by the intense secondary flow and turbulent activity which are due to the sharp turning in the bend. From Station 7 to Station 12 the intensity of the secondary flow decreases and the enhanced mixing brought about by the large variations in velocity and direction decreases as the flow progresses to the inner radius.

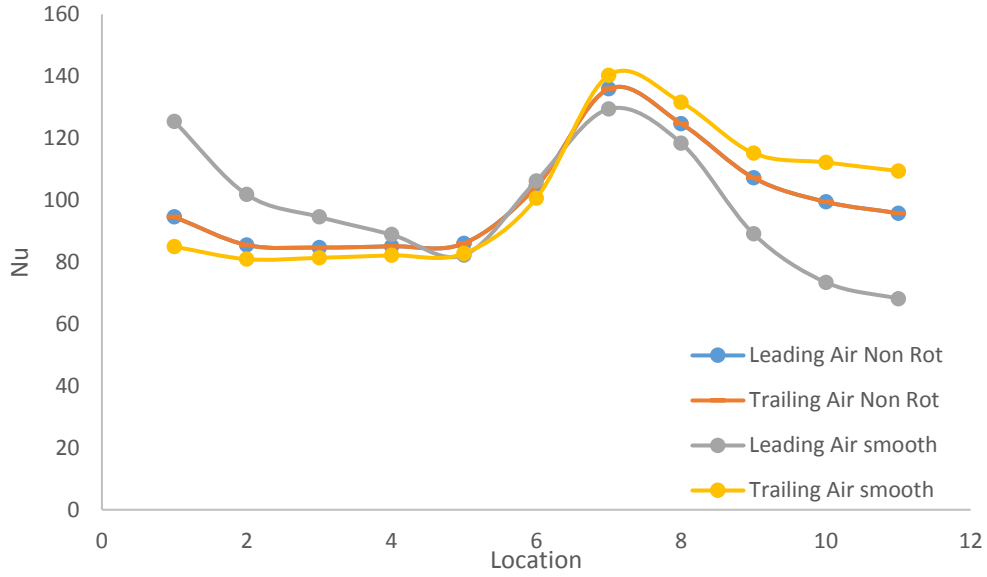

Figure 48: Nusselt number a long smooth U duct for non-rotating and rotating cases

In the absence of rotation, the Nu distribution values are essentially the same for leading and trailing roughened surfaces, Figure 49. However, the evolution of the Nusselt number is significantly altered by the introduction of the turbulators. Referring to Figure 49 it is apparent that the overall Nusselt number is higher as is to be expected for the case with turbulators. However, the three distinct regions identified in the preceding figure are not visible and this is assumed to be related to the fact that in the smooth case the presence of the bend is the single largest source of local turbulence enhancement, whereas in the case with the turbulators, the bend is just an additional feature in an environment that is fitted with a number of turbulence generation features. For this reason, the effect of the bend is on the whole secondary and it is interesting to observe that for the stationary cases the bend corresponds to a zone of decrease of heat transfer. This is quite likely due to the local slowing down of the flow corresponding to the cross-sections with the larger effective area. Similar observation is found by [146]

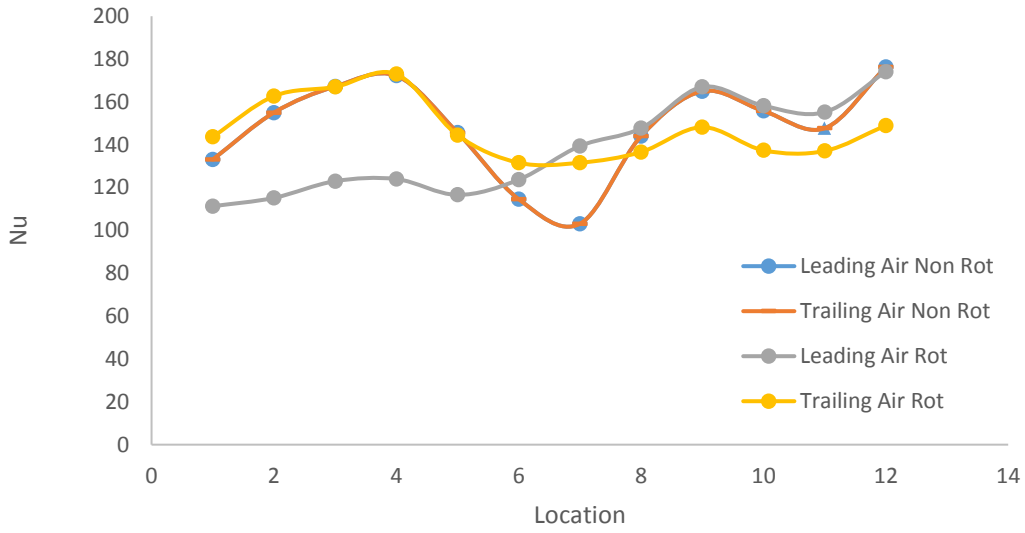

Figure 49: Nusselt number a long roughened U duct for non-rotating and rotating cases

The qualitative description of the flow for the cases described in the preceding two figures is performed in Figure 50 and Figure 51. Velocity contours are shown at a set of stations alongside the numbering system employed in the preceding plots, Figure 51 and Figure 51. The flow direction is along the increasing number disks. From the inlet to the entry to the bend section, for the non-rotating case, Figure 51 the core flow is positioned at the mid-section of the channel, the initial bend section is characterized by a sizeable low momentum region, denoted in blue, immediately after the bend, circa station 7, the high momentum flow forms a horseshoe structure as the flow is pushed against the wall opposite to the bend. As the flow progresses downstream it tends to adopt a distribution similar to that at inlet, core flow. The vector detail shows how the secondary flow structure is prevalent in the cross-section. The central region is occupied with fluid which is directed towards the end surface while the top and bottom regions show inward flows.

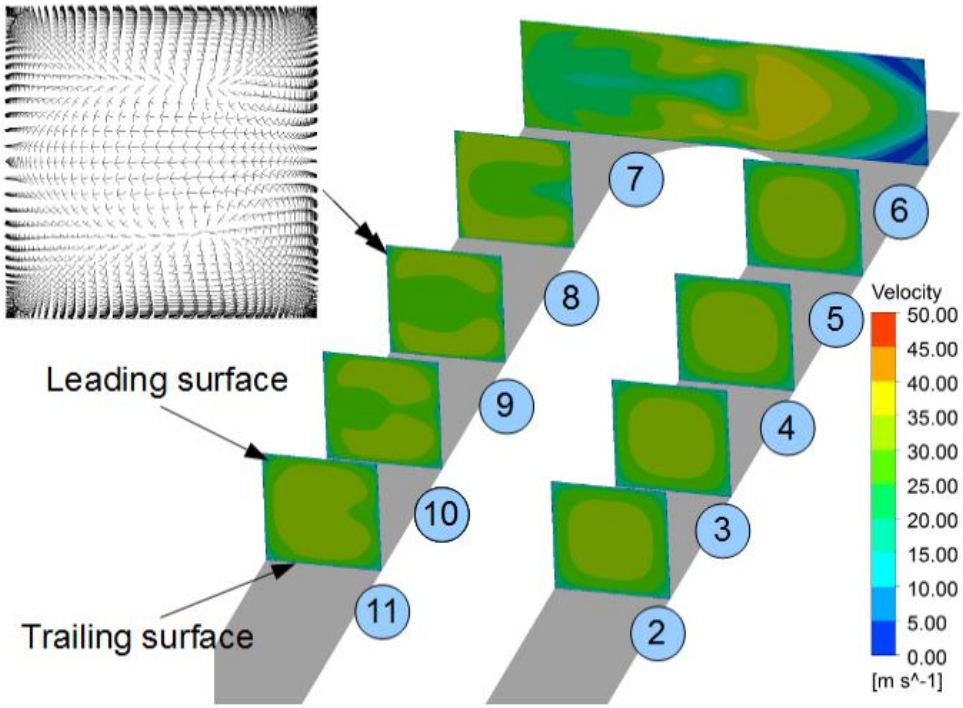

Figure 50 Velocity countour for the smooth u duct non-rotating

For the rotating case the core flow is slightly pushed towards the trailing edge due to the rotation effect. Figure 51 shows the velocity contour at nine different locations on the roughened U duct. For the both cases smooth and roughened secondary flow created after the 180 bend. Secondary flow effect on the second passage is shown in both figure were the flow take a 45-degree angle.

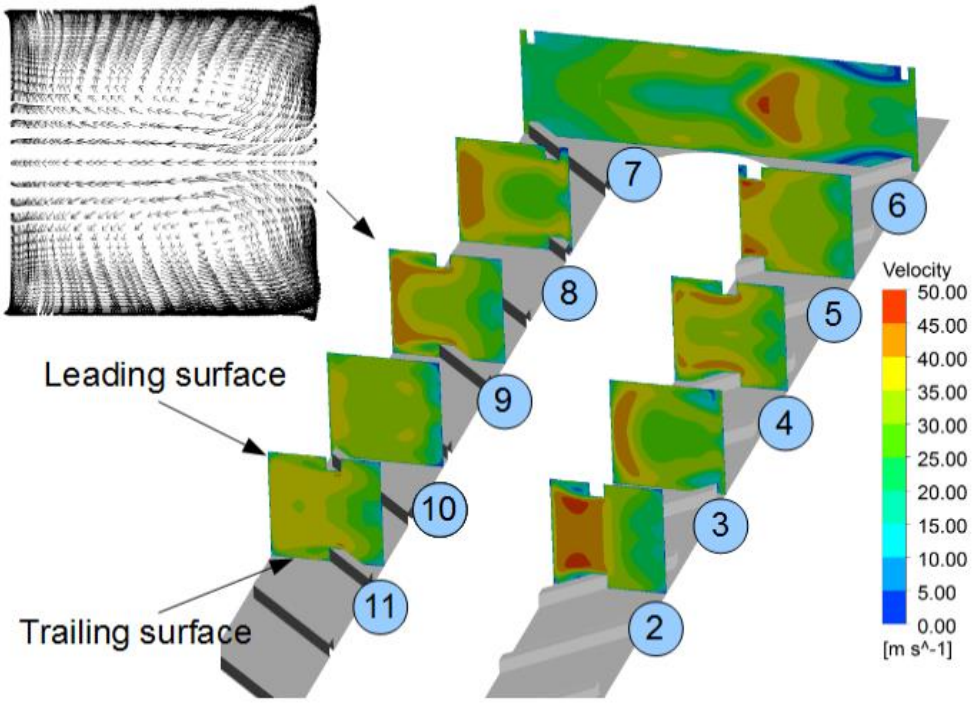

Figure 51 Velocity countour for the roughened u duct non-rotating

4.5 **Smooth U-tube**

The aim of this section is to validate of the CFD model, by comparing it with available experimental data. The experiment was carried out by Guo et al [129]. using a 180-degree bend tube. We then proceed to use the model to predict the mist/stream performance in the scenario of a gas turbine with elevated temperature and pressure. The present work is a part of a larger study aiming to validate the used CFD model under a range of conditions.

From the mist/steam experimental results done by Guo et al. [117], it shown that the outer wall of 180-degree bend had a better cooling than the inner wall for both steam and mist/steam cases. They revealed that the mist-cooled outer wall has a maximum cooling at 45 locations and considered this enhancement was due to the direct mist impingement on

the outer wall caused by the inertia of water droplets coming from the upstream straight section and centrifugal force. Furthermore, their outcomes showed that under lower heat flux conditions, the average mist cooling enhancement reached 200–300%. However, under higher heat flux conditions, the average mist cooling deteriorated to about 50%. Then, it was concerned that under the elevated wall heat flux condition, the mist cooling might not be beneficial in the real gas turbine operating environment. Although, they increased the Reynolds number more and observed the cooling enhancement returning to above 100%. According to this finding, Guo et al. [117] assumed that the mist cooling could be still attractive under elevated gas turbine operating condition. The reason

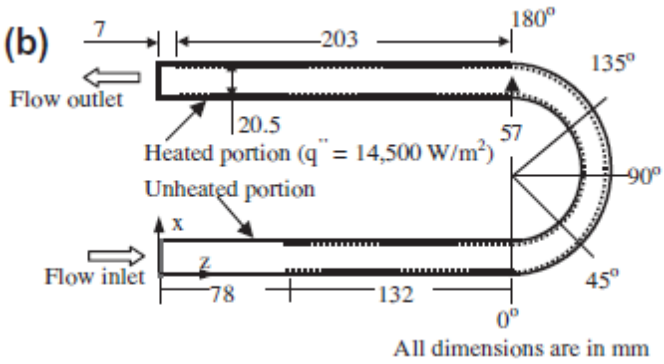

Figure 52 U-tube geometry [117]

behind that is that Reynolds number is high and the steam properties will change in favor of mist cooling in the environment of the actual gas turbine.

Boundary conditions:

The steam is considered as a continuous flow and mist is considered as a discrete flow. In order to obtain unheated fully developed flow similar to the experimental condition, a section of 78 mm unheated tube is added at the inlet in the computational domain. The uniform inlet velocity of 14.36 m/s (mass flow rate = 4.74 * 103 kg/s, Re = 20,000) was allocated in positive z-direction at the inlet as presented in Fig. 1(b). The stream-saturated temperature at the inlet was 111.4 C. For the validation case, a

constant heat flux of 14,500 W/m2 is applied in the heated tube section. The unheated tube section is used as adiabatic walls with non-slip velocity boundary condition. The inlet turbulence intensity is defined as 2%. The computational domain exit flow is assumed to be at a constant pressure of 1.0 atm. Variable properties are assigned as a function of temperature and pressure.

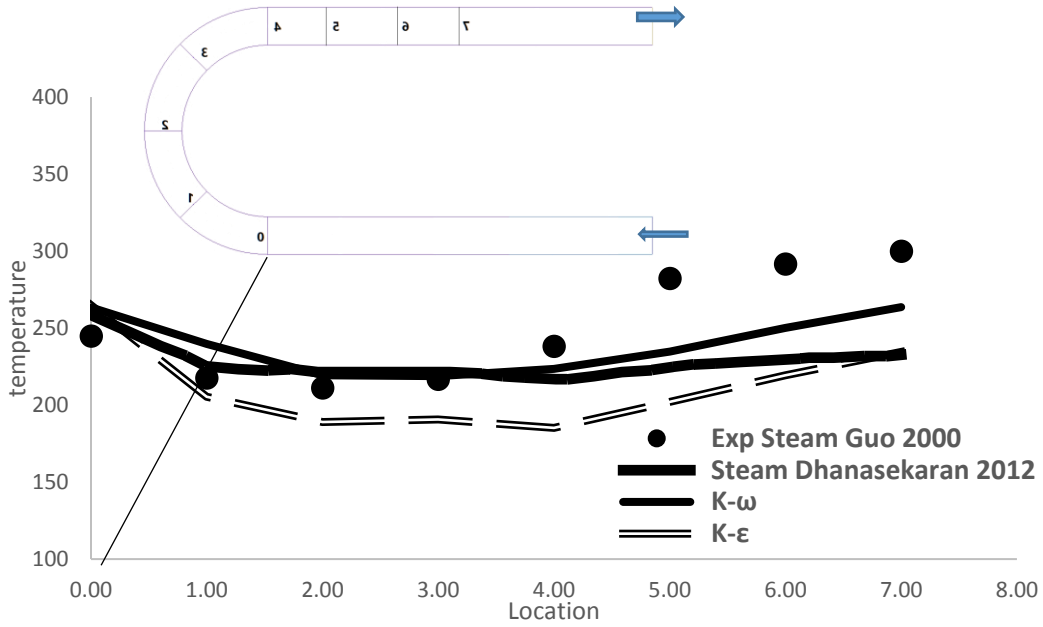

Figure 53 Comparison of CFD results with experimental data for steam outer wall

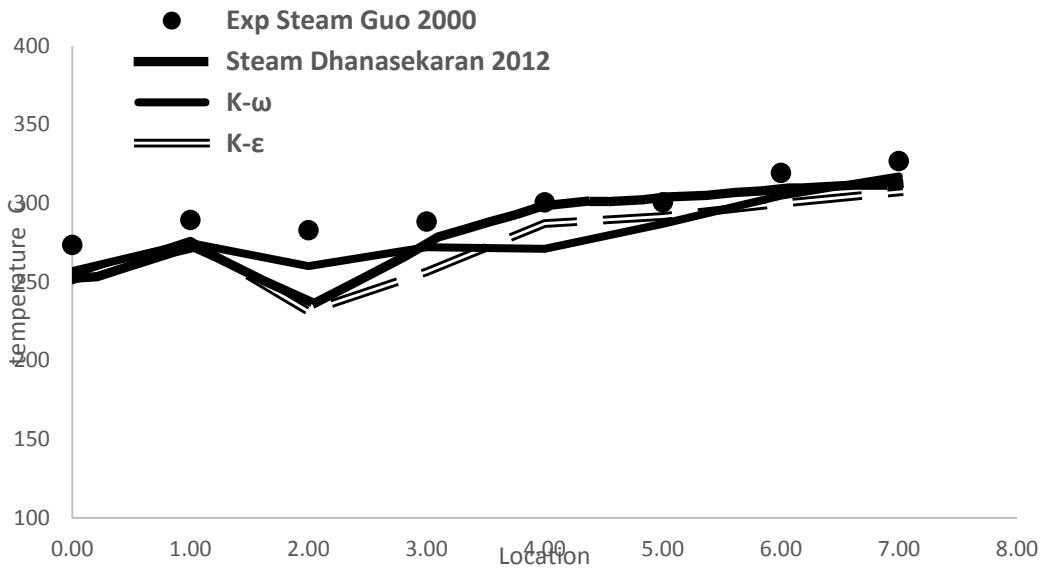

Figure 54 Comparison of CFD results with experimental data for steam inner wall

Figure 53 and Figure 54 represent the experimental data gathered from Guo et al. 2000 and computational data gathered from Dhanasekaran et al 2012 compared with two-turbulence model computed to validate the result. Y axis is the temperature and the X axis is the location of sample extracted from the test rig. Figure 53 shows the result for the inner wall and Figure 54 shows the result of the outer wall. K-ω performed better compared to the experimental and computational data available in the literature.

Mist is injected to the previous case to validate the mist cooling case. Figure 55 and Figure 56 represent the mist validation for the outer and inner wall using k-ω SST. K-ω achieved better result in both wall. Outer wall temperature was closer to the experimental value compared to the inner wall temperature

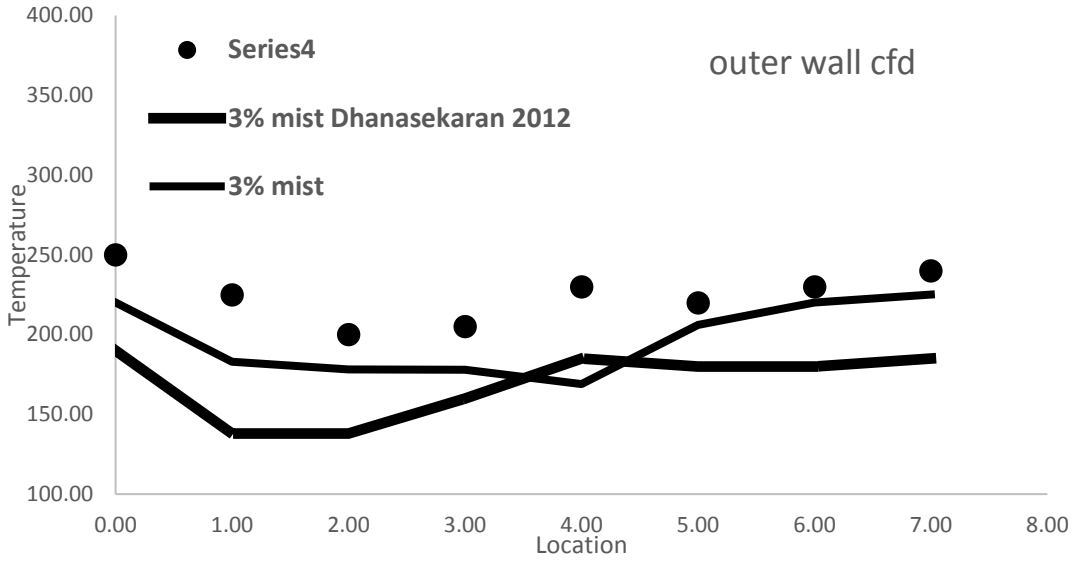

Figure 55 Comparison of CFD results with experimental data for mist outer wall

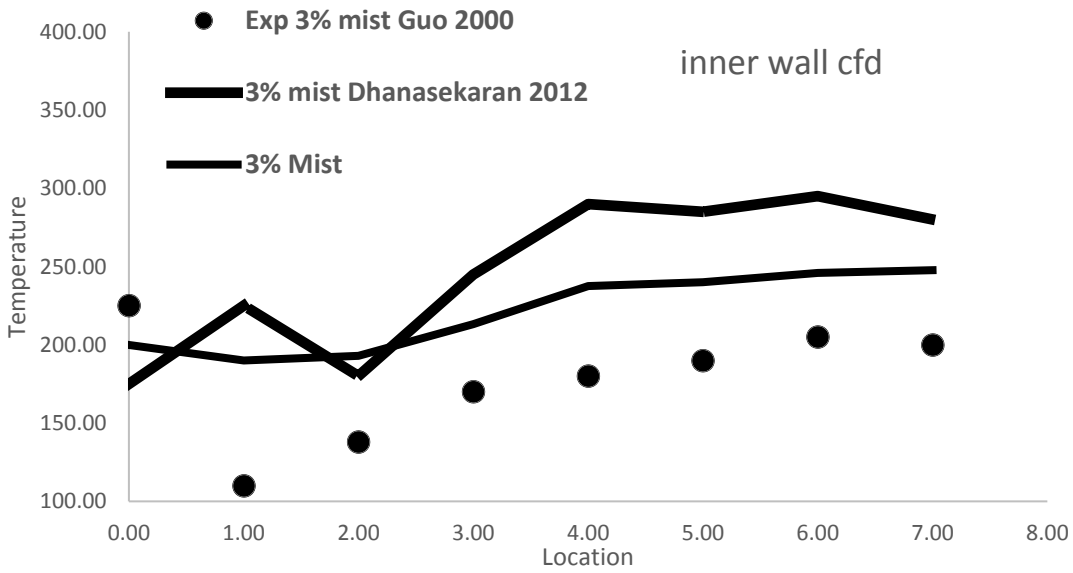

Figure 56 Comparison of CFD results with experimental data for mist inner wall

4.6 Chapter conclusion

According to the finding in this section the model is validated with the experimental data for different cases air only rotated and stationary. furthermore, mist injection in a smooth tube is also validate using the

discrete phase model with experimental and computational data available in the literature. And these cases are sufficient because we covered all the flow parameter that considered for this study. K- ω SST is chosen for the further studies for its good prediction for air only cases and multiphase flow.

5 Mist addition investigations

5.1 Introduction

With the developments in gas turbine technology, a number of ways for the thermal protection of turbine blades using different cooling techniques have been proposed. In the past, conventional cooling techniques like air film cooling, jet impingement cooling and use of extended surfaces for increased heat transfer have been employed for cooling enhancement.

However, these cooling techniques have their limitations in terms of maximum cooling advantage as discussed by Horlock [5]. Therefore, new cooling techniques are essential for getting improved cooling beyond the current limits. This chapter investigates the cooling enhancement that can be obtained by injecting water mist into the coolant air. Different studies regarding cooling improvement support the fact that a significant increase in heat transfer and cooling effectiveness (30% ~50%) can be achieved using a small amount of mist injection (1%-2% per mass).

The works of different researchers about the investigation of cooling improvement using mist injection focused on obtaining better geometric and operational parameters. The experimental and CFD analyses went side by side for determination of optimum configurations and operating conditions to get maximum cooling effectiveness and allowing higher turbine entry temperatures. The work of [117] focusses on the measurements of mist cooling effectiveness in a heated horizontal tube. The same configuration was modelled in [118]. The mist cooling enhancement problem was studied in a 180-degree bend in [129] and an impingement jet cooling on flat surface Li et al. 2001, and on a curved surface Li et al. 2003.

The work of Li and Wang [114,122,125,147] shows that a small amount of mist (2%) can increase cooling effectiveness in the range of 30% to

50% under normal operating conditions similar to a laboratory. Their research work incorporates elevated temperature and pressure conditions close to the turbine blade working environment. They also worked to see the effect of curvature of surface and found that higher cooling effectiveness (60%) can be achieved on pressure side as compared with that achieved on the suction side (30 %).

The injection of mist in coolant fluid enhances the heat transfer rates and cooling effectiveness. The small amount of water is injected in the form of droplets in the airflow. some part of these water droplets is evaporated and the remaining are either coalesced or a carried with the air flow. The phenomenon of mist addition for cooling enhancement can be modelled either using Discrete Phase Model for the water droplets injected.

5.1 **Boundary conditions**

In the present study, the air flows through a passage with square cross section of 12.7 mm × 12.7 mm area and a 180-degree bend. This geometry was chosen to make a good comparison with the air only case since are data available. The details of the rectangular cross section for CFD analysis are shown in Figure 43. The square channel has unheated sections of 558 mm length at the start and end of the channel. The heated section has ribs at an angle of 45 degrees to the flow. There are a number of ribs installed on the two internal surfaces on the top and bottom sides of the channel. These two sides are also heated at a constant rate of 4800 W/m^2. The remaining two sides are adiabatic walls and do not contribute to the heat transfer. The heated walls contain ribs surfaces acting as turbulators for enhanced turbulence and heat transfer. The square channel is 12.7mm×12.7mm and has a constant aspect ratio except in the bend region. The square ribs are 1.59×1.59 mm placed at 45-degree angle as mentioned. The pitch to height ratio for ribs is 10.

The boundary conditions for inlet and outlet are defined as velocity inlet and pressure outlet. The operating pressure and temperature are 1 atm and 300 K respectively. The turbulence intensity is assumed to be 2 % for very moderate flow regime and the hydraulic diameter is 12.7 mm which is the length or width of the square channel.

5.2 **Stationary case**

In this section the effect of mist ratio within a roughened stationary duct is investigated. This is similar to the case used for the validation stage. Five different mist percentages are investigated, 1, 2, 3, 4 and 5% of the bulk flow mass flow rate.

The particle mass concentration for the five cases is shown in Figure 57 with each plot describing the water droplets distribution on seven parallel planes. The five plots corresponding to different particle mass concentrations are plotted in a common scale. The use of a common scale means that some features that are very marked in some of the plots are less visible in the low concentration plots. However, broadly speaking it can be said that the for all particle concentration conditions there are common flow structures which are visible for all the simulations.

That is the case in station number five, the large plane placed in the bend location, where a structure composed of two convergent arms joining at the apex of the turn and stretching in a finger like geometry, is apparent. This configuration, which is visible in all cases, is due to the transportation of the water particles towards the outer walls due to the secondary flow inertial effects.

Other stations, namely number four, exhibit particle mass concentrations which are characterized by well defines spatial distributions which are similar for all cases. This is a function of the location of the ribs, the structure of the bulk flow and the secondary flow effects. In station number four it is possible to see a region of a low moment defining v like structure

for all plots corresponding to the different particle mass concentrations. It is also very apparent that the distributions in the section of the duct from inlet to the bend are not mirrored, as its to be expected, by the section between the bend and the second passage of the duct. As a rule, the distribution of particles is fairly well spread throughout the planes of the first passage of the duct that lies between the inlet and the bend and become much more polarized, much less equally distributed, in the discharge section between the bend and the outlet of the passage.

The stretch associated with the region of the bend correspond, to counter rotating vortices bought about by the turning of the flow and this secondary flow structure tends to push the flow, and hence the particles, toward the wall opposite the direction of the bend. The shape of the secondary flow structure, characterized by a pair of counter-rotating vortices, is clearly seen in station number six. These secondary flow structures tend to lose their identities progressively as one travels along the duct. However, in station number seven, eight and nine it is possible to see that the concentration remains mostly towards the outer side wall and the comparison between the station inlet number one and outlet number nine make a striking comparison.

The quasi-uniform distribution of flow at the duct start is replaced by a much more polarized distribution with particle concentrated mostly towards the walls and especially the outer wall. This need not be a problem however given that it is particularly next to the walls that the presence of concentration particle is more beneficial since a greater heat transfer takes place in the near wall region.

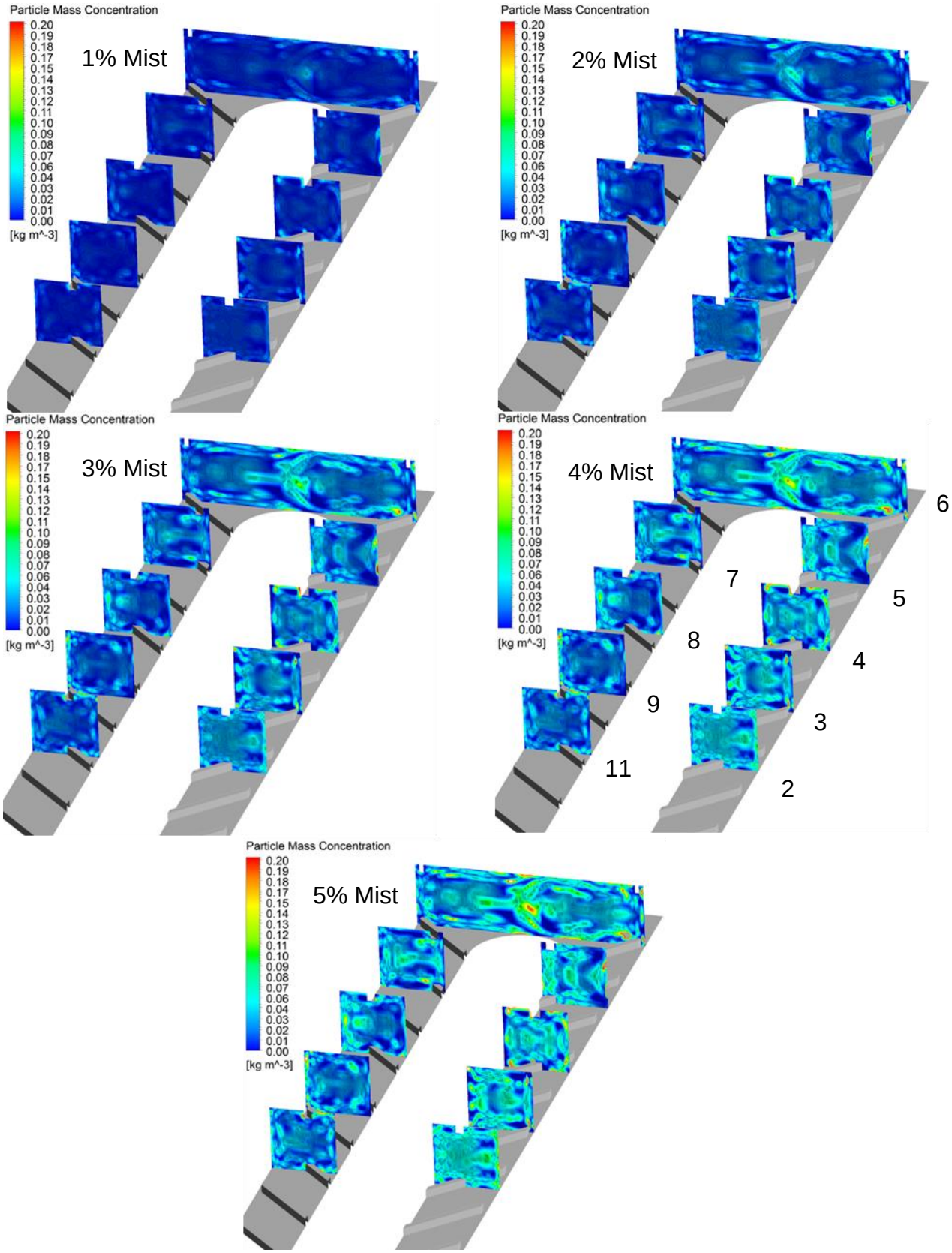

Figure 57 Water droplets concentration distribution on different axially located fluid planes under various mist/air ratio conditions

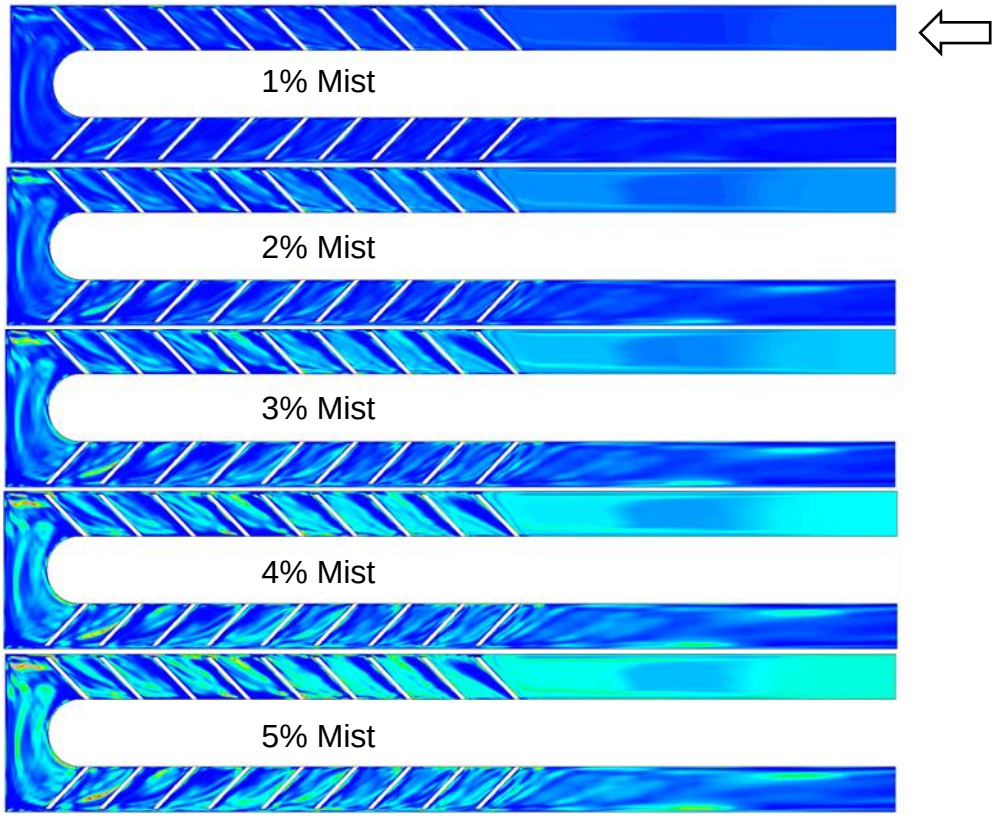

Figure 58 Water droplets concentration distribution on the trailing edge surfaces at various mist/air ratio conditions

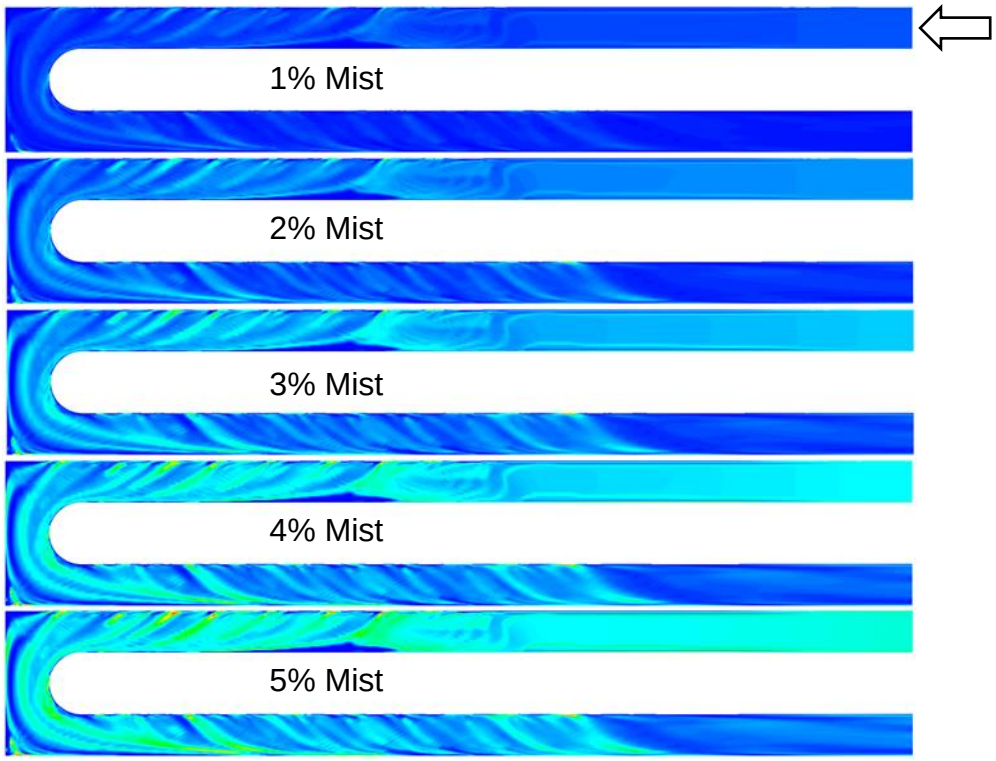

Figure 59 Water droplets concentration distribution on the mid plane fluid plane at various mist/air ration conditions

The concentration distribution of water droplets on the trailing edge surfaces at various mist/air ratio conditions is shown in Figure 67 while in Figure 68 the plots show the corresponding distributions for a plane located half way between the leading and trailing edges. In general, the initial near wall concentration seen in Figure 67 is disrupted by the action of the turbulators and especially due to the effect of the 180-degree bend. The 45 degrees turbulators contribute to pushing the flow towards the outer wall in the first pass between the inflow and the bend section. After the bend the action of the turbulators is reversed.

The mixing patterns brought about by the geometric features of the duct are, if anything, more apparent at mid-height, Figure 68. The centrifuging effect of bend at mid-span is very marked.

Figure 60 shows the Nusselt number distribution on the trailing surfaces at the different mist/air ratio conditions. The scale is not common for all plots in the interest of clarity. Generally, the Nusselt number is found to increase in the location downstream of the ribs. This region is also the recirculation region where the mixing is more pronounced.

When no mist is used (top plot), the Nusselt number within the region downstream of the ribs shows an increase beginning at the inlet location and all the way towards the location of the fourth rib. For this case the Nusselt value is at its peak before reducing towards the outlet.

In contrast, when a 5% mist/air ratio condition is applied, the Nusselt value reaches its peak at the outlet location instead.

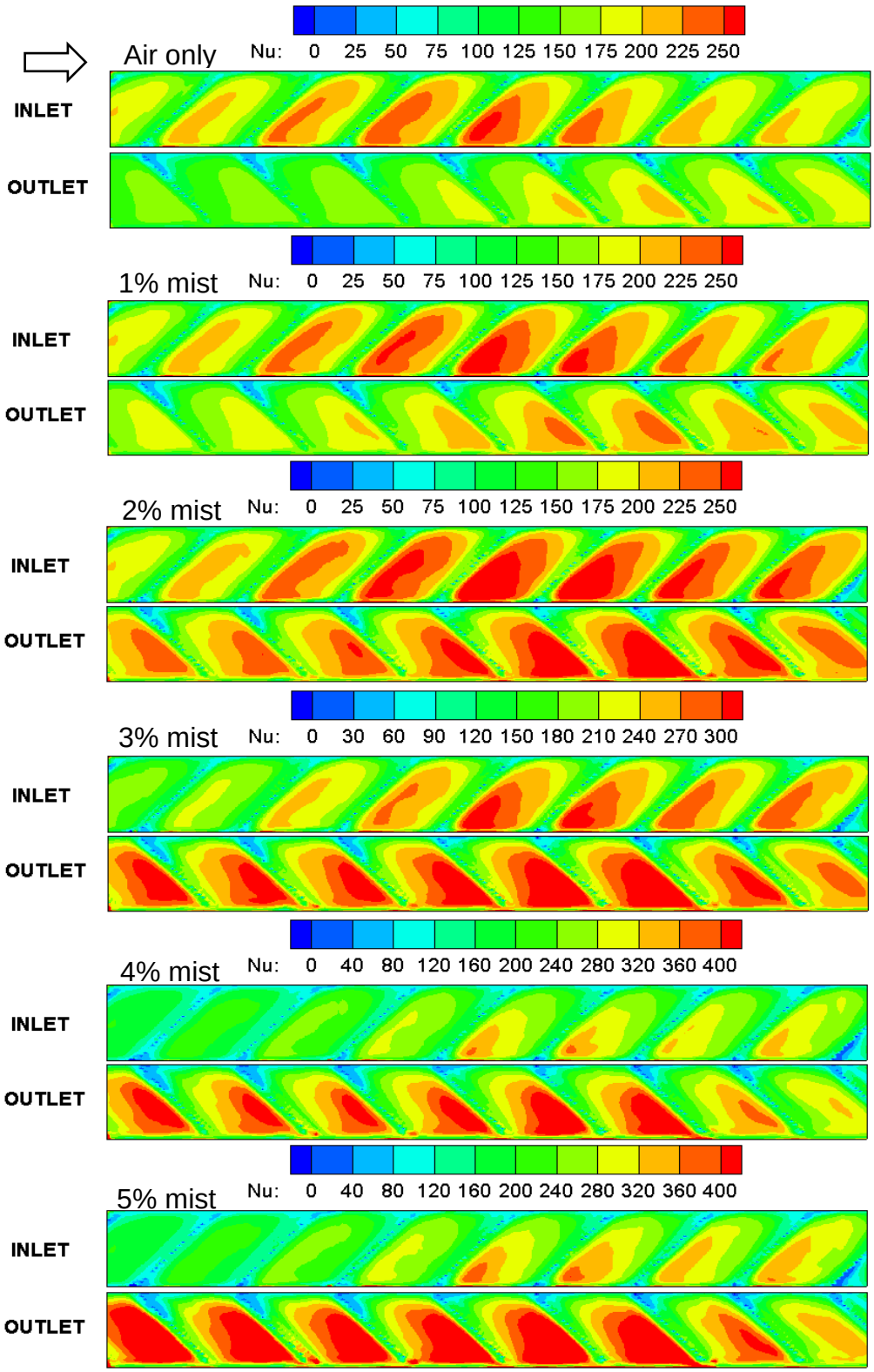

Figure 60 Trailing edge Nusselt number distribution of both first and second passages

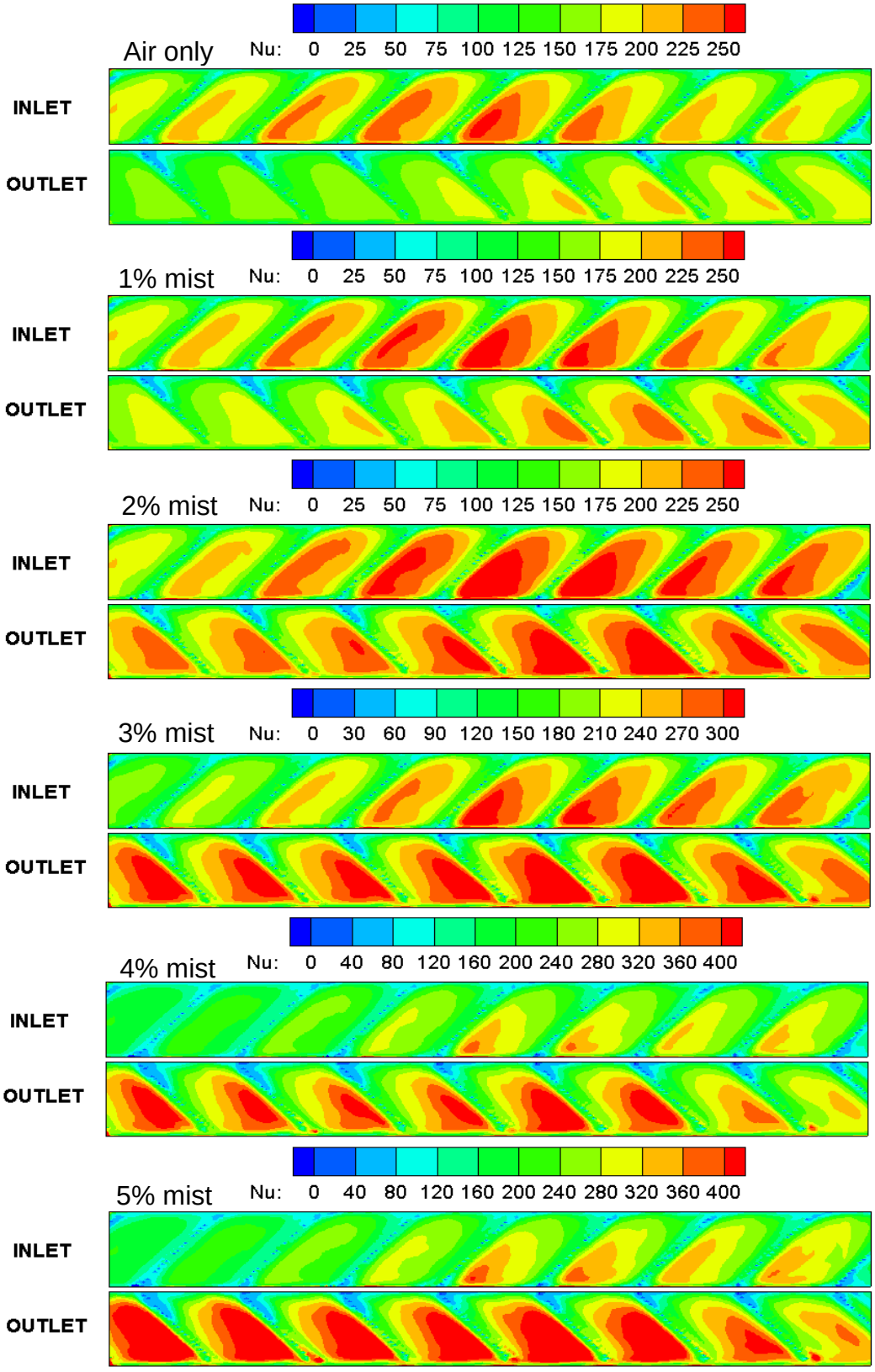

Figure 61 Leading edge Nusselt number distribution of both first and second passages

In between 1% and 4% mist/air ratio, the Nusselt distribution is consistent with the trend of the shifting of the peak Nusselt region from as early as 4th rib location towards the outlet location. Since the Nusselt value represents the heat transfer enhancement and therefore based on this contour, it is concluded that the cooling enhancement at the second passage (downstream) is rather more obvious than the first passage with the inclusion of mist injection into the airflow. These observations suggest that the location of the maximum cooling effort can be prescribed through the employment of mist injection. In this way the drawbacks of the pattern associated with the air alone can be overcome with the mist injection method.

Figure 61 show the distribution of Nusselt value on the leading edge surfaces of the 1800deg channel. As compared to the previous distribution on the trailing edge, the Nusselt number amplitude was found weaker including the peak region. However the trends are similar to the previous trailing surfaces distribution nevertheless.

The averaged Nusselt number distributions on the trailing edge surfaces at various mist conditions are presented in Figure 62. When no mist is used, the Nusselt number increases slowly from circa 160 to about 170 (~6%) at the location 4 then reduces to 140 at the last location downstream near outlet. When 5% mist is used, the Nusselt value increases significantly from 160 to 220 (37%) at location 6 then increases even more towards 320 (100%) after the flow turns around the 180deg bend. The pattern that corresponds to an increase in Nusselt number with the introduction of mist into the coolant air stream is observable for all mist ratios.

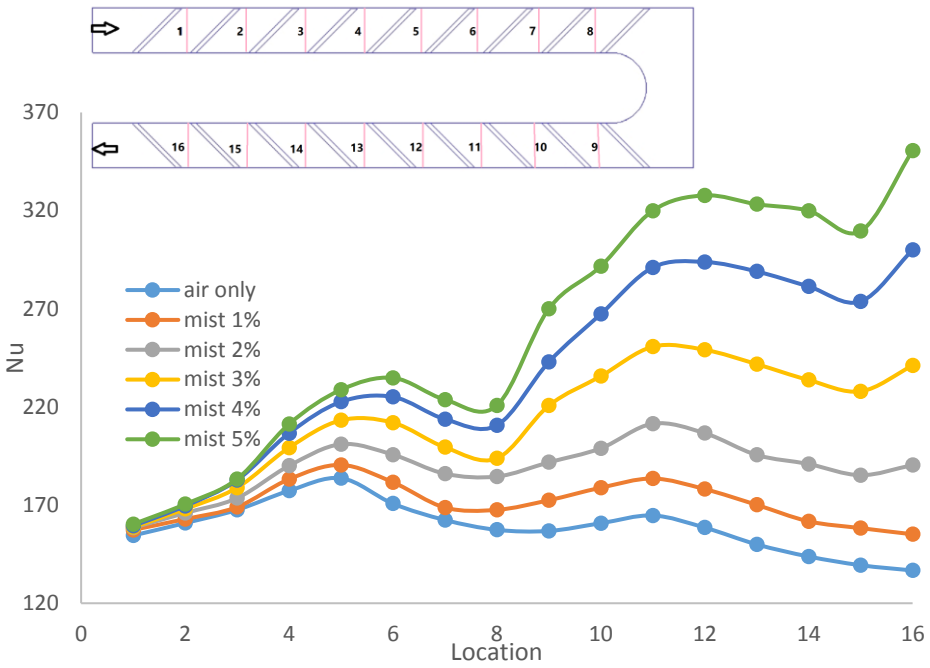

Figure 62: Trailing edge surface averaged Nusselt number downstream of the rib at various mist/air conditions

Figure 63 shows the averaged Nusselt number distribution downstream of the rib on the leading edge surfaces at various mist conditions. The results obtained is similar to that on the trailing edge surfaces Figure 61 When no mist is used, the Nusselt number increases slowly from 160 to 170 (~6%) at the location 4 then reduces to 140 at the last location downstream near outlet. When 5% mist is used, the Nusselt value increases significantly from 160 to 220 (37%) at location 6 then increases even more after the 180deg turn flow turns around 320 (100%).

The role played by the secondary flow when mist is injected is clearly demonstrated by the plots shown in Figure 63. The dramatic increase in the Nusselt number is attributable to the combination of the added mixing in the flow, once past the bend, with the enhanced effect due to the increase in mist concentration.

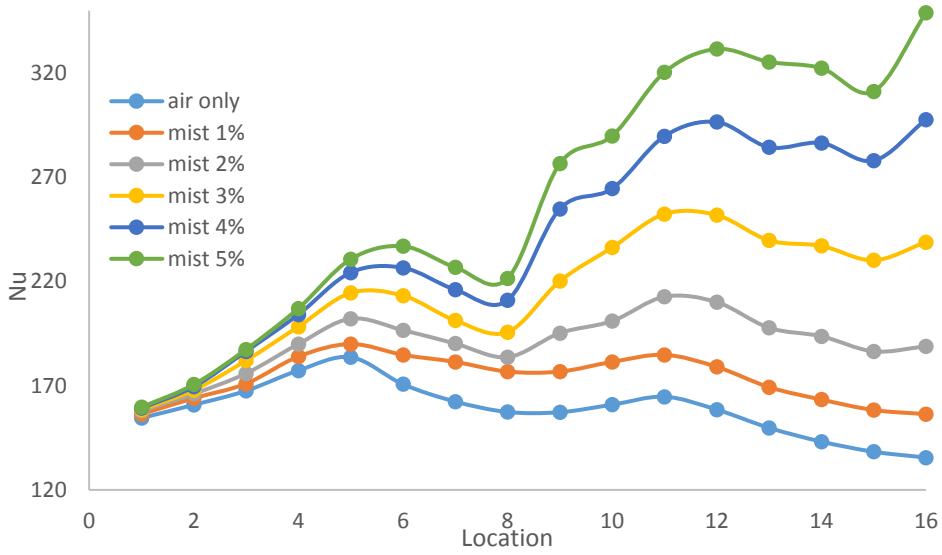

Figure 63 Leading edge surface averaged Nusselt number downstream of the rib at various mist/air conditions

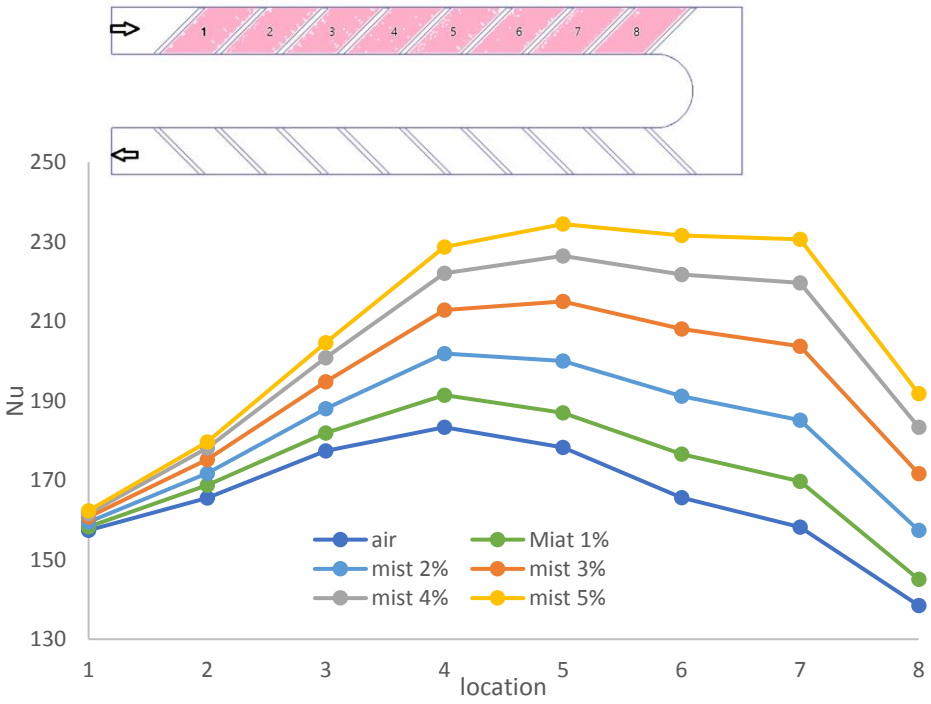

Figure 64 Averaged Nusselt number along the inlet trailing edge surfaces at various mist conditions

The averaged Nusselt number distribution along the outlet pass trailing edge surfaces, for various mist conditions, is presented in Figure Figure 65. At no mist condition, the Nusselt value increases from 125 to 140 (~12%) at the peak at 6 location and then reduces to 130 at location 8. At using 5% mist, Nusselt value decreases slightly from 290 to 270 at the lowest at location of 2 then increase to 290 again at location of 5 before reducing all the way to 8 at the outlet.

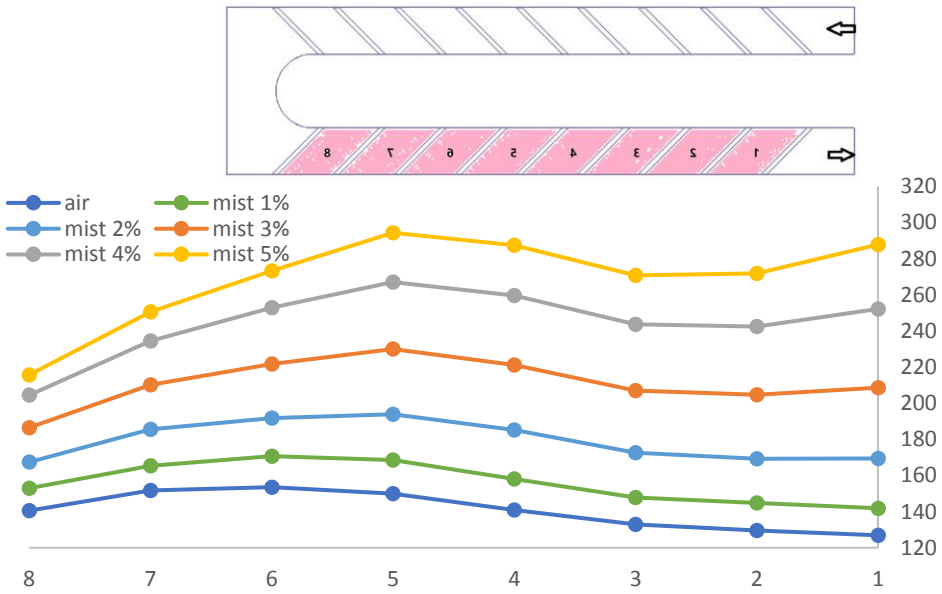

Figure 65 Average Nusselt number along the outlet trailing edge surfaces at various mist conditions

Regarding the outlet leading edge, Figure 66 shows the averaged Nusselt number distribution along the respective surfaces at various mist conditions. The trend is similar to that of the inlet trailing edge surfaces Figure 62. At no mist condition, the Nusselt value increases from 150 to 175 (16%) at the peak at 4 location and then reduces to 140 at location 8. Under 5% mist condition, Nusselt value increases from 160 to 230 (44%) peak at location of 5 then reduces towards 3 at the bend.

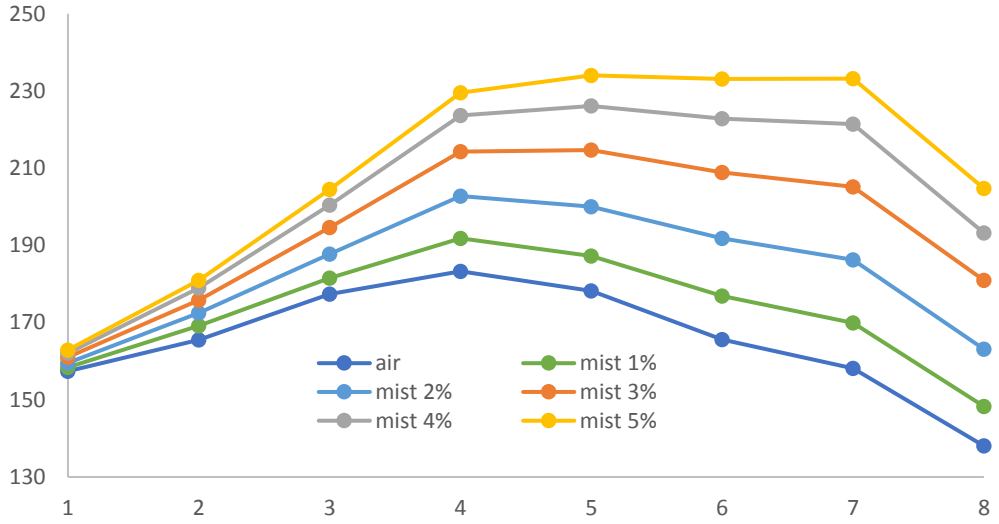

Figure 66 Averaged Nusselt number along the inlet leading edge surfaces at various mist conditions

Figure 67 presents the averaged Nusselt number distribution along the outlet leading edge surfaces at various mist conditions. A similar trend is observed to the outlet trailing edge surfaces (Figure 63). At no mist condition, the Nusselt value increases from 125 to 140 (12%) at the peak at location 6 and then reduces to 130 at location 8. At using 5% mist, Nusselt value decreases slightly from 290 to 270 at the lowest at location of 2 then increase to 280 again at location of 5 before reducing all the way to 8 at the outlet.

Finally, Figure 68 depicts the averaged inlet flow temperature at different stations under varying mist percentage conditions. The airflow temperature increases from inlet to the bend locations almost linearly. The airflow accumulates heat that is released by the surrounding heated wall surfaces when flowing downstream. The higher the mist percentage, the higher the airflow temperature. This indicates the efficiency of the extracting of the heat using airborne mist particles.

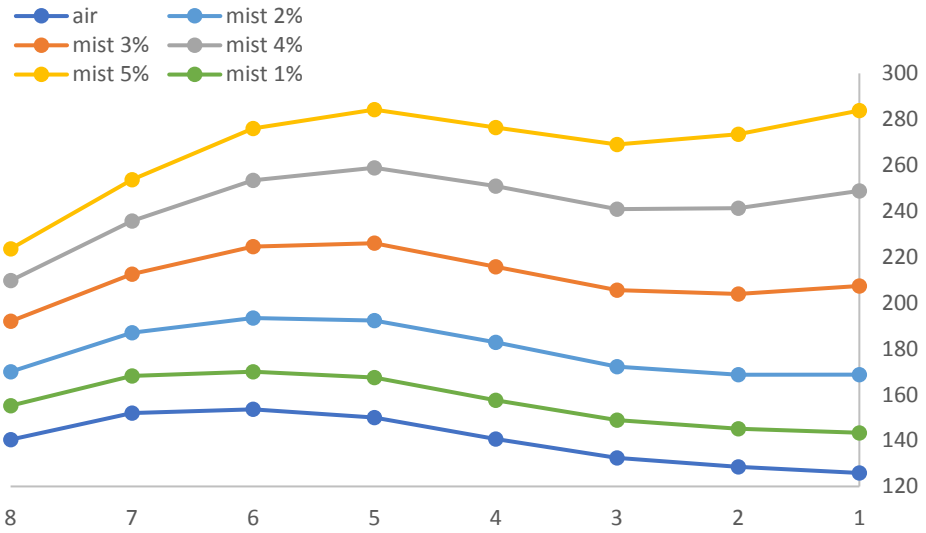

Figure 67 Average Nusselt number along the outlet leading edge surfaces at various mist conditions

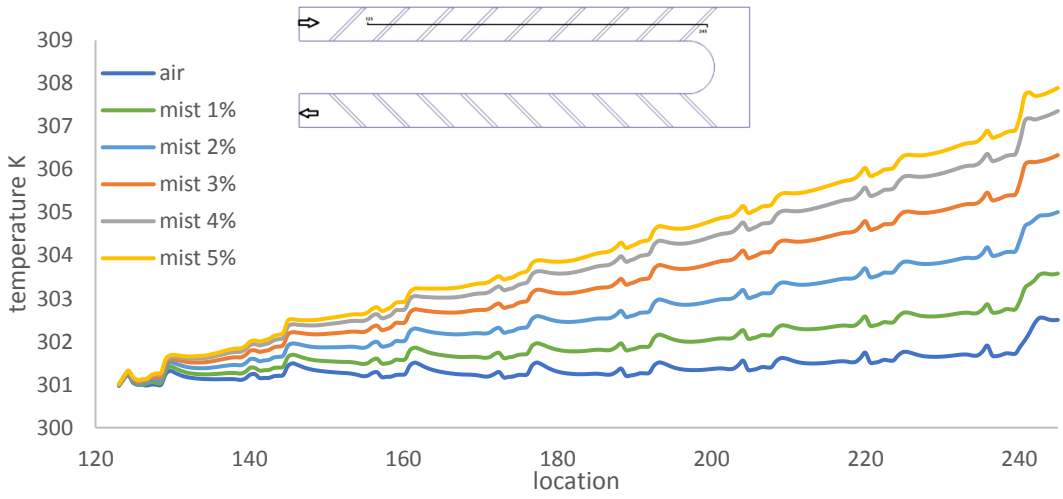

Figure 68 Averaged inlet flow temperature at various mist conditions

For the outlet pass section of the duct, the averaged outlet flow temperature at various locations under different mist conditions is presented in Figure 69. The airflow temperature decreases from the bend location to the outlet almost linearly. The airflow is therefore extracting less heat from the wall when leaving the domain. A similar trend to the inlet airflow temperature is noted, the higher the mist percentage, the higher the airflow temperature is observed.

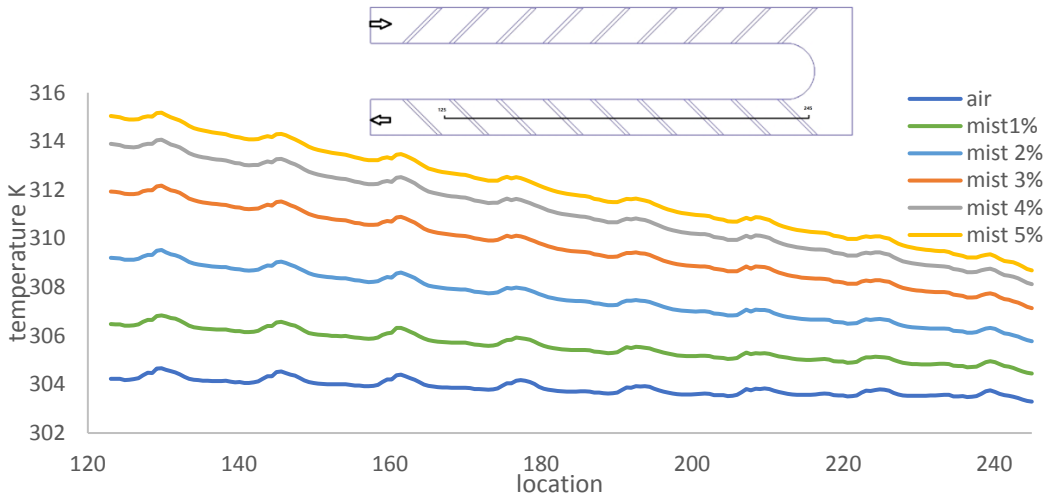

Figure 69 Averaged outlet flow temperature at various mist conditions

in Figure 70 the averaged Nusselt number distribution represented by total surfaces at inlet and outlet locations comparing trailing and leading surfaces separately is presented. Interestingly, outlet (second passage) Nusselt values significantly are higher than inlet (first passage) values. Both leading and trailing edges perform about the same with both outlet trailing and inlet leading values are slightly higher at higher mist conditions. Overall, 5% mist condition has achieved almost 92% of cooling enhancement with the second passage walls alone while only 27% by first passage wall surfaces alone.

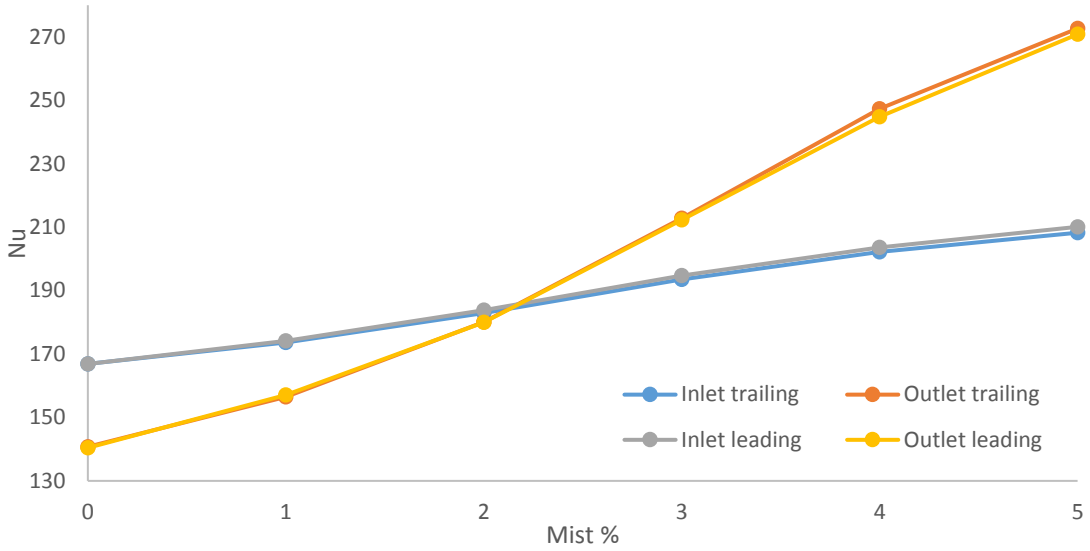

Figure 70 Averaged Nusselt number on inlet and outlet locations on trailing and leading surfaces for various Mist Percentage

The averaged Nusselt number based on the total surfaces for different mist conditions is portrayed in Figure 71. In general, the higher the mist/air ratio, the higher the Nusselt number and it achieved as much as 54% with 5% mist compared to no mist condition.

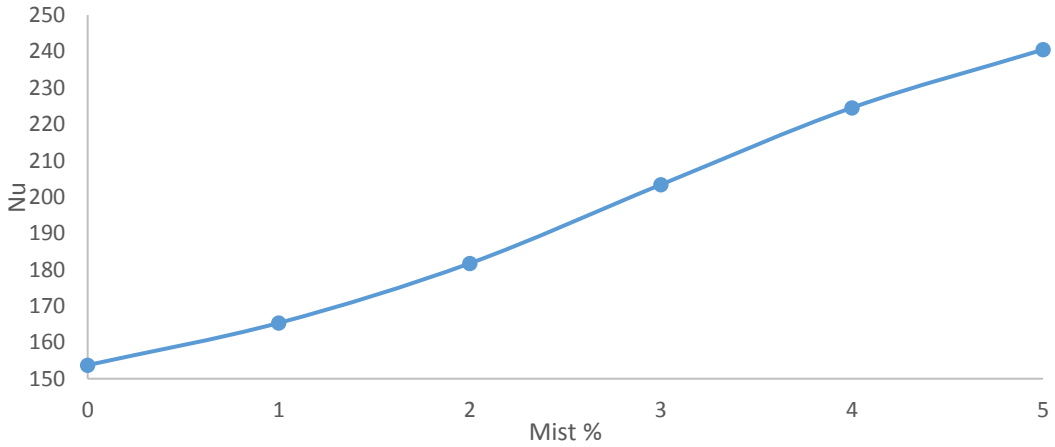

Figure 71 Averaged Nusselt number for various Mist Percentage

Finally, in Figure 72 the averaged convective efficiency predicted at various mist/air ratio is displayed. It is clear that as mist/air ratio increases, so does the convective efficiency. This indicates a direct contribution of the cooling enhancement that can be achieved with just adding mist into the airflow. The predicted results are consistent with the observations. As much as 75% efficiency can be found with 5% mist addition.

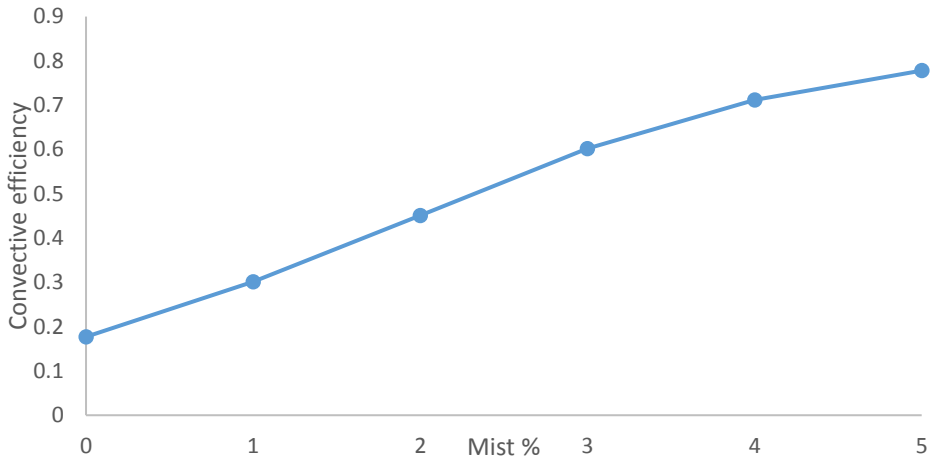

Figure 72 Convective cooling efficiency at various mist conditions

5.3 **Rotating**

The water droplets distribution on different axially located planes under various mist/air ratio conditions is presented in Figure 73. A comparison with Figure 57 enables the identification of some important differences. The quasi symmetric patterns about the mid-span plane are replaced by no symmetry structures biased towards the trailing edge on account of the Coriolis and inertial effects. As for the non-rotating case, the droplet concentration is less even after the turn. Interestingly enough there are flow structures that are common to quasi all droplet concentration cases.

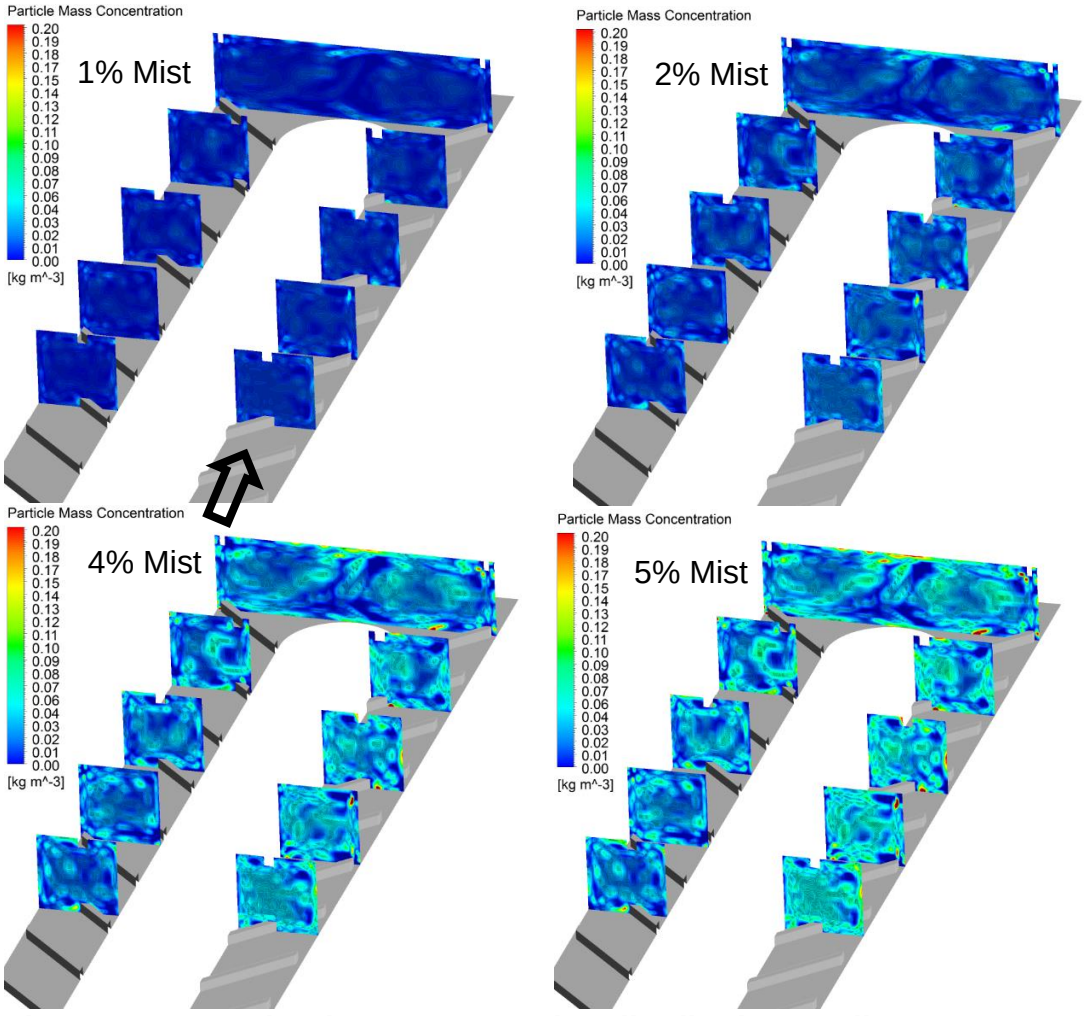

Figure 73 Water droplets concentration distribution on different axially located fluid planes under various mist/air ratio conditions

The water droplets concentration distribution on the trailing edge surfaces at various mist/air conditions is presented in Figure 74. It is clear that the water droplets concentrations increased with the mist/air ratio. The smallest concentration amount is found within the small confined flow separation region right behind each rib structure consistently for all conditions. Water droplets are indeed carried along by the flow path. Also, the water droplets can be seen more concentrated in between ribs in the first passage compared to the second one. Towards the outlet, the concentration is similarly weaker for all the cases. When concentration is reduced, heat transfer will be reduced also as seen in the following figures. Downstream of rib 6 at traling edge in all cases shows a lot of water droplet conectration compared to the other and this is due to the Turbluence intensity at that region

Figure 75 shows the water droplets concentration distribution on the leading edge surfaces at various mist/air conditions. Similar pattern is found except to the previous trailing edge distribution (Figure 74), except that the general concentration on the leading edge is found weaker and appears much more dilute. Also, the concentrations in the bend region on the leading edge surfaces are found weaker. This implies main core flow are more attached to the trailing edge surfaces and more separation occurs on the leading edge surfaces and this is due to the coriolis force created by the rotation which push the flow towards the Trailing edge . Both droplets concentration and flow turbulence have shown direct impact to the heat transfer and cooling enhancement process.

The water droplet concentration distribution on the centreline fluid plane inside the 180deg bend channel is plotted in Figure 76. At 5% mist condition, the water droplets are seen to coalesce (light blue) and breakup (dark blue) at multiple locations especially upstream and downstream in vicinity the 180deg bend due to flow swirling effect when flow is turning around the bend region. Water droplets can be traced from these thin

streak patterns exhibited due to the secondary flow created by four main factor. Ribs, ribs pattern, 180 deg. Turn and rotation are the main reason effecting the flow.

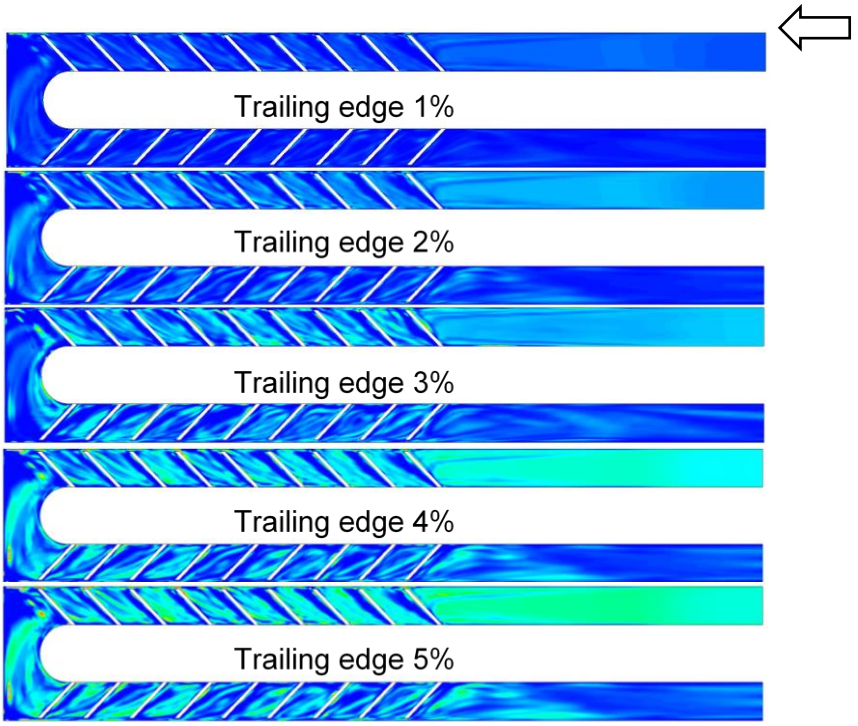

Figure 74 Water droplets concentration distribution on the trailing edge surfaces at various mist/air ration conditions

The water droplet concentration distribution on the centreline fluid plane inside the 180deg bend channel is plotted in Figure 76. At 5% mist condition, the water droplets are seen to coalesce (light blue) and breakup (dark blue) at multiple locations especially upstream and downstream in vicinity the 180deg bend due to flow swirling effect when flow is turning around the bend region. Water droplets can be traced from these thin streak patterns exhibited due to the secondary flow created by four main factor. Ribs, ribs pattern, 180 deg. Turn and rotation are the main reason effecting the flow.

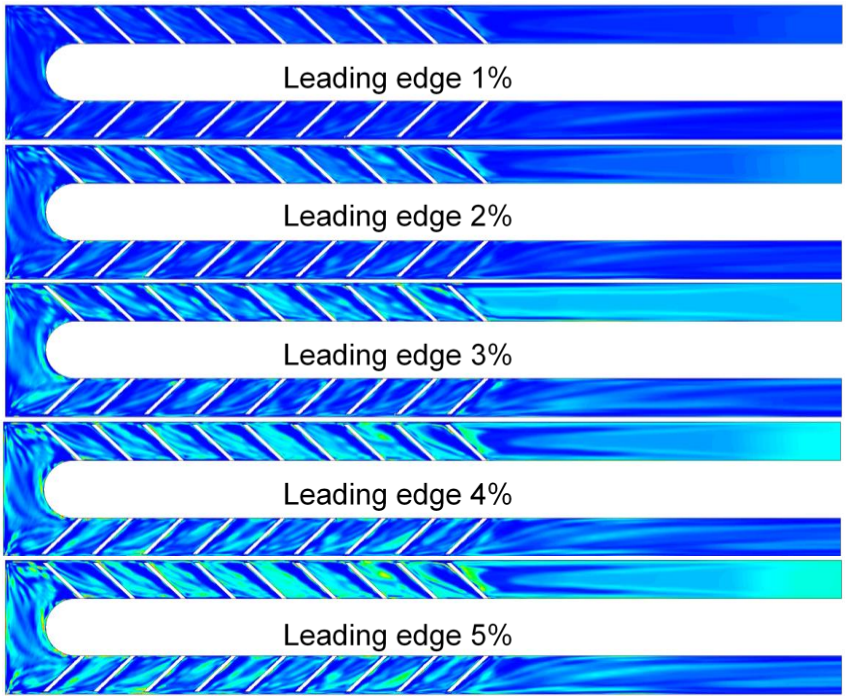

Figure 75 Water droplets concentration distribution on the leading edge surfaces at various mist/air ration conditions

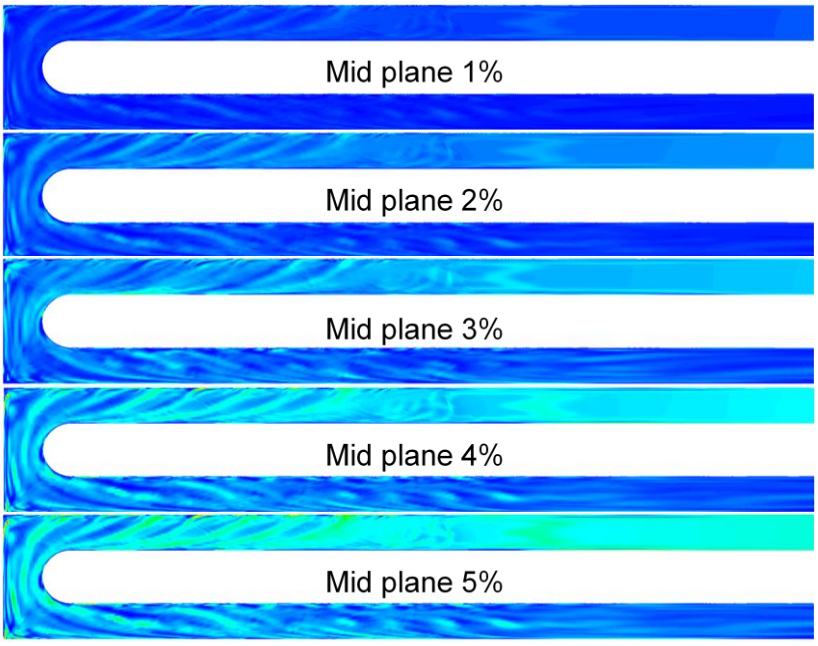

Figure 76 Water droplets concentration distribution on the mid plane fluid plane at various mist/air ration conditions

Figure 77 shows Nusselt number distribution on the trailing surfaces at different mist/air ratio conditions. Generally, the Nusselt number is found increased in the downstream region of the ribs. This region is also identified as flow reattachment region. When no mist is used for the inlet trailing edge, the Nusselt number increas rib downstream region has shown increased beginning at the inlet location towards the fourth rib location. Nusselt value is at its peak before reducing towards outlet. Then its reduces until it reach the last rib at the outlet. In between 1% and 3%, the Nusselt distribution also shows consistent with the trend that shifting of the peak Nusselt region from as early as 4^{th} rib location towards 5^{th} rib at the first passage. Whereas the 4% and 5% mist reach it Nusselt number peak half way at the seconde passage.

Overall first passage shows more heat transfer as a result of the high Nusselt number, this is the case for air and mist up to 3% but as mist increases the high Nusselt number shift to the second passage as shown in the Figure 77, further more when 5% mist/air ratio condition is applied, the Nusselt value has reached its peak at the outlet location instead. Heat transfer is signficlly higher at the seconde passge for the 4% and 5% mist. In term of consistency heat transfer is uniform along the second passage for cases with mist ratio from 3% to 5%. Not the case for 0% to 2% mist where heat transfer is increase towards the center of the first passage then decreases gradually. 3% mist was the only case where the inlet and oulet trailing passge close to each other in respect of heat transfer.

Figure 78 show the distribution of Nusselt value on the leading edges surfaces of the 180deg channel. As compared to the previous distribution on the trailing edge (Figure 77), in cases air only and 1 mist, first passage shows more heat transfer whereas cases 2% to 5% mist showes high heat tramsfer in the seconde passage. Also the seconde passage in cases 4% and 5% mist demonstrates high heat trasnfer aproximmtly double the the first passage.

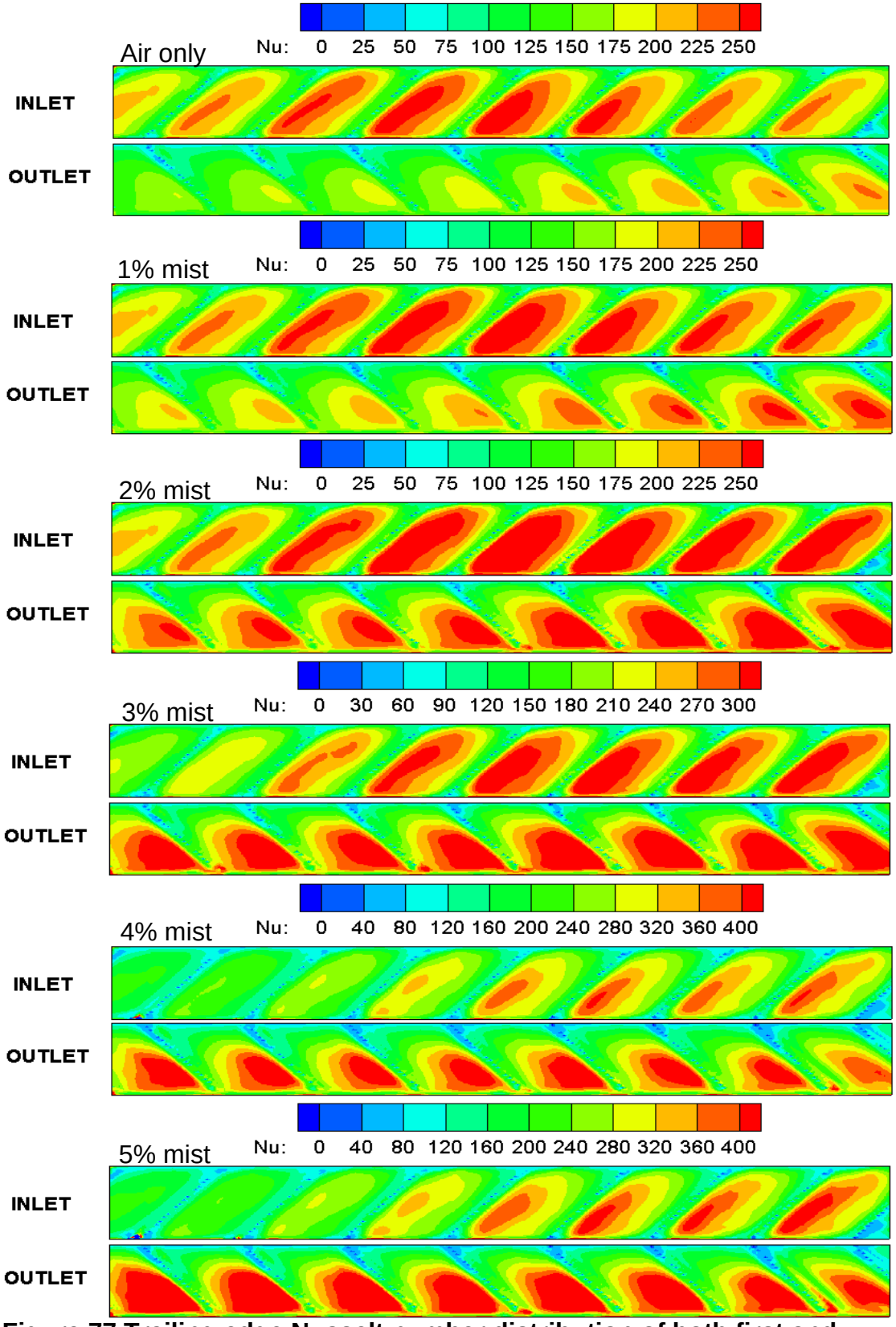

Figure 77 Trailing edge Nusselt number distribution of both first and second passages

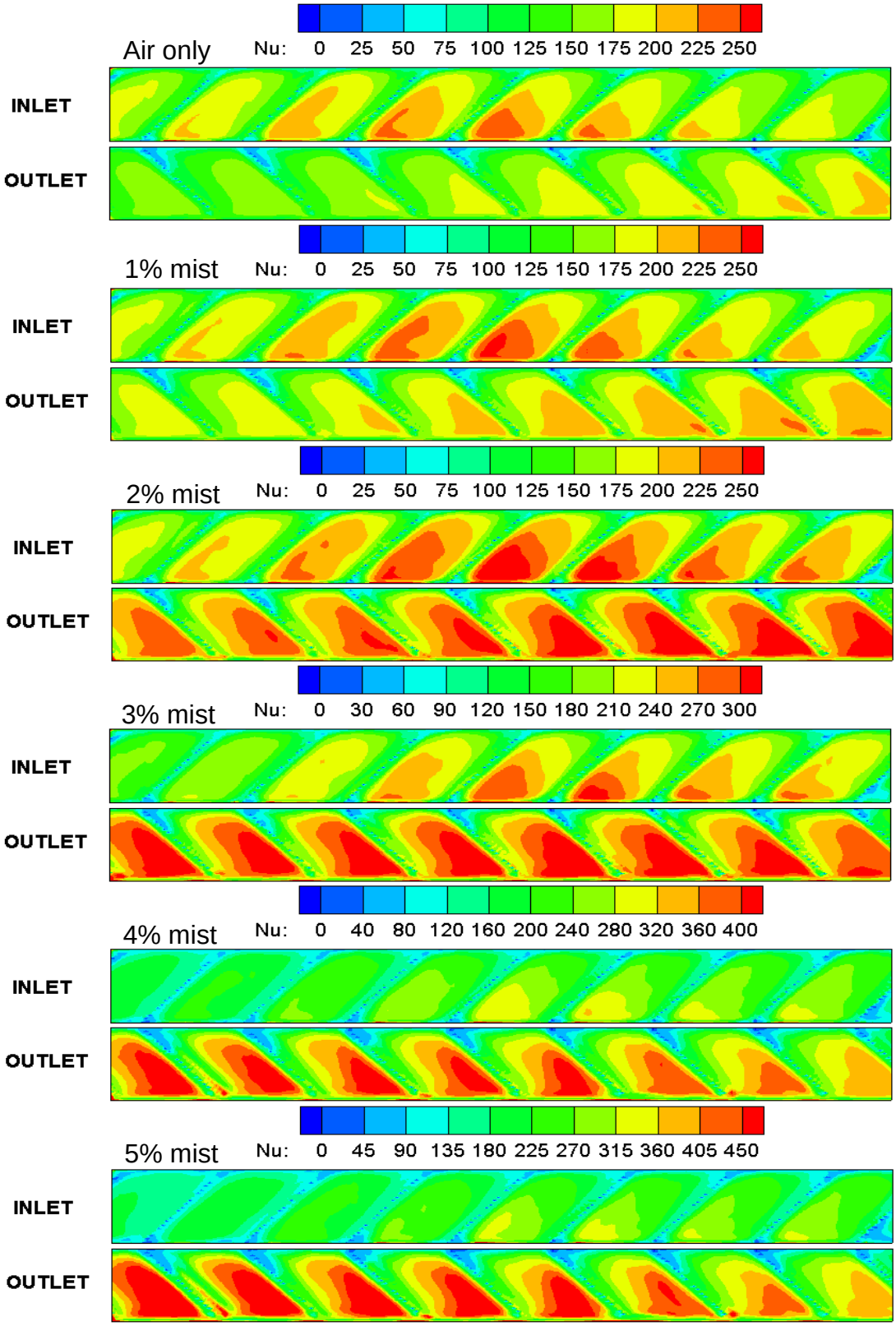

Figure 78 Leading edge Nusselt number distribution of both first and second passages

Figure 79 compares the averaged Nusselt number distribution at various inlet trailing edge locations with different mist/air ratio conditions. Compared to no mist condition, the Nusselt number has increased when the mist/air ratio is applied at all locations. As the flow enters the duct, Nusselt number for all cases is close to each other which indicates a small heat transfer rate is taking place within this region. As the flow move forward, this difference start to be more noticeable until it reaches a maximum value at approximately location x=7 where both droplet behaviour and the increases in turbulence intensity take place. For air only case, the location of the first peak occurs at location 4, this is not the situation for other mist percentage cases where the location of the first peak has been shifted due to the influence of the existence droplet. Water droplet cause the flow to delay it maximum turbulent intensity by 25%

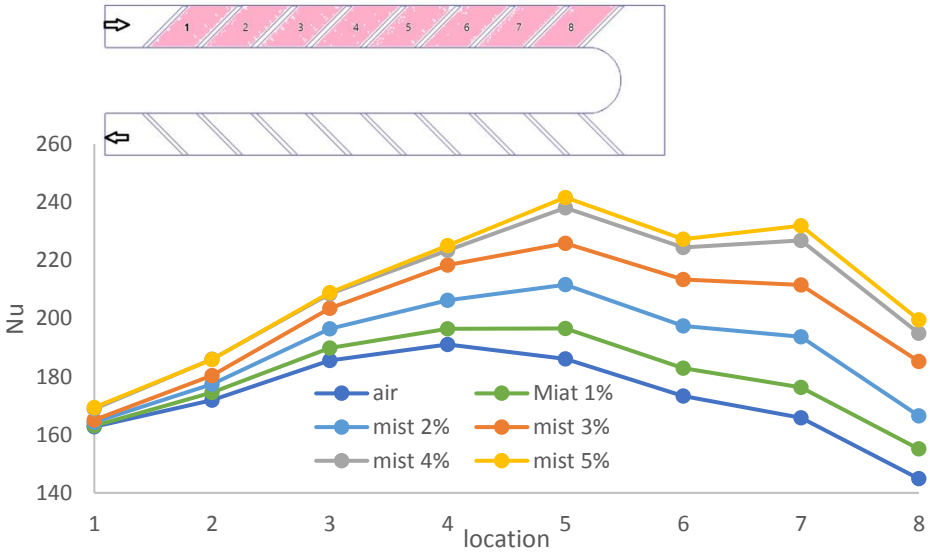

Figure 79 Averaged Nusselt number variations with mist/air ratio at different inlet trailing edge locations

The maximum Nusselt number is found in between 4-5 location depending on the mist/air ratio used. The maximum Nusselt number can achieve as

much as 23% more with using 5% mist compared to no mist situation. This location is aligned to the region where maximum heat transfer is occurred due to both droplets and flow turbulence enhancement effect. When no mist is used, it was found that the minimum Nusselt value is at location of X=8, whereas with 5% mist condition the location is at X=1. The effect of droplets is also found to play more dominant role at downstream locations compared to pure air.

Figure 80 present a comparison of averaged Nusselt number distribution at different locations at the outlet trailing edge using various mist/air ratio. In contrast to previous inlet trailing edge, Nusselt number has not increased much (<20%) from location X=1 to 7 and reached maximum at location X=5 before decreasing. General speaking, higher the mist/air ratio, higher the Nusselt number at every location. The maximum Nusselt value when using 5% mist is about 47% as compared to the maximum value at no mist condition. Whereas the biggest difference occurs at location, one towards the outlet around 82% increase between airs only case and 5% mist. Also, found that near the 180-degree turn the value of Nusselt number for cases 3% to 5% mist was close to each other compared to the rest of the cases. And heat transfer behaviour has changed for cases of air only to 2% mist the heat transfer starts to decreases after a certain point while the case for 3% mist it starts decrease gradually after location 5. In contrast, cases 4% and 5% mist it starts increase towards the outlet.

Figure 81 plots the comparison of Nusselt number distribution at different inlet leading locations with various mist/air ratio. The performance trend is very similar to that of the inlet bottom location (Figure 79) . The maximum Nusselt number is also found at near 4-5 location. The maximum Nusselt value has shown to achieve 22% more with 5% mist compared to no mist condition. Nussle value drops after reaching its peak. higher the mist/air ratio, higher the Nusselt number at every location. Similarly to inlet trailing edge location performance results, the effect of droplets is also found to

play more dominant role at downstream locations compared to pure air. The maximum heat transfer for air only to 3% mist occur at location 4 however the maximum heat transfer for cases 4% and 5% mist occur at location 5 which is shifted by one rib. In contrast for the trailing edge cases 2% and 3% mist was downstream of rib 5.

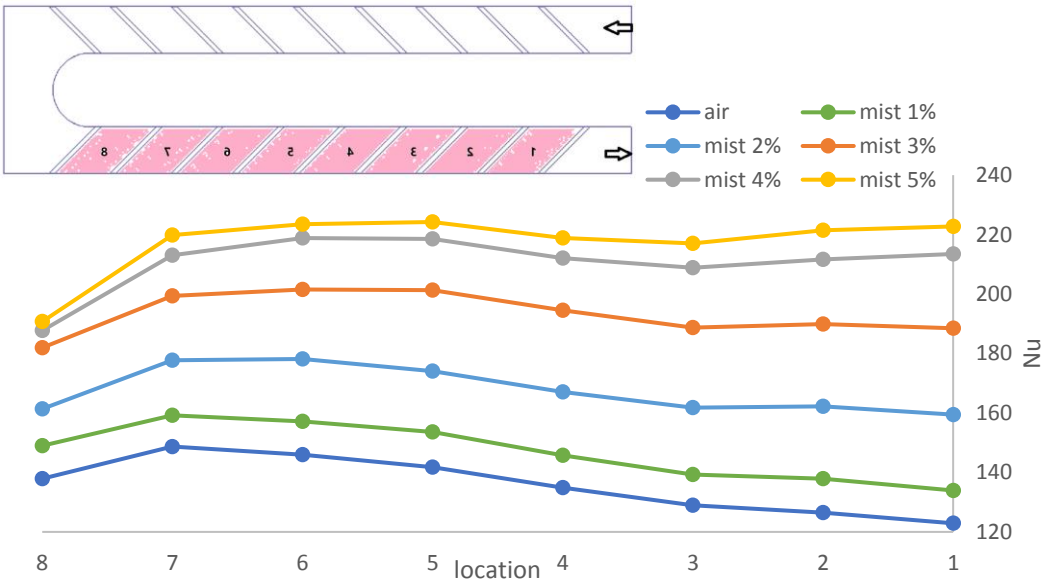

Figure 80 Averaged Nusselt number at different location at outlet trailing edge with various mist/air ratio

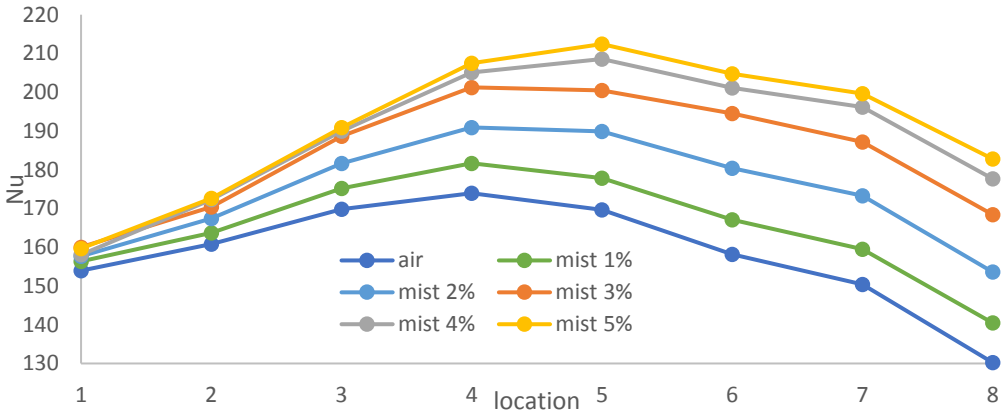

Figure 81 Averaged Nusselt number at different inlet leading edge locations with various mist/air ratio

Figure 82 shows the averaged Nusselt number distribution at different outlet leading edge locations using various mist/air ratio. Generally, the performance trend obtained is very similar to that of the outlet bottom location (Figure 80) but with different maximum value. In addition, the heat transfer decreases towards the outlet for cases air only to 2 % mist while cases 4% to 5% mist increases towards the outlet. Three% mist is the only case where the heat transfer is uniform form the 180-degree to the outlet. The maximum Nusselt value when using 5% mist is about 96% higher than the no mist condition at the same location towards the outlet.

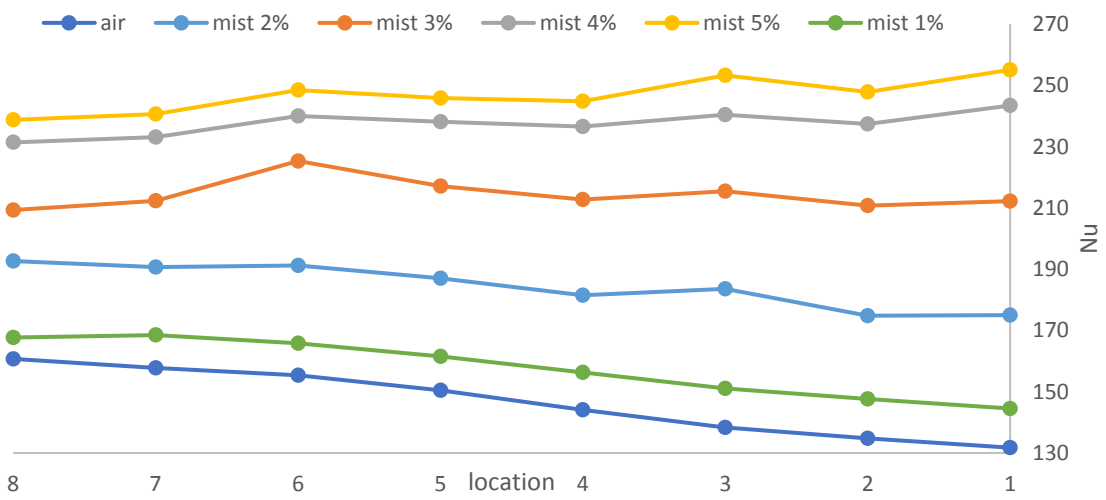

Figure 82 Averaged Nusselt number at different outlet leading edge locations with various mist/air ratio

Figure 83 displays the averaged inlet flow temperature distribution at different upstream locations using various mist/air ratio conditions. Upstream inlet flow temperature has shown increase in temperature with the distance away from the inlet location. The air temperature is heated as it travels along the channel due to the heated walls surrounding. As the

mist/air ratio is increased, the airflow temperature increase, which indicates the amount of heat absorbed by the water droplets.

The averaged outlet flow temperature at different downstream locations using various mist/air ratio conditions is shown in Figure 84. The outlet temperature increases with distance towards downstream when mist is used. This is expected. In addition, outlet flow temperature increases with mist/air ratio. This indicates heat is successfully absorbed by the mixture from the heated walls and achieved higher temperature on the mixture but lower temperature on the wall. The temperature has increased by almost 3-4 from location 125 to 245 with using 5% mist. Whereas temperature has remains almost no change at no mist condition. From upstream to downstream 5% mist achieved 250% more heat absorption then air only case.

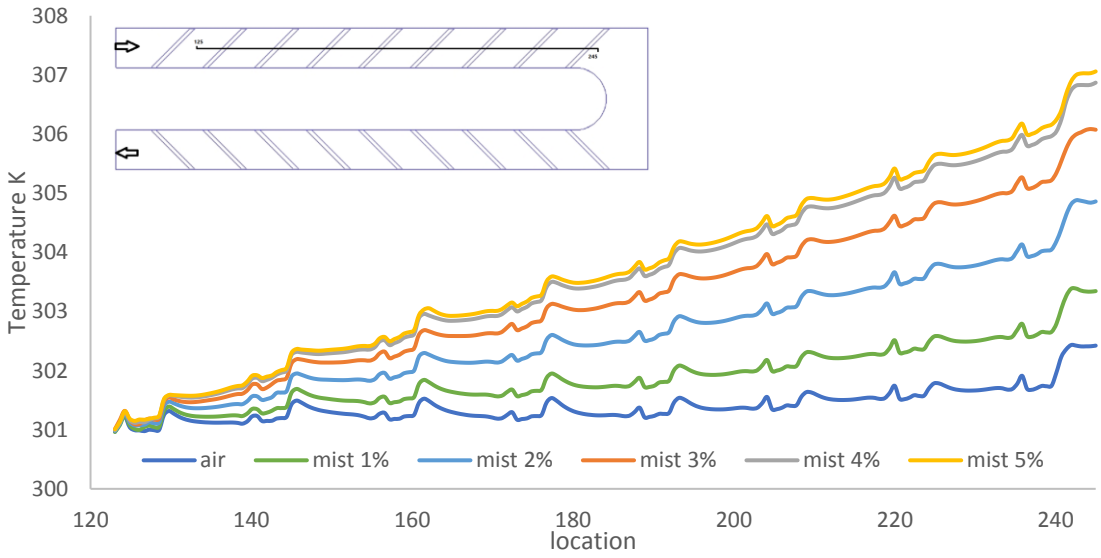

Figure 83 Averaged inlet flow temperature at different upstream locations using various mist/air ratio

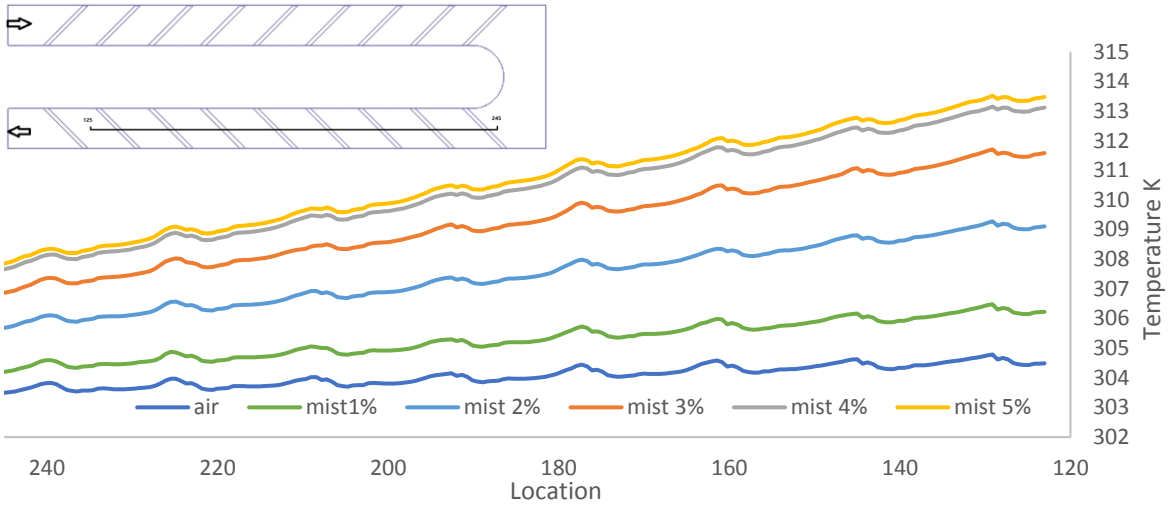

Figure 84 Averaged outlet flow temperature at different downstream locations using various mist/air ratio

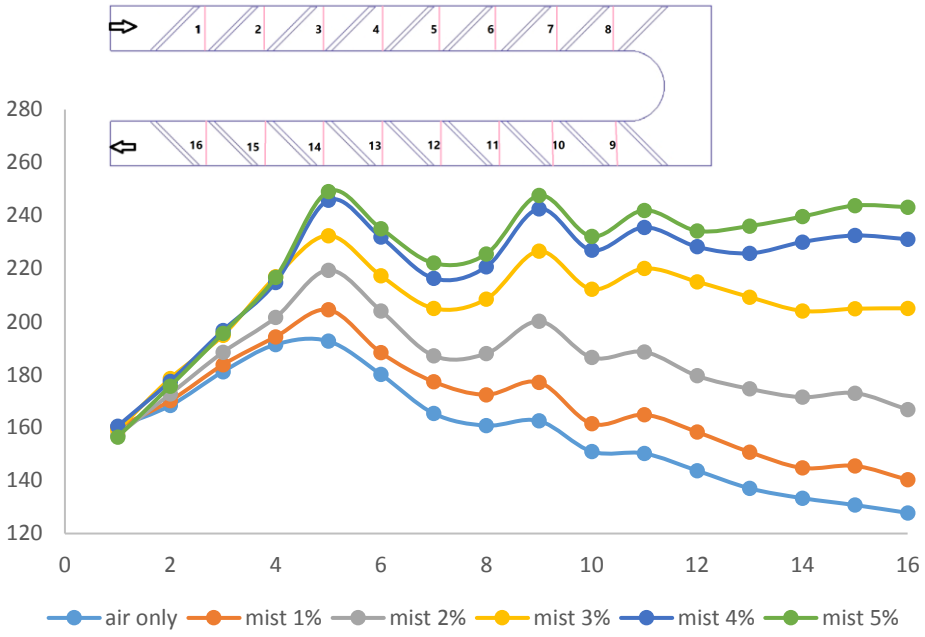

Figure 85 Averaged Nusselt number downstream of the ribs on trailing edge surface at various mist/air ratio.

Figure 85 presents the averaged Nusselt number predicted at the downstream of the ribs on trailing edge surface at various mist/air ratio. When no mist is used, the Nusselt number increases from 160 to 190 (about 19%) at the peak at location 5 then decrease to 130 at the last location. When 5% of mist is used, the Nusselt value increases from 160 to 250 (56%) at 5 location then decrease to 225 at 7 location before increase to 240 at 9 location then reach 240 at last location. the impact of mist is significant at the downstream of the ribs locations on the trailing edge surface. Similar trend take place for air only to 2% mist where heat transfer decreases after the 180-degree bend. In the other hand, 3% to 5% mist shows alike trend where heat start to increases after the 180-degree bend.

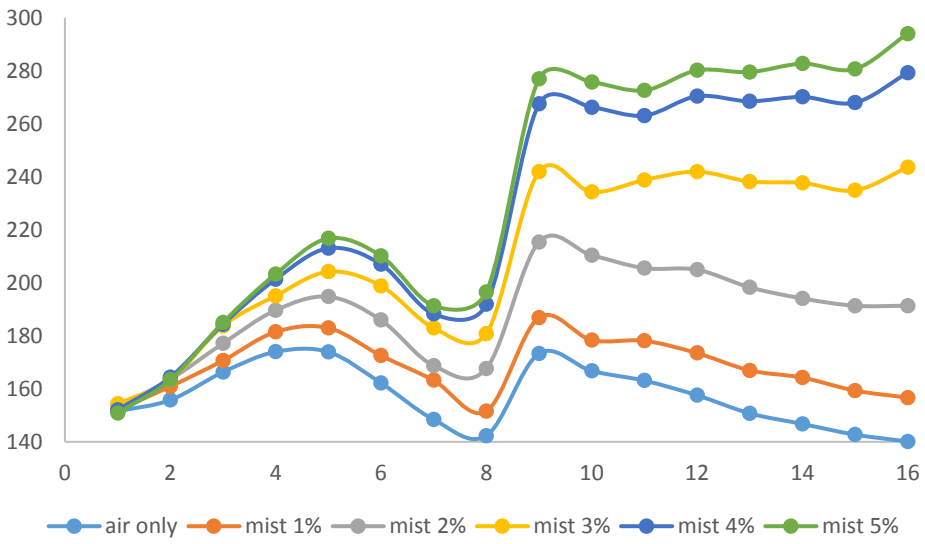

Figure 86 Averaged Nusselt number downstream of the ribs on leading edge surface at various mist/air ratio

Figure 86 demonstrates the averaged Nusselt number predicted at the downstream of the ribs on leading edge surface at various mist/air ratio. When no mist is used, the Nusselt number increases from 150 to 170 (13%) at location 4 and reduces to 140 at location 8 before rises to 170 at location 9, eventually reduces to 140 at the last location. The 180-degree bend at location 9 has caused increasing of Nusselt number on the

leading edge when centrifugal force is forcing more airflow acting on the leading surfaces locally, which greatly assist in cooling enhancement on these surfaces. This pattern remains the same and even more significance with the mist cooling. Compared to only 25% of Nusselt number jumps in the bend region, 110% Nusselt value enhancement is found when 5% mist air ratio is used at the end. In contrast, the drop of Nusselt number found compared upstream and downstream location with no mist condition has increased with 5% mist from 150 to 293 (95%).

The overall averaged Nusselt number variations with mist/air ratio at different wall surfaces is shown in Figure 87. Heat transfer was much higher on the second passage compared to the first passage. The leading edge of the second passage showed great enhancement with the increases of mist air, started at 145 Nusselt number for air only case to 248 Nusselt for the 5% mist and the least increases was the leading edge of the first passage. In addition, For the first passage leading and trailing edge there was a small difference in Nusselt number between 4% and 5% mist which mean the heat enhancement was very little after 4% mist. The Nusselt number on the first passage surfaces is increasing in much slower pace as mist/ratio increases beyond 1.5%, and eventually after such ratio reaches 3.5%, both second passage wall surfaces (leading and trailing) Nusselt number has surpassed the first passage one. Nusselt number increased by 24% in the second passage with only 2% mist, Similar observation found by [148]

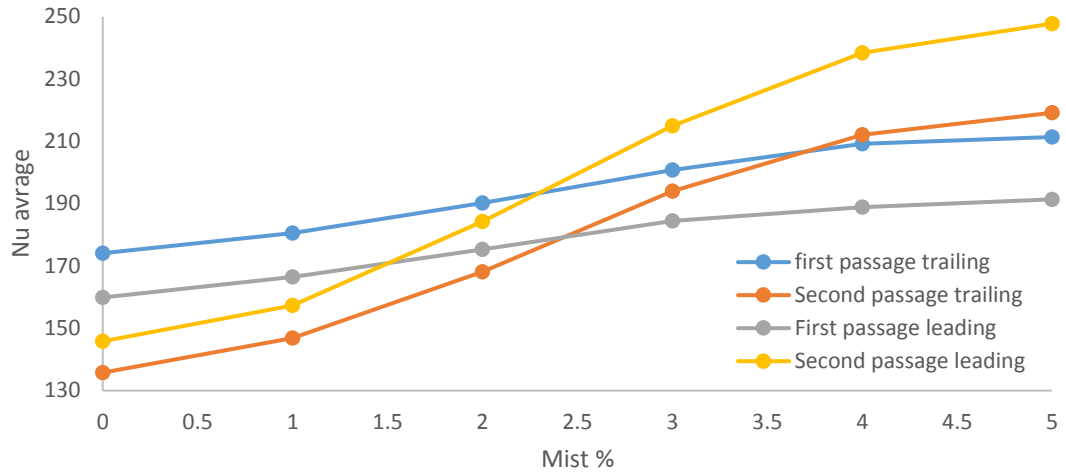

Figure 87 Averaged Nusselt number variations with mist/air ratio at both first and second passage wall surfaces

In Figure 88 the averaged Nusselt number of total wall surfaces at different mist/air ratio is shown. As mist/air ratio increased, Nusselt number is increased accordingly. The Nusselt number has increased by 12.5% by doubling the mist/air ratio from 1% to 2%. And its continue accordingly until it reaches 4% then it increases gradually. Overall, the total average Nusselt number has increased by almost 41% when 5% mist is used.

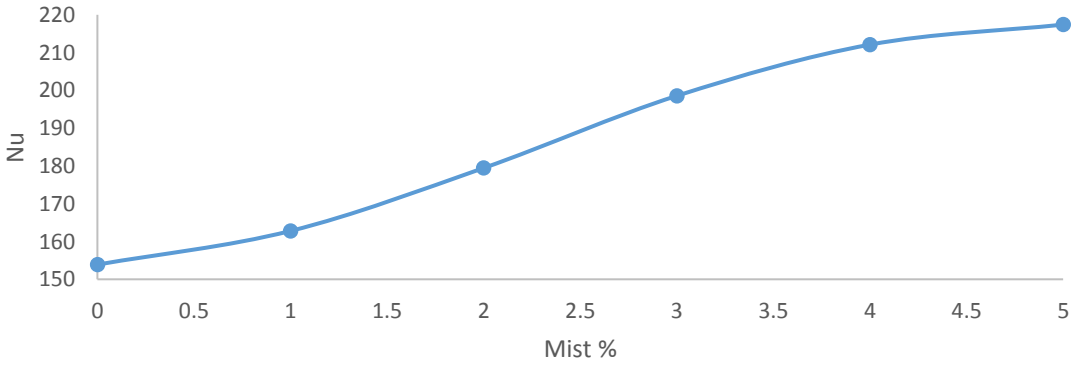

Figure 88 Averaged Nusselt number of total wall surfaces variation with mist/air ratio

Then in Figure 89 the averaged convective efficiency predicted at various mist/air ratio is presented. It is clear that as mist/air ratio increases, so

does the convective efficiency. As much as 68% efficiency can be found with 5% mist addition.

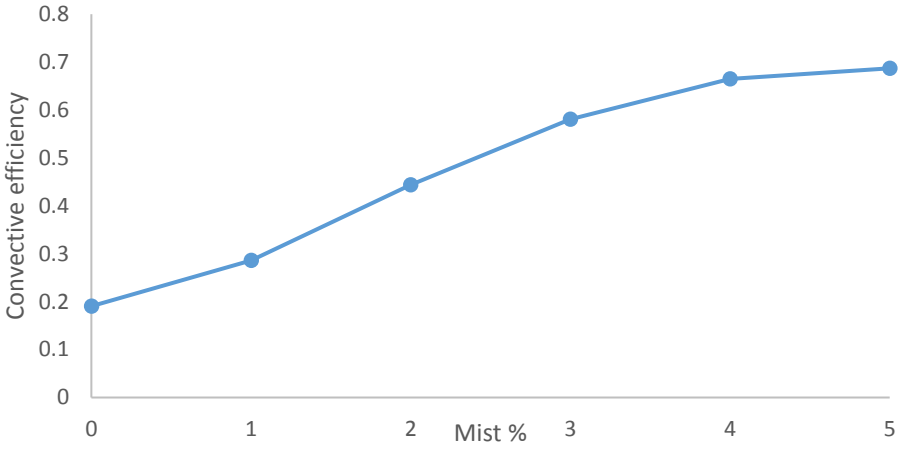

Figure 89 Averaged convective efficiency at various mist/air ratio

5.1 Chapter conclusion

Mist addation ratio anlaysis for rotating and non rotating case is studied for mist ratio from 1% to 5% which had not been done before. Figure 90 shows the avarged Nusselt number variation with mist/air ratio at both first and second passage for rotating and non-rotating cases. From the figure the difrence is clear for the leading edge, where maximum heat trasnfer enhancmet occur and the diffrence between the rotating and non rotating is presented. From 0% to 2% mist the inlet leading for both the rotating and non rotating case showed more heat trasnfer then the outlet leading edge. This is not the case for 3% mist and higher where the maxumum heat trasnfer will shift to the outlet leading edge

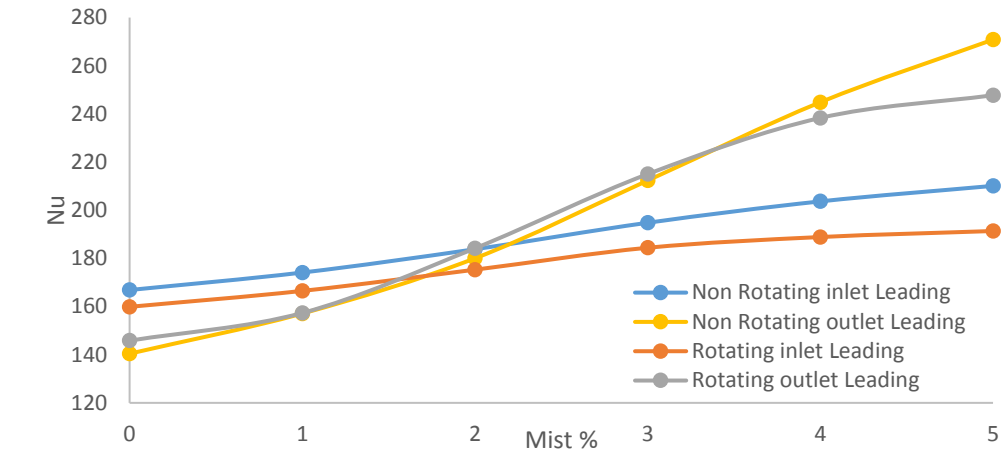

Figure 90 Averaged Nusselt number variations with mist/air ratio at both first and second passage for rotating and non-rotating cases.

Figure 91 present the averaged Nusselt number variations with mist/air ratio for rotating and non-rotating cases After 2% mist the Nusselt number will start to increses gradually for the rotating case. Nonetheless, the stationary case starts to increase linerarly.

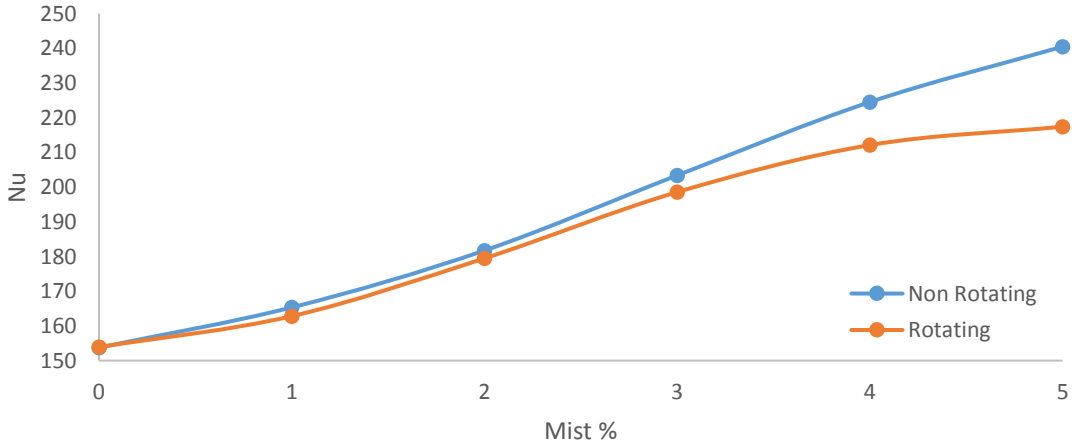

Figure 91 Averaged Nusselt number variations with mist/air ratio for rotating and non-rotating cases

6 Investigations of Heat Transfer Enhancement Through Cross-Section Manipulation

6.1 Introduction

Typical internal forced cooling technology includes turbulators, pin-fins, turns, impingement jets, swirl cooling, vortex cooling and other methods. Along with these, shape and sizing of passage must also be manipulated to investigate design options and their effect on cooling performance.

Most of the previous internal cooling investigations reported in the literature were conducted employing ducts with uniform cross-sections. One of the few instances in the literature where a varying cross-section was examined is due to [60]. It is well known that, when fluid flows are turned around a bend, a secondary motion within the flow is developed due to presence of the centrifugal and Coriolis forces. These phenomena whilst causing added aerodynamic losses also enhance mixing within the flow and therefore the heat transfer. The purpose of this section of the study is to simulate numerically the flow patterns in ducts with varying cross-sections and to identify the configurations that maximise heat transfer whilst minimising pressure loss. Ultimately it is the manipulation of secondary flow and of vorticity that is sought.

6.1 Computational domain

Six configurations have been selected and analysed. Case 1 is a smooth square cross section with sharp edge turns acting as the reference case. Case 2 is a uniform square cross section with a smooth bend section rather than an angular turning section as for the previous example. Case 3 is square-circle-square passage with a smooth turning. Case 4 is a

square-rectangular passage with a sharp expansion at the turn. Case 5 is a square-trapezoid-square passage and the last one is Case 6 which consists of a square-half diamond-square transition passage

The flow investigation on these six types of U-ducts are shown in Figure 92 six different configuration of geometry The height of channel, h, is 12.7mm, the length of sections before and after the bend are140mm, the inner diameter of the channel R_{in} is 2.6mm, the outer diameter of the channel R_{out} is 28mm.

6.2 **Boundary conditions**

In order to study the behavior of the secondary flow and vorticity, different Reynold numbers have been considered in this study (Re=5,000, 10,000, 25,000 and 40,000). The prescribed heat flux used is the same as for the previous study (4,800 W/m^2). All the cases are analysed in the stationary frame only. Rotating effects have not been studied in this analysis due to lack of opportunity given the time available. Although it is recognized that it is desirable to extend the study to the rotating cases, it is thought nevertheless that meaningful trends can be extracted from the non-rotating cases which have applicability in the evaluation of the configurations that can be used in actual blade cooling situations. Further geometry details are available in appendix.

Uniform velocity profile corresponding to the given Reynolds number, for example, Re = 25,000 (V_{inlet} = 28.76 m/s), turbulence intensity Tu = 1% and turbulent to laminar viscosity ratio TVR = 100 are defined at the inlet of the computational domain. For the first case, calculations with Reynolds number Re = 5,000, 10,000, 40,000 (V_{inlet} = 5.75m/s, 11/50m/s, 46.02m/s) were also made. At the outlet from the computational domain a uniform pressure was set (boundary condition pressure-outlet). The heat flux Q = 4,800 W/m^2 was applied to the upper and lower walls of the computational

domain. The side (inner and outer) walls of the computational domain were set as adiabatic walls as previously done.

6.1 **Grid Generation**

In order to resolve the flow features accurately, a very fine mesh has been employed near the wall. In order to keep the y^+ parameter ≤ 1.0 all along the wall, a very fine mesh has been generated for this study. The mesh is generated using ANSYS ICEM 14.5 based on the structured approach to generate hexahedral grids. The mesh distribution is shown in Figure 100 for various geometries. The computational meshes consist of 71 nodes across the width and height of the channel. The bend was resolved with 51 nodes on the computational mesh. Each rib used with 14 nodes across its width and height. The maximum aspect ratio for all the meshes is kept below 1.15. The height of the first cells at the walls is 0.01mm for all the meshes. This allows obtaining a y+ ≤ 1.0 over the whole wall surface and nearly 12 elements have been kept in the viscous sub-layer to resolve the boundary layer flow physics.

6.2 **Solution Approach**

All the simulations in this study are carried out using commercial tool ANSYS Fluent 14. The Navier-Stokes equations are solved in 3D case using the finite volume method for incompressible flow. The Fractional Step non iterative method [3] is used for the pressure and velocity coupling in the transient RANS (uRANS) analyses. In order to capture the transient phenomena produced form the non-uniform cross section turning angle. A Second Order scheme was adopted for time approximation. The inviscid fluids in the momentum equations are approximated with the use of the second order upwind scheme, the “PRESTO” interpolation is utilized for pressure and the flow gradients were approximated with use of the cell based Green-Gauss theorem.

For proper modeling of the heat transfer, it is important to accurately describe secondary flows, the transferring hot fluid from the walls to the core of the flow and vice versa. In this case one of the reasons of the secondary flows origin is the transient flow separations which originate around the bend. An attempt of modeling the flow in a steady setting may not be sufficient to predict the intensity of the secondary flows. This is exactly the motivation for conducting accurate transient calculations with further time averaging of the flow.

All the simulations were performed with the use of the SST turbulence model. For each case both steady and transient simulations have been performed. The first ten figures present a qualitative description of the transient flow for each of the geometries.

First there is comparison of the flow in the first variant of the channel for four different Reynolds numbers Re = 5000, 10,000, 25,000, 40,000. In the heat transfer section there is comparison for all the geometries of the distributions of Nusselt number at lower wall of the channel, and also the analysis of the area-averaged Nusselt numbers was carried out. Also there is the comparison of Nusselt number distribution for the transient and steady set up results. It is worth noting that steady set up does not allow obtaining a convergence of solution. It means that depending on the number of conducted iterations the flow in the channel is keep changing together with the Nusselt number distribution and its average values.

The Nusselt number was calculated on the basis of the inlet temperature of the flow in the following way:

$Nu = QD/ (\lambda (T_{scale} – T_{wall}))$

Hydraulic diameter = D in m

Wall heat flux Q = 4800W/m^2

Scale temperature Tscale = 300 K

Thermal conductivity λ = 0.0242 W/m/k.

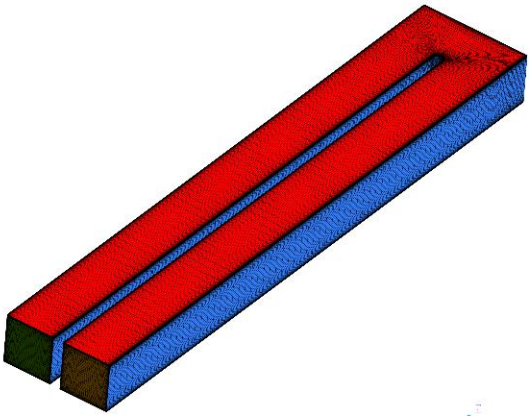

Case 1

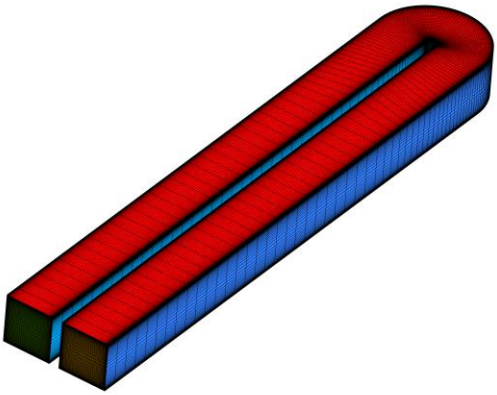

Case 2

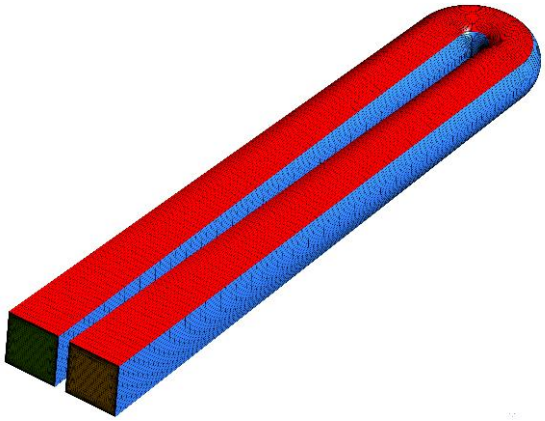

Case 3

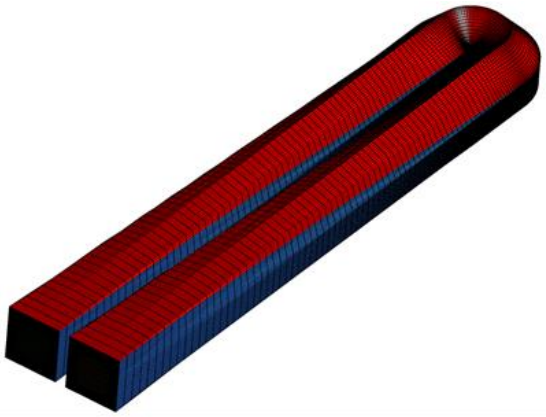

Case 4

Case 5

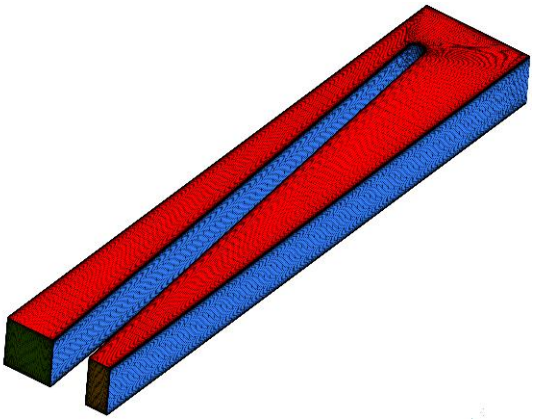

Case 6

Figure 92 six different configuration of geometry

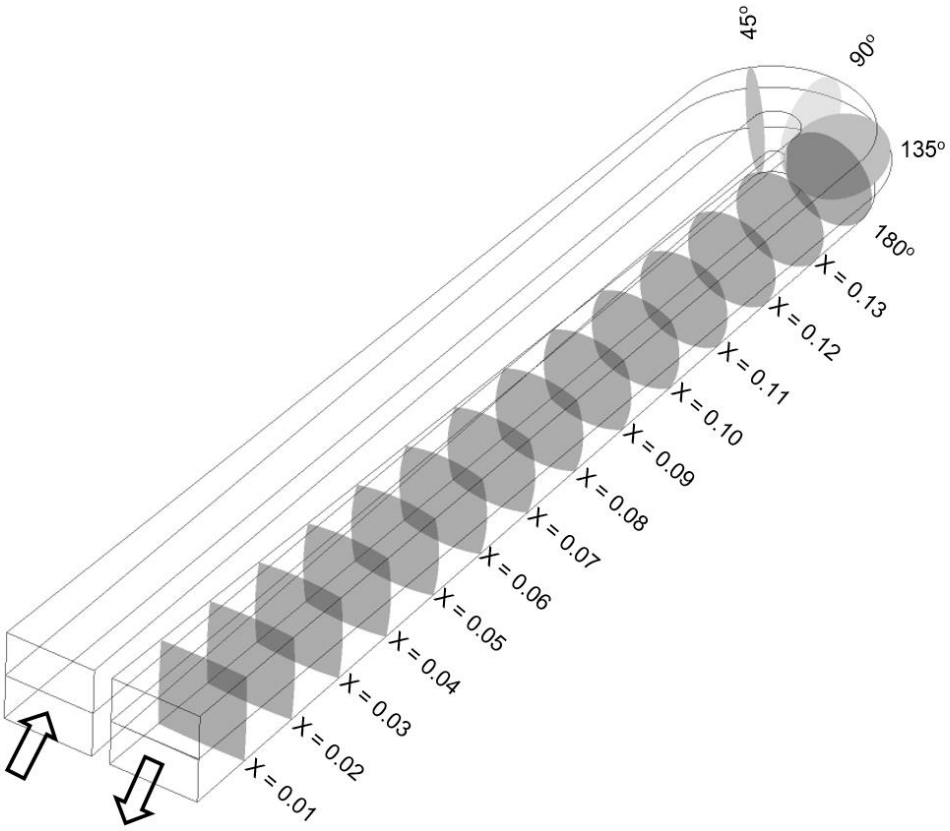

Figure 93 planes locations

6.3 **Results and discussion**

The results of these simulations to enable relating the effect of duct shape on the flow and heat transfer are presented in this section.

Figure 94 presents contours of normalised velocity for all the configurations where the reference value is the inlet velocity. In all the cases the flow separates at the inner bend wall due to the adverse pressure gradient brought about by the sharp turning. Downstream of the bend, there is formation of a large recirculation zone. As the Reynolds

number increase the pattern of the recirculation zone and reattachment location does change. For Case 4 to Case 6, the recirculation zone after the bend is gets elongated towards the outlet. From the contour plot, Case 6 has a massive flow separation among other case. Within the considered Reynolds number range, down stream flow behaviour is not impacting too much for particular case.

Figure 95, shows the velocity contour at different cross-section taken from end of the U bend to Outlet for Re 5000. For case 1, two counter rotating vortex is seen immediately after the bend and as it moves towards the end it mix out evenly. From Case 2 to Case 5, high acceleration flow is mixed with adjacent recirculation flow by turbulence. Case 5 has still high velocity gradients at the outlet due to reduction in flow area. Flow separation, re-circulation and re-attachment flow phenomena in all the Reynolds number range calls for unsteady analysis.

Figure 96 shows the vorticity contour both 5000 and 25000 Reynold number. The vorticity increase with speed and case four and five gain the most vorticity with speed compared with the other cases. Furthermore, significate increase in vorticity downstream of the bend for both cases due to the change in cross-section. Change in the cross-section helped to increases the vorticity at the end of the second passage. Also shown with higher speed for case 4 and 5 the vorticity increase significantly while the other case increases gradually.

Vorticity is a measure of rotation of fluid flow along the path. It enhances mixing of fluid and hence heat transfer. Vorticity distribution is shown at mid plane along the flow of various duct. Among all the configuration, Case 4 and Case 5 has maximum area of high vorticity flow. It increases with Reynolds number as turbulence increases.

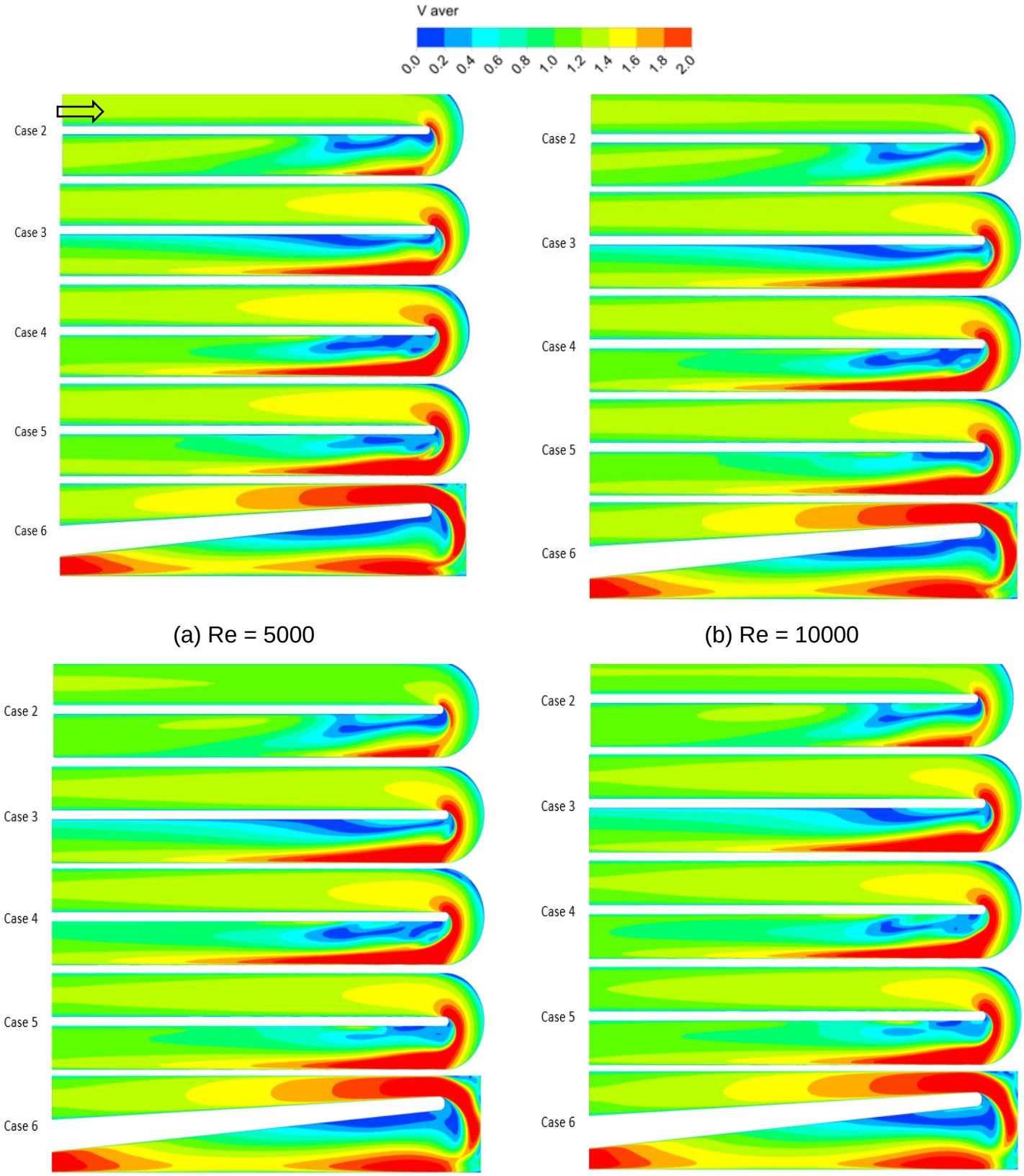

(a) Re = 5000

(b) Re = 10000

(c) Re = 25000

(d) Re = 40000

Figure 94 Velocity contour normalised at the inlet

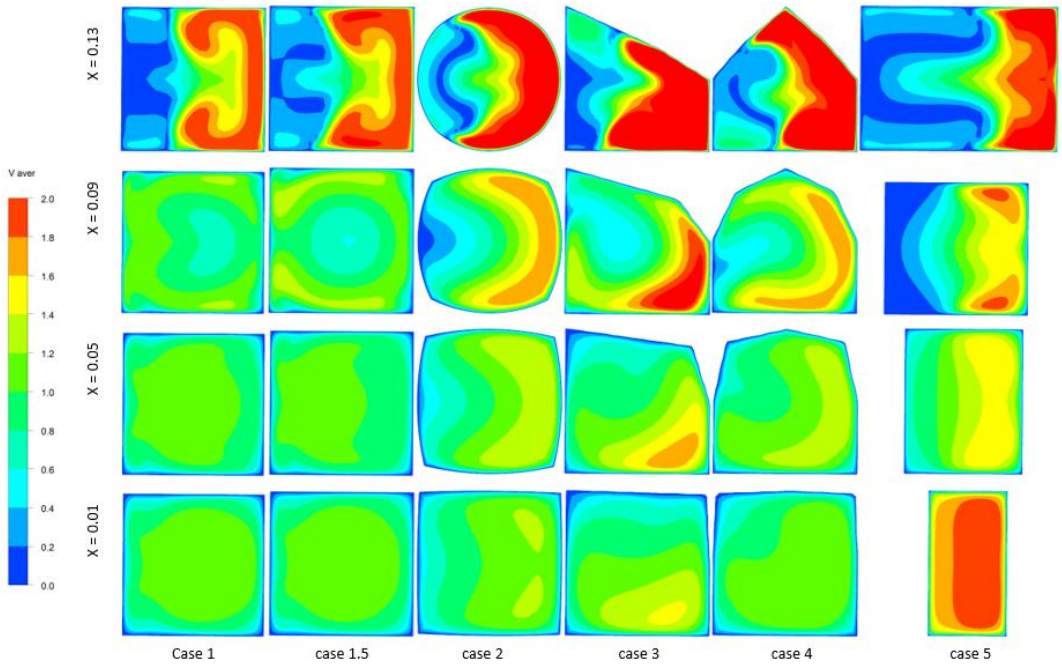

Figure 95 cross-section Velocity contour for Reynolds number 5000

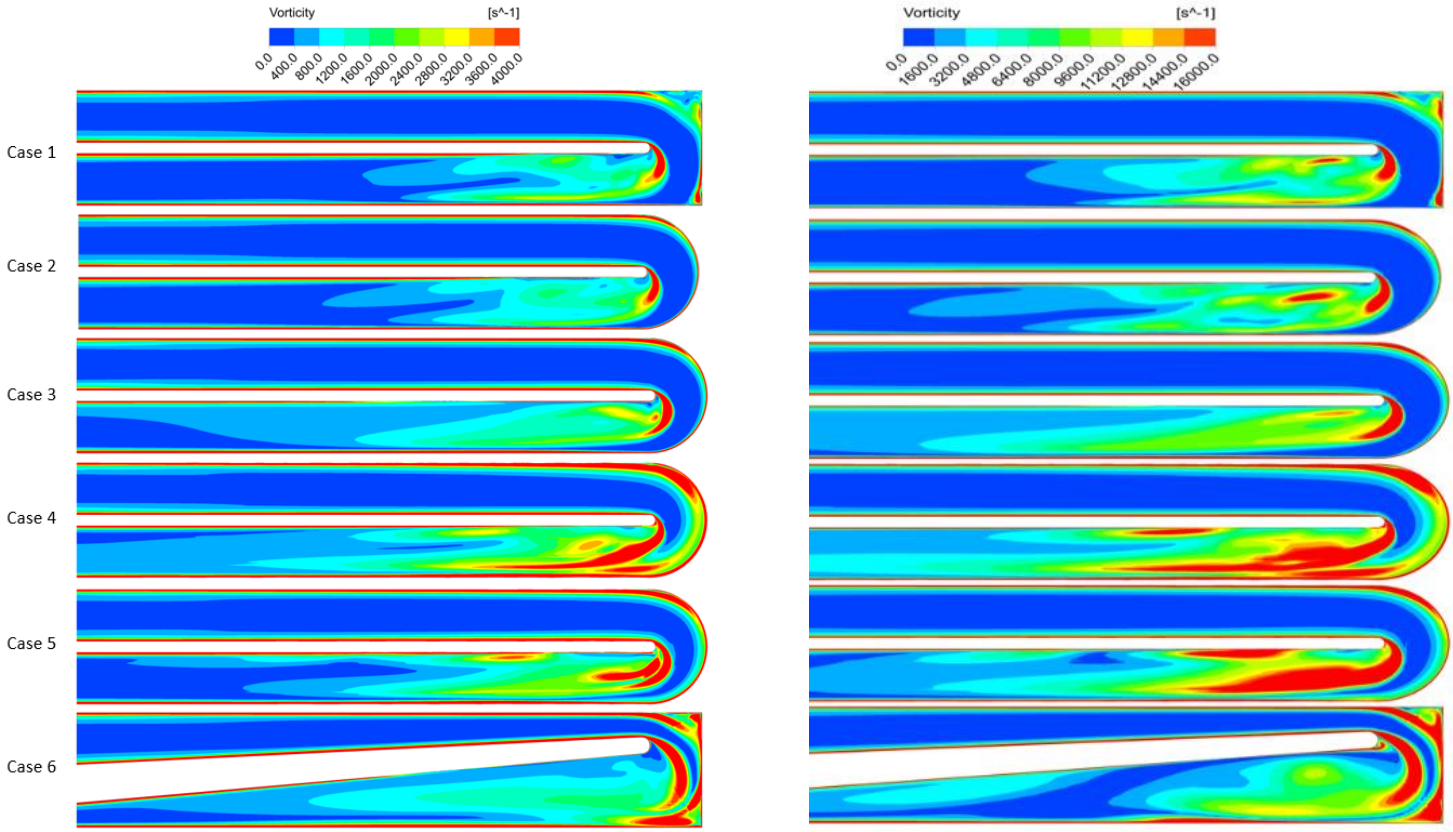

(a) Re = 5000 (b) Re = 25000

Figure 96 vorticity contour for both speed 5000 and 25000 Reynolds number

6.3.1 Secondary flow analysis:

Figure 97 presents the cross-section of the velocity stream line for all the cases at the bend. Four different angular location chosen at bend and they are at 45^o, 90^o, 135^o and 180^o. In Case 1, two symmetry curling of streamlines on inner side of the wall along with smaller, again symmetry curling of streamline on outer side of the wall has been observed in 45^o plane. As it moves towards 90^o two curling streamlines started combining and becoming one on each side and symmetry pattern is observed. Further moving towards 135^o due to centrifugal force, two streamline pattern is elongated and two more small size curling pattern inside the bigger one is observed. In addition, mid of the inside wall also having two small circular stream lines. Towards the end of the bend mid side circular stream line is moving towards centre of the passage and elongated streamlines contracted in size and flow is getting accelerated. This phenomenon is causing flow separation.

Case 2 and Case 3 is exhibiting similar phenomena and stream line pattern is slightly changing. In Case 4 and Case 5 though fluid phenomena is same but there is no symmetry in streamline pattern due to change in cross sectional area. In Case 6 flow is getting accelerated from 45^0 and this zone is on the inner side of the wall. As it moves to 90^0 almost 90% of channel flow is getting accelerated and this zone moved towards outer wall. In 135^0 flow is getting decelerated and again stream line pattern becomes symmetry. This shows separation of flow and it is enhanced while moving towards the end of the bend. Symmetry of stream line pattern continuous to exists.

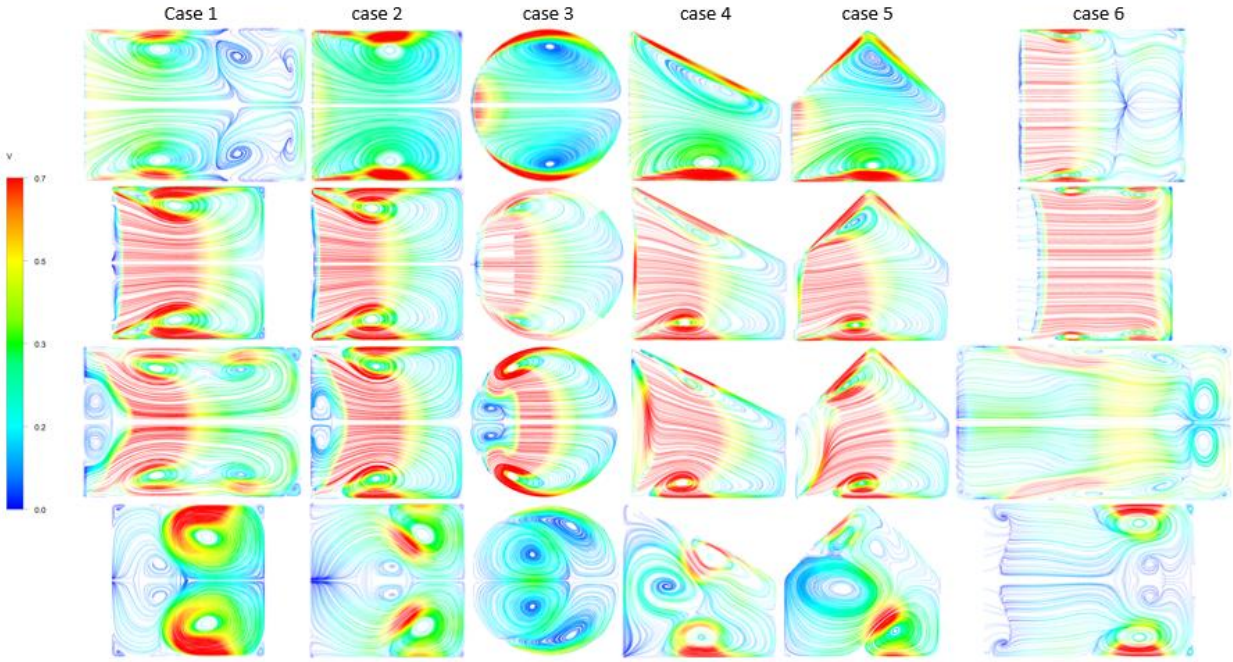

Figure 97 secondary flow cross-section at the bend

Flow pattern from bend end to outlet also has been analysed. Figure 98 presents the cross-section of the velocity stream line for all the cases from the bend to the outlet at interval of x=0.02 for two of the Reynolds number 5000, 25,000. For Case 1 and 2, two counter rotating vortex pattern is observed at the bend. This vortex pattern is keep changing and centre of the secondary flow structure is moving to passage centre. Two smaller corner vortex also developing on left hand side of the duct. Intensity of the vorticity is keep decreasing towards the outlet. For Case 3, two clockwise rotating vorticity and two anticlockwise rotating vorticity at the bend becomes bell shaped vorticity pattern as it moves. Vorticity centre is moved towards outside wall. As it moves further down, it became two symmetry and counter rotating vortex. Vortex intensity is decreasing towards the outlet. For Case 4 complex vorticity structure at the bend becomes further complex and transvers pattern of vortex disappeared. As it moves further down slowly vortex pattern picks up and one bigger clockwise rotating vortex and other two small vortex at the top. Size of vortex pattern is growing as it moves down and became one towards the outlet.

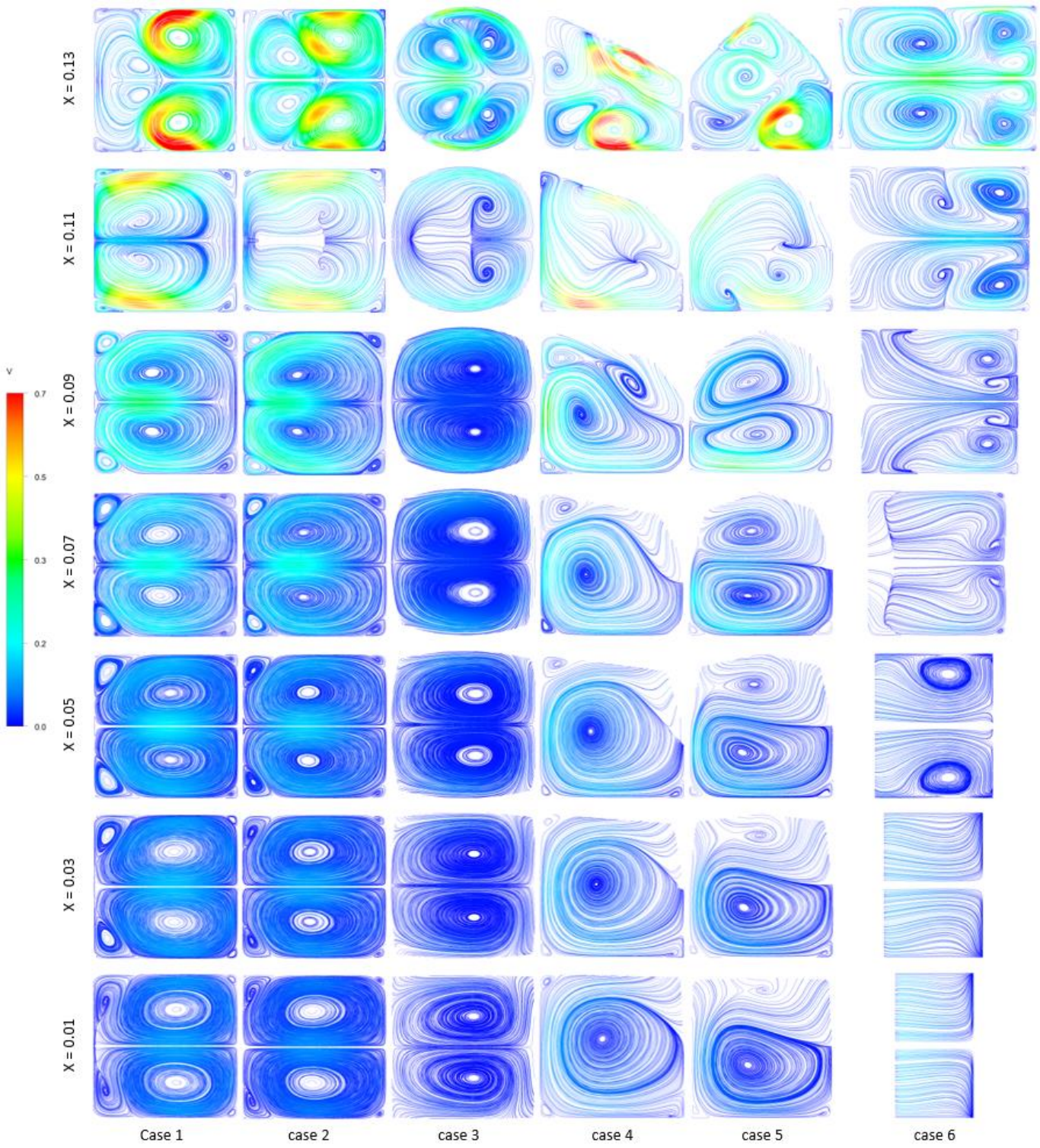

Figure 98 Streamline velocity contour at Re 5000

Case 5 complex vortex pattern at the bend becomes less in transverse direction. As it further move down transverse vorticity is picking up and two became two counter rotating vortex. Vortex at the bottom is stronger than at the top and further moving down the upper one losses its strength and bottom one becomes stronger.

For Case 6 three counter rotating vortex pair, two of which is centred towards outer wall and one pair is centred towards inner wall at the bend. As it moves down it becomes two pair and the one near the outer wall is bigger and other pair becomes smaller which is closer to it. As it moves downstream transverse vortex pattern is disappearing and forms the bell shaped flow pattern. Further down, symmetry and counter rotating vortex is formed upper and lower end of the duct. Vortex pattern is completely disappearing as it moves towards outlet.

For higher Reynolds number 25,000 flow pattern is similar for all 5 cases, strength of the vortex has been increased. For Case 6, slightly different flow pattern was observed. Two counter rotating vortex pair, which is centred towards outer wall at the bend. As it moves downstream transverse vortex pattern is disappearing and forms the bell shaped flow pattern. As it further moves down two equal and counter rotating vortex is picking up and its centre is moving towards outer wall. Size and strength of the vortex pattern is decreasing as it moves along and completely disappeared at the outlet due to reduction in flow area.

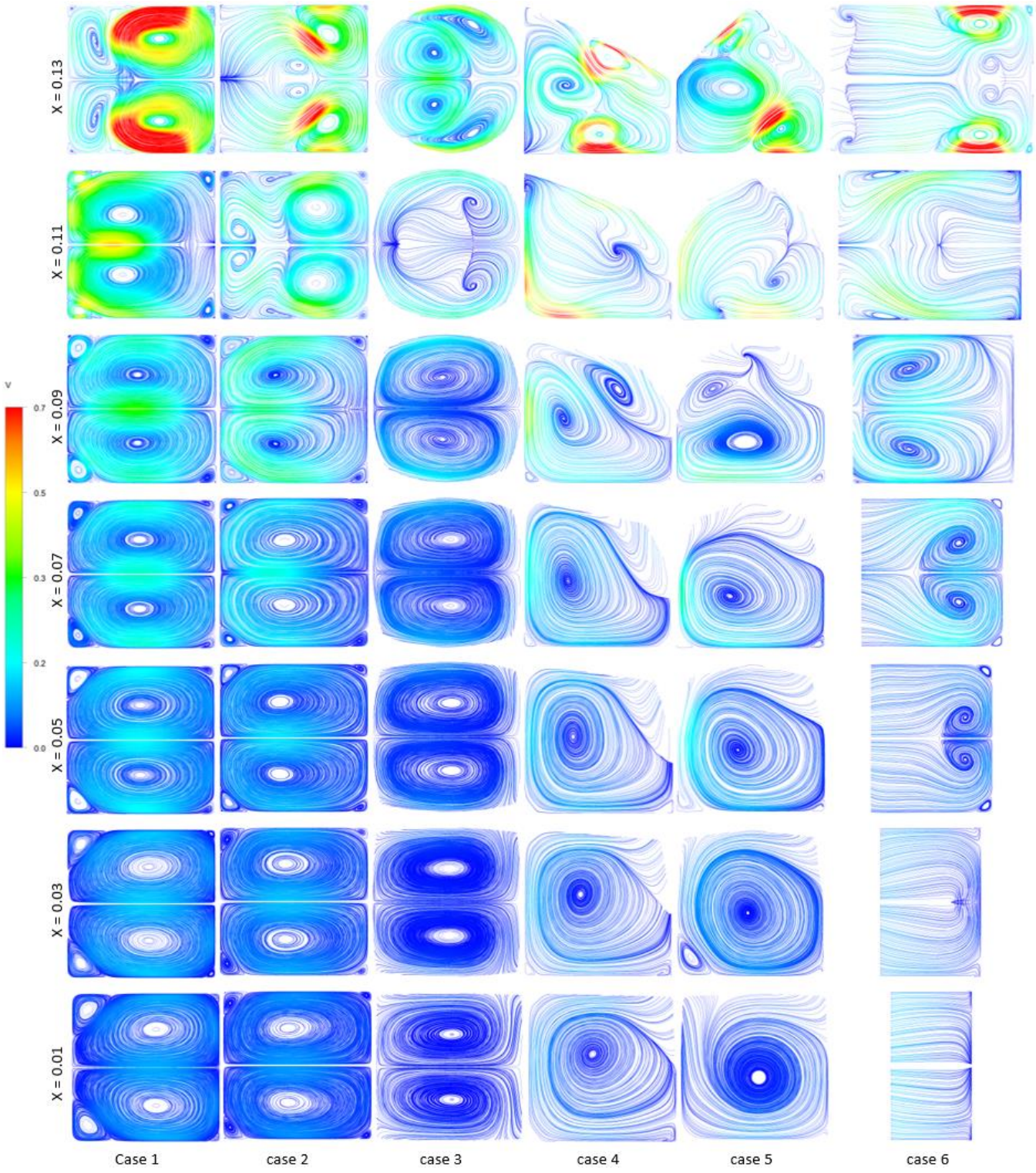

Figure 99 Streamline velocity contour at Re 25000

6.3.2 Heat transfer analysis

Heat transfer studies carried at this section for all cases. Figure 100 show the normalised Nusselt number contour for all cases. Heat is getting transferred to fluid based on the vortex pattern in the flow and the speed of the flow. At low speed case 1 and 6 shown high Nusselt number at the bend because of good mixing of fluid due to vortex pattern. As the speed i.e. Reynolds number increases, separation and recirculation zone becomes higher in case 6. This recirculation prevents transverse pattern of vortex which is main source to pick up the heat from top and bottom wall. So Nusselt number is decreasing with increase of speed for case 6. For other cases Nusselt number is increasing marginally with speed of the flow.

Interestingly for Case 5, shown significant increase in Nusselt number with speed. This is due to shape of the duct and vortex pattern. Immediately after the bend high speed transverse vortex picks up lot of heat from bottom wall and mixing well with adjacent fluid due to higher turbulent kinetic energy makes the Nusselt number high. It gradually decreasing towards the Outlet due to lack of mixing and turbulent kinetic energy also decreasing.

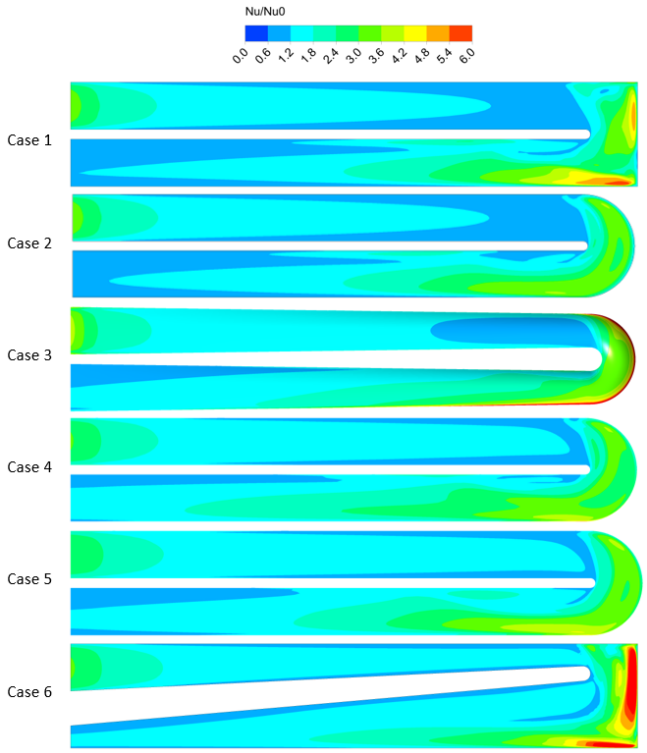

(d) Re = 5000

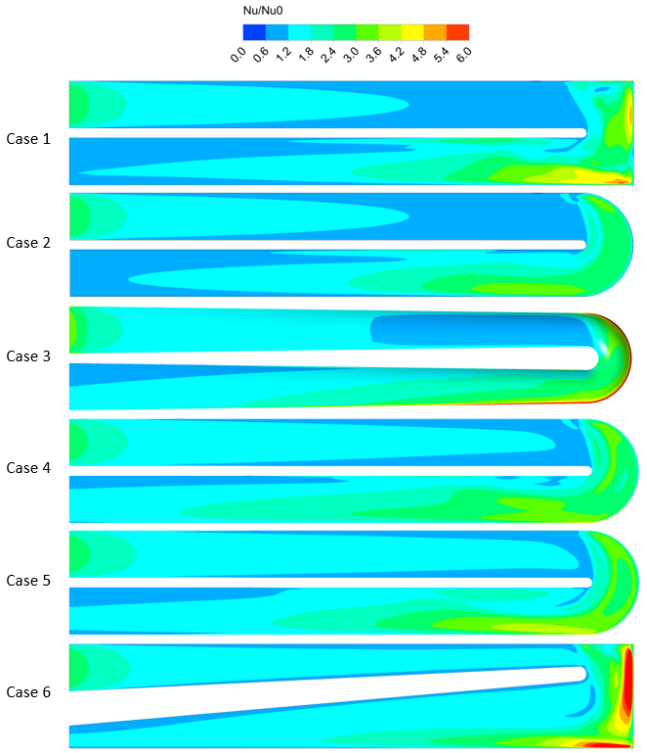

(d) Re = 10000

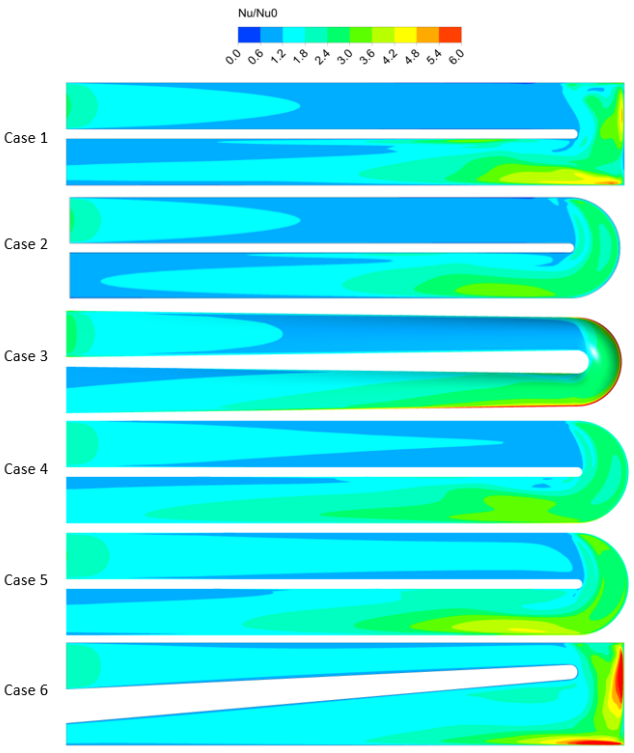

(d) Re = 25000

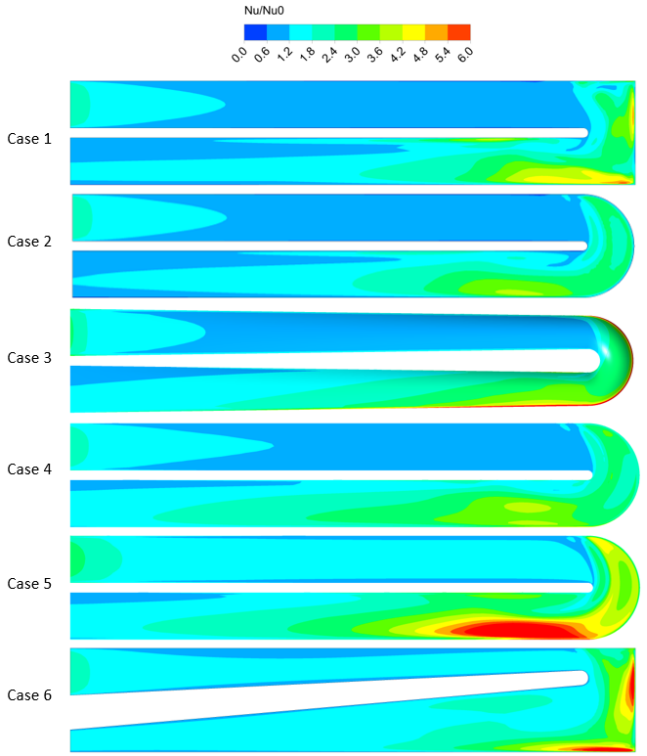

(d) Re = 40000

Figure 100 normalised Nusselt number contour for all cases

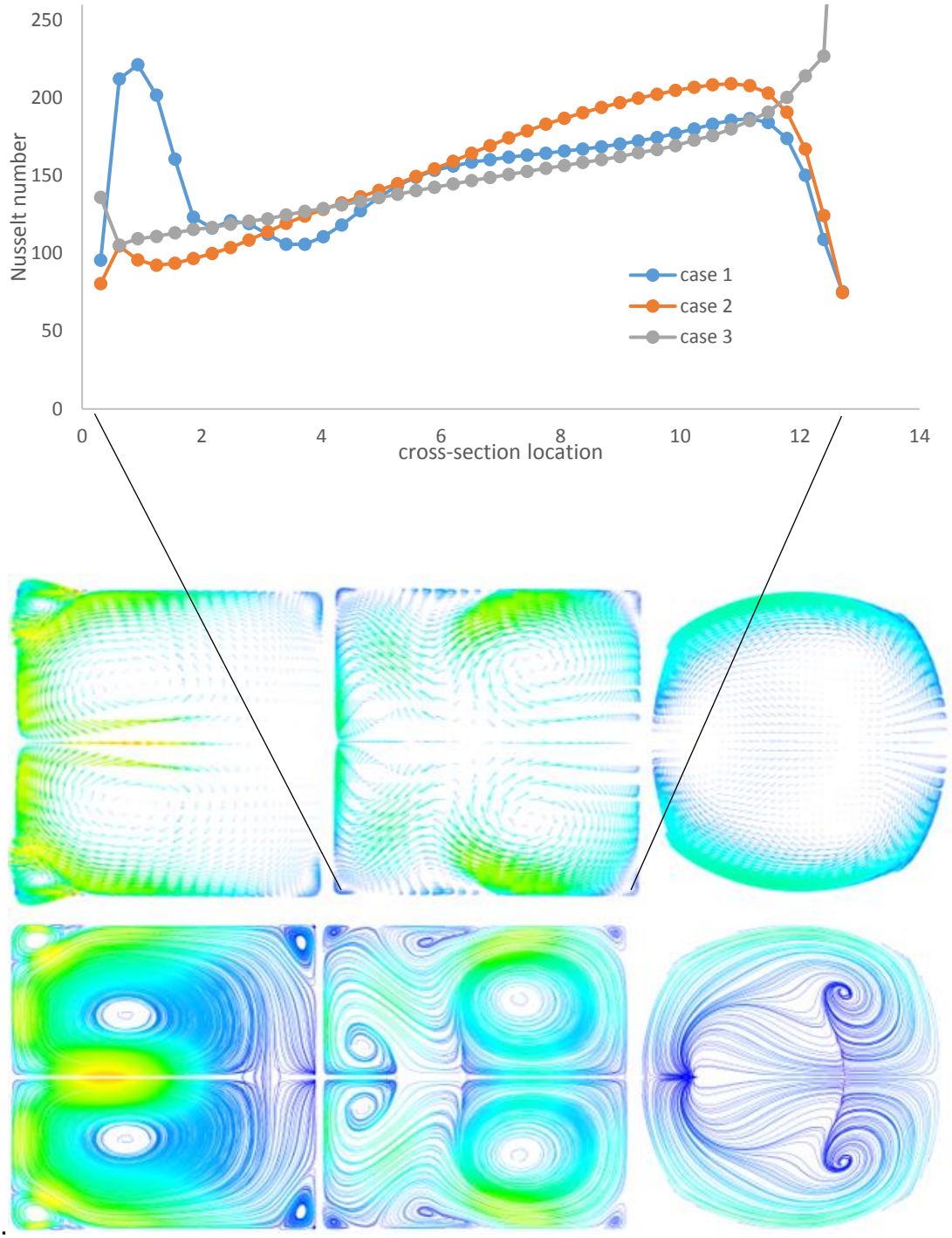

Figure 101 a) Nusselt number along the cross-section b) velocity stream line and vector cross-section

Figure 109 show the Nusselt number along the cross-section and the Velocity stream line and vector for Case 1,2 and 3 at X=0.11 just after the bend. The result shows that the Nusselt number is partially depends on the secondary flow direction and Reynolds number. From the figure 109 local peak in Nusselt value at location 0 to 2 for case 1 is due to the small corner vortex at the left. This jump is a result of high speed of the vortex and the direction of the flow where the high speed impinges on the wall and effective transfer of heat. Then it starts to gradually increase along the wall until it reaches location 11, where the big vortex direction of rotation impinge on the wall. Then Nusselt number is decreasing due to poor heat transfer. Heat transfer effectiveness is reduced due to vortex pattern, its speed of rotation and the orientation of rotation.

For Case 2, it doesn't have any local peak because of vortex pattern. Nusselt number is gradually increasing until location 11. Then it is decreasing and same flow phenomena is repeating same as Case1 from bend to Outlet.

On the other hand, Case 3 has only one big vortices on the wall and this show how the direction of the secondary flow affects the Nusselt number. Nusselt number gradually increasing from location 1 to 12. From the streamline figure and velocity vector figure it shows that the direction of the vortices starts to impinge at the wall at location 12 and the flow start to turn away from the wall at location 1 where the minimum heat transfer occurs.

Local peak nussulet number is going upto 220 for Case 1 and 185 before the location 12. For Case 2 and 3 there is no local peak and maximum Nusselt number is 203 and 226 respectively. Average Nusselt number in all the three case is around 145.

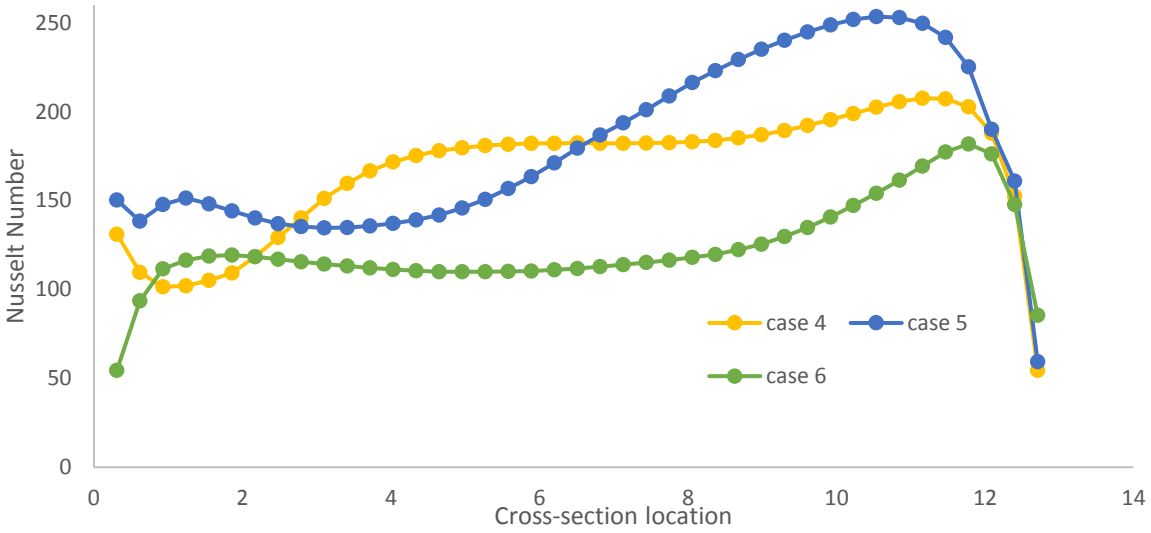

a)

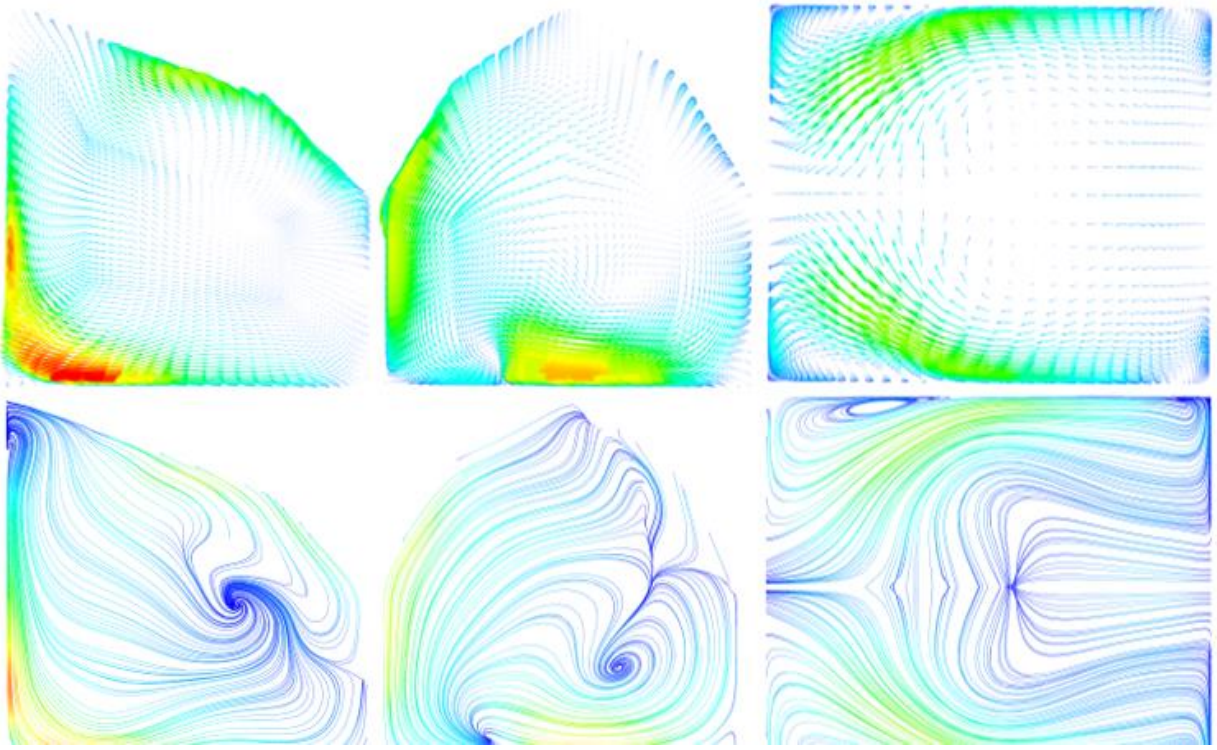

Case 4 case 5 case 6

b)

Figure 102 Nusselt number along the cross-section b) velocity stream line and vector cross-section.

Figure 102 show the Nusselt number along the cross-section and the Velocity stream line and vector for Case 4 ,5 and 6 at X=0.11 just after the bend. Case 4, 5 and 6 are more sophisticated than the other cases due to the major change in the cross-section in terms of area and shape. Similar to the pervious cases, the result shows that the Nusselt number is partially depends on the secondary flow direction and speed. From Figure 102a Case 4 has one big vortex on the lower wall and one tiny in the middle. Also noticed that the vortices become wavy near the wall which makes the wavy Nusselt number profile for Case 4 between location 4 and 12. Furthermore, there is a drop between location 1 and 4 and this due to the flow direction turning away from the wall this is shown in Figure 102b, where the flow vector starts to turn away from the wall.

Case 5 present new occurrences where the flow start to rotate on the opposite direction and this had negative impact on heat transfer and this is shown at location 4 where the two vortices interact. High Nusselt number at the far left where the flow start to impinge at the wall. Small bounce in Nusselt number at the far left due to the small vortex present there.

Case 6 Nusselt number has a maximum at location 12 and decreases at mid location then start to increase till the end. This also due to the same principle of the previous cases where there is two secondary flow one impinging in the far left and one impinging in the far right.

Secondary flow effect downstream of the bend is discussed earlier, Figure 103 presents the secondary flow effect at the end of the channel just before the outlet to understand how the strength and structure of the secondary flow changed after traveling along the channel and its effect on heat transfer. Case 1 has three vortices at the wall at three different sizes bigger, medium and small. The big vortex is in the middle and its direction from right to left and as a result the maximum heat transfer occur at location 10 which is the first interaction between the big vortex with the

wall then its decrease until it reaches location 4 then start to increase due to the mid-size vortex at the far left.

Case 2 has similar behaviour as Case 1 and the reason for that is the same cross-section along the duct and has only one difference which is the smooth turn. So both has three vortices at the same location but they are different in size, Case 2 has one big and two small vortices. Also the Nusselt number profile is relatively close to Case 1 compared to the other cases. Nusselt number remain high further then Case 1 and then drop below Case 1 and bounce back due to the small vortex at the end.

On the other hand, Case 3 is totally different due to the smooth circler bend which force the flow to one big vortex on the wall. In result will have different Nusselt number profile as shown in the figure. The heat transfer is maximum on the far right due to the beginning of the vortex and the location of the flow impingement on the wall then its decreases to the end.

Figure 104 present the secondary flow effect at the end of the channel just before the outlet for case four, five and six. Case four and five has similar Nusselt number profile behaviour because of the one big vortex and one very small vortex near the wall both start from the right with maximum value at location 11 for case four and location 10 for case five, afterword's it decreases gradually till it reaches location 1. At the end there is a small increase in Nusselt number due to the small vortex at left corner.

Case 4 has maximum Nusselt number of 110, Case5 and 6 has 96 and 92 respectively. Average Nusselt for Case 4 is 98 and for other two cases is 92.

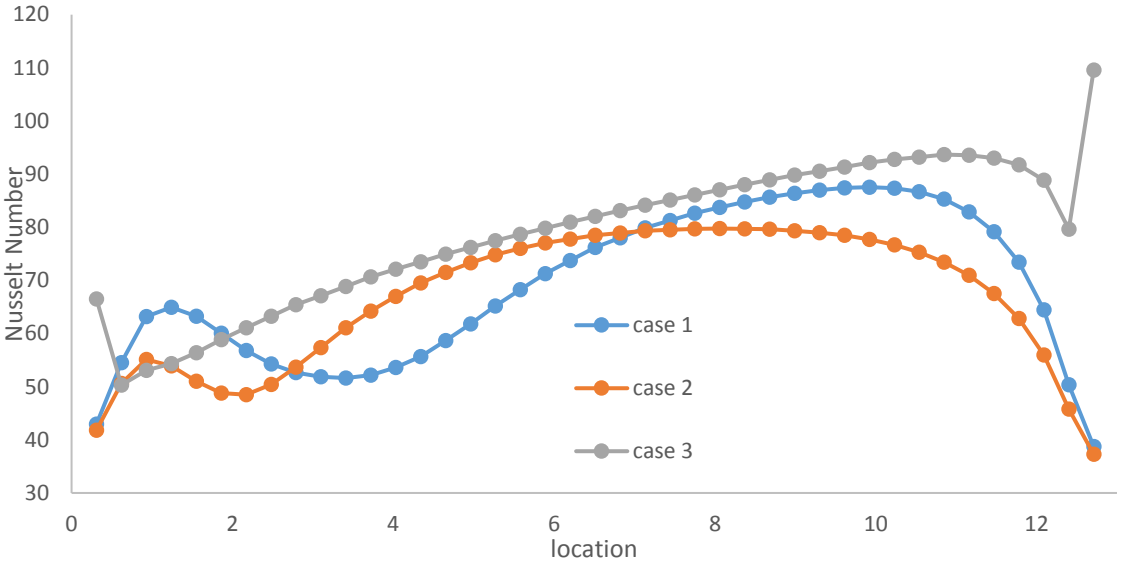

a)

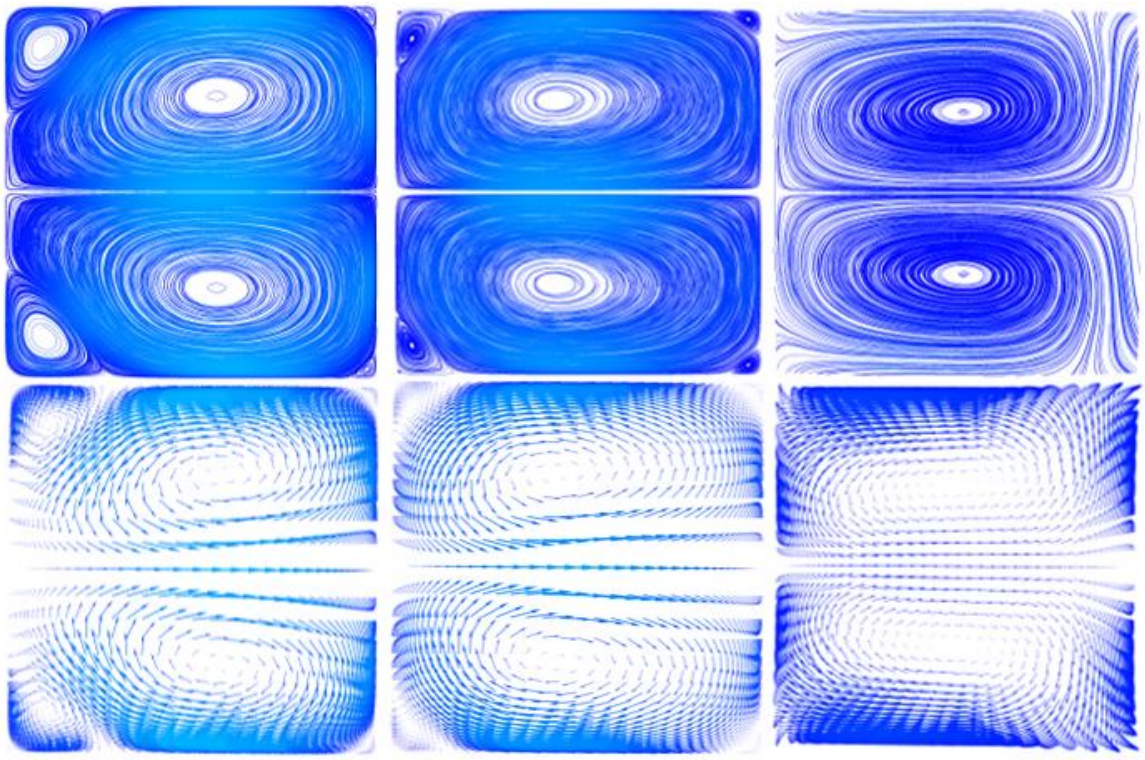

Case 1 case 2 case 3

b)

Figure 103 Nusselt number along the cross-section b) velocity stream line and vector cross-section.

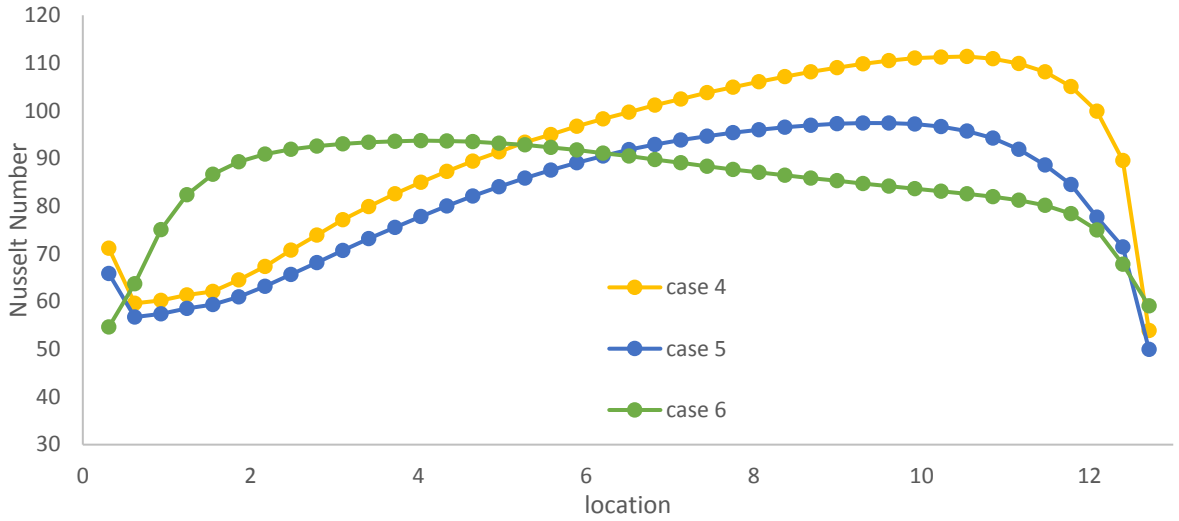

a)

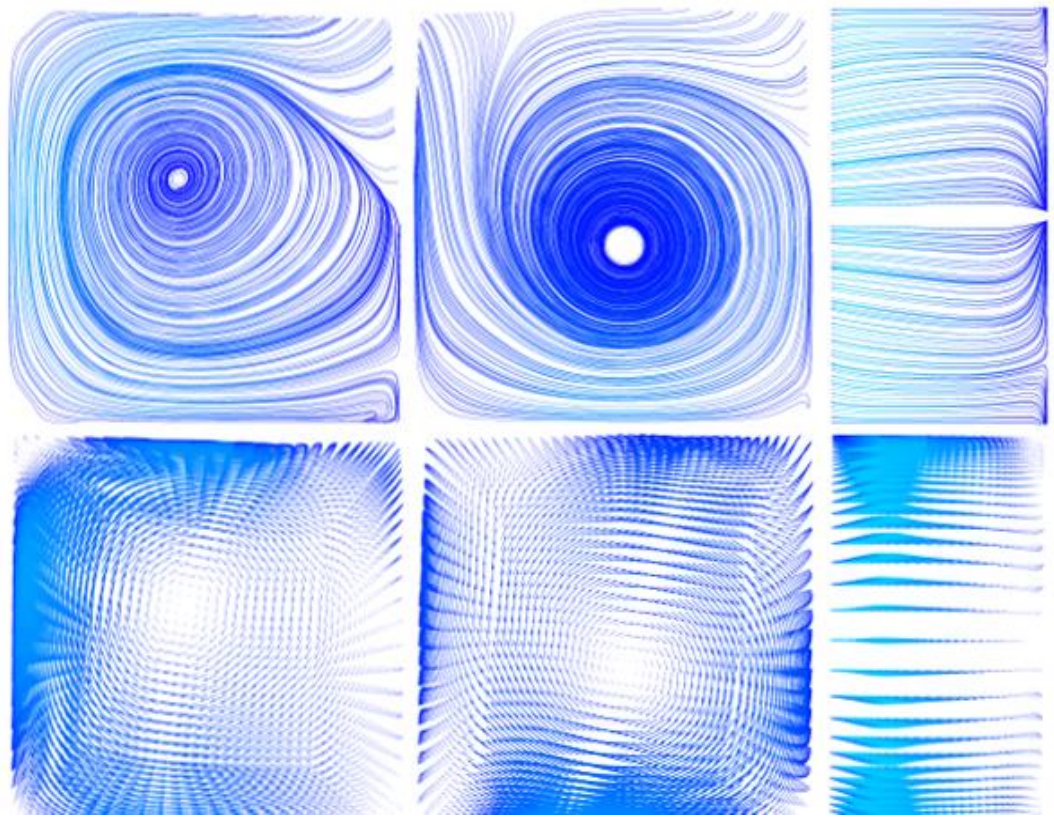

Case 4 case 5 case 6

b)

Figure 104 Nusselt number along the cross-section b) velocity stream line and vector cross-section.

The average overall heat transfer for all cases at four different speed is shown in Figure 105. At low speed all cases are close to each other and start to differ with the increase in speed. Case 2 shows the lowest heat transfer at all speed and maximum difference at Reynolds number 40,000. Case 1 and 3 are close to each other at low and high speed with slight increase for Case 3. Furthermore, Case 4, 5 and 6 show maximum heat transfer at high speed.

Figure 106 present the normalized Nusselt number for all cases at different speed. Same as seen earlier, Case 2 has the lowest heat transfer compared to the other cases. At low speed Case 6 has the highest heat transfer and Case 4 is just below it. Whereas at Reynolds number 25000 Case 5 increase and jump between Case 6 and 4. At high speed case five increases slightly over case six. Also noticed that the normalized Nusselt number decreases with speed except for Case 4 and 5.

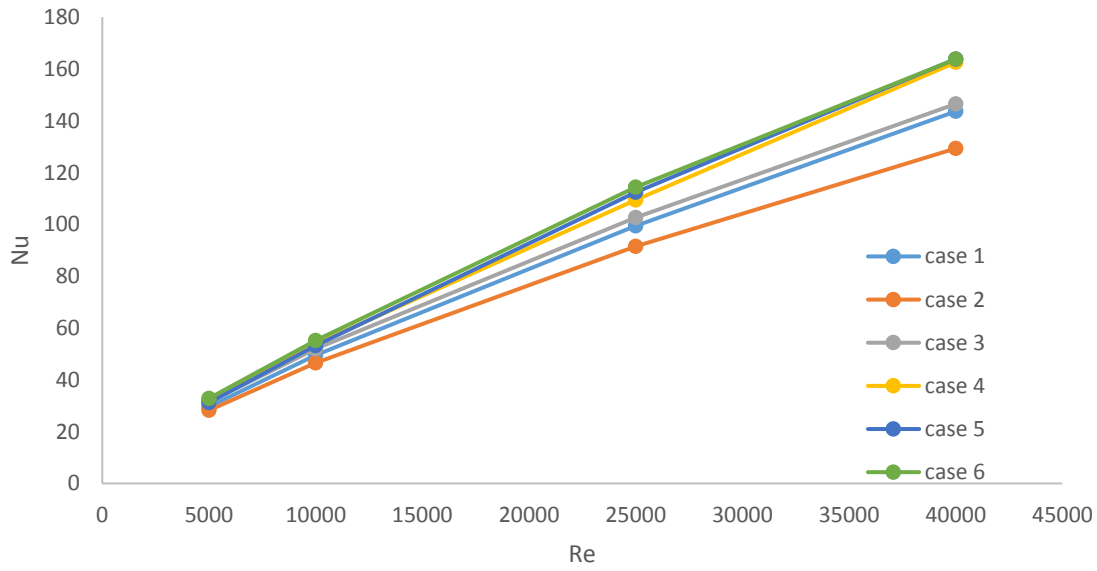

Figure 105 the average Nusselt number for all cases at different speed

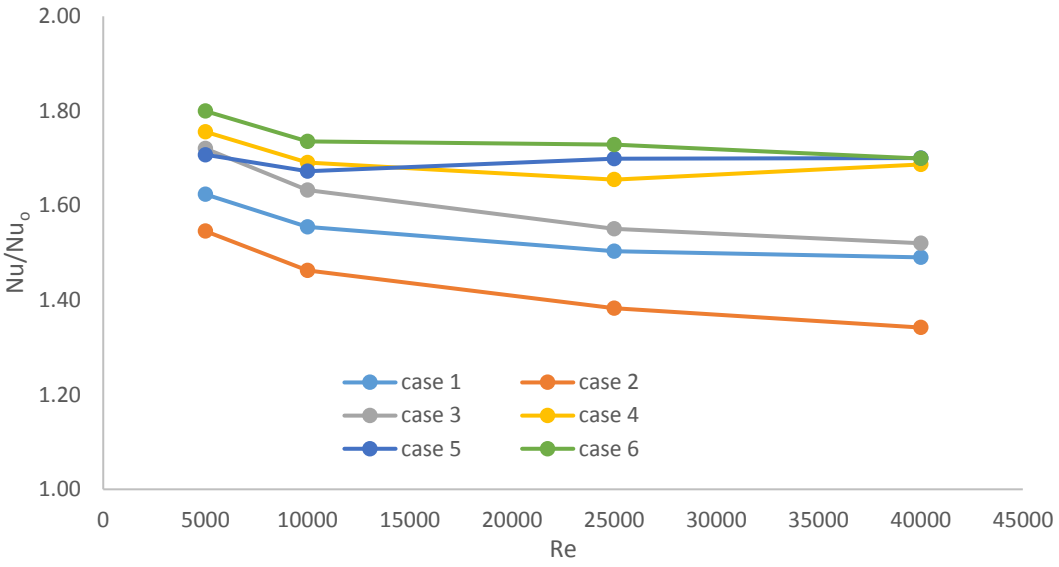

Figure 106 Normalized Nusselt number for all cases at different speed

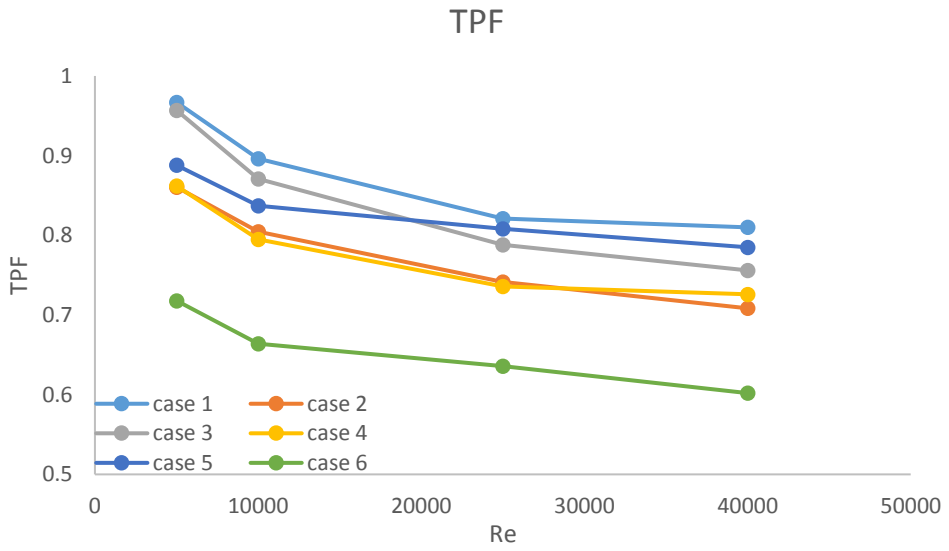

Figure 107 Thermal Performance Factor

Thermal performance factor is the normalized Nusselt number over the pressure drop. It has been applied to see the heat transfer effectiveness of the geometry compared to the pressure drop. Maximum thermal

performance factor occurs at low speed for all cases and decreases with increase of speed.

6.4 **Conclusion**

Several modified cooling passage shapes were proposed in this chapter. They permit to study the consequences on the secondary flow effects of the change of cross-section away from a uniform pattern as usually done. The intent of course is to improve the heat transfer while keeping total pressure losses at a minimum. The six geometries studied each has a different bend cross-section but all start and end with same cross-section which is a square cross-section.

Each case has a unique behaviour after its go through the modified cross-section. Some cases showed great potential for further modification and studies which will be carried out in the next chapter. Speed and cross-section has great factor in the structure of secondary flow. Case 4, 5 and 6 showed good promise at low and high speed. These cases can help in increase the heat transfer in specific area where maximum cooling is required.

7 Multi features heat enhancement technique

7.1 Introduction

In a blade cooling passage, repeated roughness elements in the form of regularly spaced ribs are commonly used to increase heat transfer rates. As a consequence of the desired increment in heat transfer rates, the pressure losses through the channel correspondingly increases. It is usually necessary to optimize the best combination of maximum heat transfer rate at the lowest possible pressure losses.

Based on the literature, a roughened square shaped duct was selected as a baseline in this research. Heat transfer analysis was conducted by applying ribs and combination of rib and slot patterns. Slots are a labyrinthinepassage start from the second passage to half way through the passage. Ribs height is less than 10% of the hydraulic diameter to avoid blockage ratio. Detailed result is presented in this section.

Five geometrical configurations of duct with different rib and slot arrangements were assembled, Figure 108. Case 1 corresponds to a square duct with uniform cross section and ribs; Case 2 is a proposed geometry from the previous chapter with ribs; in Case 3 slots are added to the proposed smooth geometry; the Case 4 geometry is the same as that of Case 3 with the addition of ribs in the first and second passages keeping the slot area smooth. Case 5 is similar to Case 4 with the addition of ribs in the bend and slot regions.

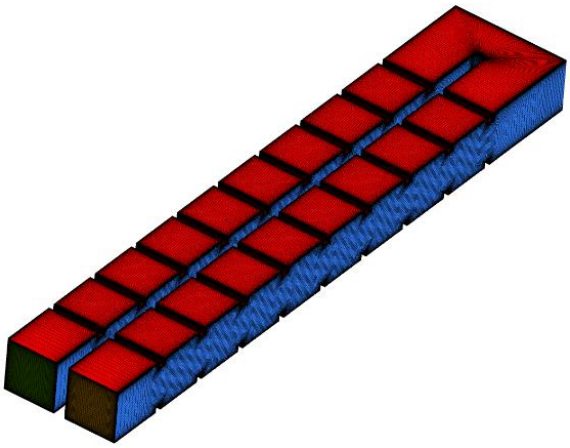

Case 1

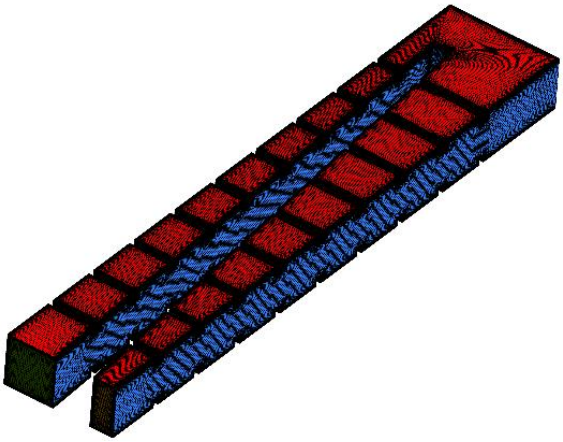

Case 2

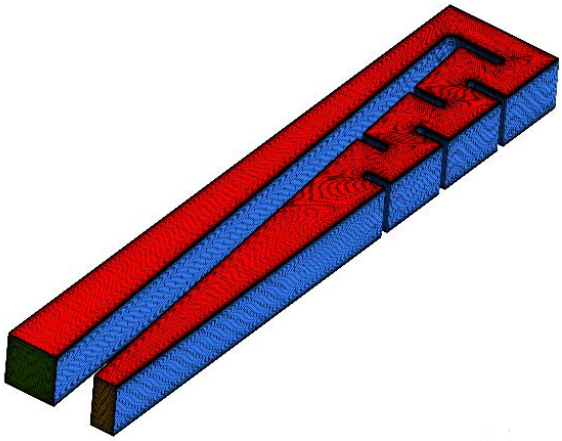

Case 3

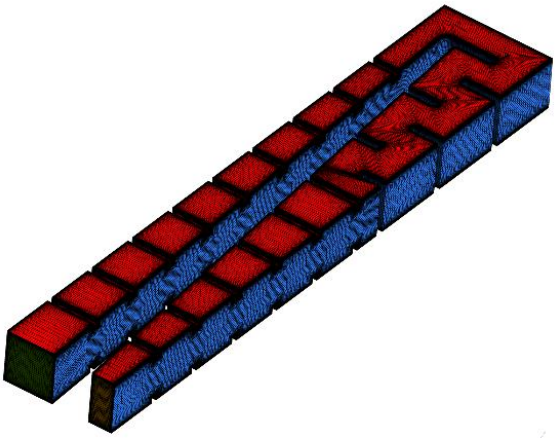

Case 4

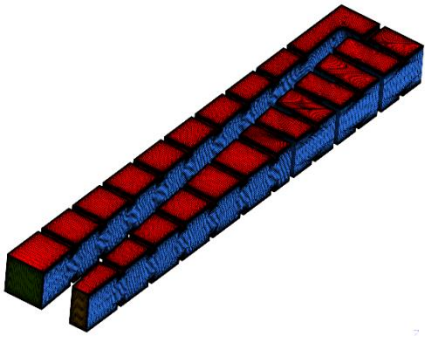

Case 5

Figure 108 Five different configuration of geometry

7.2 **Boundary condition**

In order to study the flow at high and low velocity four Reynold numbers were considered similar to those investigated in Chapter 6. (Re=5000, 10000, 25000 and 40000). The heat flux of 4800 W/m^2 was used. All the cases were analysed in stationary frame only. Geometry details are available in the appendix of this thesis.

Uniform velocity profile corresponding to Reynolds number Re = 25,000 (V_{inlet} = 28.76 m/s), turbulence intensity Tu = 1% and turbulent to laminar viscosity ratio TVR = 100 are defined at the inlet of the computational domain. For the first case calculations with Reynolds number Re = 5000, 10,000, 40,000 (Vinlet = 5.75m/s, 11/50m/s, 46.02m/s) were also made. At the outlet from the computational domain uniform pressure was set (boundary condition pressure-outlet). Heat flux Q = 4800 W/m^2 was brought to the upper and lower walls of the computational domain. Side (inner and outer) walls of the computational domain were adiabatic.

7.3 **Grid Generation**

Fine mesh has been employed near the walls and ribs to keep $y^+ \leq 1.0$ in order to resolve the flow physics. The mesh was generated using ANSYS ICEM 14.5 based on structured approach to generate hexahedral grid. Mesh distribution is shown in Figure 108 for the various geometries. Each rib was resolved with 14 nodes across the width and height of the duct. The maximum aspect ratio for all the meshes was kept at 1.15. The height of the first cells at the walls is 0.01mm for all the meshes. This allows obtaining y+ ≤ 1.0 at the whole wall surface and about 12 elements have been used to resolve the boundary layer.

7.4 **Solution Approach**

To investigate the temperature distributions and heat transfer augmentation in three-dimensional flow field, k-ω SST model was

selected. In the flow field there will be flow separation and re-attachment over the ribs which plays a major role in heat transfer and loss generation. Hence, this turbulence model was preferred given its known performance for obtaining accurate results in these types of flow. The solver settings and advection scheme used in this analysis are the same as that of Chapter 6.

7.5 Results and discussion

The motivation for placing the ribs in a channel is to increase the heat transfer rate from the channel walls to bulk fluid. The ribs act as turbulators to break-up the ordered near wall flow. This increases the turbulence level and enhances exchange of fluid in the near wall region with the core flow by action of turbulent diffusion. Nonetheless, the ribs placement is associated with increased the wall friction resulting in higher pressure loss.

Normalized velocity contours at the mid plane for all five cases, for four Reynold's numbers are shown in Figure 109. The differences, for each case, due to Reynolds numbers are on the whole minor, that is, varying the Reynolds number hardly alters the structure of the flow.

Regarding the different cases the first geometry, Case 1, is the datum configuration. The flow patterns shown in this figure are representative of the flow conditions at mid span and the full interpretation of the flow structures requires a three dimensional analysis. The datum configuration is characterised by a build up of mid span flow velocity and a rather striking ejection of the flow towards the wall once past the 180 degree bend. The flow becomes then non centred on the down stram passage. These observations are broadly valid for all the four Reynolds numbers investigated. In Case 2 the flow accelerates towards the narrowing and it is projected with a high momentum towards the end wall leading to a scraping of the wall section that is immediately placed downstream of the bend. For Case 3 the pattern is altogether different given the presence of

the slots which leads to a circuitous path in between these. In Case 3, the cross sectional area is intially decreasing towards the U bend resulting to a corresponding gradual flow acceleration towards the U bend. The first channel flow behaviour slightly changes with velocity; a similar observation is noted at the bend region. At the bend, there is slot which helps reducing the recirculation region after the bend. The slot creates wavy flow pattern which helps with fluid mixing at the same time re-circulation region around the slot. Massive separation is observed after the last slot which created large pressure losses.

For Case 4, the flow started accelerating much earlier when compared to that of Case 3 and this was due to the fact the ribs which are placed at the first passage forces the flow to start accelerating at the mid plane. The resulta shows that the flow developed pattern is changing with Reynolds number. At low Reynolds number, the flow turning jet is thin and the flow between the slot is thicker. As the Reynolds number increases, the turning jet becomes thicker and the flow between the slots reduces in size. The flow after the bend is slightly affected by the Reynolds number. The flow becomes re-attached after the last slot which assist in improving the heat transfer characteristics of flow.

Case 5 flow features is almost the same as that of Case 4 from the inlet channel untill the U bend section. The flow experienced high recirculation at the main bend region due to the placementof a rib at the bend. This recirculation feature is characterised with enhance heat transferand also has the ability to minimise the pressure loss locally. Further downstream flow is getting re-attached with bottom wall half way to the exit. From the results shown, the behaviour of the developed flow at the inlet channel is changing with the flow Reynolds number. The recirculation pattern and re-attachments point depicted to be having minimum effect with the flow Reynolds number.

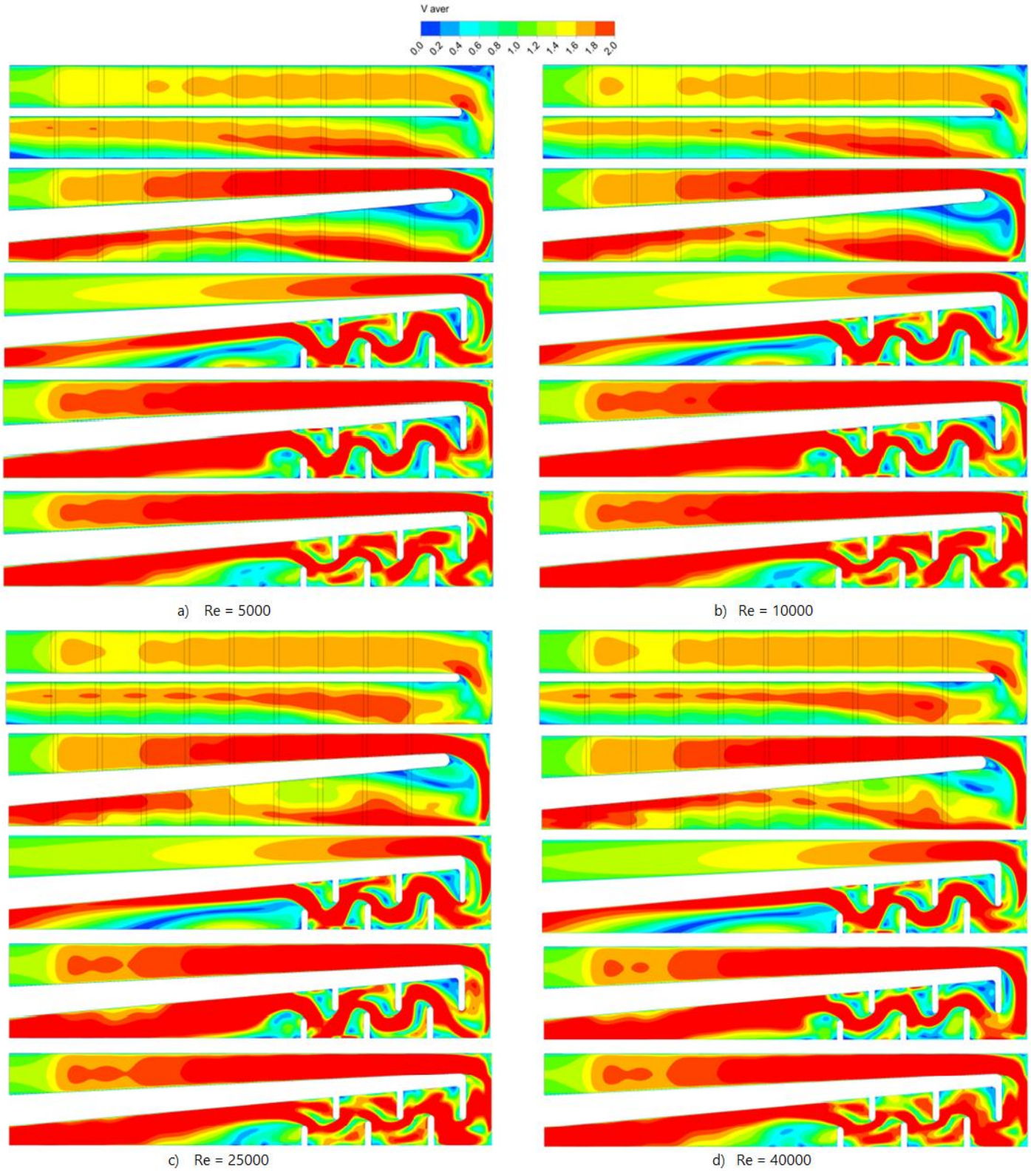

Figure 109 Velocity contour for all cases at different Reynolds number

Figure 110 shows the normlaized Nusselt number for all cases at different Reynold's numbers. Case 1 heat transfer pattern shows a gradual improvements with flow Reynolds number, especially in the turn region of high temperature zone which becomes thicker. Along the inlet and outlet channel, there is no abrubt changes with flow Reynolds number for case 1,while Case 2 performed better at high Reynolds number. The major diffrerences between cases 1 and 2 are shown at the first passage downstream of the ribs, the bend near the right and bottom wall and at the second passage upstream of the rib. Addition of slot shows better heat transfer effectiveness as simulated in case three. When compared to the other cases, the slots increased the heat transfer significantly with increasing flow Reynolds number. Slot area and second passage towards the outlet are the main areas affected by Reynolds number change. Case four shows exhibition of similar behaviour to that of case two and three combined due to the combination of roughened wall and additional slot. Case five has better fluid mixing characteristics due to inclusion of slot and rib combination. Hence, heat transfer is significantly increased with flow Reynolds number. Case 5 shows high heat transfer rate for low and high Reynolds number compared to the previous cases.

Cases with slots show great improvement in term of heat transfer as shown in the Figure 110. Case 5 demonstrate high heat transfer at the slots region compared to the other slots cases and this was due to the ribs placement between the slots and bend regions.

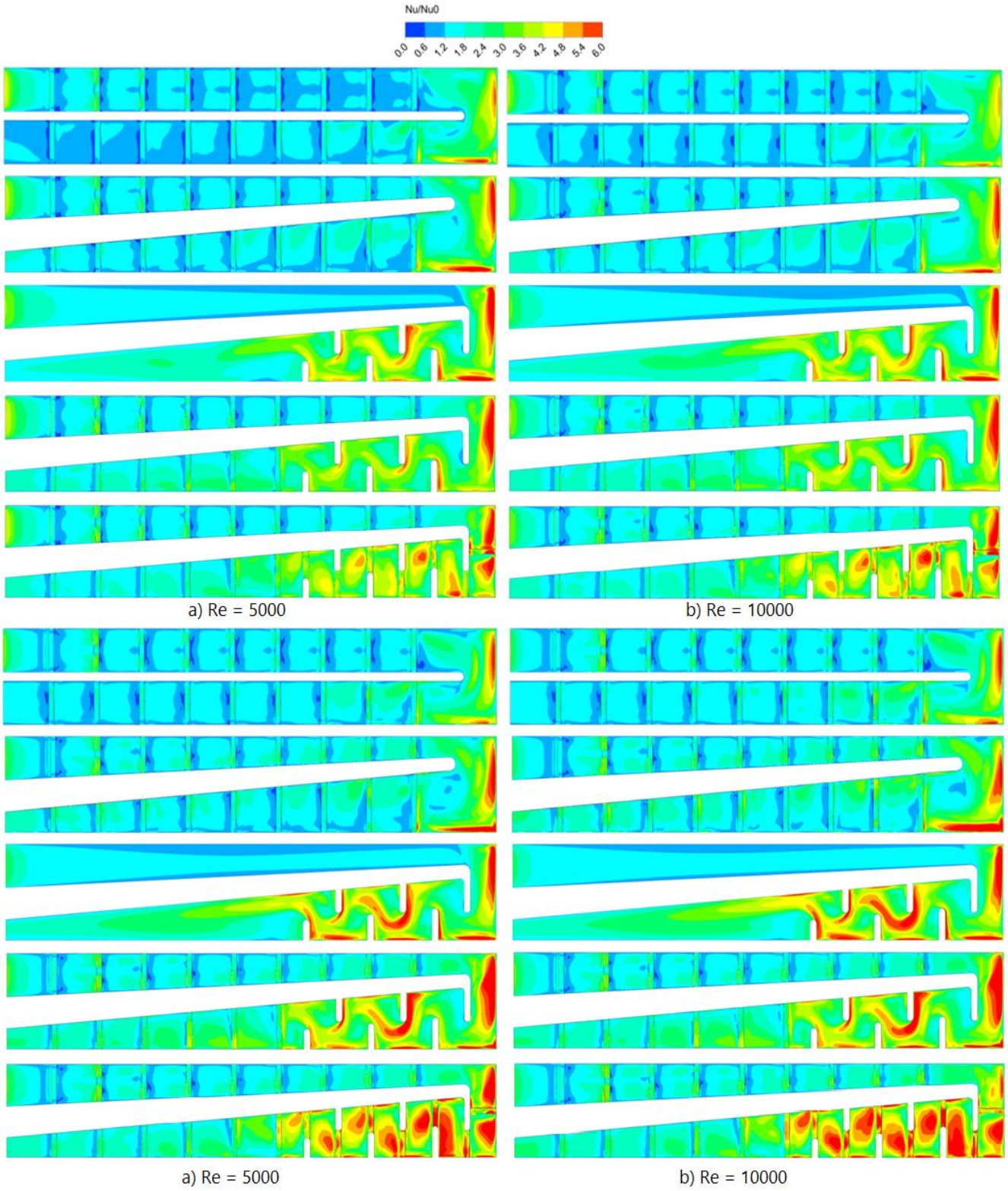

Figure 110 Normalized Nusselt number for all cases at different Reynolds number

Figure 111 shows temperature distributions over the bottom wall of the channel. In general, for low Reynolds numbers, the flow temperature has higher values than cases with high Reynolds numbers. Almost a uniform temperature distribution occurs for both cases one and two with constant temperature values in the case of Re=5,000 with no significant effect as the flow travels further. This uniformity does not exist for both cases three and four for all Reynolds numbers due to the geometry affect. For cases one and two, the temperature distribution starts to be effected at the bend but for the remaining cases this effect starts a bit earlier than the bend. This is due the existence of the opposite ribs in the second part which creates higher turbulence.

At low Reynolds number the bend region for case one and two show lower temperature in the range of 50^{c}s, cooled area expands to the slot area for case three, four and five, and case five shows the most cooled area in the slot region. Ribs has little effect on low Reynolds number for all cases at the first passage. In the other hand ribs on the slot region has great effect on heat removal. at Reynolds number 25000 the area near the bend and slot region is cooled to 35^{c}s. case three show more cooled area after the slots towards the outlet. and the highest cooled area occurred between the slots for case three compared to the other cases. This phenomenon is shown clearly at higher speed. The average temperature is lowered by 20^{c} by adding slots and ribs at high Reynolds number.

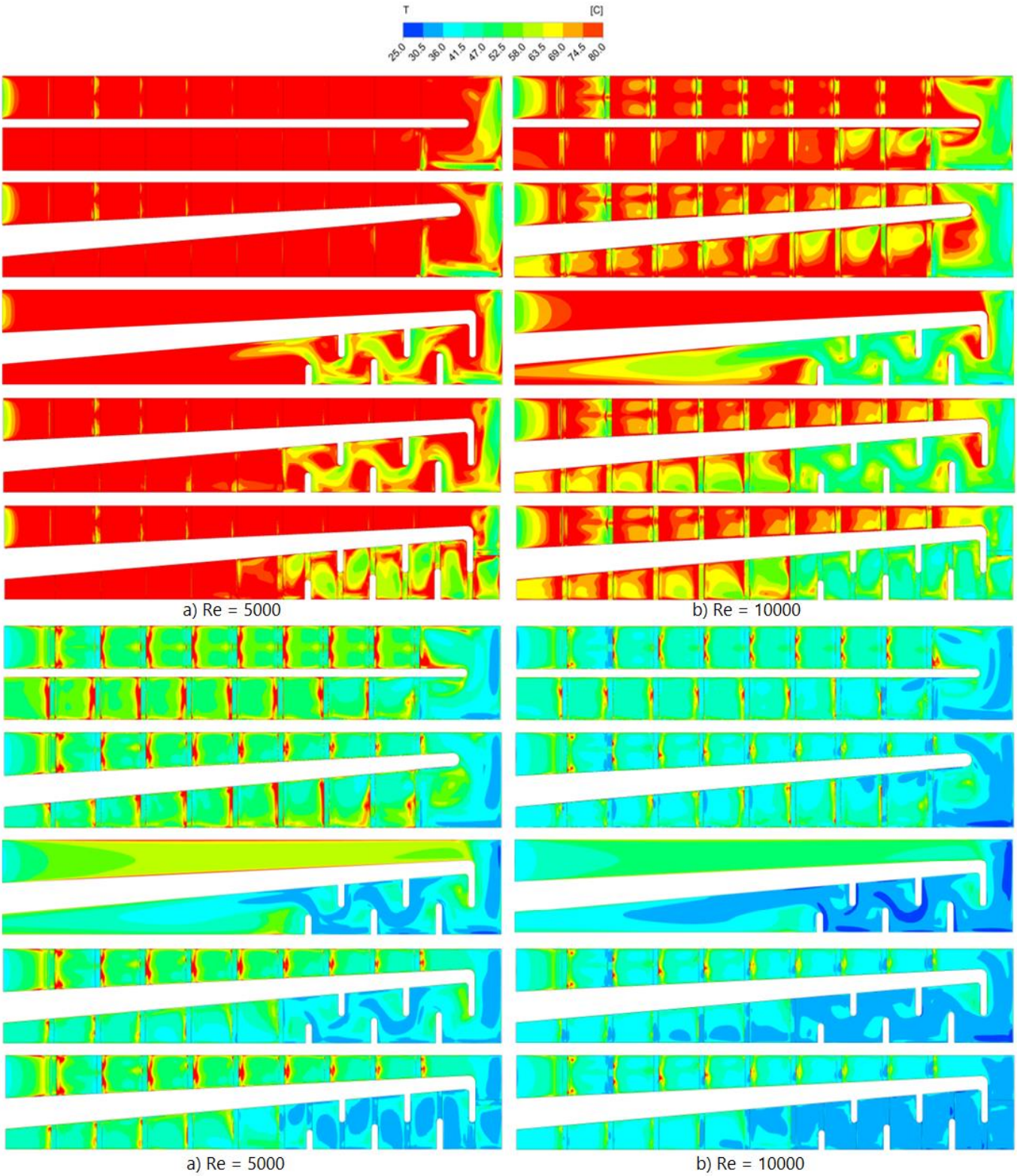

Figure 111 temperature contour for all cases at different Reynolds number

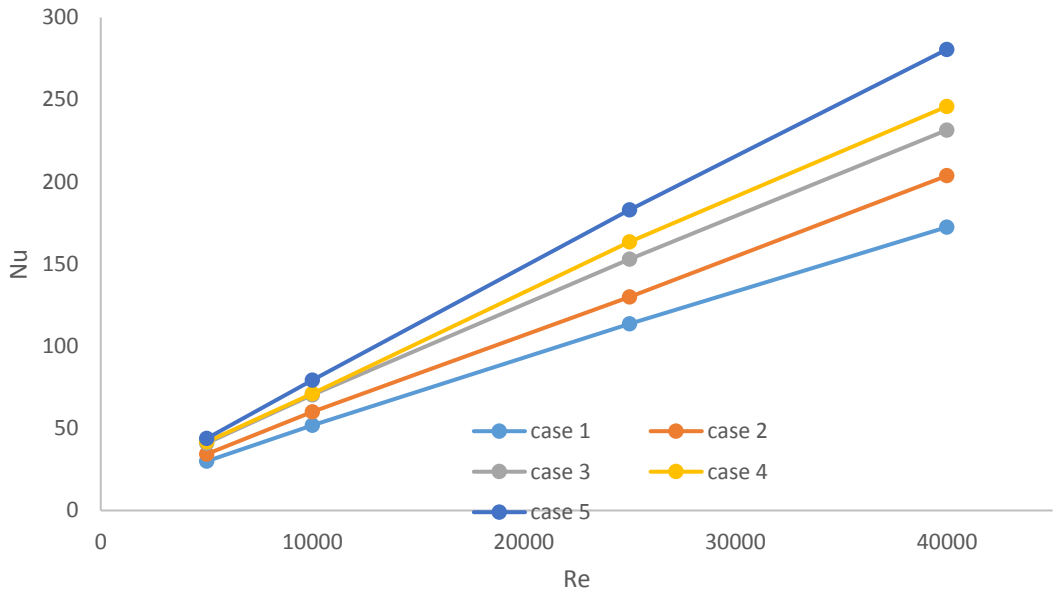

Figure 112 Comparison of Averaged Nusselt number

Figure 112 shows the averaged Nusselt number for all cases at different Reynolds numbers. As shown in the figure, Nu increases almost linearly as Re increases for the four different geometry configurations. At lower Re, the variation in Nu between the five configurations is not that noticeable, however as Re increases above 10,000 this variation starts to be more noticeable except for cases three and four where this variation maintains at minimum. This is due to the slight effects of the ribs before the bend on average heat transfer. Case five, as shown in the figure consider to be the best geometry configuration among all the other four cases as it shows high heat transfer due the geometry and the distribution of the ribs. A total increase in Nu of about 40% between case 1 and case 5 showing the importance of geometry configurations and ribs distribution on heat transfer rate.

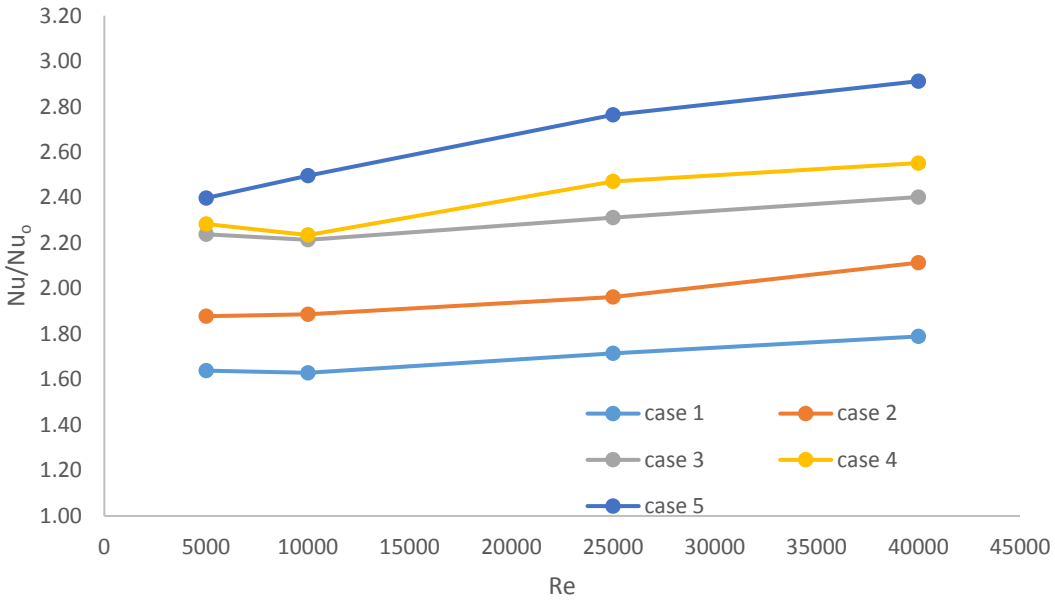

Figure 113 Comparison of Normalized Nusselt number

Figure 113 shows the normalized local Nusselt number to Nu^0 calculated from equation. Configurations from one to three show an improvement in normalized Nu as Re increases. Normalized Nu for cases four and five show a slight difference especially for Re less than 10,000 with an initial diminish in Nu for case four before it starts to increase when Re above 10,000. Almost a constant trend is shown in this figure for the first three configurations which then starts to be more like a linear trend for both cases four and five. The latter case shows a linear trend of normalized Nu with an increase of about 20% between Re=5,000 and 40,000. This percentage is less than 10% for all the other configurations.

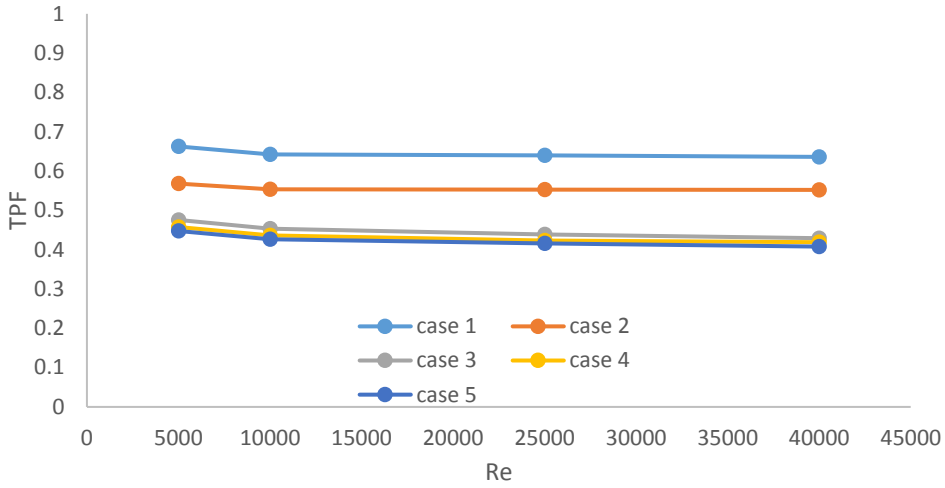

Figure 114 Comparison of thermal performance factor

Figure 114 shows thermal performance factor which is defined as the ratio of heat transfer to pressure drop against Re for all configurations. This figure shows that Re has no significant effect on this factor especially for Re more than 10,000 where it has a slight effect before this value. It is shown that the last three configurations have high pressure drop due to their complicated configurations which in general give a close TPF value to all these cases. However, for cases one and two, a noticeable TPF value difference between the two configurations indicating a minor flow pressure drop.

7.6 Chapter conclusion

The above studies were carried out to investigate how changing the geometry configurations affects the rate of heat transfer for a stationary heated duct. With different geometry configurations, the flow behaves significantly differently which is then reflected on the heat transfer rate. The placement of ribs and slots in general improves the heat transfer due to the flow turbulence caused by these. Also, the heat transfer contact

area is increased by the existence of these ribs and slots providing better heat transfer rate. A further investigation of the different numbers and arrangements of these ribs and slots were made by this study improved that, a proper number and configuration can be an effective heat transfer rate enhancement tool. Five different configurations were tested in this study, each configuration has its own ribs or slots number and configuration which should give a clear idea how the flow behaviour changes based on these configurations. The new introduced internal cooling geometry helped increase the heat transfer rate by 63%

8 Conclusion and Future Work

8.1 Preliminary consideration

Increases in gas turbine firing temperature have exceeded the temperature gains obtained by the improvements in gas turbine blade and nozzle guide vane materials. Current cooling approach still cannot satisfy the new high combustion chamber temperature. New approaches towards cooling is therefore required to satisfy these higher temperature trends. Current blade cooling configurations consist of internal and external cooling. Internal cooling research is the main purpose of these studies. Internal cooling methods include cooling passages within blades, impingement cooling, pin fin cooling and the roughening of walls with ribs to enhance the mixing in the flow through added turbulence. These techniques apply to both nozzle guide vanes and turbine rotor blades.

This thesis is concentrated with improving the heat removal performance of the internal cooling passages for gas turbine blade and nozzle guide vanes. The research covers three main area of investigation. The first one concerns the supply of mist on to the coolant flow as a mean to enhance heat transfer. The second area of investigation is the manipulation of secondary flows through cross section variation as means to improve the heat transfer.

Finally, a combination of a number of geometrical features in the passage is examined. Different configurations of labyrinth within the passage are studied together in combination with turbulators on order to accelerate heat transfer.

8.2 **Main Conclusions**

The analysis of the results obtained throughout this study permits the drawing of the following main conclusions. These are organised section by section.

Validation (objective 4):

- The backward facing step was chosen as a first case to be examined due to the separation and reattachment of the boundary layer occurring at the step. Grid dependency studies were carried out and the result was essentially identical for all meshes. The RNG k-ε turbulence model predicted the experimental result with an acceptable degree of accuracy and captured correctly the full profile shape and the maximum value of the Nusselt number.

- A simplified roughened channel was investigated numerically with periodic inlet and outlet boundary conditions and the results were compared with ERCOFTAC data A turbulence model study was carried out

- Results obtained with the k-ε and V2-F turbulence models returned velocity profiles which were closer to the experimental data when compared to the output of the other turbulence models used. However, the V2-F failed to capture the maximum value at the middle of the channel. Regarding the heat transfer calculations, the predictions for the Nusselt number failed to achieve the same level of accuracy as obtained for the velocity results. The k-ε turbulence model results were closer to the experimental average Nusselt number value but failed to capture the same profile. Furthermore, structured and unstructured mesh studies were conducted with two turbulence models and the k-ε result was different for the structured

and unstructured meshes, whilst the results obtained with the V2F model were similar for both types of meshes

- The 180-degree internal blade passages were examined with smooth and roughened walls. The wall roughening employs ribs in both passages upstream and downstream of the 180-degree bend which is kept smooth. Extra lengths were specified before the inlet in order for the fluid to become fully developed. The leading and trailing edges are heated and the side walls are kept as adiabatic walls. Non-rotating and rotating boundary conditions are considered to capture the rotating blade effects. The turbulence modelling studies were carried out with four models. For the rotating case, the RNG k-ε and k-ω SST computations of the Nusselt number were close to the experimental values at high and low speeds. In the presence of rotation, the leading and trailing edge Nusselt numbers are different due to the secondary flow created by rotation. In contrast the non-rotating case has identical Nusselt number profiles for the leading and trailing edges.

- A smooth duct with 180^{o} turn is investigated with injection of water droplets at the inlet. Validation studies were carried out and results compared with both experimental data and other numerical data available in the literature. Two turbulence models were employed. The results of these investigations were close to the experimental values but the better agreement was achieved at the outer wall when compared to the inner wall of the duct.

Mist addition studies (non-rotating cases) (objective 6):

- For the mist injection studies the injection is in the form of water droplets at the inlet surface. The droplets are distributed evenly

over the surface. Five mist ratios were employed to investigate the effects on heat transfer for non-rotating and rotating cases.

- It was observed that the ribs help recirculate the water particles and the concentration of water droplets near the trailing and leading edge walls just downstream of the ribs.

- As the mist ratio increases the Nusselt number is also seen to increase. The maximum heat transfer occurs in the first passage between the sixth and seventh rib for 0% and 1% mist. Furthermore, as the mist concentration increased beyond 2% the maximum heat transfer is shifted to the second passage. The heat transfer increases then significantly towards the outlet as the mist ratio increases. A 160% improvement, by comparison to the dry case, was achieved near the outlet with a 5% mist concentration.

- The average heat transfer exceeded 92% for the second passage and 26% enhancement for the first passage when compared to the dry case. While the overall heat transfer increased by 57% with 5% mist addition for the non-rotating case. Mist injection into the coolant stream helped to achieve up to a 300% increase in the average duct flow discharge temperature resulting into the extracting of more heat from the walls.

Mist addition studies (rotating cases):

- Particle concentration for the rotation cases downstream of the ribs is higher in the first passage. In the second passage due to the secondary flows created by the turning, the concentration of particles is less uniform. Furthermore, particles concentration near the trailing edge is higher than the leading edge and this is due to the rotation effects.

- For the trailing edge the maximum heat transfer occurs at the first passage just upstream of rib four. As the mist ratio increased the maximum heat transfer location start shifting upstream. With the mist injection beyond 3% the maximum heat transfer location moved to the second passage. The same observation is seen in the leading edge where the maximum heat transfer starts to move to the second passage.

- The average Nusselt number for the second passage leading edge increased by 71% for a 5% mist addition. This corresponded to an increase of 20% for the first passage leading edge. The overall average Nusselt number for the rotating case increased 41% with 5% mist injection.

- The overall Nusselt number for the rotating and non-rotating cases increased linearly as the mist ratio increased and were close in value until they reach 2% ratios. Beyond 3% mist ratios the difference in Nusselt number started to increase gradually. At high mist ratios the non-rotating case achieved an increase of 36% in heat transfer when compared to the rotating case.

Cross-section manipulation investigations (objective 5)

- Secondary flow investigations through cross-section manipulation were carried out for several modified cooling passages.

- Each case has a unique behaviour as the flow progresses through the modified cross section. This said the intensity of the secondary generally flow decreases when approaching the outlet.

- All result showed that the velocity and the structure of the secondary flow plays a large role on the heat transfer performance of the individual duct configurations.

- Some of the cases, 4, 5 and 6 showed good promise at low and high speeds. These cases can help to increase the heat transfer in specific areas where the maximum cooling is required.

- Cases 4 and 5 showed good results while employing the thermal performance factor as means of evaluation of the heat transfer. These results were combined with low pressure losses.

Multi heat removal enhancement techniques (objective 5):

- A number of new geometries were proposed for the cooling passage of either turbine rotor blades or nozzle guide vanes. Changes in cross section, wall turbulators and slots are heat removal enhancement features used in the new geometry.

- The highest heat transfer rate was obtained when all the features are used together. Slots accounted for the biggest factor in improving the heat transfer rate. The Nusselt number increased by 42% when slots are employed. And when ribs were added to the slots the Nusselt number increased by 63%.

Heat transfer enhancement arose when all technique is implemented. Mist addition showed great heat transfer enhancement among all technique studied.

8.3 **Future work**

A number of areas have been identified in which further work would improve the internal cooling of gas turbine. Recommendations regarding the potential for improvement of the internal cooling strategies and for possible future research avenues are outlined below.

- Investigate the effect of angled mist injection boundary conditions.

- Consider different mist ratios, from below 1% to higher than 5%. These high mist ratios can be employed in specific engine transients and are therefore worthy of further investigation.
- Examine the mist injection in combination with different rib patterns. These might include using orthogonal, v-shaped and w-shaped rib patterns.
- Explore further cross-section shapes to explore further enhancements of the heat transfer and secondary flows.
- Increase the second passage length in the U-duct to investigate its effect on the secondary flow strength and structure.
- Use different aspect ratios for the trapezoid duct and different trapezoid direction.
- Apply soft edges for the new proposed geometry to lower the pressure drop and maintain high heat transfer rate.
- Examine different rib pattern for the new geometry and investigate its effect the heat transfer and pressure drop.

REFERENCES

[1] R. Royce, The Jet Engine, Wiley, 2015.

[2] H.I.H. Saravanamuttoo, G.F.C. Rogers, H. Cohen, Gas Turbine Theory, Prentice Hall, 2001.

[3] J.H. Horlock, L. Torbidoni, Calculations of Cooled Turbine Efficiency, Journal of Engineering for Gas Turbines and Power. 130 (2008) 011703.

[4] J.H. Horlock, L. Torbidoni, Turbine Blade Cooling: The Blade Temperature Distribution, Proceedings of the Institution of Mechanical Engineers, Part A: Journal of Power and Energy. 220 (2006) 343–353.

[5] J.B. Young, J.H. Horlock, Defining the Efficiency of a Cooled Turbine, Journal of Turbomachinery. 128 (2006) 658.

[6] L. Torbidoni, J.H. Horlock, A New Method to Calculate the Coolant Requirements of a High-Temperature Gas Turbine Blade, Journal of Turbomachinery. 127 (2005) 191.

[7] H. Barrow, C.W. Pope, Droplet evaporation with reference to the effectiveness of water-mist cooling, Applied Energy. 84 (2007) 404–412.

[8] H. Montazeri, B. Blocken, J.L.M. Hensen, CFD analysis of the impact of physical parameters on evaporative cooling by a mist spray system, Applied Thermal Engineering. 75 (2015) 608–622.

[9] D.E. Metzger, W.B. Shepard, S.W. Haley, ROW RESOLVED HEAT TRANSFER VARIATIONS IN PIN-FIN ARRAYS INCLUDING EFFECTS OF NON-UNIFORM ARRAYS AND FLOW CONVERGENCE., in: American Society of Mechanical Engineers (Paper), Affiliation: Arizona State Univ, Tempe, AZ, USA, Arizona State Univ, Tempe, AZ, USA, 1986.

[10] G.S. Azad, M.J. Uddin, J.-C. Han, H.-K. Moon, B. Glezer, Heat Transfer in a Two-Pass Rectangular Rotating Channel With 45-deg Angled Rib Turbulators, Journal of Turbomachinery. 124 (2002) 251.

[11] G.M.S. Azad, J.M. Uddin, J.C. Han, H.K. Moon, B. Glezer, Heat Transfer in a Two-Pass Rectangular Rotating Channel with 45-Degree Angled Rib Turbulators, ASME Journal of Turbomachinery. 124 (2002) 251–259.

[12] T.S. Griffith, L. Al-Hadhrami, J.-C. Han, Heat transfer in rotating rectangular cooling channels (AR=4) with angled ribs, Journal of Heat Transfer. 124 (2002) 617–625.

[13] T.S. Griffith, L. Al-Hadhrami, J.-C. Han, Heat transfer in rotating rectangular cooling channels (AR = 4) with dimples, Journal of Turbomachinery. 125 (2003) 555–563.

[14] L. Al-Hadhrami, T. Griffith, J.-C.-C. Han, Heat transfer in two-pass

rotating rectangular channels (AR=2) with five different orientations of 45 deg v-shaped rib turbulators, Journal of Heat Transfer. 125 (2003) 232–242.

[15] J. Schabacker, A. Bolcs, B. V. Johnson, PIV investigation of the flow characteristics in an internal coolant passage with two ducts connected by a sharp 180° bend, in: American Society of Mechanical Engineers (Paper), ASME, 1998.

[16] E. a. Sewall, D.K. Tafti, Large Eddy Simulation of Flow and Heat Transfer in the 180-Deg Bend Region of a Stationary Gas Turbine Blade Ribbed Internal Cooling Duct, Journal of Turbomachinery. 128 (2006) 763.

[17] M. Amro, B. Weigand, R. Poser, M. Schnieder, An experimental investigation of the heat transfer in a ribbed triangular cooling channel, International Journal of Thermal Sciences. 46 (2007) 491–500.

[18] R. Jia, B. Sundén, M. Faghri, Computational Analysis of Heat Transfer Enhancement in Square Ducts With V-Shaped Ribs: Turbine Blade Cooling, Journal of Heat Transfer. 127 (2005) 425.

[19] H. Nakayama, M. Hirota, H. Fujita, T. Yamada, Y. Koide, Fluid Flow and Heat Transfer in Two-Pass Smooth Rectangular Channels With Different Turn Clearances, Journal of Turbomachinery. 128 (2006) 772.

[20] and C.R.S. Sushi S. G., Numerical Simulation of Gas Turbine Blade Cooling for Enhancement of Heat Transfer of the Blade Tip, International Journal of Research in Engineering and Technology. Vol. 03 (2014).

[21] Bunker, R.S., The Augmentation of Internal Blade Tip-Cap Cooling by Arrays of Shaped Pins, Journal of Turbomachinery. 130 (2008) 041007.

[22] S. Fujimoto, Y. Okita, Y. Fukuyama, T. Yamane, F. Mimura, M. Matsushita, Study on advanced internal cooling technologies for the development of next-generation small-class aircraft engines, in: Journal of Turbomachinery, Affiliation: IHI Corporation, Tokyo 190-1297, Japan; Affiliation: Japan Aerospace Exploration Agency, Tokyo 182-8522, Japan; Affiliation: Tokyo University of Agriculture and Technology, Tokyo 184-8588, Japan, 2008: pp. 431–441.

[23] S. Fujimoto, Y. Okita, C. Nakamata, Experimental study on the cooling performance of a turbine nozzle with an innovative internal cooling structure, in: Proceedings of the ASME Turbo Expo, Affiliation: IHI Corporation, Tokyo 190-1297, Japan, 2009: pp. 587–598.

[24] Y. Maikusa, T. Yoshida, S. Fujimoto, Y. Okita, Study on visualization of cooling airflow in a turbine nozzle with multiple slot cooling configuration, in: 9th International Symposium on Fluid Control Measurement and Visualization 2007, FLUCOME 2007, 2007: pp.

321–328.

[25] S. Fujimoto, Y. Okita, Y. Fukuyama, T. Yamane, F. Mimura, M. Matsushita, et al., Study on Advanced Internal Cooling Technologies for the Development of Next-Generation Small-Class Aircraft Engines, Journal of Turbomachinery. 132 (2010) 031019.

[26] C.W. Metzger, D. E., and Plevich, Effects of Turn Region Treatments on Pressure Loss Through Sharp 180 deg Bends, in: Third International Symposium on Transport Phenomena and Dynamics of Rotating Machinery, 1990: pp. 301–312.

[27] M. Gallo, T. Astarita, G.M. Carlomagno, Heat transfer measurements in a rotating two-pass square channel, Quantitative InfraRed Thermography Journal. 4 (2007) 41–62.

[28] H. Iacovides, B.E. Launder, H.Y. Li, The computation of flow development through stationary and rotating U-ducts of strong curvature, International Journal of Heat and Fluid Flow. 17 (1996) 22–33.

[29] S. Acharya, R.G. Hibbs, Y. Chen, D.E. Nikitopoulos, Mass/Heat Transfer in a Ribbed Passage With Cylindrical Vortex Generators: The Effect of Generator-Rib Spacing, Journal of Heat Transfer. 122 (2000) 641.

[30] M. Elfert, M. Voges, J. Winner, Detailed flow investigation using PIV in a rotating square-sectioned two-pass cooling system with ribbed walls, in: Proceedings of the ASME Turbo Expo, 2008: pp. 1039–1050.

[31] D.C. Wilcox, Simulation of transition with a two-equation turbulence model, AIAA Journal. 32 (1994) 247–255.

[32] Y.-L. Lin, T.I.-P. Shih, M. a. Stephens, M.K. Chyu, A Numerical Study of Flow and Heat Transfer in a Smooth and Ribbed U-Duct With and Without Rotation, Journal of Heat Transfer. 123 (2001) 219.

[33] M.A. Stephens, T.I.P. Shih, Flow and heat transfer in a smooth U-duct with and without rotation, Journal of Propulsion and Power. 15 (1999) 272–279.

[34] J.-C. Han, H.-C. Chen, Turbine Blade Internal Cooling Passages with Rib Turbulators, Journal of Propulsion and Power. 22 (2006) 226–248.

[35] W.-L.-L. Fu, L.M. Wright, J.-C.-C. Han, Rotational buoyancy effects on heat transfer in five different aspect-ratio rectangular channels with smooth walls and 45 degree ribbed walls, Journal of Heat Transfer. 128 (2006) 1130–1141.

[36] M. Al-Qahtani, Y.-J. Jang, H.-C. Chen, J.-C. Han, Flow and heat transfer in rotating two-pass rectangular channels (AR=2) by Reynolds stress turbulence model, International Journal of Heat and Mass Transfer. 45 (2002) 1823–1838.

[37] Y. Li, H. Deng, G. Xu, S. Tian, Heat transfer investigation in rotating smooth square U-duct with different wall-temperature ratios and channel orientations, International Journal of Heat and Mass Transfer. 89 (2015) 10–23.

[38] J.C. Han, S. Dutta, S. Ekkad, Gas Turbine Heat Transfer and Cooling Technology, Taylor & Francis, 2001.

[39] E. Lee, L.M. Wright, J.-C. Han, Heat Transfer in Rotating Rectangular Channels with V-Shaped and Angled Ribs, Journal of Thermophysics and Heat Transfer. 19 (2005) 48–56.

[40] a. K. Saha, S. Acharya, Unsteady Flow and Heat Transfer in Parallel-Plate Heat Exchangers With in-Line and Staggered Arrays of Posts, 2004.

[41] H. Iacovides, B.E. Launder, Parametric and numerical study of fully developed flow and heat transfer in rotating rectangular ducts, Journal of Turbomachinery. 113 (1991) 331–338.

[42] C. Prakash, R. Zerkle, Prediction of turbulent flow and heat transfer in a radially rotating square duct, in: TRANS.ASME-J.TURBOMACHINERY, Affiliation: General Electric Co, Cincinnati, United States, 1992: pp. 835–846.

[43] T. Bo, H. Iacovides, B.E. Launder, Developing buoyancy-modified turbulent flow in ducts rotating in orthogonal mode, Transactions - ASME: Journal of Turbomachinery. 117 (1995) 474–484.

[44] J.H. Wagner, B. V Johnson, F.C. Kopper, Heat transfer in rotating serpentine passages with smooth walls, Journal of Turbomachinery. 113 (1991) 321–330.

[45] J.C. Han, Y.M. Zhang, C.P. Lee, Influence of Surface Heat Flux Ratio on Heat Transfer Augmentation in Square Channels With Parallel, Crossed, and V-Shaped Angled Ribs, Journal of Turbomachinery. 114 (1992) 872.

[46] S.P. Harasgama, W.D. Morris, The Influence of Rotation on the Heat Transfer Characteristics of Circular, Triangular and Square-Sectioned Coolant Passages of Gas Turbine Rotor Blades, ASME Journal of Turbomachinery. 110 (1988) 44–50.

[47] Y.-H.-H. Liu, M. Huh, D.-H.-H. Rhee, J.-C.-C. Han, H.-K.-K. Moon, Heat Transfer in Leading Edge, Triangular Shaped Cooling Channels With Angled Ribs Under High Rotation Numbers, Journal of Turbomachinery. 131 (2009) 041017.

[48] S. Dutta, J.-C. Han, C.P. Lee, Local heat transfer in a rotating two-pass ribbed triangular duct with two model orientations, International Journal of Heat and Mass Transfer. 39 (1996) 707–715.

[49] S. Dutta, J.-C.-C. Han, Y. Zhang, C.P. Lee, Local Heat Transfer in a Rotating Two-Pass Triangular Duct With Smooth Walls, Journal of Turbomachinery. 118 (1996) 435.

[50] W.D. Morris, R. Salemi, An attempt to uncouple the effect of Coriolis and buoyancy forces experimentally on heat transfer in smooth circular tubes that rotate in the orthogonal mode, TRANS.ASME-J.TURBOMACHINERY. 114 (1992) 858–864.

[51] J.H. Wagner, B. V Johnson, R.A. Graziani, F.C. Yeh, Heat transfer in rotating serpentine passages with trips normal to the flow, in: American Society of Mechanical Engineers (Paper), Affiliation: United Technologies Research Cent, East Hartford, United States, 1991.

[52] T.-M. Liou, C.-C. Chen, M.-Y. Chen, Rotating Effect on Fluid Flow in Two Smooth Ducts Connected by a 180-Degree Bend, Journal of Fluids Engineering. 125 (2003) 138.

[53] T.-M. Liou, M.-Y. Chen, Y.-M. Wang, Heat Transfer, Fluid Flow, and Pressure Measurements Inside a Rotating Two-Pass Duct With Detached 90-Deg Ribs, Journal of Turbomachinery. 125 (2003) 565.

[54] T.-S. Wang, M.K. Chyu, Heat convection in a 180-deg turning duct with different turn configurations, Journal of Thermophysics and Heat Transfer. 8 (1994) 595–601.

[55] M. Hirota, H. Fujita, L. Cai, H. Nakayama, M. Yanagida, A. Syafa'at, Heat (mass) transfer in rectangular cross-sectioned two-pass channels with an inclined divider wall, International Journal of Heat and Mass Transfer. 45 (2002) 1093–1107.

[56] D. V. Rao, C. Babu, S. Prabhu, Effect of Turn Region Treatments on the Pressure Loss Distribution in a Smooth Square Channel with Sharp 180 Bend, The International Journal of Rotating Machinery. 10 (2004) 459–468.

[57] J. Luo, E.H. Razinsky, Analysis of Turbulent Flow in 180 deg Turning Ducts With and Without Guide Vanes, Journal of Turbomachinery. 131 (2009) 021011.

[58] M. Schüler, F. Zehnder, B. Weigand, J. von Wolfersdorf, S.O. Neumann, The Effect of Side Wall Mass Extraction on Pressure Loss and Heat Transfer of a Ribbed Rectangular Two-Pass Internal Cooling Channel, Journal of Turbomachinery. 133 (2011) 021002.

[59] K. Saha, S. Acharya, Effect of Bend Geometry on Heat Transfer and Pressure Drop in a Two-Pass Coolant Square Channel for a Turbine, Journal of Turbomachinery. 135 (2012) 021035.

[60] K. Saha, S. Acharya, Bend Geometries in Internal Cooling Channels for Improved Thermal Performance, Journal of Turbomachinery. 135 (2013) 031028. doi:10.1115/1.4007582.

[61] H. Namgoong, H. Namgoong, C. Son, C. Son, P. Ireland, P. Ireland, U-bend Shaped Turbine Blade Cooling Passage Optimization, Aiaa. (2008) 1–9.

[62] B. Wang, W. Zhang, G. Xie, Y. Xu, M. Xiao, Multiconfiguration Shape Optimization of Internal Cooling Systems of a Turbine Guide

Vane Based on Thermomechanical and Conjugate Heat Transfer Analysis, Journal of Heat Transfer. 137 (2015) 061004.

[63] S.C. Siw, M.K. Chyu, M.A. Alvin, Investigation of Heat Transfer Enhancement and Pressure Characteristics, (2012) 1–11.

[64] J.C. Han, HEAT TRANSFER AND FRICTION CHARACTERISTICS IN RECTANGULAR CHANNELS WITH RIB TURBULATORS., Journal of Heat Transfer. 110 (1988) 321–328.

[65] W. Peng, P.-X. Jiang, Y.-P. Wang, B.-Y. Wei, Experimental and numerical investigation of convection heat transfer in channels with different types of ribs, Applied Thermal Engineering. 31 (2011) 2702–2708.

[66] G.A. Ledezma, R.S. Bunker, The Optimal Distribution of Chordwise Rib Fin Arrays for Blade Tip Cap Underside Cooling, Journal of Turbomachinery. 136 (2013) 11007.

[67] G. Xie, B. Sundén, Numerical predictions of augmented heat transfer of an internal blade tip-wall by hemispherical dimples, International Journal of Heat and Mass Transfer. 53 (2010) 5639–5650.

[68] C. Wang, L. Wang, B. Sundén, Heat transfer and pressure drop in a smooth and ribbed turn region of a two-pass channel, Applied Thermal Engineering. 85 (2015) 225–233.

[69] G. Xie, W. Zhang, B. Sunden, Computational analysis of the influences of guide ribs/vanes on enhanced heat transfer of a turbine blade tip-wall, International Journal of Thermal Sciences. 51 (2012) 184–194.

[70] H. Chung, J.S. Park, S. Park, S.M. Choi, D.-H. Rhee, H.H. Cho, Augmented heat transfer with intersecting rib in rectangular channels having different aspect ratios, International Journal of Heat and Mass Transfer. 88 (2015) 357–367.

[71] A.P. Rallabandi, H. Yang, J.-C. Han, Heat Transfer and Pressure Drop Correlations for Square Channels With 45 Deg Ribs at High Reynolds Numbers, Journal of Heat Transfer. 131 (2009) 071703.

[72] F. Coletti, M. Scialanga, T. Arts, Experimental Investigation of Conjugate Heat Transfer in a Rib-Roughened Trailing Edge Channel With Crossing Jets, Journal of Turbomachinery. 134 (2012) 041016.

[73] A. Murata, S. Mochizuki, Large eddy simulation with a dynamic subgrid-scale model of turbulent heat transfer in an orthogonally rotating rectangular duct with transverse rib turbulators, International Journal of Heat and Mass Transfer. 43 (2000) 1243–1259.

[74] A.K. Viswanathan, D.K. Tafti, Detached eddy simulation of flow and heat transfer in fully developed rotating internal cooling channel with normal ribs, International Journal of Heat and Fluid Flow. 27 (2006) 351–370.

[75] A.K. Viswanathan, D.K. Tafti, Detached eddy simulation of turbulent flow and heat transfer in a two-pass internal cooling duct, International Journal of Heat and Fluid Flow. 27 (2006) 1–20.

[76] J.C. Han, L.M. Wright, Enhanced internal cooling of turbine blades and vanes lecture, Texas A&M University, College Station, Texas 77843-3123, USA, n.d.

[77] R. Jia, B. Sundén, Prediction of Turbulent Heat Transfer and Fluid Flow in 2D Channels Roughened by Square and Deformed Ribs, Volume 5: Turbo Expo 2003, Parts A and B. (2003) 143–152.

[78] G. Xie, J. Liu, W. Zhang, G. Lorenzini, C. Biserni, Numerical Prediction of Turbulent Flow and Heat Transfer Enhancement in a Square Passage With Various Truncated Ribs on One Wall, Journal of Heat Transfer. 136 (2013) 011902.

[79] T. Arts, G. Rau, M. Çakan, J. Vialonga, D. Fernandez, F. Tarnowski, et al., Experimental and numerical investigation on flow and heat transfer in large-scale, turbine cooling, representative, rib-roughened channels, Proceedings of the Institution of Mechanical Engineers, Part A: Journal of Power and Energy . 211 (1997) 263–272.

[80] H. Iacovides, D.C. Jackson, H. Ji, G. Kelemenis, B.E. Launder, K. Nikas, LDA study of the flow development through an orthogonally rotating u-bend of strong curvature and rib roughened walls, in: American Society of Mechanical Engineers (Paper), Affiliation: Department of Mechanical Engineering, UMIST, P.O. Box 88, Manchester M60 1QD, United Kingdom, 1996: pp. 386–391.

[81] J.C. Han, L.R. Glicksman, W.M. Rohsenow, An investigation of heat transfer and friction for rib-roughened surfaces, International Journal of Heat and Mass Transfer. 21 (1978) 1143–1156.

[82] J.C. Han, J.S. Park, C.K. Lei, HEAT TRANSFER ENHANCEMENT IN CHANNELS WITH TURBULENCE PROMOTERS., Journal of Engineering for Gas Turbines and Power. 107 (1985) 628–635.

[83] J.C. Han, J.S. Park, Developing heat transfer in rectangular channels with rib turbulators, International Journal of Heat and Mass Transfer. 31 (1988) 183–195.

[84] J.C. Han, S. Ou, J.S. Park, C.K. Lei, Augmented heat transfer in rectangular channels of narrow aspect ratios with rib turbulators, International Journal of Heat and Mass Transfer. 32 (1989) 1619–1630.

[85] J.C. Han, P. Zhang, Effect of rib-angle orientation on local mass transfer distribution in a three-pass rib-roughened channel, Journal of Turbomachinery. 113 (1991) 123–130.

[86] D.N. Ryu, D.H. Choi, V.C. Patel, Analysis of turbulent flow in channels roughened by two-dimensional ribs and three-dimensional blocks. Part II: Heat transfer, International Journal of Heat and Fluid Flow. 28 (2007) 1112–1124.

[87] D.N. Ryua, D.H. Choia, V.C. Patel, Analysis of turbulent flow in channels roughenedby two-dimensional ribs and three-dimensional blocks. Part I: heat transfer, International Journal of Heat and Fluid Flow. 28 (2007) 1112–1124.

[88] Y.-J.J. Jang, H.-C.C. Chen, J.-C.C. Han, Flow and Heat Transfer in a Rotating Square Channel With 45 deg Angled Ribs by Reynolds Stress Turbulence Model, ASME Journal of Turbomachinery. 123 (2001) 124.

[89] J.C. Han, Y.M. Zhang, High performance heat transfer ducts with parallel broken and V-shaped broken ribs, International Journal of Heat and Mass Transfer. 35 (1992) 513–523.

[90] J.-C. Han, J.J. Huang, C.P. Lee, Augmented heat transfer in square channels with wedge-shaped and delta-shaped turbulence promoters, Journal of Enhanced Heat Transfer. 1 (1993) 37–52.

[91] S. V Ekkad, Y. Huang, J.-C. Han, Detailed heat transfer distributions in two-pass square channels with rib turbulators and bleed holes, International Journal of Heat and Mass Transfer. 41 (1998) 3781–3791.

[92] S.C. Lau, R.T. Kukreja, R.D. Mcmillin, Effects of V-shaped rib arrays on turbulent heat transfer and friction of fully developed flow in a square channel, International Journal of Heat and Mass Transfer. 34 (1991) 1605–1616.

[93] M.E. Taslim, L.A. Bondi, D.M. Kercher, Experimental investigation of heat transfer in an orthogonally rotating channel roughened with 45 deg criss-cross ribs on two opposite walls, Journal of Turbomachinery. 113 (1991) 346–353.

[94] M.E. Taslim, T. Li, D.M. Kercher, D.M. Kerchar, Experimental heat transfer and friction in channels roughened with angled, V-shaped, and discrete ribs on two opposite walls, Journal of Turbomachinery. 118 (1996) 20–28.

[95] X. Gao, B. Sundén, Heat transfer and pressure drop measurements in rib-roughened rectangular ducts, Experimental Thermal and Fluid Science. 24 (2001) 25–34.

[96] X. Gao, B. Sund´en, B. Sundén, Effects of inclination angle of ribs on the flow behavior in rectangular ducts, Journal of Fluids Engineering, Transactions of the ASME. 126 (2004) 692–699.

[97] H.H. Cho, S.J. Wu, H.J. Kwon, Local heat/mass transfer measurements in a rectangular duct with discrete ribs, Journal of Turbomachinery. 122 (2000) 579–586.

[98] H.H. Cho, Y.Y. Kim, K.M. Kim, D.H. Rhee, Effects of rib arrangements and rotation speed on heat transfer in a two-pass duct, in: American Society of Mechanical Engineers, International Gas Turbine Institute, Turbo Expo (Publication) IGTI, Affiliation: Department of Mechanical Engineering, Yonsei University, Seoul

120-749, South Korea, 2003: pp. 433–442.

[99] H.H. Cho, S.Y. Lee, J.H. Won, D.H. Rhee, Heat/mass transfer in a two-pass rotating rectangular duct with and without 70°-angled ribs, Heat and Mass Transfer/Waerme- Und Stoffuebertragung. 40 (2004) 467–475.

[100] D.H. Lee, D.-H. Rhee, K.M. Kim, H.H. Cho, H.K. Moon, Detailed measurement of heat/mass transfer with continuous and multiple V-shaped ribs in rectangular channel, Energy. 34 (2009) 1770–1778.

[101] E. Lee, L.M. Wright, J.-C. Han, Heat transfer in rotating rectangular channels (AR = 4:1) with V-shaped and angled rib turbulators with and without gaps, in: American Society of Mechanical Engineers, International Gas Turbine Institute, Turbo Expo (Publication) IGTI, Affiliation: Turbine Heat Transfer Laboratory, Department of Mechanical Engineering, Texas A and M University, College Station, TX, United States, 2003: pp. 661–670.

[102] L.M. Wright, W.-L.-L. Fu, J.-C.-C. Han, Thermal performance of angled, V-shaped, and W-shaped rib turbulators in rotating rectangular cooling channels (AR=4:1), Journal of Turbomachinery. 126 (2004) 604–614.

[103] H. Iacovides, G. Kelemenis, M. Raisee, Flow and heat transfer in straight cooling passages with inclined ribs on opposite walls: An experimental and computational study, Experimental Thermal and Fluid Science. 27 (2003) 283–294.

[104] L. Al-Hadhrami, J.-C. Han, Effect of rotation on heat transfer in two-pass square channels with five different orientations of 45° angled rib turbulators, International Journal of Heat and Mass Transfer. 46 (2003) 653–669.

[105] S.W. Chang, T.L. Yang, T.-M.M. Liou, G.F. Hong, Heat transfer of rotating rectangular duct with compound scaled roughness and V-ribs at high rotation numbers, International Journal of Thermal Sciences. 48 (2009) 174–187.

[106] M. Huh, J.-C. Han, Recent Studies in Turbine Blade Internal Cooling, Heat Transfer Research. 41 (2010) 803–828.

[107] R. Bhargava, C.B. Meher-Homji, Parametric Analysis of Existing Gas Turbines With Inlet Evaporative and Overspray Fogging, in: Volume 4: Turbo Expo 2002, Parts A and B, ASME, 2002: pp. 387–401.

[108] M. Chaker, C.B. Meher-Homji, T. Mee, Inlet Fogging of Gas Turbine Engines: Part B — Fog Droplet Sizing Analysis, Nozzle Types, Measurement and Testing, in: Volume 4: Turbo Expo 2002, Parts A and B, ASME, 2002: pp. 429–441.

[109] M. Chaker, C.B. Meher-Homji, T. Mee, Inlet Fogging of Gas Turbine Engines: Part C — Fog Behavior in Inlet Ducts, CFD Analysis and Wind Tunnel Experiments, in: Volume 4: Turbo Expo 2002, Parts A

and B, ASME, 2002: pp. 443–455.

[110] M. Chaker, C.B. Meher-Homji, T. Mee, Inlet Fogging of Gas Turbine Engines: Part A — Fog Droplet Thermodynamics, Heat Transfer and Practical Considerations, in: Volume 4: Turbo Expo 2002, Parts A and B, ASME, 2002: pp. 413–428.

[111] T. Wang, X. Li, V. Pinninti, Simulation of Mist Transport for Gas Turbine Inlet Air Cooling, Numerical Heat Transfer, Part A: Applications. 53 (2008) 1013–1036.

[112] V. Bahadur, M. Hodes, A. Lyons, S. Krishnan, S. V. Garimella, Enhanced cooling in a sealed cabinet using an evaporating-condensing dielectric mist, 2008 11th IEEE Intersociety Conference on Thermal and Thermomechanical Phenomena in Electronic Systems, I-THERM. (2008) 1191–1198.

[113] N. Kumari, V. Bahadur, M. Hodes, T. Salamon, P. Kolodner, A. Lyons, et al., Analysis of evaporating mist flow for enhanced convective heat transfer, International Journal of Heat and Mass Transfer. 53 (2010) 3346–3356.

[114] X. Li, T. Wang, Two-Phase Flow Simulation of Mist Film Cooling on Turbine Blades With Conjugate Internal Cooling, Journal of Heat Transfer. 130 (2008) 102901.

[115] T.S. Dhanasekaran, T. Wang, Simulation of Mist Film Cooling on Rotating Gas Turbine Blades, Journal of Heat Transfer. 134 (2012) 011501.

[116] Y. Jiang, Q. Zheng, P. Dong, G. Yue, J. Gao, Numerical Simulation on Turbine Blade Leading-Edge High-Efficiency Film Cooling by the Application of Water Mist, Numerical Heat Transfer, Part A: Applications. 66 (2014) 1341–1364.

[117] T. Guo, T. Wang, J.L. Gaddis, Mist/steam cooling in a heated horizontal tube-Part 1: Experimental system, Journal of Turbomachinery. 122 (2000) 360–365.

[118] T. Guo, T. Wang, J.L. Gaddis, Mist / Steam Cooling in a Heated Horizontal Tube — Part 2 : Results and Modeling, 122 (2000).

[119] M.A. a. Pakhomov, V.I.I. Terekhov, Enhancement of an impingement heat transfer between turbulent mist jet and flat surface, International Journal of Heat and Mass Transfer. 53 (2010) 3156–3165.

[120] T. Wang, R. Ragab, Investigation of Applicability of Transporting Water Mist for Cooling Turbine Blades, (2014).

[121] M.Q. Brewster, Evaporation and condensation of water mist/cloud droplets with thermal radiation, International Journal of Heat and Mass Transfer. 88 (2015) 695–712.

[122] X. Li, J.L. Gaddis, T. Wang, Multiple flow patterns and heat transfer in confined jet impingement, International Journal of Heat and Fluid

Flow. 26 (2005) 746–754.

[123] X. Li, J.L. Gaddis, T. Wang, Mist/steam heat transfer with jet impingement onto a concave surface, Journal of Heat Transfer. 125 (2003) 438–446.

[124] N. V Nirmalan, J.A. Weaver, L.D. Hylton, An experimental study of turbine vane heat transfer with water-air cooling, Journal of Turbomachinery. 120 (1998) 50–60.

[125] T. Wang, J.L. Gaddis, X. Li, Mist/steam heat transfer of multiple rows of impinging jets, International Journal of Heat and Mass Transfer. 48 (2005) 5179–5191.

[126] X. Tan, J. Zhang, B. Liu, X. Zhu, Experimental investigation on heat transfer enhancement of mist/air impingement jet, Science China Technological Sciences. 56 (2013) 2456–2464.

[127] T.S. Dhanasekaran, T. Wang, Computational analysis of mist/air cooling in a two-pass rectangular rotating channel with 45-deg angled rib turbulators, International Journal of Heat and Mass Transfer. 61 (2013) 554–564.

[128] T.S. Dhanasekaran, T. Wang, Numerical model validation and prediction of mist/steam cooling in a 180-degree bend tube, International Journal of Heat and Mass Transfer. 55 (2012) 3818–3828.

[129] T. Guo, T. Wang, J.L. Gaddis, Mist/steam cooling in a 180-degree tube bend, Journal of Heat Transfer. 122 (2000) 749–756.

[130] Y. Mori, K. Hijikata, T. Yasunaga, Mist cooling of very hot tubules with reference to through-hole cooling of gas turbine blades, International Journal of Heat and Mass Transfer. 25 (1982) 1271–1278.

[131] Ting Wang J. Leo Gaddi Xianchang Li, Mist/Steam Cooling for Advanced Turbine Systems, in: n.d.

[132] V.I.T. and M.A. Pakhomov, Particle dispersion and turbulence modification in a dilute mist non-isothermal turbulent flow downstream of a sudden pipe expansion, Journal of Physics: Conference Series. 318 (2011) 92019.

[133] B. BALDWIN, H. LOMAX, Thin-layer approximation and algebraic model for separated turbulentflows, in: 16th Aerospace Sciences Meeting, American Institute of Aeronautics and Astronautics, 1978.

[134] M. Kato, B. Launder E., The Modelling of Turbulent Flow Around Stationary and Vibrating Square Cylinders, (1993).

[135] N.Z. Ince, B.E. Launder, Three-dimensional and heat-loss effects on turbulent flow in a nominally two-dimensional cavity, International Journal of Heat and Fluid Flow. 16 (1995) 171–177.

[136] J.H. Ferziger, Computational methods for fluid dynamics, Springer, Berlin ; London, 1999.

[137] F.R. Menter, Two-equation eddy-viscosity turbulence models for engineering applications, AIAA Journal. 32 (1994) 1598–1605.

[138] B.E. Launder, D.B. Spaulding, Mathematical Models of Turbulence, Academic Press, 1972.

[139] P.A. Durbin, Near-wall turbulence closure modeling without “damping functions,” Theoretical and Computational Fluid Dynamics. 3 (1991) 1–13.

[140] P.A. Durbin, A Reynolds stress model for near-wall turbulence, Journal of Fluid Mechanics. 249 (1993) 465–498.

[141] P.A. Durbin, Separated flow computations with the k-ε-v2 model, AIAA Journal. 33 (1995) 659–664.

[142] F.-S. Lien, G. Kalitzin, Computations of transonic flow with the v2-f turbulence model, International Journal of Heat and Fluid Flow. 22 (2001) 53–61.

[143] I. Ansys, Fluent 14 theory guide, Ansys, Inc, NH USA, 2012.

[144] P.J. O’Rourke, A.A. Amsden, The tab method for numerical calculation of spray droplet breakup, SAE Technical Papers. (1987).

[145] H. Le, P. Moin, Direct numerical simulation of turbulent flow over a backward-facing step, 1993.

[146] W.-L. Fu, aspect ratio effect on heat transfer in rotating two-pass rectangular channels with smooth walls and ribbed walls, (2005).

[147] X. Li, T. Wang, Simulation of Film Cooling Enhancement With Mist Injection, Journal of Heat Transfer. 128 (2006) 509.

[148] T.S. Dhanasekaran, T. Wang, mist/air cooling in a two-pass rectangular rotating channel with 45-deg angled rib turbulators, (2011) 1–10.

9 Appendix

Case 1

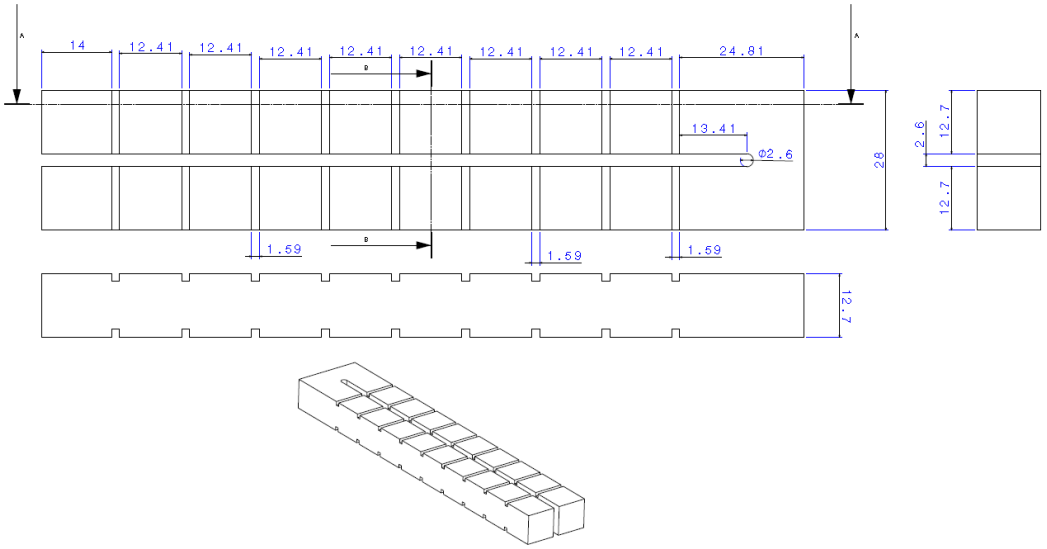

Case 2

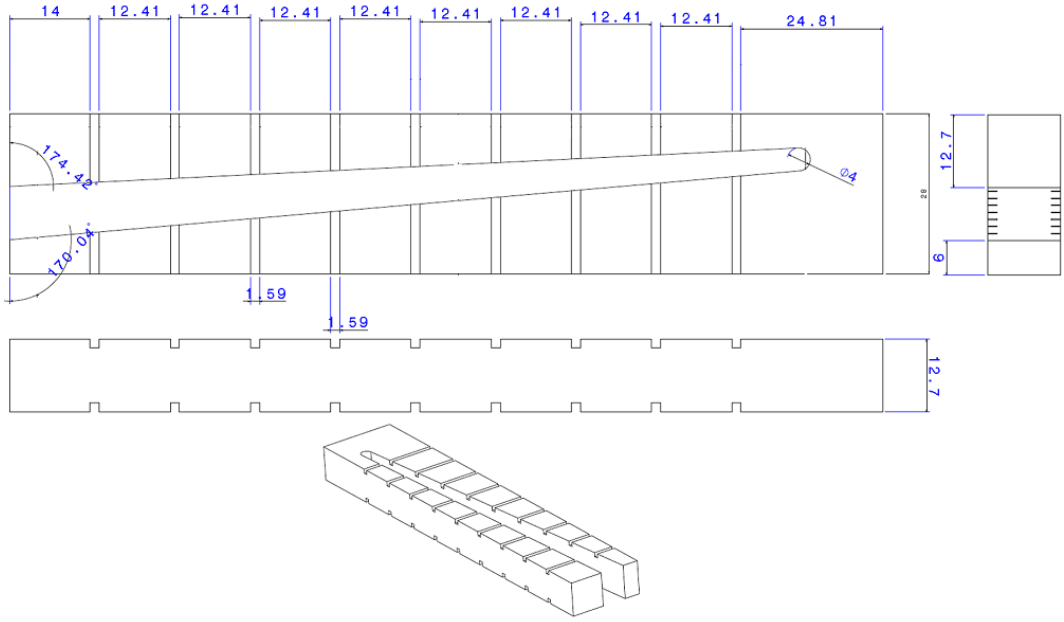

Case 3

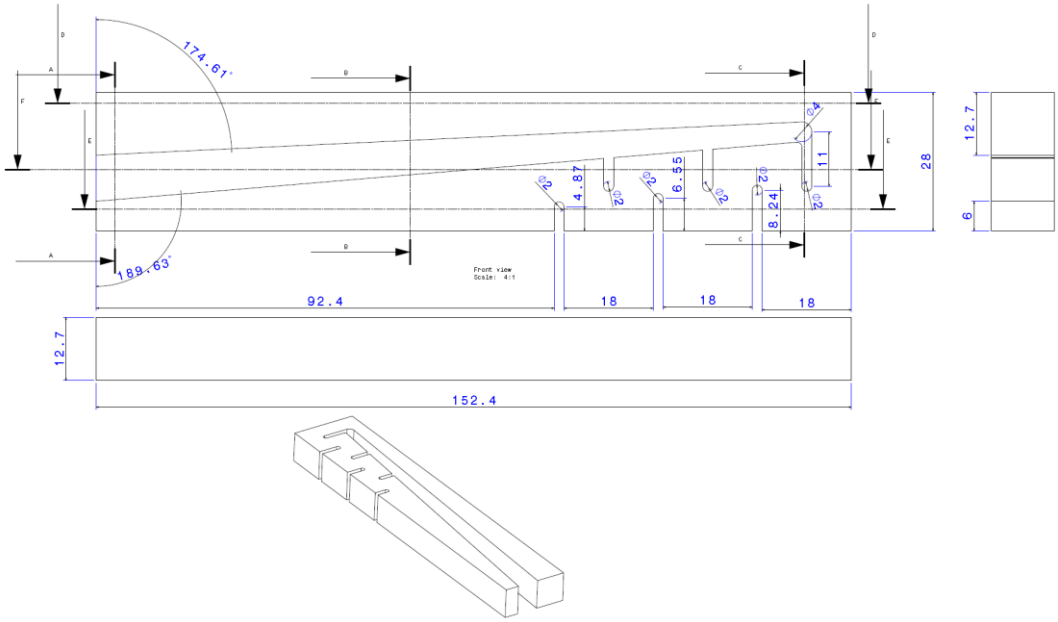
174.61°
189.63°
92.4
18
18
18
152.4
12.7
28
6
4.87
6.55
8.24
11
Front view
Scale: 4:1

Case 4

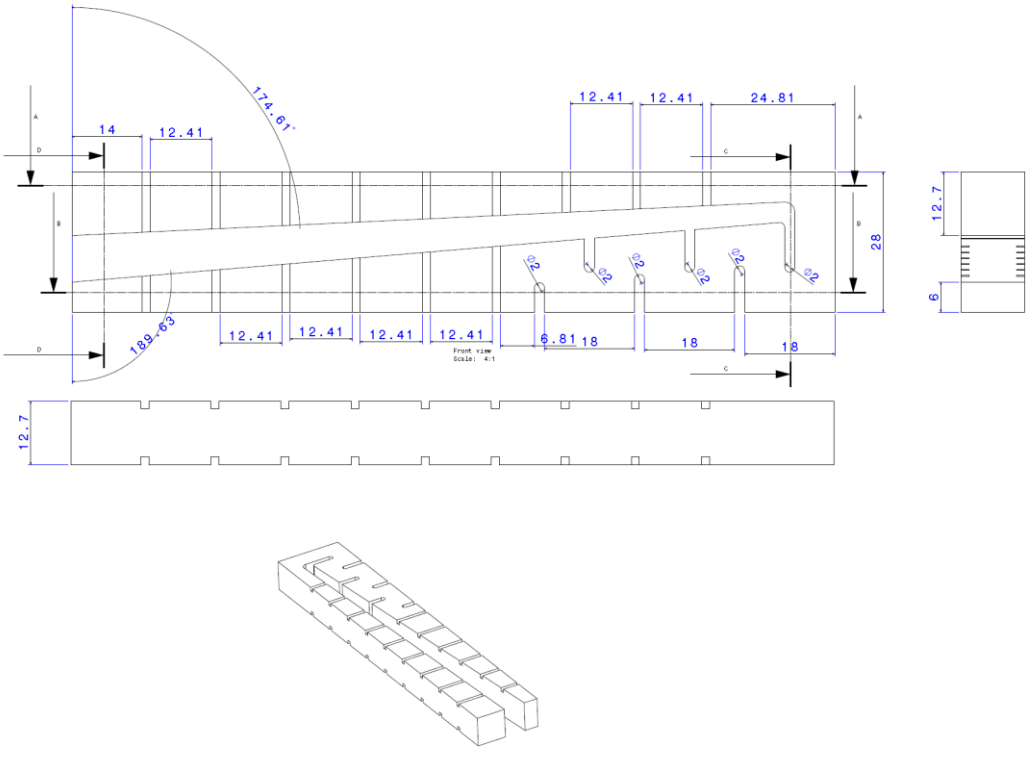
174.61°
189.63°
14
12.41
12.41
12.41
12.41
12.41
12.41
24.81
6.81
18
18
18
12.7
28
6
Front view
Scale: 4:1

Case 5

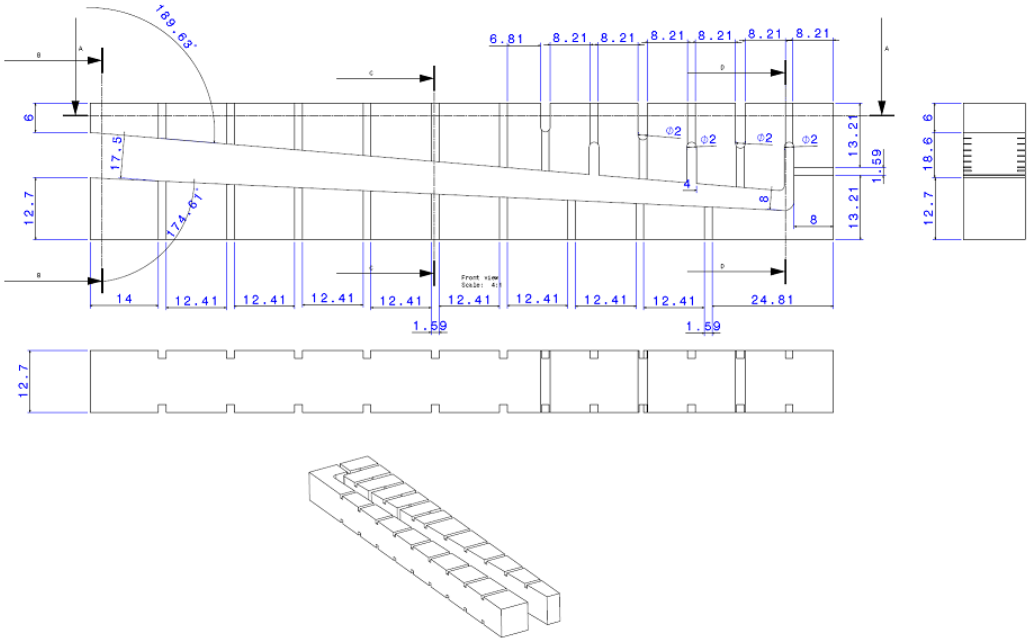
189.63°
6.81
8.21
8.21
8.21
8.21
8.21
8.21
6
17.5
12.7
174.67°
Ø2
Ø2
Ø2
Ø2
4
8
8
13.21
1.59
13.21
18.6
6
12.7
14
12.41
12.41
12.41
12.41
12.41
12.41
12.41
12.41
24.81
1.59
1.59
12.7